THE UNIVERSITY
of ADELAIDE

PhD Thesis

MILD Combustion of Prevaporised Liquid Fuels

Jingjing Ye

School of Mechanical Engineering

July 2017

Declaration

I certify that this work contains no material which has been accepted for the award of any other degree or diploma in my name, in any university or other tertiary institution and, to the best of my knowledge and belief, contains no material previously published or written by another person, except where due reference has been made in the text. In addition, I certify that no part of this work will, in the future, be used in a submission in my name, for any other degree or diploma in any university or other tertiary institution without the prior approval of the University of Adelaide and where applicable, any partner institution responsible for the joint-award of this degree.

I give consent to this copy of my thesis when deposited in the University Library, being made available for loan and photocopying, subject to the provisions of the Copyright Act 1968.

I acknowledge that copyright of published works contained within this thesis resides with the copyright holder(s) of those works.

I also give permission for the digital version of my thesis to be made available on the web, via the Universitys digital research repository, the Library Search and also through web search engines, unless permission has been granted by the University to restrict access for a period of time.

Jingjing Ye

Signed: _____

Date: _____

Acknowledgements

It is impossible to thank the countless people who have helped and encouraged me here. I apologise to those people whom I missed in this acknowledgements.

I am deeply grateful for the continuous support and guidance that my supervisors, Prof. Bassam Dally and Assoc. Prof. Paul Medwell, have offered to me throughout my PhD. Their superb knowledge and expertise have proved invaluable in helping me produce scientific work. Their never-ending passion for science and persistent efforts to improve my work have always inspired me to become a better researcher. It has been a great pleasure and I consider myself very fortunate to have worked with them.

I want to thank Prof. Bassam Dally for teaching me a well-structured approach to tackle scientific challenges and present my ideas. I also want to thank Assoc. Prof. Paul Medwell for providing me with guidance and training during my experiments. I will never forget his wholehearted dedication to work, and I am deeply grateful for the large amount of informative and enjoyable time we spent together in the lab. While working with him, I have learned many useful skills and the great value of having a good sense of humour, particularly in a full-of-surprises laboratory life.

I am also grateful to Prof. Heinz Pitsch for hosting and advising me at RWTH Aachen University. I also would like to thank Dr Emilien Varea and Dr Michael Evans, who are amongst the most friendly, helpful, and intelligent people I have ever met. I have lots of fond memories of working with them in the lab and drinking with them at the pub. I also want to thank Chia Xiong Thong, Dr Kathleen Lask, and Veronica Wassmuth for their kind assistance in the lab. Thanks also go to Dr Zhiwei Sun, Stephan Kruse, and Dr Alfonso Chinnici, with whom I had lots of intriguing discussions on laser diagnostic techniques and flame chemistry.

I am also very happy that I got to know Dr Zahra Bagheri, Chia Xiong Thong, Dr Manabendra Saha, Kimberley Andersen, Xiao Chen, Dr Dahe Gu, Kae Ken Foo, Thomas Kirch, Nicholas Sullivan and many other friendly colleagues during my PhD. It was very nice to share the frustration and the joy with people who can sympathise with it. Their friendship and encouragement have helped me to go through all the ups and downs of research life.

I would like to acknowledge the work of the support staff at the school of Mechanical Engineering. In particular, I want to thank the workshop staff, who are not only funny, but also helpfully manufactured and maintained the equipment.

Last, but not least, I am deeply grateful to my family for their boundless support and endless love. I want to thank Guy who has always been very caring and understanding. I thank him for encouraging me during the most difficult times and

for tolerating my crazy work hours (65 hours plus per week). I also want to thank him for being a stable rock against the endless tide of my rage and frustration. I would also like to thank Jan and David for all the care they have given to me and all the last-minute lifts to the bus stop. I really want to thank my parents and grandparents for their immense effort to provide me with access to a better education. It would not have been possible for me to even start my PhD without them being extremely supportive and open-mined. Words cannot convey how grateful I feel for having them as my family.

Abstract

Combustion of liquid fuels is the dominant source in the global energy supply, and its crucial importance is expected to remain well into the foreseeable future. Whilst providing human beings with energy, combustion of liquid fuels also produces undesired byproducts, including pollutants and greenhouse gases. In response to the mounting concern for energy sustainability and the environment, concerted efforts have been invested in the development of advanced combustion technologies. Moderate or Intense Low-oxygen Dilution (MILD) combustion technology has a great potential to abate pollutant and greenhouse emissions while maintaining a high thermal efficiency. In practical applications of MILD combustion, hot exhaust gases are recirculated inside the combustion chamber, simultaneously preheating and diluting reactants. A combination of hot reactants' temperature and low local oxygen concentration across the entire combustion chamber lead to volumetric reactions, resulting in a more uniform temperature and heat distribution. As a consequence, the peak flame temperature is reduced, thereby suppressing the formation of pollutants, such as nitrogen oxides.

Most of the previous studies on MILD combustion have been focused on simple gaseous fuels. There is a paucity of information concerning liquid fuels burning under MILD combustion conditions, despite their critical role in the world energy supply. This thesis aims to advance the understanding of MILD combustion of liquid fuels through a combined experimental and computational investigation. In this investigation, liquid fuels are prevaporised in order to avoid the complexity of spray dynamics. Thus the focus is on the fundamental aspects of chemical kinetics of these fuels under MILD combustion.

This thesis consists of a compilation of four journal articles, presenting results and findings from a combination of experimental and numerical studies. The first part of the experimental studies were conducted in a pressurised reverse-flow MILD combustor burning prevaporised ethanol, acetone, and n-heptane. These fuels are chosen to represent different classes of hydrocarbons, namely, an alcohol, a ketone, and a long-chain alkane. The pollutant emissions and the combustion stability under a wide range of operating conditions are examined. This investigation identifies several key operating parameters, namely, fuel type, equivalence ratio, carrier gas, air jet velocity, and operating pressure inside the combustion chamber. In order to further investigate the stabilisation of MILD flames and assess the impact of important parameters independently, parametric studies of prevaporised ethanol, acetone, and n-heptane are performed in a well-controlled environment, namely in a Jet in Hot Coflow (JHC) burner. Turbulent jet flames of dimethyl ether (an isomer of

ethanol) are also investigated and compared to ethanol flames. Simultaneous imaging of OH, CH_2O, and temperature, together with digital photography and imaging of OH^* chemiluminescence, are performed to reveal the flame structure. Reaction flux analyses of various fuels are conducted to complement the experimental results.

These results reveal that the local oxygen concentration plays a significant role in the flame structure. A transitional flame structure (a strong OH layer connected with a weaker "tail") is observed in the ethanol and the DME flames in a 9% O_2 coflow instead of a 3% O_2 coflow. This occurrence of the transitional flame structure is considered as an indicator of flames deviating from the MILD combustion regime. Simulations of ethanol and DME flames reveal that the importance of H_2/O_2 pathways in their oxidation processes decreases and intermediate species pool changes as the oxygen level increases from 3% to 9%. This suggests that a three-fold increase in the oxygen concentration leads to fundamental changes in the chemical kinetics of ethanol and DME.

It is also found that *n*-heptane flames do not have the characteristics of a typical MILD combustion flame as observed in the ethanol and the DME flames. A transitional flame structure is seen in the *n*-heptane flames even at the 3% O_2 coflow. In the reverse-flow combustor, stable combustion of ethanol is established under all tested conditions. However, *n*-heptane flames become more unstable than ethanol and acetone flames at high equivalence ratios and pressures. Calculations suggest that *n*-heptane flames burn faster than acetone and ethanol flames under elevated pressures. This indicates that *n*-heptane flames may ignite prior to a thorough mixing with hot combustion products. Furthermore, the jet velocity also decreases linearly with the increasing operating pressure inside the combustor. This is suspected to weaken the mixing of fresh reactants and exhaust gases, thus contributing to the unsuccessful establishment of MILD combustion.

One criteria of MILD combustion, based on heat release profiles, is adopted to investigate the distinctive behaviour of *n*-heptane. This numerical investigation is focused on two unique features identified in flames in the MILD combustion regime: the mismatch between the location of the peak net heat release rate (Z_{hmax}) and the location of stoichiometric mixture fraction (Z_{st}); the absence of a net negative heat release region. For ethanol flames, Z_{hmax} and Z_{st} are uncorrelated under all the oxygen levels and strain rates investigated, while the absence of a net negative heat release region is dependent on the strain rate. These results indicate that the transition boundary between the conventional combustion regime and the MILD combustion regime cannot be determined by the oxygen level alone. For *n*-heptane flames, a net negative heat release region exists despite a low O_2 level and a high strain rate. This is attributed to changes between alternative pyrolytic channels of *n*-heptane under different conditions due to its complex chemistry.

The fundamental aspects revealed by this study shed more light on the MILD combustion of more complex fuels. An improved understanding on the role of fuel structure in the establishment of MILD combustion is achieved by this work. The findings of this study are relevant to the implementation of MILD combustion technology in a variety of combustion devices.

Contents

List of Figures

List of Tables

Chapter 1

Introduction

1.1 Energy and Combustion

At the end of 2016, the World Energy Council released a report forecasting the global energy demand over the following four decades [1]. The report assesses different areas of energy use, based on a range of scenarios, and it predicts that combustion of fossil fuels will provide between 50% to 70% of the overall supply until at least 2060. The International Energy Outlook 2016 [2] similarly predicts that until 2040 approximately 80% of overall world energy consumption will be supplied by the combustion of fossil fuels.

Figure 1.1 presents historical and projected world energy consumption by fuel type. The data presented in Fig. 1.1 demonstrates that liquid fuels are predicted to remain the single largest contributor to the global energy supply over the entire forecast period [2]. The growing consumption of liquid fuels is mainly due to the increasing use in the transportation and industrial sectors. Globally, the consumption of liquid fuels from 2012 to 2040 is predicted to increase by 1.1% per annum and 1.0% per annum in the transportation sector and industrial sector, respectively. The wide use of liquid fuels is attributed to their high energy density and ease of storage and transport.

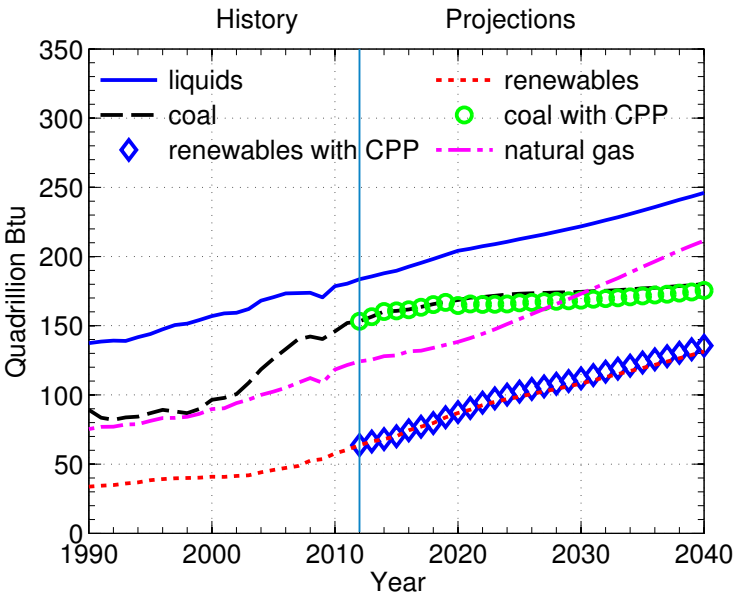

Figure 1.1: Historical and Projected world energy consumption by fuel type, regenerated from [2]. Fuel with CPP means the consumption of a particular type of fuel when Clean Power Plan (CPP) regulations are considered [2].

The annual report from the World Energy Council predicts the decreasing trend in the overall energy demand per capita because of stricter environmental policies and more advanced technology, nevertheless it also points out that the demand for electricity would double by 2060 [1]. In order to satisfy the growing demand in a more sustainable way, improving the energy efficiency is extremely important. Another report has shown that during the last 15 years, 3.1 Gigatons of oil equivalent of energy has been saved and 7 Gt of CO_2 emissions have been reduced due to the improved energy efficiency, which are approximately equivalent to a quarter of the worldwide energy consumption and CO_2 emissions in 2015 [3]. Despite significant improvements, the report authors [3] also emphasise that much greater efforts should be invested to improve the energy efficiency to enhance the security of energy supply and reduce emissions. Due to the importance of liquid fuels, more efficient and sustainable spray combustion technologies are required to meet these future challenges.

1.2 Liquid Fuels

Liquid fuels, such as gasoline, diesel, and kerosene are used in many practical combustion devices spanning from internal combustion engines to liquid-fueled rockets. However, there are growing concerns that the continued reliance on combustion is not sustainable due to the finite amounts of fossil fuel reserves. Fossil fuels capture energy that is originally produced from photosynthesis and store it for millions of years in a form of fossil. They are inevitably considered to be non-renewable given their long production cycle. Whilst common liquid fuels are petroleum-derived fuels, there are various types of non-petroleum liquid fuels, such as biodiesel, alcohols, liquefied hydrogen, and liquefied ammonia.

In response to the challenge of diminishing fossil fuel reserves, global efforts have been invested in developing and promoting renewable fuels. The main types of renewable fuels by source include solar fuels, biomass, and bio-fuels. The production of solar fuels involves using materials that can absorb sunlight via natural or artificial photosynthesis [4]. The stored solar energy is then converted to electrochemical energy, which is eventually harvested to produce fuels like lipids in a catalytic system [4]. Biomass refers to agricultural materials and forest products, which have a variety of uses to human beings, such as food and clothing. Energy can also be harvested from biomass through combustion. Bio-fuels are fuels derived from plant and animal matters. Liquid fuels that can be manufactured from ubiquitous biomass resources are also bio-fuels. For example, ethanol is the most widely used bio-fuels all over the world, particularly in the transportation sector. Blends of 90% petrol and 10% ethanol (E10) are available in thousands of petrol stations in Australia [5]. Furthermore, the popularity of vehicles compatible with ethanol blends up to E85 has been increasing in Brazil, America and the Europe [5]. Ethanol can be extracted from different feedstock, including simple sugars, wheat starch, and lignocellulose, through gasification, hydrolysis, fermentation, and distillation processes

[6]. In countries such as Brazil and India, ethanol is predominantly produced from sugar cane [7]. The reduction in the production cost of ethanol, due to technologies improvement, makes it an even more attractive renewable fuel.

Renewable liquid fuels have obvious advantages over fossil fuels in terms of the availability and sustainability. Despite this, the potential of renewable liquid fuels has not been fully realised. One factor that hampers the wide application of renewable fuels is the limited understanding of the impact of the fuel type when it comes to more complex fuels. Biomass and bio-fuels are often made of a variety components. For instance, softwood like pine typically contains cellulose, glucan 6C, hemicellulose, lignin, and other components [6]. Biodiesel consists a list of different esters, and their compositions depends on the raw materials used for production. Therefore, it is important to understand the impact of different fuel chemistries and the resultant flame characteristics, particularly when fuels are burnt using relatively new combustion technologies.

1.3 Combustion Pollutant Emissions

Whilst providing society with its energy needs, the combustion of liquid fuels also impacts on the environment and the health of the population. Combustion of fossil fuels always produces carbon dioxide, one of the primary greenhouse gases. In order to reduce carbon dioxide emissions, the fuel consumption needs to be reduced for the same energy output, in other words, the energy efficiency needs to be improved. In addition, other harmful pollutants are often produced from the combustion of liquid fuels, including nitrogen oxides (NO_x), unburned hydrocarbons (UHCs), carbon monoxide, and solid particles, such as soot.

The formation, oxidation and transportation of soot particles are governed by several parameters, including temperature, pressure, strain rate, fuel type, fuel flow rate and local mixture composition [8–10], and these parameters interplay with each

other in a complex manner. Numerous work [11, 12] has shown that soot formation has a strong sensitivity to temperature, therefore one approach to reduce soot formation is to lower the flame temperature. During the combustion of hydrocarbons, carbon monoxide is always produced as an intermediate species, which is oxidized to carbon dioxide when the residence time and temperature are sufficient at high oxygen concentration conditions [13]. Note that the equilibrium concentration of carbon monoxide increases considerably at a high temperature. For instance, its concentration is greater than 1% when the burned gas temperature ranges from 2400 K to 2800 K in a reciprocating engine [13]. Similar to carbon monoxide, UHCs are also produced due to incomplete combustion. Hence an enhanced mixing to complete reactions can reduce the formation of both carbon monoxide and UHCs.

The term nitrogen oxides (NO_x) refers to an important family of air polluting chemical compounds, consisting of nitrogen oxide (NO) and nitrogen dioxide (NO_2). NO_x are common pollutants in combustion because they are not only produced from chemically-bounded nitrogen in the fuel, but also from prevalent molecular nitrogen in the air. Due to the severe environmental effects of NO_x emissions and their related hazards such as acid rain, stringent regulations have been placed on NO_x emissions. The formation mechanisms and control strategies of NO_x will be discussed in detail in Chapter 2.

1.4 Overview of MILD combustion

Acting in response to the increasing concern for the environment, relentless efforts have been made to develop combustion technologies to help abate pollutant formation and greenhouse emissions. However, there is often a trade-off between high efficiency and low pollutant emissions. For example, lean premixed combustion conditions can reduce NO_x emissions by lowering the flame temperature. Due to very lean conditions, unstable combustion with fluctuating heat release and pressure

may occur, challenging the successful implementation of this technique [14]. Some combustion technologies utilise the hot exhaust gases to preheat the reactants and increase the initial enthalpy, thereby improving the thermal efficiency [15]. However, a higher reactant temperature typically results in a rise in the flame temperature, which enhances the pollutant formation, such as NO_x. In order to reduce both the pollutant formation and the energy consumption at the same time, the concept of exhaust gas recirculation (EGR) has been utilised in a range of combustion technologies, amongst which Moderate or Intense Low-oxygen Dilution (MILD) combustion is a very promising candidate [15–17].

Due to the absence of a visible flame, MILD combustion is also referred to as flameless oxidation (FLOX®) or flameless combustion. In order to achieve lower pollutant emissions and energy consumption simultaneously, MILD combustion is operated in a hot and diluted environment. Specifically, MILD combustion often takes place wherein the local oxygen concentration is less than 5% and the reactant temperature is higher than the autoignition temperature of the mixture [12, 16, 18]. This hot vitiated environment is created by a strong recirculation of hot products in commercial combustion apparatus. The recirculation of exhaust gases can be enhanced by several fluid dynamics designs. For instance, high inlet velocity of fuel and air mixtures was found to increase the entrainment of hot exhaust gases and lead to a more homogeneously distributed reaction zone, as revealed by imaging of OH^* and OH-LIF in a FLOX® burner [19]. A reverse-flow configuration was reported to achieve similar effects in a pressurised MILD combustor [20] and a parallel jet MILD combustion burner [21].

The features associated with MILD combustion are highly desired in many combustion processes. A lower local oxygen concentration in MILD combustion helps retard the reaction, giving more time for the fresh reactants to thoroughly mix with the hot products before the reactions proceed. Moreover, the increase in the flame

temperature is suppressed, restraining NO_x and soot emissions drastically [22, 23]. A low peak flame temperature also provides more freedom in the choice of materials for construction of a combustion chamber [12]. In addition, a larger radiating volume, resulting from volumetric reactions under MILD combustion conditions, is desired in furnaces and boilers [24]. This high radiant flux is not necessarily advantageous when it comes to application in gas turbines, where excessive heating of the walls may lead to material degradation and heat losses. However, due to a semi-uniform temperature distribution with a lower peak temperature under MILD combustion conditions, a higher efficiency can be achieved by raising the mean temperature of products, while maintaining low NO_x formation and the durability of gas turbine components. This semi-uniform spatial distribution of temperature is also desired in material treatment process [12].

Different from lean premixed combustion [25], extinction limits under conventional modes are eliminated under MILD combustion conditions because the temperature of the reactants is higher than the autoignition temperature of the mixture. Typically under very lean conditions, the coupling of pressure oscillations, acoustic oscillations and the heat transfer process, associated with extinction and re-ignition events, can amplify each oscillation and cause serious combustion instability [14]. MILD combustion maintains the combustor temperature above autoignition which eliminates thermo-acoustics effects, leading to a more stable combustion device across a wide range of equivalence ratios.

The establishment of MILD combustion requires certain operating conditions, including minimum and maximum values of temperature and oxygen concentration, scalar dissipation rate and residence time, to be reached everywhere within a combustion system. The interdependency of these parameters can manifest as a strong turbulence-chemistry interaction. An important dimensionless parameter under MILD combustion conditions is the Damköhler number, which describes the

ratio of the characteristic flow timescale to the chemical timescale. Under MILD combustion conditions, the recirculation of exhaust gases dilute the fresh reactants and lead to very low local oxygen concentration, thereby prolonging the chemical timescale. Meanwhile, high momentum jets are often used to promote fast mixing of hot exhaust gases and fresh mixture, indicating a relatively short characteristic timescale of the fluid flow. Therefore, MILD combustion is often characterised by a Damköhler number near unity. Indeed, the significance of the close interplay of turbulence and chemistry has been reported in previous studies [16, 18].

In order to apply MILD combustion technique in wide areas involving various fuel types and combustors' geometry, it is essential to understand the interdependency of these parameters to control the resulting reacting environment, thereby exploiting the full benefits of MILD combustion. In particular, based on a detailed literature review in Chapter 2, the understanding on the impact of more important liquid fuels with respect to simple methane- and ethylene-based fuels is rather limited.

1.5 Thesis Outline

This thesis describes a combined experimental and computational study on MILD combustion of prevaporised liquid fuels. The next chapter provides a detailed literature review on relevant topics, based on which important research gaps are identified. Chapter 3 elaborates on the major measurement techniques used in this thesis, including Rayleigh scattering, laser-induced fluorescence of the hydroxyl radical (OH) and formaldehyde (CH_2O).

A compilation of two published, one accepted, and one submitted papers is included in Chapters 4–7. These papers present the results and findings in this thesis. In Chapter 4, the applicability of MILD combustion of prevaporised liquid fuels under atmospheric and elevated pressure is explored via a series of experiments in a reverse-flow combustor. Ethanol, acetone, and *n*-heptane are investigated as

representatives for alcohol, ketone, and long-chain alkane, respectively. Results on the formation of emissions and the operating range are described and discussed. The crucial role of important operating parameters like the fuel type is highlighted in these experiments. In order to further examine the impact of various parameters independently, parametric studies are performed on a Jet in Hot Coflow (JHC) burner, the results and findings are presented in Chapter 5–7. The jet Reynolds number, the type of fuel and carrier gas, the coflow temperature and coflow oxygen level are varied independently. The distribution and evolution of OH, CH_2O, and temperature are presented and discussed. Reaction flux analyses of different fuels are also presented and discussed. Chapter 5 is dedicated to the impact of various parameters on the transition of ethanol flames from the conventional combustion regime to the MILD combustion regime. Chapter 6 compares *n*-heptane flames with the ethanol flames under the same coflow condition, and comparisons to ethylene- and methane-based flames under similar conditions are also made. Differences in the fuel chemistry and the resultant flame characteristics of these fuels are discussed. Chapter 7 extends the investigation to dimethyl ether (an isomer of ethanol) to study the impact of fuel structure on flames under MILD combustion conditions. Finally, Chapter 8 ties together all the findings and provides conclusions to this work.

Chapter 2

Literature Review

2.1 Combustion of Liquid Fuels

Combustion of liquid fuels is predicted to remain the greatest contributor to the global energy supply in the foreseeable future [1, 2]. Whilst providing human beings with energy, combustion of liquid fuels also generates harmful pollutants and contributes to the global warming. It is important to develop advanced combustion technologies for liquid fuels to improve energy efficiency and reduce pollutant emissions, which requires a better understanding of the underlying fundamentals governing the combustion of these fuels.

Combustion of liquid fuels is often referred to as spray combustion. Liquid fuels need to be vaporised before burning. The surface-to-volume ratio of liquid fuels increases dramatically after atomisation, enhancing the heat transfer with the surroundings. Hence, the combustion of liquid fuels usually occurs in the form of spray combustion rather than pool combustion. Spray combustion is a complex process, where several important mechanisms interact with each other simultaneously. These mechanisms include atomisation, vaporisation, mixing, and burning. These mechanisms are discussed in the following sections.

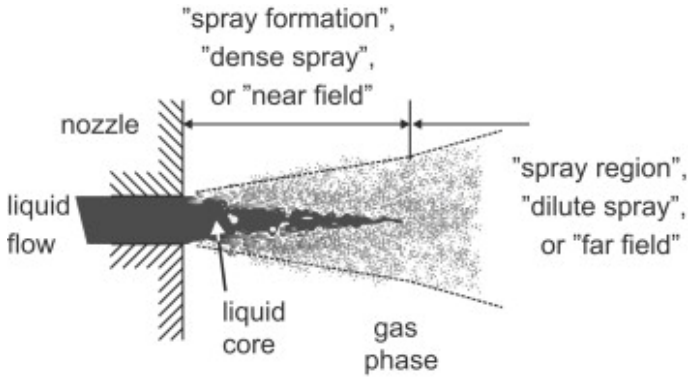

Figure 2.1: Schematic of a typical spray [27].

2.1.1 Spray Atomisation

In the context of spray combustion, spray can be understood as a jet of liquid droplets around a liquid core injected into hot surrounding gas after atomisation. As depicted in Fig. 2.1, spray typically consists of two regimes: a "dense spray" regime and a "dilute spray" regime. Intact liquid structures, including the liquid core and ligaments, extrude into the surrounding gas at the nozzle exit. During the primary atomisation process, the intact liquid structures break up, leading to the formation of a dense spray of large droplets. As these large droplets travel further downstream, they disintegrate into smaller droplets mainly due to the shear force between the liquid and the gas phase. This secondary atomisation process produces a dilute spray. The secondary breakup are classified into several modes, namely, vibrational, bag, multi-mode, sheet thinning, and catastrophic modes [26]. The mode of secondary breakup is described by three main dimensionless numbers, including droplet Weber (We_d), Ohnesorge (Oh_d), and Reynolds numbers (Re_d) [26].

There are several types of nozzles that are commonly used for atomisation. In one type of nozzles (hydraulic nozzles), liquid fuel travels through a very tiny orifice alone under high pressure and breaks into small droplets when subjected to hydraulic force [28]. Alternatively, in twin-fluid atomisation, such as in an air-blast nozzle, a gas stream with high velocity is applied to break the liquid fuel into droplets

by creating a very strong shear layer between the two phases [28]. Another type of atomisers are electrically-driven ultrasonic atomisers [29]. Piezoelectric elements inside the atomiser body receive high frequency electrical energy from an ultrasonic generator, and convert it to vibratory mechanical energy at the same frequency. When liquid is introduced to the atomising surface (atomiser tip), it absorbs part of the vibration energy, which is transformed to capillary waves within the liquid. When the amplitude of the vibration goes beyond the stability limit of capillary waves, the instability on the liquid surface results in the collapse of the waves and droplets formation [29].

Sprays have various shapes, such as a flat fan, a hollow-cone, or a full-cone. Several characteristics are used to define a spray, including the spray angle, the breakup length, the spray tip penetration length, and the droplet size distribution. As shown in Fig. 2.2, the spray angle is the angle over which the spray spreads out. The breakup length refers to the distance between the liquid discharge point of an atomising device and the point where the breakup of the intact liquid jet commences [30]. The characteristics of a spray are affected by many factors. These factors include the physical properties of the liquid and the surrounding gas, the design of the orifice, the inherent flow structure as a consequence of a particular orifice passage, the pressure of the combustion chamber, the turbulence properties of the surrounding gas and so forth. Further information on the spray formation can be found in a comprehensive study by Marmottant and Villermaux [31].

2.1.2 Droplets Evaporation and Burning

The spray atomisation process is followed by the spray breakup, penetration, entrainment, mixing, evaporation, and burning processes. After being discharged from the nozzle, droplets are normally released into a convective environment [33]. In the presence of a stream of carrier gas or atomising gas, droplets are first accelerated

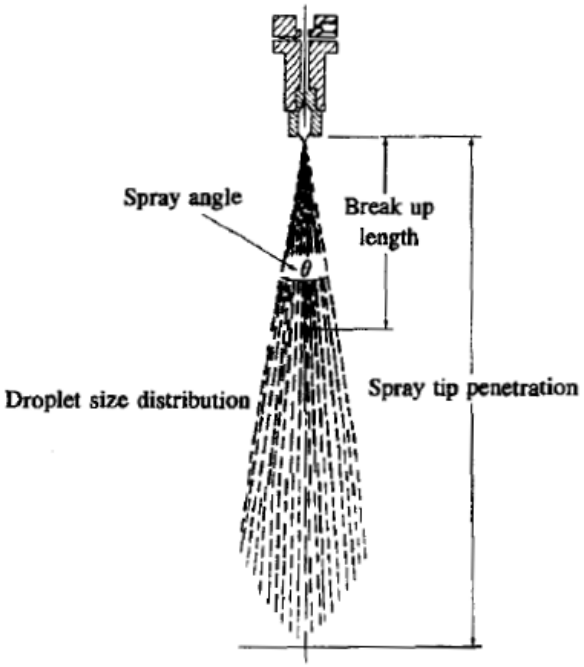

Figure 2.2: Schematic of a diesel fuel spray defining its major parameters [32].

by the drag force of the gas stream before eventually being slowed down [34]. Small droplets with lower Stokes numbers are able to follow the gas flow more closely than large droplets. Hence, the velocities of small droplets and gas are higher than those of large droplets immediately downstream of the nozzle. However, the velocities of the size-classified droplets tend to be similar to each other further downstream, due to the bigger inertia of large droplets [30]. While being transported downstream, the spray entrains and mixes with the surrounding gas. Consequently, the spray becomes more diluted as its volume increases. In the mean time, droplets are disintegrated further into smaller droplets due to the instabilities at the liquid-gas interface resulting from the shear mechanism.

Droplets are evaporated due to the heat transfer from the surrounding hot gas in a combustion device. At the periphery of the spray, droplets vaporise faster and mix with the hot surrounding gas first. The mixture of fuel vapour and hot gas ignites at the periphery of the spray, the heat from which vaporises more droplets

and more fuel vapour is burnt, hence the flame propagates.

2.1.3 Spray Combustion

Turbulent combustion consists of many complicated physical and chemical subprocesses. The presence of a spray brings additional complexities to the turbulent combustion of liquid fuels. In order to better understand spray combustion, visualisation and measurement of a spray from inside a nozzle to the very diluted regime are very important yet challenging. The intact liquid core and large droplets emanating around it render the "dense spray" regime difficult to probe optically. Due to the recent advancements in measurement techniques, more information are becoming available for optically dense sprays, which are summarised in a review article by Linne [27]. As an essential building block to understand the entire spray, continuous efforts have also been made to characterise turbulent diluted sprays. Key findings of turbulent diluted sprays have been presented in the series of International Workshops on Turbulent Spray Combustion. In particular, comprehensive measurements performed for a range of liquid fuels by Masri et al. [26, 34–40] have formed a benchmark for modelling work. One of the most investigated configurations is a turbulent diluted spray injecting into either heated air or a hot and vitiated coflow. In this configuration, ignition kernels were found upstream of the main flame front [26]. The main heat release occurs in the downstream flame region, the structure of which was determined by the parent fuel [26]. Hence this configuration provides a good platform for experimentalists and modellers to investigate the autoignition of a spray flame and its strong dependence on the chemical kinetics [26].

Previous studies have highlighted the important role of spray characteristics in the combustion process [26, 34–41]. For instance, a spray with a wide angle or a long penetration length may impinge on the chamber wall, leading to incomplete combustion. The spray angle and penetration length also significantly affect the

entrainment of the surrounding air, consequently affecting the mixing and burning processes. The complicated aerodynamic interaction between the liquid and the gas phase in a spray flame has been a subject in many previous studies [42–46]. Abraham et al. [43] performed a computational study to compare the air entrainment of a hollow-cone spray with a solid-cone spray produced by a multi-hole injector. The entrainment rate of the hollow-cone spray was found to be smaller than that of the solid-cone spray [43]. This is because the hollow-cone spray impinged on the wall, and its surface area for entrainment is smaller [43]. A stronger entrainment of the surrounding air lowers the mixture fraction gradient. Thus the scalar dissipation rate decreases, which could shorten the ignition delay. Friedman and Renksizbulut [44] investigated the interaction between a methanol spray and an annular air jet. The presence of the annual air jet was found to create a recirculating flow at the flame front near the fuel jet exit plane [44]. This in turn changes the reaction zone structure. When the annual air flow was on, a single reaction zone with a tulip shape structure occurred instead of a dual reaction zone [44].

As mentioned earlier, liquid droplet size distribution is also a defining spray characteristic. Small liquid droplets vaporise and burn fast, while coarse droplets may not have enough time for complete combustion, contributing to CO and soot emissions. For instance, Sharma et al. [47] reported that the size of droplets considerably affected the combustion performance in a flameless combustor fired with kerosene. Specifically, when the liquid spray became coarser, CO, NO_x, and acoustic emissions increased [47]. It is worth mentioning that besides droplets, ligaments and irregular objects are also produced in reality. Kourmatzis et al. [48] reported that the size and the probability of occurrence of droplets, ligaments, and irregular objects are determined by the initial Weber number and the fuel/air mass ratio during an air assisted atomisation process. The presence of non-spherical fragments lead to considerably different rates of evaporation within the spray, which may partly affect

the flame structure downstream [48].

The impact of spray characteristics is further complicated by the presence of turbulence. In a spray, a higher jet velocity leads to an increase in the bulk jet Reynolds number as well as the Weber number [26]. As a consequence, the shear at the droplet-air interface also increases, which in turn affects the modes of secondary breakup [26]. At a constant fuel/air mass ratio (liquid fuel loading) in an air-blast atomiser, a higher bulk jet Reynolds number was found to enhance the atomisation [39]. Specifically, the relative population of ligaments decreased, meanwhile more droplets were produced due to a higher turbulence level [39].

Turbulence was also found to affect the spray evaporation, mixing, and burning processes. Stårner et al. [36] studied the behaviour of acetone spray flames at different turbulence levels in a piloted burner. Phase-Doppler anemometry was performed to measure the droplet velocity and flux [36]. It was revealed that the bulk jet velocity or Reynolds number has a minor effect on the droplet evaporation rate. In contrast, the turbulence intensity greatly influenced the spray evaporation rate of kerosene flames as reported by Sornek et al. [49]. A more uniform droplet size distribution and a faster evaporation rate were found at a smaller turbulence intensity [49]. This was attributed to that droplets were less likely to cluster at a lower turbulence intensity, thus droplets vaporised faster [49]. Due to a higher evaporation rate, the spray combustion became mixing dominant, and the spray flame behaved closer to a gaseous diffusion flame [49]. The mixing between two gaseous streams was thought to be slower than that between the liquid and the gas phase, resulting in a longer flame and a slower temperature rise [49]. Therefore, they concluded that increasing the evaporation rate may not be an effective measure to increase the reaction rate because a faster evaporation not necessarily leads to a faster burning [49].

2.1.4 Prevaporised Liquid Fuels

The literature review presented in the preceding sections demonstrates that the spray formation is a complicated process in its own. Moreover, the close coupling of the spray development and combustion processes makes spray combustion a challenging topic to date. In order to better understand spray combustion and to advance the capabilities to predict the spray flame characteristics, each subprocess and the interaction between them must be well understood. To isolate the impact of various spray characteristics, liquid fuels are vaporised before injecting into a combustion device in this project.

2.2 MILD Combustion

2.2.1 Introduction to MILD Combustion

Increasingly stringent regulations on emissions and growing demand for energy supply have been the main drivers to develop combustion technologies that are clean and efficient. A well-recognised concept to improve thermal efficiency is Excess Enthalpy Combustion, where the mixture is burnt with increased initial enthalpy than fuel-air combustion at room temperature [15]. Various combustion technologies involving hot reactants exploit this concept. For instance, in some applications of High Temperature Air Combustion Technology (HiTAC), air is preheated above 1000°C prior to reactions [15].

The initial enthalpy of reactants is usually increased via exhaust gas recirculation (EGR), which can be implemented either externally or internally. In an external EGR application, part of hot combustion products is collected and utilised to preheat and/or dilute fresh reactants before they are injected into a combustion chamber. In an internal EGR application, hot exhaust gases are recirculated inside the combustion chamber, simultaneously preheating and diluting reactants.

In practical applications of MILD combustion, a strong internal recirculation of hot exhaust gases is required. This can be achieved via various designs, such as a reverse-flow configuration [20, 21]. The use of an internal EGR affects combustion processes and performance in many ways. Firstly, extinction and reignition events are avoided as the initial temperature is above the autoignition temperature. Secondly, volumetric reactions occur when a mixture of hot products and fresh reactants above the autoignition temperature is uniformly distributed across the whole furnace. Thirdly, given the same mass flow rate of fuel, the peak flame temperature is lowered partially because a larger volume of gases is required to be heated. Last but not least, a lower local oxygen concentration may lead to changes in the chemical pathways of the fuel, thus changing the combustion process and the resultant products.

The successful implementation of MILD combustion requires certain conditions of mixture compositions and temperature to be met everywhere inside the combustion chamber, which are governed by many operating parameters that couple with each other. For instance, increasing the Reynolds number of a fuel jet leads to a stronger entrainment of surrounding air and hot products in a furnace environment. As a consequence, the local composition and temperature change. This in turn alters the chemical pathways, thereby affecting the composition and temperature of the combustion products, which are recycled inside the combustion chamber to preheat and dilute fresh reactants. However, it is challenging to monitor and probe temporal and spatial changes inside a practical combustion equipment due to often limited optical access. Furthermore, it is also difficult to control various parameters and isolate their impact. The effect of EGR is usually simulated via a well-controlled cold-fuel-hot-coflow configuration like a Jet in Hot Coflow (JHC) burner in laboratory studies [50, 51]. In this configuration, cold fuel can be mixed with a hot vitiated coflow, with ability to vary the oxidiser temperature and compositions independently.

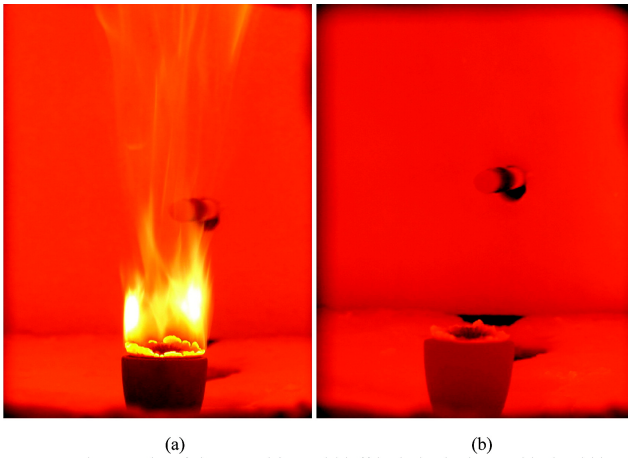

Figure 2.3: Photographs of natural gas burning in (a) conventional combustion mode and (b) MILD combustion mode in a reverse-flow furnace with 10 kW heat input [21].

2.2.2 Characteristics and Definitions of MILD Combustion

The establishment of MILD combustion requires the recirculation of not only the thermal energy released during combustion but also the combustion products. The strong EGR creates a hot and diluted environment. This peculiar environment results in unique characteristics in the flame appearance and structure, which have been used to define MILD combustion in literature [12, 52–59].

Visual Observations

As mentioned previously, MILD combustion is also called flameless combustion due to the absence of a visible flame. An example of "flameless" MILD combustion is displayed in Fig. 2.3. Natural gas flame was burnt in a laboratory-scale furnace, where the reactants inlets and the exhaust gas outlets are mounted on the same plane, and the fuel jets are separated from the central air jet by a relatively large distance [21]. As demonstrated in Fig. 2.3, a bright and yellow flame attached on the bluff body became invisible when the furnace was operated in the MILD combustion mode [21].

In conventional combustion, flames can be observed by the naked eye because

of natural and luminous emissions from radiative species like CH^* and OH^*. These species are at an excited state due to the elevated temperature. As the electrons fall back to their original energy states, photons are naturally emitted, referred to as chemiluminescence. The frequency of the emitted photons is determined by the amount of energy released, which is species specific. Species can be identified via a flame test as each excited species has its own signature line emission spectrum. Those emitted photons sometimes fall within the range of visible light, for instance the chemiluminescence of CH^*. Due to the nature of chemiluminescence, it is expected that its occurrence requires high energy and strongly depends on temperature. Indeed, Saha et al. [60] found that CH^* chemiluminescence signal considerably decreased when the flame temperature was lowered in the combustion of coal in a MILD furnace.

This "flameless" characteristic has been reported for various gaseous, liquid, and solid fuels burning under MILD combustion conditions. It has been used as an indicator for the successful establishment of MILD combustion [21, 60, 61]. For example, Medwell et al. [62] reported the ambiguity to identify the flame base from digital photography and imaging of CH^* chemiluminescence when turbulent ethylene flames were burnt in a vitiated coflow with 3% O_2 instead of 9% O_2. Similarly, Choi et al. [53] investigated laminar lifted flames of propane diluted by nitrogen in a preheated coflow air. One of the criteria they used for MILD combustion regime is very faint blue emission from the flames [53]. In a jet in cross-flow configuration, Sidey et al. [63] also found that the OH^* chemiluminescence was much lower from flames burning with hot exhaust gases than that from flames burning in cold air.

Another signature associated with the MILD combustion regime in terms of flame appearance is the absence of a tribrachial structure [53]. Chung et al. [52–56] investigated the autoignition characteristics of laminar lifted flames of methane/hydrogen [55], methane [54], propane [53, 54], *n*-butane [54], ethane [54], syngas [56], pre-

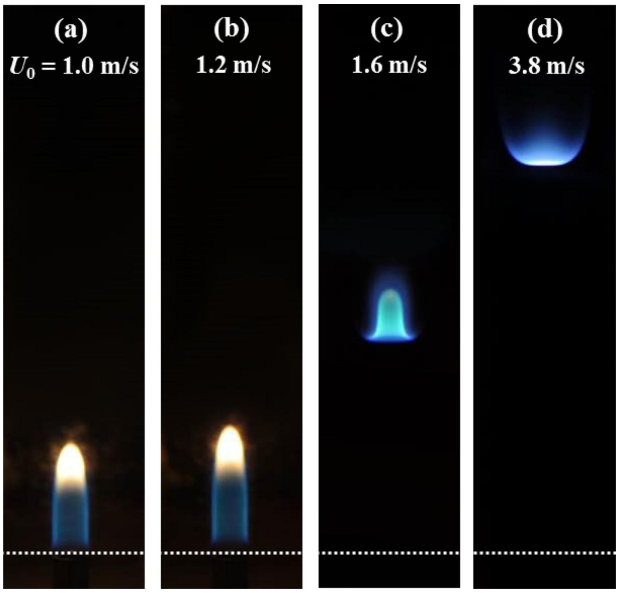

Figure 2.4: Photographs of prevaporised *iso*-octane jet flames coflowing by 800-K heated air. The prevaporised *iso*-octane jet is diluted by 97% of nitrogen by volume: nozzle-attached flames for (a) U_0 = 1.0 m/s and (b) 1.2 m/s; lifted flames with tribrachial edges for (c) 1.6 m/s and (d) 3.8 m/s [52].

vaporised *iso*-octane, and *n*-heptane [52]. Photographs of these flames demonstrate that for conventional autoignited laminar lifted flames, a tribrachial structure existed at the flame base, which consists of a lean premixed branch, a rich premixed branch, and a diffusion flame anchored at the same location [52–56]. Figure 2.4 (c) and (d) show lifted *iso*-octane flames with tribrachial edges that can be revealed via conventional photography [52]. As the preheating level of the air and the dilution level of the fuel increased, the MILD combustion regime was reached. In this regime, a lifted flame was established without a tribrachial structure [52, 53, 55, 56]. Photographs displayed in Fig. 2.5 demonstrate that MILD propane flames were stabilised when the fuel jet was diluted by 98.6% of nitrogen by volume and surrounded by 900-K heated air [53].

Flame Structure and Important Scalars

Cavaliere and de Joannon [12] defined MILD combustion as a combustion process in which the temperature of reactants is above the autoignition temperature, mean-

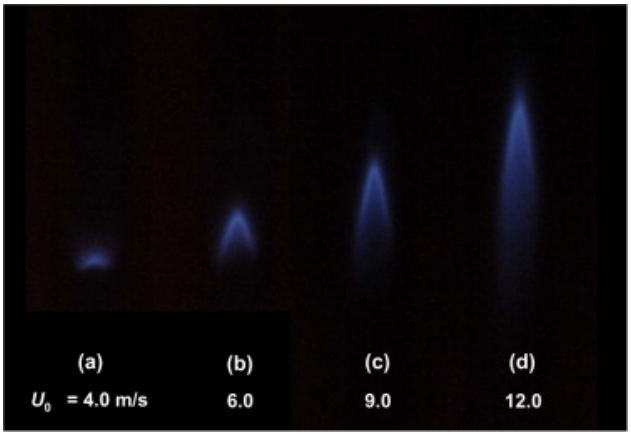

Figure 2.5: Photographs of MILD propane flames without tribrachial edges at different jet velocities. This propane jet is diluted by 98.6% of nitrogen by volume, coflowing by 900-K heated air [53].

while the maximum allowable temperature increase is lower than the autoignition temperature of the mixture. However, considerable differences in the flame structure and behaviour have been reported in previous experimental studies [50, 51, 62, 64–67], though those experimental conditions all meet this MILD regime definition. One example is the different response of the liftoff heights to the change in the same variable, such as coflow oxygen concentration, which suggests different flame stabilisation mechanisms may exist across various hot and diluted coflow conditions. An in-depth discussion on this topic was presented in a previous study by Medwell et al. [62], and relevant studies will be discussed in Section 2.3.

MILD combustion is often considered to be a volumetric combustion process. Thus it produces a smaller gradient of any thermodynamic variable with respect to conventional combustion [12, 15, 17]. For instance, Weber et al. [24] reported a slower combustion process with uniform radiative heat fluxes when natural gas was burnt in a highly preheated and vitiated air in a furnace. This agrees with a numerical study by Kumar et al. [68], who reported that reactions take place over a larger volume with a lower magnitude in the MILD combustion mode than the conventional combustion mode. Duwig et al. [69] performed planar laser-induced fluorescence of OH and CH_2O, and Rayleigh scattering for temperature measurement

in a Distributed and Flameless Combustion Burner (DFCB), mimicking very high Karlovitz number combustion. In the DFCB, premixed methane-air jet (U_{jet} = 60 m/s) is surrounded by a 1850-K hot coflow, which is produced from a McKenna burner located 2 mm upstream of the jet nozzle. Their results indicated a complicated and intermittent turbulence-chemistry interaction [69]. In specific, the large coherent structures in the jet shear layer thickened both the OH and CH_2O structure, and made the reaction zone more distributed [69].

Flamelet-like structure has also been reported under MILD combustion conditions [63, 70, 71] despite the common claim that MILD combustion consists of a distributed reaction zone. A three-dimensional DNS study of MILD methane flames by Minamoto and Swaminathan [70] identified thin reaction zone with flamelet-like behaviour [70]. They found thin regions of intense reactions, suggesting the existence of flamelets. This seemed to contradict the often-cited MILD combustion characteristic – a distributed reaction zone [70]. However, they also noticed a frequent interaction between these flamelets both spatially and temporally, resulting in the thickening of the reaction zone and the appearance of non-flamelets behaviour [70, 71]. This finding is supported by an experimental study on MILD combustion by Sidey and Mastorakos [63], where a methane jet was injected into cross-flow of hot products. Instantaneous planar imaging of OH showed a sharp transition from regions without OH to regions with OH [63]. They concluded that MILD methane flame was burnt in thin and distinct regions despite a low flame luminosity [63]. Dally et al. [18] also reported similar observations of multiple adjacent pockets of reacting and non-reacting mixtures such that a patchy appearance is shown in instantaneous imaging of temperature and OH.

A semi-uniform temperature distribution with a reduced peak flame temperature restrains the emissions of CO, NO_x, and soot [23, 51, 72]. Findings from a study by de Joannon et al. [57] suggested that this soot reduction is related to unique

characteristics in the heat production profiles under MILD combustion conditions. They performed laminar flame calculations for methane flames with the OPPDIF code in the Chemkin software considering three configurations, namely, Hot-Diluted-Oxidant, Hot-Fuel-Diluted-Fuel, and Hot-Oxidant-Diluted-Fuel [57–59]. They identified several common features of the heat release profiles in the MILD combustion regime [58]. The first feature is a broad heat production profile with a single heat release peak in mixture fraction space. The second feature is the lack of a net negative heat release region due to the suppression of fuel pyrolysis [58]. Outside the MILD combustion regime, a net negative heat release region occurs when endothermic reactions overtake the oxidation reactions [59]. In the case of methane, the pyrolytic channel is dominated by the decomposition of methane or the recombination and dehydrogenation of methyl radical. It is beneficial to inhibit this pyrolytic region as soot tends to be produced in this region in industrial combustion devices [73]. The third signature is the lack of correlation between the location of the maximum heat release rate (Z_{hmax}) and the location of stoichiometric mixture fraction (Z_{st}) [58]. The maximum heat release rate always occurred close to Z_{st} up to a certain level of fuel dilution [59]. When the fuel was diluted further, Z_{st} kept increasing, meanwhile Z_{hmax} began to shift towards the lean side.

In summary, various criteria have been used to characterise and define MILD flames in previous studies [12, 52–59]. Most of the experimental studies were focused on laminar flames. These criteria are focused on different aspects of a flame, ranging from the flame appearance to the heat release profile in mixture fraction space, which are very different in nature. Hence, the applicability of these criteria need to be examined, particularly for experimental turbulent flames of various fuels.

2.3 Flame Stabilisation Mechanisms

2.3.1 Introduction

The hot vitiated environment required for MILD combustion is often simulated by a cold-fuel-hot-coflow configuration in laboratory research. This configuration offers independent control over operating parameters and optical access for *in situ* measurements. The mechanism that governs the flame stabilisation under this configuration has also been the focus of ongoing research as it provides a relatively simple platform to explore a wide-range of issues, such as local autoignition/extinction and turbulent-chemistry interaction. It is also relevant to various commercial devices, spanning from boilers to gas turbines.

A review paper by Pitts [74] provides a comprehensive assessment of well-known theories on the flame stabilisation mechanism for lifted turbulent diffusion jet flames. One popular theory is that a lifted flame is stabilised at a certain height where the local mean flow velocity is equal to the turbulent burning velocity [75–77]. Vanquickenborne and Tigglen [76] proposed the premixed flame propagation model, which assumes that reactants are fully mixed at the lifted flame base, consisting of a bright outer ring with the same geometry as the burner mouth and a less bright inner core. Based on this model, Kalghatgi [78] proposed "Turbulence intensity theory" or "Turbulent premixed propagation theory". The propagation speed of the lifted flame base is assumed to be controlled by the turbulent intensity. The maximum turbulent burning velocity is determined by the maximum laminar flame speed ($S_{L,max}$) and local turbulent parameters [78]. These parameters as well as local mean flow velocity are dependent on the density ratio (r) of the jet and surrounding gases, the jet velocity (U_{jet}), and viscosity (ν_{jet}) [78]. Kalghatgi [78] proposed a

correlation for liftoff heights of turbulent diffusion jet flames in still air as follows:

$$H = 50\frac{\nu_{jet}U_{jet}}{S_{L,max}^2}r^{1.5} \tag{2.1}$$

Another prevalent theory for flame stabilisation mechanism is the "edge flame" theory. According to this theory, the leading edge of a flame is partially premixed, and the propagation speed of which can either be positive or negative [79, 80]. Based on this theory, despite a large turbulence level, the edge flame creates a low local flow velocity due to streamline divergences as a consequence of heat release at the stabilisation point [81].

According to this theory, a flame with a tribrachial structure (a triple flame) is considered to be one type of edge flames. A triple flame is composed of a lean premixed wing, a rich premixed wing, and a trailing diffusion flame, and all of them are anchored at a single point [82]. The tribrachial structure is stabilised based on the balance between the flame propagation speed and local flow speed [82]. In order to help explain the triple flame behaviour, the region between the nozzle exit and the edge of the lifted flame is approximated as a cold jet on the assumption that the impact of gas expansion on this region is negligible [83].

Experimental measurements [77, 81, 84–86] have shown inconsistencies with the "Turbulence intensity theory" or "Turbulent premixed propagation theory". In these laboratory-scale jet flames, the measured mean propagation speed of the flame base is near the laminar flame speed even at a Reynolds number as high as 29,700 [77, 81]. Furthermore, Upanieks et al. [81] reported that the flame propagation speed did not change when the turbulent intensity varied by a factor of 3 in the Reynolds number range of 4300 to 8500. However, at a higher Reynolds number, a strong influence of Reynolds number on the local flow speed has been reported [84]. Kumar et al. [68] suggested that the apparent conflicting experimental results can be interpreted as the impact of Reynolds number or turbulence level on the dominant role of different

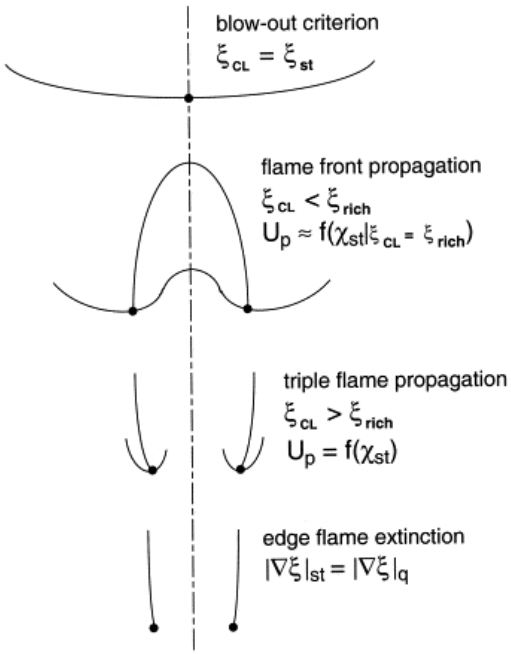

Figure 2.6: Schematic of flame front contours and corresponding criteria of flame stability and blow-out limits for a lifted laminar flame in an axisymmetric geometry [75]: U_p refers to the propagation velocity of triple flames; U_{st} refers to the flow velocity along the stoichiometric mixture fraction contour; ξ_{st} is the stoichiometric mixture fraction; ξ_{CL} is the mixture fraction at the jet centreline; ξ_{rich} is the rich flammability limit [75].

flame stabilisation mechanisms. When the jet Reynolds number is high, turbulent premixed propagation is important in the flame stabilisation [68]. However, the flame is predominantly stabilised via the edge flame concept at a low jet Reynolds number [68]. Chen and Bilger [75] identified three stabilisation mechanisms for lifted laminar flames based on jet velocity, scalar dissipation rate, and liftoff height, which may help with the understanding of different flame stabilisation mechanisms for lifted turbulent flames via a triple flame concept. As depicted in Fig. 2.6, at the stabilisation point (denoted by solid circles), the propagation velocity of triple flames U_p is equal to the upstream flow velocity U_{st} along the stoichiometric mixture fraction contour [75]. Figure 2.6 also demonstrates the stability criteria for different flame conditions. When the mixture fraction at the jet centreline is larger than the rich flammability limit, the flame is stabilised by the triple flame propagation [75].

2.3.2 Flame Stabilisation Mechanisms under MILD Combustion Conditions

The theories described in the preceding section were proposed based on standard fuel-air combustion. Under conditions relevant to MILD combustion, the existence of a hot and diluted oxidant brings additional complexities to the flame stabilisation mechanism: reactants are likely to autoignite rapidly at a high temperature, meanwhile the low local oxygen concentration increases the chemical timescale and ensure enough time for mixing, rendering turbulence-chemistry interaction important. Towards solving this complicated issue, numerical and experimental efforts have been made to investigate laminar lifted flames under elevated temperature [52, 53, 55, 56, 87].

Experimental Studies

Choi et al. [53] investigated the autoignition characteristics of laminar propane jet diluted with nitrogen coflowing by heated air. Conventional photography revealed distinct flame structure at varied temperature of coflow air, based on which flames are classified into three categories: (a) when the air temperature was below the autoignition temperature, non-autoignited conventional lifted flame was observed; (b) when the air temperature was above the autoignition temperature, together with a high concentration of propane in the fuel jet, an autoignited lifted flame with a tribrachial structure was established; (c) when the temperature was above the autoignition temperature and the fuel jet was highly diluted, an autoignited lifted flame without a tribrachial structure was stabilised [53]. Flames in the last regime, having low flame luminosity and obscure flame bases, were referred to as MILD flames by the authors [53]. Simulation by Evans et al. [87] shows that the formation of a tribrachial structure is fuel-dependent such that CH_4 flame in a 1300-K coflow with 3% O_2 by volume is a MILD flame without a tribrachial structure, meanwhile

C_2H_4 flame is an edge flame with a triple point under the same coflow condition.

The tribrachial structure in laminar flames was also found to occur at an increased jet velocity [55]. At a coflow air temperature of 900 K, a jet flame, composed of methane, hydrogen, and nitrogen, was found to shift away from the MILD combustion regime at a higher jet velocity such that the flame base became tribrachial [55]. The liftoff height decreased with the increasing jet velocity, and the differential diffusion between methane and hydrogen was suspected to be partially responsible for the change in the liftoff height, though further computational work was required to fully understand it [55]. It is worth noting that molecular diffusion may still be important even for turbulent jet flames in the MILD combustion regime due to the lower gradient of scalars like temperature [88, 89].

The unusual liftoff height behaviour has also been reported previously for turbulent flames under conditions relevant to MILD combustion, such as methane-based flames in a recuperative MILD combustion furnace [18] and ethylene-based flames in a JHC burner [51]. Particularly, the liftoff height of ethylene-based flames initially reduced as the jet Reynolds number increased from 5000 to 10000, however, it barely changed with the jet Reynolds number varying from 10000 to 20000 [51]. This is consistent with experimental studies by Oldenhof et al. [65, 66], who reported that the liftoff height of Dutch natural gas flames initially reduced at a higher jet velocity or Reynolds number in a hot coflow with 7.6%–8.8% O_2 by mass. However, these experimental results contradict measured liftoff heights of methane-air flames reported by Cabra et al. [67]. The discrepancy may be attributed to a higher O_2 level in the coflow ($X_{O_2} \geq 12\%$) in the study by Cabra et al. [67].

The liftoff heights of flames were also reported to increase at a higher coflow temperature or oxygen level under conditions relevant to MILD combustion [62]. The transition from the MILD combustion regime to the conventional combustion regime was thought to be responsible for this unusual trend in the liftoff height [62].

This reasoning is supported by marked differences in the jet stabilisation mechanism caused by the change in the coflow oxygen level. Gordon et al. [64] argued that the base of lifted methane flames in a hot coflow with 11% to 12% O_2 by volume were stabilised by a build-up of ignition kernels. The autoignition process was divided into three stages: the build-up of formaldehyde, the formation of hydroxyl radicals, the consumption of formaldehyde and formation of a stable lifted flame [64]. The formaldehyde molecules were consumed after ignition, while the concentration of hydroxyl radicals peaked at ignition, and those peaks were maintained into the steady lifted flames [64]. In a coflow with 3% O_2 by volume, the role of formaldehyde as an ignition precursor remained, while a faint OH tail was found to extend from the nozzle exit, which suggested that the flame was attached [51].

The coflow composition and temperature were found to affect the formation of ignition kernels and their statistics [63–65, 90, 91]. This also indicates fundamental changes in the flame stabilisation mechanisms. Markides and Mastorakos [90] studied the ignition kernel formation of hydrogen in a turbulent coflow of heated air via OH^* chemiluminescence. The fuel jet was pure hydrogen or hydrogen diluted with nitrogen with a velocity ranging from 20 to 120 m/s [90]. The fuel jet temperature varied from 650 to 930 K [90]. The velocity of coflowing air was up to 35 m/s, and its temperature was up to 1015 K [90]. Depending on the frequency of occurrence of ignition kernels, four regimes, including 'No Ignition', 'Random Spots', 'Flashback', and 'Lifted Flames', were identified [90]. In the 'Random Spots' regime, isolated ignition kernels appeared and disappeared frequently with intense noise, indicating extinction and reignition events. The frequency was found to correlate with the temperature and velocity [90]. Similar 'Random Spots' autoignition phenomenon has also been reported for acetylene and a gaseous n-heptane plume [91]. The transition between these regimes was found to be highly sensitive to the air temperature such that a less than 5 K change in the air temperature can cause the transition [90].

This is consistent with a previous study by Cabra et al. [67], where the liftoff height of methane flames varied with a departure on the coflow temperature as small as 10 K.

Oldenhof et al. [65] investigated the ignition behaviour of Dutch natural gas flames in both a cold air coflow and a hot vitiated coflow. Two hot coflow cases were studied: a coflow with 8.4% oxygen by mass at a maximum temperature of 1540 K; a coflow with 9.5% oxygen by mass with a maximum coflow temperature of 1460 K [65]. They found that the lifted flame in a cold air coflow has a sharp and connected interface that moved up and down [65]. In contrast, isolated ignition kernels were found upstream of the main flame front, and these kernels grew in size while being convected downstream and eventually merged together [65]. The formation and growth of ignition kernels that induce a continuous flaming combustion further downstream were also reported by Masri et al. [26] for turbulent spray flames in a hot vitiated coflow. Oldenhof et al. [65] reported that increasing the jet Reynolds number above 5000 reduced the frequency of occurrence of the ignition kernels. This agrees with simulations performed with the conditional moment closure and a CFD code [91], which demonstrated that a higher scalar dissipation rate as a consequence of increased coflowing air velocity retarded the ignition [91].

It is worth noting that the presence of ignition kernels is not a common feature in all cold-fuel-hot-coflow configurations. For instance, the formation of ignition kernels were not revealed by imaging of flames in experimental studies by Medwell et al. [51, 92], Cabra et al. [93, 94], and Choi et al. [53, 55]. This can be attributed to differences in the boundary conditions, or fuel chemistry, or a combination of both. These results suggest that different flame stabilisation mechanisms may exist in cold-fuel-hot-coflow configurations. Therefore, simulations taking into account of both autoignition and flame propagation will serve to provide more insights to this topic.

Numerical Studies

A considerable number of numerical studies [50, 68, 87–89, 95–101] have been conducted to investigate the flame stabilisation mechanism under MILD combustion conditions. Kumar et al. [68] applied a flame extinction model to simulate various jet flames issuing into ambient air, preheated air, and hot vitiated coflow. They reported that the flame is stabilised near the stoichiometric mixture fraction contour, where the local flow velocity matches with the local flame propagation speed [68]. The local flow velocity is found to change considerably with the bulk jet Reynolds number of the fuel jet, suggesting that different flame stabilisation mechanisms may occur at various jet Reynolds numbers [68].

Mardani et al. [88] investigated the role of molecular diffusion based on experimental CH_4/H_2 flames measured by Dally et al. [50]. They found that the molecular diffusion has a considerable importance in comparison to the turbulent transport [88], supported by results from Conditional Moment Closure modelling of the same flames [89]. They also reported that the significance of molecular diffusion increases at a lower jet Reynolds number, a lower coflow oxygen level, or a higher hydrogen concentration in the fuel jet [88]. They found that the accuracy of simulation results is affected by the method of including the molecular diffusion [88]. A better agreement with experimental data is achieved when the differential diffusion method is used instead of using constant and equal diffusion coefficients for all species [88]. The accuracy of the differential diffusion method did not change if the multi-component diffusion equation is used of the mixture-averaged equation [88].

Abtahizadeh et al. [95] performed a numerical study to investigate the stabilisation mechanism of flames in both the conventional combustion regime and the MILD combustion regime. The peak heat release was found to locate closer to the stoichiometric contour and formed the edge of a trailing diffusion flame in non-preheated

and preheated only cases, while flames under diluted and preheated conditions were more akin to autoignited flames [95]. The autoignition structure of MILD flames is further supported by an improved prediction for the distribution and concentration of O_2 when unsteady flamelet model was applied instead of steady flamelet [95]. This is in accordance with a numerical study by Coelho and Peters [96]. They found that NO emissions calculated by unsteady flamelet agreed more closely with experimental data than steady flamelet model [96].

Similar conclusions were also drawn from premixed laminar flame calculations for methane/air mixture diluted with hot exhaust gases by Sidey et al. [97]. Species profiles demonstrated that a large amount of intermediate species, such as CH_3 and H_2O_2, were produced upstream of the flame front when the mixture became highly diluted. Moreover, as the mixture became more diluted, the initial pre-ignition event merged with the primary ignition event to form a prolonged ignition process, thus the sharp rise in the temperature profile disappeared [97]. This elongated ignition event has also been reported by Medwell et al. [98] for simulated ethylene flames in a well-stirred reactor.

The importance of both autoignition and turbulent transport is highlighted in a LES investigation of lifted H_2/N_2 flames in a hot and diluted coflow by Duwig and Fuchs [99]. They found that pockets of flammable mixture ignited on the lean side of the shear layer, which were then transported by large coherent structures towards the strong jet shear layer [99]. The enhanced mixing of fuel lean pockets and fuel rich pockets contributed to further heat-release and stabilised the lifted flame [99].

The role of minor species in the hot and diluted oxidant on the flame stabilisation has been investigated numerically [87, 100, 101]. The change in the dilution ratio was found to have a complex effect on the ignition delay times, which could be caused by differences in the resultant temperature and the amount of minor species in the mixture [100]. For example, the presence of H_2 molecules and its conver-

sion to hydrogen radicals in the hot oxidant can promote the ignition process by initiating chain branching reactions [100]. It was also found that NO can promote the oxidation of hydrocarbons by activating peroxy radicals at low temperatures. However, this effect became less pronounced at higher temperatures because of the reduced importance of peroxy radicals [101]. Numerical analysis by Evans et al. [87] reported that MILD CH_4 flames became attached at the inclusion of equilibrium levels of hydroxyl radical (< 10 ppm), however, this inclusion did not shift the flame between the MILD combustion regime and the conventional spontaneously-ignitive regime.

To summarise, unusual experimental observations of MILD flames in literature suggest that the flame stabilisation mechanism is different in MILD combustion with respect to its counterpart – standard fuel-air combustion. Numerous studies [18, 53, 55, 56, 62, 65, 66, 87] based on simple gaseous fuels have been performed to improve the understanding of the flame stabilisation mechanism. These studies emphasise the important role of the temperature and oxygen concentration of the hot coflow, as well as the fuel type. However, there is a paucity of information on the establishment of MILD combustion of more complicated fuels. In order to extend MILD combustion to wider areas in the future, the sensitivity of the flame stabilisation and structure to the fuel type needs to be better understood. Previous studies [55, 99] also found that molecular diffusion, turbulent transport, and autoignition all play a role in the flame stabilisation, highlighting the importance of turbulence-chemistry interaction, which will be discussed in detail in the following section.

2.4 Turbulence-Chemistry Interaction

2.4.1 Overview of Turbulence-Chemistry Interaction

The coupling of turbulence and chemistry affects the flame ignition, the flame stabilisation mechanism, and the flame structure in general. Combustion only takes place when reactants are mixed at a molecular level. Turbulent mixing, the dissipation of scalar variance, promotes the molecular mixing indirectly [102]. Important scalars include temperature and the concentration of reactive species. Specifically, turbulence forces the transportation and dissipation of scalars through a large scale of flow fluctuation. The scalar fluctuation progressively occurs at a smaller turbulent scale until molecular mixing occurs at the smallest turbulent scale and eliminates the scalar gradient. The rate of molecular mixing is calculated as the scalar dissipation rate. The scalar dissipation rate is of great importance when the reacting system is operated close to ignition or extinction [103]. For instance, Markides et al. [91] found that ignition is retarded by an increasing co-flowing air velocity due to the resultant increase in the scalar dissipation rate.

The establishment of MILD combustion requires a thorough mixing of hot exhaust gases and fresh reactants, therefore the scalar dissipation rate is important. Indeed, the MILD combustion regime is associated with a low Damköhler number, where both turbulence and chemistry play an important role [104]. For instance, a RANS-based numerical study [105] revealed that an appropriate turbulence-chemistry model is required to improve predictions of MILD flame temperature. Important parameters in the aspect of turbulence include velocity, velocity fluctuations, Reynolds number, momentum, entrainment ratio and so forth. Important parameters in the aspect of chemistry include temperature, pressure, fuel type and so forth. These parameters interact and affect each other frequently in both space and time under MILD combustion conditions. For example, the momentum of a

fuel jet determines its entrainment ratio of surrounding hot exhaust gases, leading to changes in the local temperature and mixture compositions, which subsequently affect the chemical reactions. The progress of chemical reactions change the gradient of temperature and concentrations of species, in turn changing the scalar dissipation rate.

2.4.2 Impact of Fuel Properties

There are experimental evidence related to the role of fuel properties and chemistry [106]. Severin et al. [106] investigated the flame stabilisation mechanisms at a high-pressure combustion test rig fired with natural gas (NG) and pure hydrogen (H_2) under conditions relevant to MILD combustion. Particle Image Velocimetry (PIV) was performed to characterise the flow field, while OH*-chemiluminescence (OH*-CL) and laser Raman scattering were performed to measure the location of the heat release zone and the distribution of major species, respectively [106]. The PIV results demonstrated that the NG and the H_2 cases each had similar flow fields. The standard deviations of the velocity fields (u') were calculated to indicate the turbulent fluctuation and the location of shear layer [106]. The overlay of OH*-CL and u' contours revealed a fundamentally different turbulence-chemistry interaction between the NG case and the H_2 case [106]. Particularly, most of the NG reaction zone was found to locate within the shear layer between fresh and hot burned gas, while the reaction zone of the H_2 flame was located close to the nozzle with little disturbance from the shear layer [106]. They concluded that flame propagation stabilised the H_2 flame, meanwhile spontaneous ignition was more likely to be the dominating stabilisation mechanism for the NG flame, though a closer look at the recirculation and ignition process was suggested to confirm this finding [106].

Arghode et al. [107] investigated differences between methane and ethanol flames in an ultra-high thermal intensity distributed combustor. When the ethanol spray

was directly injected into the combustor, a large amount of carbon monoxide emissions were emitted, considerably higher than those produced from combustion of methane or prevaporised ethanol [107]. The increased level of CO emissions was attributed to a reduced residence time as the reaction zone was shifted towards the combustion chamber exit when ethanol spray was injected directly [107].

Weber et al. [61] performed a comparison study of various fuels in a furnace at The International Flame Research Foundation (IFRF) under MILD combustion conditions. These fuels included natural gas, light fuel oil (LFO), heavy fuel oil (HFO) and coal. When natural gas and LFO were fired, the entire furnace was illuminated without the existence of visible flames [61]. However, in the combustion of coal and HFO, high NO_x emissions and visible flames were always observed. It is worth mentioning that NO_x emissions produced from coal and HFO in the MILD combustion mode were still lower than those produced from the conventional combustion mode using the same furnace [61]. Therefore, it was concluded that strong recirculation of hot products can effectively reduce NO_x by enhancing the NO reburning mechanism as it provides locally sub-stoichiometric conditions, though it has little effect in restraining NO_x production via fuel-NO mechanism [61]. Simulation results of pulverized coal combustion also revealed that fuel-NO mechanism is the primary mechanism for NO_x production under MILD combustion conditions [108].

The critical role of fuel type on the flame structure and behaviour under MILD combustion conditions is not hard to understand. When the temperature of a reacting system is really high, the oxidation pathways for most of hydrocarbons are dominated by the H_2/O_2 pathway [109–111]. At a temperature ranging from 850 K to 1200 K, the reacting system can undergo a two-stage ignition, namely, the cool ignition and the thermal runaway of ignition. The thermal runaway of ignition is governed by the high-temperature ignition mechanism, while the cool ignition is dominated by fuel-specific low temperature hydrocarbon oxidation mechanisms

[112]. The temperature of a MILD combustion system in previous studies was commonly between 800 K and 1600 K, thus the system probably experiences a two-stage ignition. Therefore, the impact of fuel type under MILD combustion conditions can be expected, and its significance is directly coupled with the coflow temperature.

2.4.3 Impact of Coflow Temperature and Composition

It is essential to prepare a uniformly hot and diluted environment before ignition to establish MILD combustion. In the majority of laboratory studies, this environment is created by the hot coflow. The impact of coflow temperature and composition has been a focus in many previous studies due to its significance [50, 62, 67, 87, 113–117].

Dally et al. [50] reported up to a 400-K reduction in the peak flame temperature and a three-fold decrease in the CO and OH concentration when the coflow oxygen concentration dropped from 9% to 3% by mass. Rodrigues et al. [113] found that the coflow temperature significantly affected ethanol spray flames in the Delft-Spray-in-Hot-Coflow (SHC) burner. Particularly, a lower coflow flame temperature lead to a reduction in the peak spray flame temperature and an increase in the liftoff height due to a longer droplet vaporisation timescale and chemical timescale [113]. The strong sensitivity of liftoff height to coflow temperature was also highlighted for methane flame by Cabra et al. [67]. Medwell et al. [62] found that the liftoff height for methane- and ethylene-based flames initially increased at an increasing coflow temperature or oxygen concentration, and the flames became less lifted at a further increase in the coflow temperature and oxygen concentration. The initial increase in the liftoff height was thought to be caused by a transition from the MILD combustion regime to the conventional combustion regime [62]. This is consistent with experimental and numerical studies by Evans et al. [87]. They reported that the simulated methane flame in a 1300-K oxidant with 3% O_2 behaved like a MILD flame, while a tribrachial flame structure occurred in the methane flame burning in

a 1300-K oxidant with 6% or 9% O_2 [87]. They also investigated the role of active radicals in the hot oxidants on the flame stabilisation, which has been discussed in the preceding Section 2.3.2.

The role of inert species have been investigated in previous studies [114, 115]. Sabia et al. [114] investigated the ignition process of propane/oxygen mixtures diluted by CO_2 or H_2O in a Tubular Flow Reactor (TFR) at atmospheric pressure. Compared to mixtures diluted by N_2, the system reactivity was greatly reduced when CO_2 or H_2O was used as a diluent. Further numerical analyses [114, 115] show that at low temperature CO_2 and H_2O mostly worked as a third body with high third-body efficiencies participating in termolecular and/or decomposition reactions. At high temperature they changed the relative importance of methyl radical recombination channel compared to the oxidation channel [115]. They also compete for H atoms with main H_2/O_2 branching reactions [115].

The coflow temperature and composition, as boundary conditions, affect the accuracy of modelling predictions considerably. A three-stream Large-eddy simulations (LES) of experimental flames by Dally et al. [50] was performed by Ihme and See [116]. The agreement between numerical results and experimental measurements for the flame structure and the flow field was improved by adopting a three-stream LES instead of the single-mixture-fraction flamelet/progress variable (FPV) formulation [116]. These MILD flames were found to be highly sensitive to temporal fluctuations in scalar boundary conditions, the impact of which extended from the nozzle-near area to the whole flame [116]. This conclusion is consistent with a numerical study of the same flames by Mardani et al. [117]. They found that up to 15% error in the simulated temperature and species concentration fields occurred when the fluctuations on the temperature and mass concentration of species were ignored in reaction rate calculations [117].

2.4.4 Impact of Entrainment and Mixing

An enhanced mixing of fresh reactants and hot exhaust gases is the prerequisite for a slow, steady, and homogeneous ignition. Indeed, Katsuki and Hasegawa [16] found that a strong dilution of reactants, created by a shear motion of high-velocity air, was necessary for establishing MILD combustion in a hot and diluted environment inside a furnace. This is further supported by an experimental study conducted in a recuperative MILD combustion furnace by Dally et al. [18], who highlighted the important role of the scalar dissipation rate in the nozzle-near region. In specific, the scalar dissipation rate should be sufficiently high to inhibit early ignition, resulted from downstream flame propagation, before the reactants are mixed with hot burned gases [18]. A high scalar dissipation rate can be achieved by various means, such as increasing the jet Reynolds number and increasing the relative velocity between fuel and air jets. Furthermore, it was found that diluting the fuel jet with inert gases resulted in a shift in the stoichiometric ratio towards the jet shear layer with a higher scalar dissipation rate, which helped delay the reactions near the jet exit plane [18].

In practical MILD combustion burners, the strong recirculation of hot exhaust gases is controlled by the flow dynamics. Researchers have explored various approaches to promote the exhaust gas recirculation, including the use of high-speed jets [21, 118, 119], tangential air injection [47], a reverse-flow design [20, 120], and a cross-flow design [120]. Previous studies [20, 121] found that an enhanced exhaust gas recirculation, resulted from a higher jet velocity, effectively suppressed the temperature increase, thereby reducing the emissions. Szegö et al. [21] reported that changing the fuel/air jet momentum ratio caused a transition from conventional combustion with visible flames to MILD combustion in a parallel-jet arrangement. In order to prepare a hot and diluted mixture before ignition takes place, a minimum fuel jet penetration distance is necessary in this arrangement, which is determined

by the minimum fuel/air jet momentum ratio [21]. Arghode et al. [120] performed an experimental study in a colorless distributed combustion (CDC) combustor operated under a reverse cross-flow mode, where air is injected from the top and fuel is injected in the cross-flow to the air stream. Extremely low levels of NO and CO emissions were measured when the combustor was operated in this mode [120]. Sharma et al. [47] adopted tangential air injection to enhance the recirculation in a liquid fuel fired flameless combustor. They found that the improved recirculation and mixing led to a more uniform temperature distribution, thereby reducing the CO and NO_x emissions [47].

The importance of entrainment and mixing is also highlighted in numerical studies. For example, Mancini et al. [122] reported that large discrepancies of the fuel jet between several RANS-based models and IFRF experimental data by Weber et al. [24] were caused by poor predictions of the entrainment rather than any chemistry sub-models.

2.4.5 Impact of Pressure

Most of the previous studies on MILD combustion [61, 88, 89, 95–101, 123] were performed for simple gaseous fuels under atmospheric pressure. However, limited information is available on MILD combustion under pressurised conditions, particularly when complex fuels, such as long-chain alkanes, are used as fuels. Many combustion devices, such as automobiles and gas turbines, are operated under high pressure. Considering the great advantages and attractiveness of MILD combustion, it is beneficial to apply MILD combustion in a variety of areas.

The establishment of MILD combustion requires a homogeneous mixture of preheated and diluted reactants, created by a strong recirculation of hot exhaust gases. The preparation of such a uniform mixture with certain temperature and compositions becomes increasingly important and challenging under elevated pressures. As

mentioned in the preceding section, the recirculation of hot burned gases is often achieved by high velocities. Based on the ideal gas law, velocity decreases linearly as pressure increases. This implies a weakened entrainment of hot exhaust gases, a longer characteristic timescale of the fluid flow, and residence time, which affects the formation of emissions. For example, Biagioli and Güthe [124] found that assuming a perfect mixture of fuel and air under adiabatic conditions, the amount of NO_x emissions produced in hot gases downstream of the main heat-release region is dominated by residence time.

Pressure also affects the chemistry and flame structure significantly. For instance, pressure alters the direction and rate of chemical reactions, where the volume of recants and products are not equal. Taking H_2/CO reaction pathway as an example, $H+O_2 \rightleftharpoons OH+O$ (R1) is a chain branching reaction that is sensitive to temperature [125]. However, reaction $H+O_2+M \rightleftharpoons HO_2+M$ (R2) is a three-body and chain inhibiting reaction that is insensitive to temperature [125]. When pressure increases while keeping everything else the same, the three-body reaction R2 is promoted in comparison to R1 [125]. This produces a decaying effect on the overall oxidation process [125]. The importance of pressure-sensitive reactions in the fuel chemistry is suggested to be responsible for changes in the laminar flame speed under elevated pressures [125]. As shown in Fig. 2.7, at a constant equivalence ratio, the laminar flame speeds of propane-air [126] and ethanol-air [127] flames decrease as pressure increases.

The influence of pressure on the ignition temperature and ignition delay has also been studied extensively in literature [125, 126, 128–130]. Autoignition for many fuels can be achieved at a lower temperature with a shorter ignition delay under pressurised conditions in comparison to atmospheric condition [12]. For example, Jomaas et al. [126] reported that the ignition temperature for ethylene, propylene, ethane, and propane rapidly decreases as pressure increases from 0 to 10 bar. The

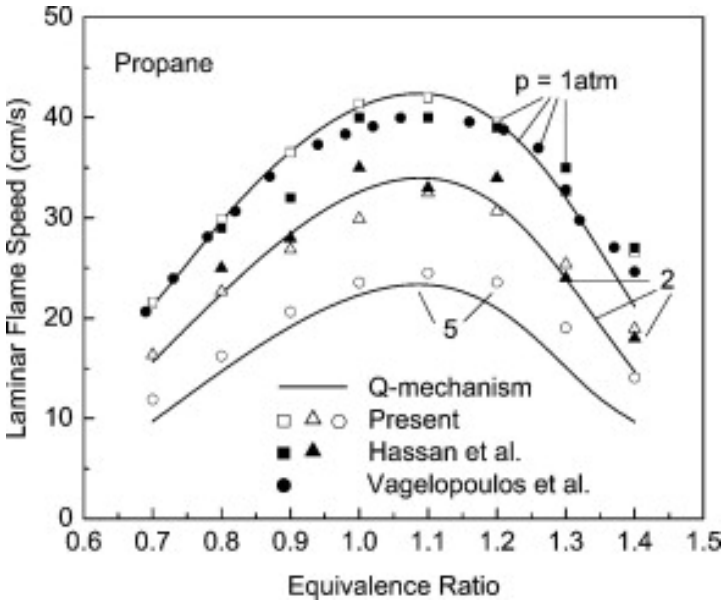

(a) propane

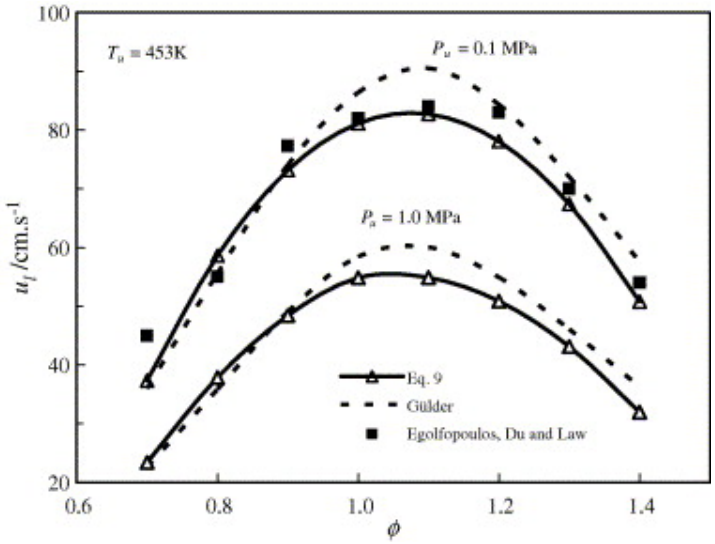

(b) ethanol

Figure 2.7: Laminar flame speed as a function of equivalence ratio and pressure: (a) propane-air flame [126]; (b) ethanol-air flame [127].

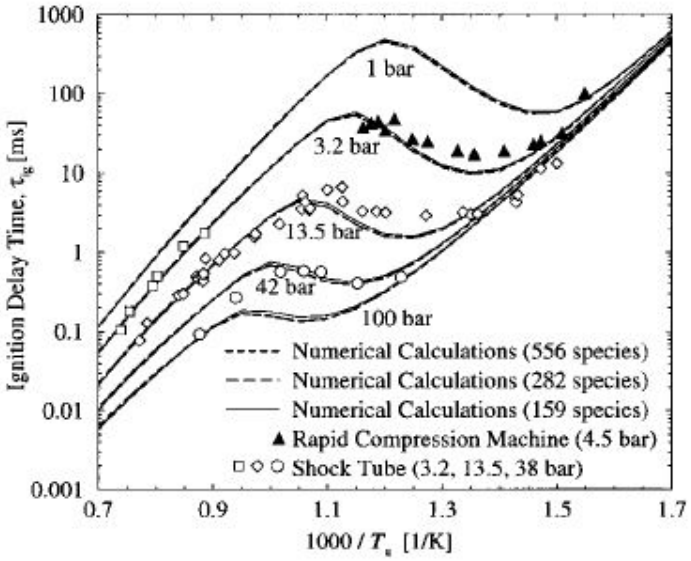

Figure 2.8: Ignition delay time (τ_{ig}) in stoichiometric mixtures of n-heptane vapour and air as a function of the reciprocal of initial temperature (T_u) for various pressures [128].

role of pressure on the negative temperature coefficient behaviour has also been investigated for fuels like n-heptane and n-decane [128, 130]. As displayed in Fig. 2.8, the ignition delay times for n-heptane-air flames decrease considerably with pressure, especially at a high initial temperature. Furthermore, the NTC behaviour of n-heptane is less pronounced under elevated pressures for two main reasons. The temperature at the start of the NTC region is higher under elevated pressures, which is attributed to the enhanced reaction rate of $R+O_2 \rightleftharpoons RO_2$ in the forward direction [128]. Meanwhile, as the dissociation of H_2O_2 via $H_2O_2+M \rightleftharpoons OH+OH+M$ is highly dependent on pressure, the dissociation of H_2O_2 is promoted to terminate the NTC region as pressure increases [128].

As discussed previously in Section 2.4.1, MILD combustion is associated with low Damköhler number. Pressure affects chemical reactions and burning rates significantly, thereby changing the chemical timescale and the resultant Damköhler number. Therefore, it is postulated that pressure plays a role on the stabilisation of MILD combustion, consequently altering the flame behaviour and pollutants for-

mation.

The important role of pressure on MILD combustion can also be inferred from previous studies on homogeneous charge compression ignition (HCCI) engines [131, 132]. The fundamental defining characteristic of HCCI engines is that a well-mixed fuel-air mixture is injected into the engine chamber under particular conditions such that autoignition occurs homogeneously across the entire chamber [131, 132]. The autoignition can be achieved by a combination of high compression ratios, high intake pressures and temperatures, using fuels with great reactivity, or using EGR [131]. Hence, HCCI combustion can be considered as MILD combustion under pressurised conditions to some extent. One of the principal obstacles in HCCI engines is the difficulty of controlling the combustion timing [132]. The onset of combustion in HCCI engines is autoignition, which is a kinetically controlled process that is sensitive to boundary conditions like intake pressure [132]. For instance, higher intake temperatures and pressures result in an earlier ignition due to faster chemical kinetics [131]. These operating conditions also interact with each other and make the combustion phasing more challenging. For instance, differences in the temporal heat release between single- and two-stage ignition fuels affect the timing control [131], and the two-stage ignition in turn is affected by pressure as discussed above.

A few studies [19, 20, 121] have attempted to explore the suitability of MILD combustion of natural gas under elevated pressures. Lückerath et al. [19] applied MILD combustion to a FLOX® combustor fired with natural gas at a pressure of 20 bar for the first time. A stable operating range with less than 10 ppm CO and NO_x emissions was achieved for natural gas with equivalence ratio approximately spanning from 0.37 to 0.48 [19]. They also found that the stable operating range could be widened when natural gas was mixed with hydrogen due to the extended flammability limit, and thus lower the amount of CO emissions at very lean con-

ditions [19]. However, NO_x emissions increased with the admixture of hydrogen [19], which was investigated further by Sadanandan et al. [121]. They found that higher NO_x emissions were caused by enhanced thermal NO and N_2O-intermediate mechanisms at a higher flame temperature when hydrogen was added to natural gas [121]. Under this circumstance, the recirculation rate of hot exhaust gases, directly affected by inlet velocities and pressure, can be manipulated to reduce emissions [121]. In specific, they found that the recirculation rate should be sufficiently high to guarantee a thorough mixing of the fresh reactants and burned gases prior to ignition, while it should not be too high in order to ensure the ignition delay is short enough for flame stabilisation [121]. Similarly, the residence time inside the combustion chamber also produces competing effects on emissions formation [121]. Specifically, NO_x formation via the thermal-NO route is suppressed at a shorter residence time, meanwhile a long enough residence time is required for the oxidisation of CO to CO_2 [121].

Kruse et al. [20] investigated the impact of pressure in a reverse-flow MILD combustor with pressure up to 5 bar. They reported that a joint regime of low CO and NO_x emissions became narrower at a higher pressure due to increased NO_x emissions [20]. This was partly attributed to the enhanced N_2O-intermediate mechanism, particularly a higher reaction rate of $N_2+O+M \rightleftharpoons N_2O +M$ under pressurised conditions [20]. The impact of pressure on NO_x formation at a constant inlet velocity was also investigated by reducing the nozzle diameter accordingly [20]. It was reported that NO_x emissions decreased under elevated pressure given a smaller nozzle diameter [20]. The recirculated mass flow rate is found to be inversely proportional to the nozzle diameter [20]. Hence, a lower amount of NO_x emissions suggested that the impact of an enhanced recirculation on reducing NO_x emissions overcompensated the impact of pressure on increasing the emissions [20].

Gupta et al. [119, 120, 133–135] performed experimental studies in a colorless

distributed combustion (CDC) combustor under elevated pressures, and similar conclusions were drawn as the previous study by Kruse et al. [20]. Colorless distributed combustion is based on high temperature air combustion technology, but is operated with a low residence time and high combustion intensity [107]. Khalil and Gupta also reported an increase in NO emission as the pressure increased at a constant mass flow rate [134]. This was attributed to a longer residence time, reduced entrainment of hot exhaust gases, and earlier flame stabilisation [134]. Imaging of OH^* chemiluminescence indicated that the flame zone was shifted upstream at a higher pressure, indicating earlier ignition prior to a thorough mixing [134].

In summary, previous studies [19, 20, 50, 106, 114, 115, 121], mostly on simple gaseous fossil fuels, have identified several important parameters coupled in the turbulence-chemistry interaction, such as the entrainment ratio and pressure. However, parametric studies of different types of fuels like long-chain alkane and oxygenated fuels should be performed in a way analogous to previous studies on simple gaseous fuels. Findings from these studies will be valuable for the implementation of MILD combustion in various combustion systems.

2.5 Pollutant Emissions and Control

Harmful pollutants can be emitted from the combustion of liquid fuels, such as nitrogen oxides (NO_x), soot, and particulates. The term nitrogen oxides (NO_x) refers to nitrogen oxide (NO) and nitrogen dioxide (NO_2). The emissions of NO_x directly impact on public health, and they also contribute to the formation of ground-level ozone, particulate matter (PM), and acid rain [136]. It was found that PM is strongly correlated with morbidity and mortality [136]. Acid rain, a form of precipitation with acidic components like nitric acid, has significant impacts on surface water, soil, and other parts of the ecosystem, thereby affecting the economy and public health [136].

Increasingly stricter regulations on NO_x emissions have made NO_x control an important consideration in the design of combustion devices. It has also motivated the development of various combustion technologies including MILD combustion. In order to develop strategies to reduce NO_x emissions effectively, it is essential to understand NO_x formation mechanisms. Three main mechanisms contribute to NO_x formation during the combustion of hydrocarbons, namely, the thermal NO_x or Zel'dovich mechanism, the prompt or Fenimore mechanism, and the N_2O-intermediate mechanism [137]. It is worth noting that fuel-NO_x mechanism is not considered important as liquid fuels used in this thesis do not have chemically-bounded nitrogen in their molecular structure. Three key reactions produce NO via the thermal mechanism [137]:

$$O + N_2 \rightleftharpoons NO + N \tag{2.2}$$

$$N + O_2 \rightleftharpoons NO + O \tag{2.3}$$

$$N + OH \rightleftharpoons NO + H \tag{2.4}$$

As indicated by its name, the thermal NO_x mechanism is endothermic, especially reaction 2.2, which often occurs in the post-flame zone [138]. Under conventional combustion conditions, the thermal NO mechanism only dominates where equivalence ratios range from 0.8 to 1.0 for methane flames as the flame temperature is not high enough at equivalence ratio below 0.8 [139].

Some rapidly-formed NO_x in the flame zone was first discovered by Fenimore via the prompt mechanism in 1971 [138]. The prompt mechanism involves reactions with low activation energy and reaction rate comparable to fuel oxidation, particularly by reaction 2.5 [13]. The prompt mechanism is less dependent on the temperature

due to the low activation energy of its key reaction with respect to the thermal NO_x mechanism.

$$CH + N_2 \rightleftharpoons HCN + N \tag{2.5}$$

Then NO is produced rapidly via HCN through the following chain reactions under some fuel-rich conditions [13, 137]:

$$HCN + O \rightleftharpoons NCO + H \tag{2.6}$$

$$NCO + H \rightleftharpoons NH + CO \tag{2.7}$$

$$NH + H \rightleftharpoons N + H_2 \tag{2.8}$$

$$N + OH \rightleftharpoons NO + H \tag{2.9}$$

The concentration of CH is usually very low because of the fast oxidation of the fuel [13]. Nevertheless, the significance of the prompt mechanism increases at high concentration of CH under some fuel-rich conditions [13]. However, when the equivalence ratio is too high, for example higher than 1.2 for methane flames, a slower conversion of HCN to NO and the onset of the destruction of NO lead to a drop in NO_x emissions [139].

Generally speaking, the N_2O-intermediate mechanism is promoted under fuel-clean ($\Phi < 0.8$) conditions. There is an increasing interest in operating combustion devices under fuel-lean conditions to reduce emissions, rendering N_2O-intermediate mechanism important [137]. The relevant reactions at these conditions are as follows: [137]:

$$O + N_2 + M \rightleftharpoons N_2O + M \tag{2.10}$$

$$N_2O + H \rightleftharpoons NO + NH \tag{2.11}$$

$$N_2O + O \rightleftharpoons NO + NO \tag{2.12}$$

NO_x control approaches can be divided into three categories, namely, changing the fuel, modifying the combustion conditions, and post-combustion treatment [140]. The freedom to change the fuel is rather limited because the choice of the fuel is mostly determined by its cost, availability and the design of combustion devices. The most widely-used post-combustion technologies, selective catalytic reduction (SCR) and selective non-catalytic reduction (SNCR), are effective yet expensive [141]. The SNCR process involves injecting the reagent (nitrogen compounds) into the exhaust gases with temperature ranging from 870–1150°C [141]. Because of this narrow temperature window and the SNCR process′ inherent sensitivity to temperature, implementation of the SNCR process is challenging. In the SCR process, ammonia is injected into the exhaust gases and reacts with NO_x across a catalyst [141]. These reactions take place at a temperature of nominally 260–455°C [141]. Real-life shortcomings, such as mixing ammonia and NO_x before the catalyst and loss of catalyst reactivity over time, limit the amount of NO_x reduction in the SCR process [141].

Many low-NO_x combustion technologies focus on the modification of combustion conditions. These technologies mainly aim to reducing thermal NO by restricting high temperature zones, such as staged combustion and exhaust gas recirculation. The formation of thermal NO requires both high temperature and high local oxygen concentration [12]. It is effective to abate NO_x by avoiding the concurrence of locally high temperature and high availability of oxygen, or by reducing the residence time at those favourable conditions.

Under MILD combustion conditions, NO_x emissions were found to be reduced effectively not only due to the avoidance of conditions promoting NO_x formation, but also due to the enhanced NO reburning mechanism [61, 72]. For instance, Weber et al. [61] reported that NO_x emissions produced from heavy fuel oil and coal were considerably lowered when they were burnt under MILD combustion conditions instead of normal air combustion condition in the same furnace. They found that the abatement of NO_x emissions was achieved through a strong recirculation of exhaust gases, which provided locally sub-stoichiometric conditions, thus promoting the NO reburning mechanism [61]. Saha et al. [72] found that the amount of NO_x emissions produced from brown coal varied with vertical distance above the jet inlet in a reverse-flow MILD combustion furnace. Particularly, the NO mole fraction at the top part of the furnace was significantly lower than that at the bottom part of the furnace [72]. This was attributed to the reburning of NO with the strong recirculation of hot products at the top [72]. The enhanced exhaust gas recirculation creates an environment rich in hydrocarbon radicals, where NO can be consumed via reactions with hydrocarbons and hydrocarbon intermediates [137, 142]:

$$CH + NO \rightarrow HCN + O \tag{2.13}$$

$$CH_2 + NO \rightarrow HCNO + H \tag{2.14}$$

$$CH_2 + NO \rightarrow HCN + OH \tag{2.15}$$

As HCNO is converted to HCN subsequently, these chemical reactions in the NO reburning mechanism can be represented by this general equation:

$$CH_i + NO \rightarrow HCN + ... \tag{2.16}$$

2.6 Research Gaps

MILD combustion is an attractive technology that can meet criteria of low emissions and high thermal efficiency simultaneously. As discussed in this chapter, due to its advantages, substantial research has been performed on MILD combustion of simple gaseous fuels, such as hydrogen and methane. A significant proportion of the global energy, however, is expected to be supplied by the combustion of liquid fuels in the foreseeable future [2]. Hence, it is of immense value to apply MILD combustion to a variety of liquid fuels in response to the acceleration in environmental awareness and global energy demand. According to the detailed literature review presented in this chapter, several important research gaps in MILD combustion are identified as follows:

- The majority of previous studies were focused on simple gaseous fuels, while little attention has been paid to more complex liquid fuels despite their important role in the global energy supply. A limited number of studies have been conducted on MILD combustion of liquid fuels under atmospheric pressure. Nevertheless, the applicability of MILD combustion of liquid fuels at elevated pressures, and the impact of pressure on the resulting flame structure, combustion stability, and pollutant formation have not been investigated in detail. This impedes the extension of MILD combustion to industrial combustion devices that are operated at higher pressures, for instance gas turbines.

- Previous research on MILD combustion of simple gaseous fuels have found that the establishment and optimisation of MILD combustion are governed by the coupling of several important parameters, manifested in the turbulence-chemistry interaction. In order to control the reacting environment and thus to obtain the maximum benefits of MILD combustion, it is crucial to understand the interdependency of these parameters, especially when it is applied

to different fuels and combustion apparatuses. Nevertheless, most of previous studies on MILD combustion of liquid fuels were not performed in a well-controlled environment with optical access. Hence, a systematic investigation of these parameters and *in situ* measurements were difficult to achieve, thereby limiting the understanding of the effects of these parameters.

- MILD combustion is associated with some unique characteristics, based on which MILD combustion regime is defined in several different ways. However, flames, satisfying one of the MILD combustion definitions, were found to behave remarkably different in terms of the flame structure and liftoff behaviour. The transition from the conventional combustion regime to the MILD combustion regime is not well understood. Importantly, a deeper understanding of the impact of complicated fuel structure and chemistry on the transition to the MILD combustion regime is required.

2.7 Research Aims and Objectives

The extension of MILD combustion to liquid fuels, particularly renewable fuels, is invaluable for the sustainable energy supply. However, there is a deficit of information in this field. This thesis aims to advance the understanding of the flame structure of prevaporised liquid fuels burning under MILD combustion conditions at atmospheric and elevated pressures. To achieve this aim, this thesis will accomplish the following objectives:

- The first objective is to investigate the impact of pressure on MILD combustion of prevaporised liquid fuels, particularly on the establishment of MILD combustion and the resultant pollutant formation. The influence of the coupling of pressure with other parameters, including fuel type, equivalence ratio, and jet velocity, on MILD combustion of prevaporised liquid fuels will also be

examined.

- The second objective is to independently evaluate the impact of important operating parameters, including the type of fuel and carrier gas, the coflow temperature and oxygen level, and the jet Reynolds number. This investigation will be focused on the flame appearance, the liftoff behaviour, and the distribution of temperature, ignition radicals, and intermediate species.

- The third objective is to explore the transition between the MILD combustion regime and the conventional combustion regime at the change of operating parameters. In particular, the effect of fuel chemistry on the transition to MILD combustion will be investigated.

Chapter 3

Methodology

This chapter describes the primary experimental and numerical techniques used in this project. To achieve the aims of this project, important scalars, including temperature, ignition radicals, and intermediate species, are measured in the experiments, and the fuel chemistry is investigated in detail via calculations and simulations.

Experimental studies have been performed in a reverse-flow MILD combustor and on a Jet in Hot Coflow (JHC) burner. In order to reveal and compare the flame structure of various flames investigated in this project, digital photography and imaging of the excited hydroxyl radical (OH^*) chemiluminescence have been conducted. Furthermore, to obtain *in situ* information of the flames, three laser diagnostic techniques have also been performed, including Rayleigh scattering, laser-induced fluorescence (LIF) of hydroxyl radical (OH) and formaldehyde molecule (CH_2O). Relevant concepts and knowledge in spectroscopy are prerequisites for understanding the principle of these laser diagnostic techniques. These concepts will be introduced in Section 3.1.

Numerical modelling has been performed to complement the experimental investigations. Laminar flame calculations have been conducted using the OPPDIF code for computing diffusion or premixed opposed-flow flames. These calculations allow a detailed examination of the chemistry kinetics effects while ignoring the complex-

ity of a turbulent flow field. Results from laminar flame calculations are also used to assist the image processing, hence they will be described in Section 3.6.1 as a step in the temperature quantification procedure. Transient laminar flamelet modelling, based on a turbulent flow field modelled by Large-Eddy simulations (LES), has also been performed to take account of the time-dependent features of ignition processes. Details of these numerical simulations will be provided in Section 3.8. It is worth noting that part of the experimental and numerical details will be repeated in individual papers included in this thesis wherever it is applicable.

3.1 Background in Spectroscopy

3.1.1 Photons

Probing OH and CH_2O with LIF involves the excitation of these species upon the absorption of electromagnetic radiation provided by the laser. According to the photon theory developed by Planck and generalised by Einstein, light can be viewed as a collection of discrete energy packets called photons [143]. The energy possessed by a photon is determined by its frequency (denoted by ν) as shown in the following relation [143]:

$$E = h\nu \tag{3.1}$$

where h is the Planck's constant ($h = 6.626\times10^{-34}$ J·s). Thus, the total energy of a wave of light is a function of the number of light quanta and their frequencies [143].

3.1.2 Quantum Numbers

Based on the photon theory, Bohr put forth a new model of atomic structure, in which the nucleus is surrounded by discrete electron orbits or shells [144]. The orbital angular momentum can only be integral multiples of $\frac{h}{2\pi}$ [144]. Each allowed

principal electron shell can be represented by a principal quantum number n, which takes on positive integer values. The radii of the possible orbits r is a function of n [144]:

$$r = a_0 n^2 \tag{3.2}$$

where a_0 is the Bohr radius. The orbital angular momentum quantum number ℓ, designating the subshell and determining the shape of the orbital, is an integer ranging from 0 to n-1. This quantum number can be represented by a letter, such as s(ℓ=0), p(ℓ=1), d(ℓ=2), e(ℓ=3), and alphabetically afterwards. The electron on the subshell also has orbit and spin angular momenta, characterised by m_l and m_s. The magnetic quantum number m_l determines the number of orbitals and their orientation within a subshell. Thus m_l is determined by ℓ, and its value ranges from -ℓ to ℓ. The spin vector aligns parallel or antiparallel with respect to the field, therefore m_s is $\pm\frac{1}{2}$. Every electron within an atom is characterised by the four quantum numbers, namely, n, ℓ, m_l, m_s, which completely specify the energy state of the electron.

3.1.3 Energy Transitions

Species can be identified and measured via spectroscopic methods as each species has its own particular energy transitions. According to Heisenberg Uncertainty Principle, there are many possible ways to distribute electrons over a set of orbits. In reality, electrons move around the nucleus unpredictably, which is commonly visualised as unevenly coloured electron cloud. Figure 3.1 shows a pictorial representation of the electron cloud, where the colour gradient represents the likelihood of the presence of an electron at a certain location. It demonstrates that the probabilities of the existence of an electron at some locations are much higher than others. Figure 3.1 shows that the colour becomes darker when it is closer to the nucleus because electrons normally are most likely to exist at lower quantum states.

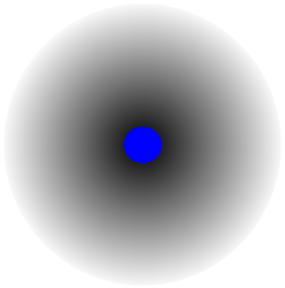

Figure 3.1: Pictorial representation of the electron cloud. The blue circle in the centre represents the nucleus, and the colour gradient indicates the likelihood of the presence of an electron at a certain location.

The electron configurations can be altered by exciting the electron, resulting in the change in the electronic energy of the atom. Figure 3.2 shows an example of an atomic energy transition. An electron (denoted by a red circle) of an atom originally resides at an electron shell represented by $n = 1$. This electron is excited by absorbing a particular amount of energy $E = hv$ and is elevated to a shell at a higher energy state represented by $n = 2$. This excited electron normally relaxes quickly and returns to the lower energy state. During this relaxation process, photons of the same frequency as the excitation process are emitted. It is worth noting that the frequency of the emitted photons can be changed by many factors, which will be discussed in the next section.

Each atom has distinct energy changes, which allows the examination of the desired atom via atomic spectroscopy techniques [145]. The specific energy transition due to changes in the electron configurations can be expressed via the following equation:

$$\Delta\nu = \Delta E_{ele}/h \tag{3.3}$$

where ΔE_{ele} is the change in the electronic energy.

When atomic spectroscopy is extended to molecular spectroscopy, it becomes much more complex as molecules can vibrate and rotate in addition to electronic transitions [145]. Therefore, when a molecule is excited, the energy transition

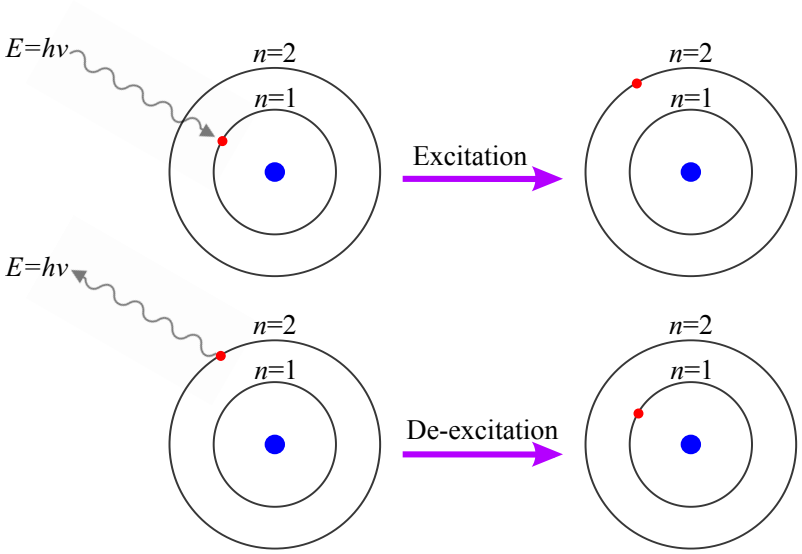

Figure 3.2: An example of atomic energy transition: the blue circle in the centre represents the nucleus and the red circle represents an electron.

can happen in three possible modes, namely, electronic, vibrational, and rotational modes. Therefore, equation 3.3 becomes:

$$\Delta\nu = (\Delta E_{ele} + \Delta E_{vib} + \Delta E_{rot})/h \tag{3.4}$$

where ΔE_{vib} represents the vibrational energy change and ΔE_{rot} represents the rotational energy change.

3.2 Background in Laser Diagnostics

3.2.1 Laser-Induced Fluorescence

Laser-induced fluorescence (LIF) is employed in this study to image the distribution and concentration of OH and CH_2O. The species of interest at a lower energy state (denoted by i), such as OH, is elevated to a particular rotational energy level of a particular vibrational energy level of a higher electronic state (denoted by j) via the absorption of a photon from a laser. The energy possessed by the photon needs to

match the energy required for the particular energy transition. These excited species then relax via several means, including the emission of a photon. In the context of LIF, fluorescence refers to the emission of photons by excited species when they relax to a lower energy state. In this study, these released photons are collected by a camera in order to generate a two-dimensional image, which readily demonstrates the distribution of the detected species. More details on the principle of LIF can be found in [146].

In the linear regime of LIF, the fluorescence yield F is proportional to the laser energy fluence E [147, 148]:

$$F = CB_{ij}NEf_i\Phi_f \tag{3.5}$$

where C is a constant obtained from experiments, which takes account of the speed of light, the linewidth of the laser beam, the overlap integral between the laser lineshape and the absorption lineshape, the fraction of fluorescence bandwidth collected, the laser path length sampled by the collection optics and the efficiency of the optical and detection system. B_{ij} is the Einstein coefficient of absorption from state i to state j, N is the total number density of the detected species, Φ_f represents the fluorescence quantum yield, and f_i is called Boltzmann fraction, representing the fraction of the total population existing at a given state i.

The energy state of a single molecule can be specified by quantum numbers. However, in a system of molecules, each molecule may reside in different states. The fraction of the population with a given energy level (E_i) can be determined by Boltzmann fraction f_i:

$$f_i = \frac{g_i exp(-\frac{E_i}{\kappa T})}{Q} \tag{3.6}$$

where g_i is the degeneracy of the energy level, which dictates the number of quantum states with the same energy E_i. κ is the Boltzmann constant, T is the temperature

of the system, and Q is the partition function. Q is determined by the following relation [149]:

$$Q = \Sigma_i g_i exp(-\frac{E_i}{\kappa T}) \tag{3.7}$$

The fluorescence quantum yield Φ_f in equation 3.5 represents the fraction of the energy transition that emits photons. It is calculated via the following equation [150]:

$$\Phi_f = \frac{A_{ji}}{A_{ji} + Q_{ji}} \tag{3.8}$$

where Q_{ji} is the quenching rate, A_{ji} is the Einstein coefficient of spontaneous emission from state j to state i, and A_{ji} indicates the probability of the excited species spontaneously falling back to the lower energy state i and emitting a photon. It should be noted that the emission of a photon by the excited species can also be triggered by an incoming photon, and this emission process is called stimulated emission. Spontaneously emitted photons have random phases, and they can propagate in all directions. In contrast, photons emitted during stimulated emission have the same frequency, phase, and propagation direction as the incoming laser photon.

The fluorescence quantum yield Φ_f needs to be determined in order to quantify the fluorescence signal as the excited species may relax via non-radiative ways, ie. no fluorescence is emitted. The excited species may collide with other species present, which results in the changes in the frequency and/or the quantity of the emitted photons [150]. Among these changes, the energy transition that changes the electronic state is called electronic transfer, the energy transfer that changes the vibrational energy level is called Vibrational Energy Transfer (VET), and the energy transition that changes the rotational energy level is called Rotational Energy Transfer (RET) [150]. A broadband detection scheme may be applied to account for the shift and broadening of the frequency of the emitted photons. However, when

electronic transfer happens due to collisions with other species, sometimes no photon is emitted [150]. This form of energy transition is referred to as quenching, which affects the magnitude of the fluorescence signal [150]. Some studies use quenching to represent collisions in general, which should not be confused with the definition of quenching in this study.

Quenching is affected by pressure, temperature, and collision partners at the site, which makes it difficult to quantify the fluorescence signal [151]. Moreover, only a few species' quenching processes are well studied, greatly restricting the application of quantitative LIF measurements [151]. Several approaches can be taken to account for, or circumvent quenching: using short-pulse spectroscopy; direct measurement of the quenching rate Q; performing saturated LIF or calculation of Q using previously measured collisional cross-sections.

A short-pulse laser can be used to excite the desired species in order to reduce the uncertainties caused by quenching [152]. The laser pulse width should be sufficiently short such that there is not enough time for quenching to occur [152]. In the short-pulse spectroscopy, the laser pulse width is usually in the order of picoseconds or less [152].

Quenching rate can also be directly measured *in situ*. Assuming a total number of molecules N_0 are pumped by a short-pulse laser to an upper energy level initially, the population of the excited molecules will decay exponentially according to the following equation [150]:

$$N_t = N_0 exp[-(Q + A)t] \tag{3.9}$$

Therefore, Q can be deduced from the time-dependent decay curve of the excited species [150]. Similar to short-pulse spectroscopy, the excitation time needs to be in the order of picoseconds or less for a meaningful measurement of the quenching rate. Otherwise, the change in the fluorescence signal is largely affected by the temporal

variation in the laser energy in addition to quenching.

The first two possible approaches to address the quenching effects require a specialised short-pulse laser, which is not available in this project. Another way to avoid correction for quenching is to perform LIF in saturation regime. As shown in equation 3.5, the fluorescence signal is proportional to the incident laser fluence in the linear regime. When the laser fluence is sufficiently high, the fluorescence signal stops increasing despite the increase in the laser power, which is called saturation. In saturated LIF, the stimulated emission events overtake the spontaneous emission and quenching events, therefore the signal can be considered to be independent of the quenching rate [150]. This feature is rather advantageous especially in a turbulent flame, where temperature, the mixture composition, and the number density vary both temporarily and spatially, imposing great challenges in the estimation of quenching rate [150]. However, the spatial and temporal variations in the laser energy profile make it difficult to achieve a complete saturation LIF. For instance, Daily [153] found that a Gaussian laser beam profile significantly changes the relationship between the fluorescence signal and laser power, imposing great challenges in quantifying the fluorescence signal. Therefore, laser-induced fluorescence is performed in linear regime in this project. Quenching rate is calculated in this project, and the calculation process will be described in detail in Section 3.7.1.

Given the knowledge of the major collision partners (denoted by c), Q is calculated with the equation below [147, 152]:

$$Q_{ji} = \Sigma_c N_c \sigma_c \nu_c \tag{3.10}$$

$$\nu_c = (8\kappa T/\pi\mu_c)^{0.5} \tag{3.11}$$

$$\mu_c = \frac{m_c m_q}{m_c + m_q} \tag{3.12}$$

where N_c is the number density of a collision partner; σ_c is the independently determined collision cross-sections of the collision partner, which is a function of temperature; ν_c is the relative velocity of the collision partner and the quenched species (denoted by q); μ_c is the reduced mass of the collision species and the quenched species.

Both σ_c and ν_c are properties of the collision partner as a function of temperature, hence equation 3.10 can also be expressed as:

$$Q_{ji} = \Sigma_c N_c k_c \tag{3.13}$$

where k_c is referred to quenching rate coefficient.

3.2.2 Rayleigh Scattering

Rayleigh scattering thermometry is adopted in this project to determine the distribution of temperature in a flame. Rayleigh scattering refers to the elastic scattering of light by atoms, molecules, or small particles [154]. It is an elastic process because the frequency of the scattered light is the same as the incident light. The Rayleigh scattering signal (I_R) is proportional to the incident laser intensity (I), the total number density (N) and the effective Rayleigh cross-section (σ_{eff}) of the gas mixture as shown in the following equation:

$$I_R = KNI\sigma_{eff} \tag{3.14}$$

where K is a constant determined from calibration, which accounts for the geometry and the optical collection efficiency of the system.

In practice, a gas mixture or a flame with known temperature and compositions is used as a reference point in Rayleigh scattering thermometry. Provided that the optical system is invariant, the Rayleigh scattering signal collected from the reference point ($I_{R,ref}$) can be written as:

$$I_{R,ref} = KN_{ref}I\sigma_{eff,ref} \tag{3.15}$$

where N_{ref} is the total number density of the gas mixture at the reference point, and $\sigma_{eff,ref}$ is the effective Rayleigh cross-section of that gas mixture.

According to the ideal gas law, the total number density is inversely proportional to the temperature at constant pressure, hence the above two equations can be combined and lead to:

$$\frac{I_R}{I_{R,ref}} = \frac{\sigma_{eff}}{\sigma_{eff,ref}} \times \frac{T_{ref}}{T} \tag{3.16}$$

Hence, the flame temperature can be deduced from the above equation:

$$T = \frac{\sigma_{eff}}{\sigma_{eff,ref}} \times \frac{I_{R,ref}}{I_R} \times T_{ref} \tag{3.17}$$

3.3 Experimental Details

3.3.1 Fuel Properties

Four different fuels namely ethanol, acetone, *n*-heptane, and dimethyl ether (DME) have been studied in this project. Ethanol, acetone, and *n*-heptane are chosen to represent different classes of hydrocarbons, namely, an alcohol, a ketone, and a long-chain alkane. The flame structure of dimethyl ether (an isomer of ethanol) is compared to ethanol to further investigate the impact of fuel structure. Relevant properties of fuels investigated in this project are listed in Table 3.1.

Fuels used in a reverse-flow MILD combustor at the RWTH Aachen Univer-

sity include ethanol (purity over 96%), acetone (purity over 99.8%), and *n*-heptane (purity over 99%). Fuels used in the JHC burner at The University of Adelaide include ethanol (purity over 95%), acetone (purity over 99.8%), *n*-heptane (purity over 95%), and DME (100%). There are minor variations in the purity of some of the fuels used in this project. Most of the impurity present in the liquid fuels is water. Hence, the impurity may slightly affect the flame temperature of prevaporised liquid fuels.

Fuel	M (g/mol)	ρ (kg/m^3)	T_{boil} (K)	T_{ig} (K)	HHV (MJ/kg)
ethanol (CH_3CH_2OH)	46.07	785	351	638	29.7
acetone (CH_3COCH_3)	58.08	785	330	738	28.5
n-heptane (C_7H_{16})	100.2	680	371	493	48.1
DME (CH_3OCH_3)	46.07	1.89	248	623	31.6

Table 3.1: Properties of the fuels investigated in this project: M refers to molecular weight; ρ is density; T_{boil} is the boiling temperature; E_{vap} stands for the enthalpy of vaporisation; T_{ig} is the ignition temperature; HHV stands for high heating value. Values for density are evaluated at 298 K under atmospheric pressure.

3.3.2 Reverse-Flow MILD Combustor

Experiments have been performed in a reverse-flow MILD combustor. These experiments mainly investigate the pressure influence on the stabilisation of MILD combustion and the resultant emission formation. This MILD combustor shown in Fig 3.3 is designed for applications relevant to gas turbines, thus it can be operated under elevated pressures. The MILD combustor includes an ignition chamber, a main combustion chamber, and a recuperator for preheating the air with the heat recovered from the exhaust gases. The main combustion chamber has a 58 mm×58 mm square cross-section that is 200 mm long. Quartz glass windows (40 mm×50 mm) are installed on three sides of the combustor walls at different heights for visual observations and photography.

During the experiments, MILD combustor is first warmed up by operating in a preheat mode, as shown in Fig. 3.4(a). Fuel and air are injected to the small ignition

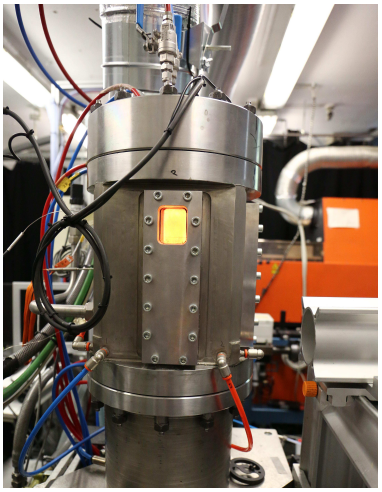

Figure 3.3: Photograph of the reverse-flow MILD combustor

chamber (V $\approx$ 115000 mm^3) from the top, and the mixture is ignited by a spark plug. The hot combustion products (denoted by the red arrows) produced in the ignition chamber fill the main combustion chamber before exiting from the bottom.

When the exhaust temperature at the bottom reaches approximately 1100 K, the combustor is switched to the MILD combustion mode. The exhaust temperature is measured by a K-type thermocouple placed in the exhaust tube. As depicted in Fig. 3.4(b), a mixture of prevaporised liquid fuel and carrier gas is injected to the main combustion chamber via the central nozzle from the bottom. Primary air is preheated by the exhaust gas. Bypass air pipes are installed in the centre of the recuperator, away from the exhaust gas pipes. Preheated primary air are mixed with a certain amount of cold bypass air to ensure that the preheat temperature in various cases is maintained at 873 $\pm$ 50 K, which is higher than the required autoignition temperature. This preheat temperature is measured by a K-type thermocouple installed close to the air nozzle outlet. Two air nozzle diameters, 10 mm and 6.2 mm, are used in this project while the fuel nozzle diameter is kept constant at 2 mm. The fuel nozzle and the air nozzle are concentric, but the fuel nozzle protrudes 1.44 mm above the air nozzle, as demonstrated in Fig. 3.5. The concentric fuel and air nozzles

are located at the same plane as the exhaust gas outlets in the MILD combustion mode. This reverse-flow design enhances the internal recirculation of the exhaust gas and dilutes the reactants prior to combustion. Furthermore, the hemispherical top of the main combustion chamber deflects the gas and forces it to recirculate back to the chamber. The combination of air preheating and strong recirculation of hot products help creating the MILD combustion environment. Figure 3.6 displays a photograph taken during the MILD combustion mode, suggesting the absence of visible flames.

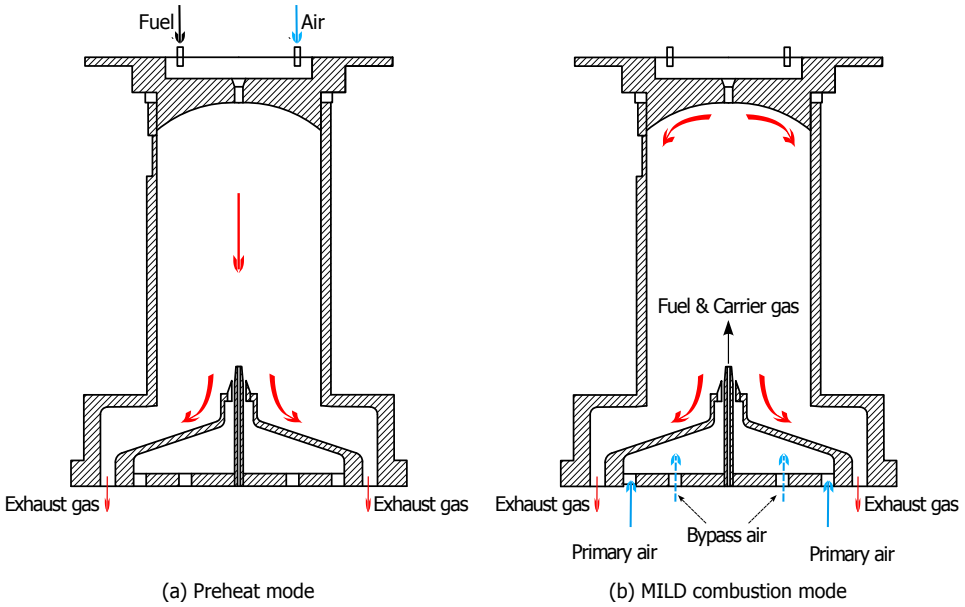

Figure 3.4: Schematic of the (a) preheat mode and (b) MILD combustion mode.

3.3.3 JHC Burner

In order to achieve a better understanding of the effect of EGR and relevant parameters, the effect of EGR is usually simulated via a cold-fuel-hot-coflow configuration in laboratory research. For instance, a JHC burner has been used in many previous studies [50, 51, 62, 155] to mimic a furnace operating under MILD combustion conditions, where the gas mixture inside the furnace is hot and diluted, with cold

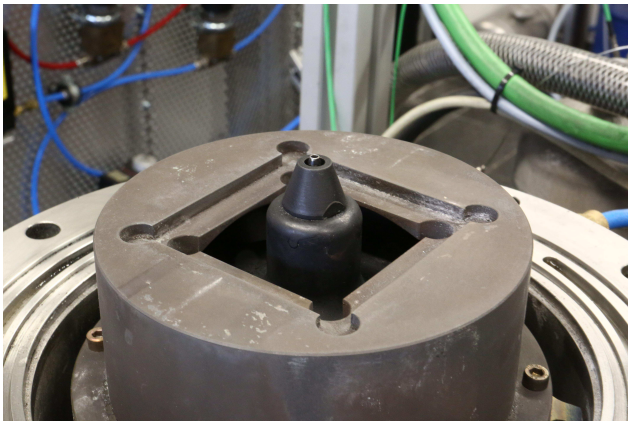

Figure 3.5: The concentric arrangement of fuel and air nozzles in the MILD combustor. The diameter of the fuel nozzle and the air nozzle in this photograph is 2 mm and 10 mm, respectively.

Figure 3.6: Photograph of flameless appearance.

fuel injecting into it. Compared to a furnace, the design of this burner allows more control over operating parameters such that the jet Reynolds number, the coflow composition and temperature can be varied independently. Furthermore, this burner also provides easy optical access for *in situ* measurements. Hence this burner will be used for parametric studies in this thesis.

As demonstrated in Fig. 3.7, this burner consists of a central insulated fuel jet surrounded by an annular coflow. The inner and outer diameter of the fuel jet is 4.6 mm and 5.0 mm, respectively. The length of the fuel pipe is more than 100 jet

diameters in order to obtain a fully developed pipe flow at the jet exit. The fuel jet protrudes 15 mm above the annular coflow. The inner and outer diameter of the annular coflow is 82 mm and 90 mm, respectively. This coflow is made of hot combustion products generated from a secondary porous burner, which is located 90 mm upstream of the jet exit plane. The porous bed consists of a 55 mm thick layer of flint clay on top of a thick perforated plate. As shown in Fig. 3.7, coflow fuel is injected to the burner from the bottom in a direction perpendicular to the coflow oxidant, consequently enhancing the mixing between them. The coflow fuel used in this project is a mixture of hydrogen and natural gas, and the coflow oxidant is made of air and nitrogen. The composition of natural gas used in this project is shown in Table 3.2. The mole fractions of coflow reactants are adjusted to achieve the desired coflow temperature and oxygen level during the experiments. The outer wall of the JHC burner is wrapped with insulation to minimise heat losses to the environment.

Components	% (vol./vol.)
methane	91.99%
ethane	4.28%
carbon dioxide	2.56%
nitrogen	0.93%
oxygen	<0.2%
propane plus*	0.24%

Table 3.2: The composition of natural gas used in this project: propane plus* refers to propane and higher-order hydrocarbons.

3.3.4 Slot Burner

A slot burner is installed before the JHC burner in the laser path to provide reference and calibration for image processing. This rectangular burner consists of a central fuel slot with an air slot on each side. Partially-premixed natural gas and air are fed through the central slot at a low velocity, coflowing by two streams of low-velocity

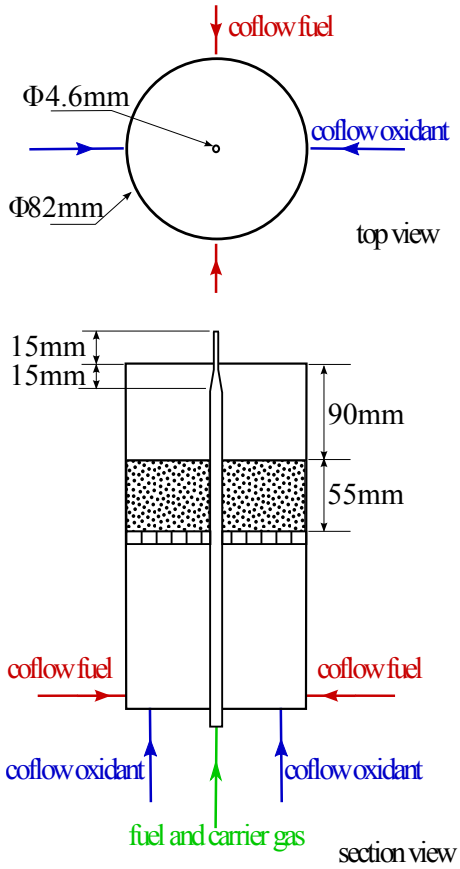

Figure 3.7: Schematic of the Jet in Hot Coflow (JHC) burner.

air. This arrangement produces a uniform and laminar flame in the slot burner, hence variations in the signal of this laminar flame can be considered solely due to the laser energy fluctuations. The prerequisite for accurate laser energy correction is that the laser beam remains collimated between the slot burner and the JHC burner, which has been taken great care of.

3.4 Optical Details

The optical layout for all the laser and camera systems is shown in Fig. 3.15. In order to reveal the flame structure for various cases, OH-LIF, CH_2O-LIF, and Rayleigh scattering are performed simultaneously and instantaneously. In addition, imaging of OH^* chemiluminescence is also conducted. Details of these measurements will be described in the following sections.

3.4.1 Imaging of OH^* Chemiluminescence

Chemiluminescence refers to the spontaneous emission of light by species like OH^* that are excited via chemical reactions. The most likely route to produce OH at the excited state in hydrocarbon flames is via the following reaction [156, 157]:

$$CH + O_2 \rightleftharpoons CO + OH^* \tag{3.18}$$

The excited OH^* is relaxed via two main channels [157]: (1) chemiluminescence via $OH^* \rightarrow OH+h\nu$, where $h\nu$ represents emitting one photon at 305.4 nm, ignoring the frequency broadening caused by vibrational and/or rotational energy transfers; (2) de-excitation via collision $OH^*+M \rightleftharpoons OH+M$. The chemiluminescence of OH^* was found to correlate with heat release rate in premixed flames [14, 156, 158, 159]. The interpretation of OH^* chemiluminescence signal in non-premixed MILD flames will be investigated in this project, results of which will be presented in Chapter 5.

Imaging of OH^* chemiluminescence is performed with an electronically gated pco.pixelfly camera (#13 in Fig. 3.15) equipped with a Lambert Instruments intensifier. A bandpass optical filter centred at 310 nm with a bandwidth of 10 nm is mounted in front of a 50 mm f/3.5 UV lens of the intensifier and the camera.

3.4.2 Rayleigh Scattering

Temperature is an important scalar in a combustion process, which is determined via Rayleigh scattering in this study. A frequency-doubled Q-switched Nd:YAG laser (#1 in Fig. 3.15) is used to generate a 532 nm laser beam for Rayleigh scattering. The measured output energy was approximately 90 mJ/pulse before the slot burner. A Princeton Instruments intensified CCD (ICCD) camera (#11 in Fig. 3.15), mounted normal to the laser sheets, is used to detect Rayleigh scattering signal. A 50 mm f/1.4 lens is equipped with the camera, and no filter has been used to maximise the collected Rayleigh signal. As particulate matter and soot are not observed during the experiments, filters are not required for Rayleigh scattering thermometry.

3.4.3 CH_2O-LIF

Formaldehyde molecules are measured as they are important ignition precursors and intermediates under conditions relevant to MILD combustion [51, 64, 160]. The CH_2O-LIF is performed with a 355 nm laser beam generated from a frequency-tripled Nd:YAG laser (#16 in Fig. 3.15). The measured output energy is around 32 mJ/pulse before the slot burner. The CH_2O-LIF signal is collected using an Andor iStar ICCD camera (#12 in Fig. 3.15) equipped with a 50 mm f/1.4 lens. This camera is installed next to the ICCD camera for Rayleigh scattering. A combination of long-wave-pass Andover Optics 395 FG03-50 and short-wave-pass Andover Optics 450 FL07-50 filters is installed in front of the collecting lens.

3.4.4 OH-LIF

The distribution and concentration of OH are measured as it is an important radical during the ignition process [64] and it has been used as a flame marker in previous studies [51, 63]. The A-X (1,0) $Q_1(7)$ line (283.222 nm) is chosen to excite OH due to its low sensitivity to ground-state population distribution in the expected temperature range [92]. The 532-nm output from a Q-smart 850 pulsed Nd:YAG laser (#23 in Fig. 3.15) is used to pump a Lambda-Physik ScanMate 2E dye laser (#27 in Fig. 3.15) with Rhodamine 6G dye. The output of the dye laser is frequency doubled to match the desired OH transition. As displayed in Fig. 3.15, the detection of OH-LIF signal is achieved with a Princeton Instruments ICCD camera (#15 in Fig. 3.15), fitted with a 78 mm f/3.8 UV lens. This camera is mounted parallel to the laser sheets. A dichroic mirror, mounted at a 45 degree angle to the laser sheets, is placed between the JHC burner and the ICCD camera. This mirror has a greater than 80% reflectance in the range of 270 to 340 nm, thus acting as a bandpass filter.

The 532 nm laser, 283.222 nm laser, and 355 nm laser sheets overlap with each other and form co-planar laser sheets. The heights of the 532 nm and 355 nm laser sheets are approximately 20 mm, while the 283.222 nm laser sheet height is slightly shorter. Images of the central 8 mm laser sheets are presented in this thesis.

In order to ensure OH-LIF is performed in a linear regime, imaging of OH-LIF is performed for ethylene flames in a flat flame burner under various laser fluence. Filters with different optical densities are placed before the flat flame burner to adjust the laser energy. The rest of optical setup is kept the same as the actual experiments. Upon changing the filter the laser energy is measured and recorded for five minutes with a power meter for each test. Afterwards 500 OH-LIF images for each laser energy is collected. Figure 3.8 shows the OH signal as a function of laser energy. The presented OH signal is averaged from 500 images, and its standard deviation is shown as vertical (red) error bars in Fig. 3.8. The horizontal (blue)

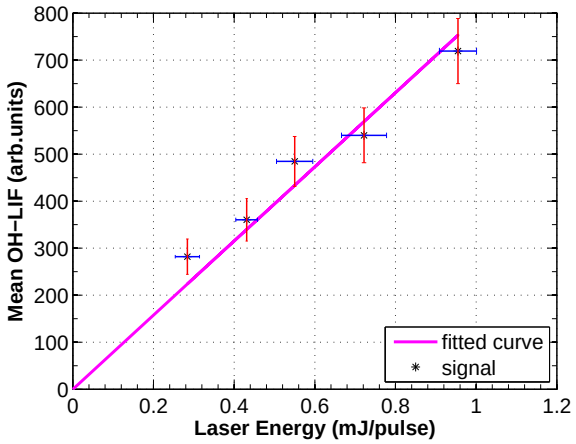

Figure 3.8: Mean OH-LIF signal as a function of laser energy. The pink straight line is a fitted curve based on the data points.

error bars represent the standard deviation in the laser energy measured by the power meter. Figure 3.8 demonstrates that the OH-LIF signal can be considered to be linearly dependent on the laser energy up to approximately 1 mJ/pulse. During the data image acquisition, the energy of the 283.222 nm laser beam is measured to be 0.9 mJ/pulse. Hence the OH-LIF measurements are within the linear regime.

3.5 Image Pre-processing

3.5.1 Dark-Charge and Background Correction

The signal recorded by the ICCD camera can originate from a variety of sources. In addition to the desired signal excited by laser sources within the flame, signal from thermally created dark current in the camera, reflection by the surroundings, and interferences by species other than the probed species are also recorded. Fifty images are acquired while the laser is blocked and the flame is extinguished. In these images, signal is solely caused by the dark current in the ICCD camera due to the short gate-width. These images are averaged to generate a mean dark-charge image. All the data images are corrected for dark-charge simply by subtracting the

mean dark-charge image from them.

Signal is still observed outside the laser sheet after dark-charge correction. This is caused by the laser stray light reflected by the surroundings, which exists as long as the laser is fired and is not dependent on the presence of a flame. This background signal varies shot-by-shot due to the temporal fluctuation in the laser energy profile. It is also found that this background signal varies considerably column-by-column, while it is relatively constant across different rows in an image. Hence a background profile is generated by averaging the signal above and below the laser sheet in the direction perpendicular to the laser propagation in each instantaneous image. This background profile is an array, whose size is the same as the column number of each image. A background image is then constructed for each instantaneous image by replicating this background profile n times, where n is the row number of the image. Afterwards the background image is subtracted from each instantaneous image. To ensure the background profile is not biased by scattering off some unexpected particles (dust), the ratio of the mean profiles above and below the laser sheet is compared to a threshold value. If the ratio exceeds the threshold value, the image is considered to be invalid.

Signal originating from sources such as fuel-LIF causes interferences in OH-LIF. These interferences are recorded via imaging of the flame of interest while firing an off-wavelength laser beam. These interferences are found to contribute to approximately 15% of the signal when OH-LIF signal is very weak, for example in the case of flames issuing to a coflow with 3% O_2. However, these interferences are typically less than 4% of the signal where strong OH signal exists. As no visible soot particulates or smoke has been observed during the experiments, interferences from PAH-LIF, soot incandescence, or scattering off soot particulates are negligible in OH-LIF, CH_2O-LIF, and Rayleigh scattering images.

3.5.2 Detector Attenuation Correction

The amount of photons falling on the detector is not the same everywhere due to the vignetting of optics, which contributes to the variation in the signal across the entire image. Therefore, 50 images are taken of a uniformly illuminated paper to reflect the detector attenuation, and the averaged image after dark-charge correction is referred to as uniformity image. Each data image is first normalised to this uniformity image, then it is multiplied by the mean value of the uniformity image pixel-by-pixel.

3.5.3 Laser Energy Profile Correction

The laser power fluctuates both temporarily and spatially during the image acquisition. The OH-LIF, CH_2O-LIF, and Rayleigh scattering signals are proportional to both the laser power and the number density of the probed species or the gas mixture, hence the fluctuations in the laser energy should be accounted for in order to interpret the signal in the images.

Each image consists of signal from the flame of interest in the JHC burner and signal from the laminar flame in the slot burner. The area of the laminar flame is 40-pixel wide at minimum in an image depending on the measurement technique. In each instantaneous image, a laser energy profile is obtained by averaging the signal from the laminar flame along the laser propagation direction. Thus this laser energy profile is an array, whose size is the same as the row number of the instantaneous image. In order to correct the spatial variation in the laser energy, the entire instantaneous image is normalised by the laser energy profile column-by-column. To account for the temporal fluctuation, each instantaneous image is then timed by a fixed value (same order as the peak signal in the laminar flame) pixel-by-pixel.

3.5.4 Image Matching

The three cameras are placed at different positions relative to the flame, hence each pixel in the three sets of images does not represent the same area of a flame. To correlate the information on the three sets of images to each other, these images have to be spatially matched such that each corresponding pixel in them represents the same physical location.

A transparent film with printed letters and grids of known spacing is used as a target, which is imaged by the three cameras. The letters are used to help identify a particular grid on the film. Four grid intersection points on the target are chosen as calibration marks in a pair of images to be matched. As Rayleigh scattering image is the smallest one, OH-LIF and CH_2O-LIF images are matched to it, respectively. A built-in MATLAB image transform algorithm, namely projective, is applied to rotate, translate, and resize the images during the matching process. After the matching, the four chosen points are at the same pixels in the pair of images. On average, the correlation within the region of interest is less than one pixel.

The above image pre-processing steps are applied to Rayleigh scattering, OH-LIF, and CH_2O-LIF images. After these steps, quantification of Rayleigh scattering and OH-LIF are performed, the procedure of which will be explained in detail in the following sections. Considering the same geometry and optical system, and the small temperature change in the fuel-rich region, the CH_2O-LIF signal is expected to reflect the relative concentration of CH_2O of various flames. According to previous measurements in [147, 161], the effect of temperature on the CH_2O partition function and the quenching rate partially offsets one another within a temperature range of 500 K to 1600 K, thus the CH_2O-LIF signal is directly proportional to the number density of CH_2O within 15%–25%. Therefore the CH_2O signal will not be quantified in this project.

3.6 Temperature Quantification

The principle of Rayleigh scattering thermometry has been described in Section 3.2.2. The flame temperature can be determined using previously defined equation 3.17:

$$T = \frac{\sigma_{eff}}{\sigma_{eff,ref}} \times \frac{I_{R,ref}}{I_R} \times T_{ref} \qquad \text{(3.17 revisited)}$$

To simplify the quantification process, the above equation is written as follows:

$$T^* = \frac{T}{\sigma_{eff}} = \frac{1}{I_R} \times H \qquad (3.19)$$

$$H = \frac{T_{ref} \times I_{R,ref}}{\sigma_{eff,ref}} \qquad (3.20)$$

where, $\frac{T_{ref} \times I_{R,ref}}{\sigma_{eff,ref}}$ is grouped together as a constant H. The ratio $\frac{T}{\sigma_{eff}}$, referred to as T^*, is inversely proportional to the recorded signal. To deduce T from T^*, σ_{eff} needs to be determined. The value of σ_{eff} is determined by the composition of the gas mixture at a given location.

In the combustion of complex fuels, the effective Rayleigh cross-section often varies considerably with the mixture fraction throughout the flame. For example, the Rayleigh cross-section of ethanol is 8 times that of air, and the σ of n-heptane is 60 times that of air. In the case of a jet in a hot and diluted coflow, the scattered signal is very high in the cold fuel jet due to the combination of high σ_{eff} and low temperature. In contrast, the scattered signal in the hot coflow is much weaker, which produces a wide dynamic range of signal. Particularly, prevaporised n-heptane flames have the widest dynamic range of signal as the Rayleigh cross-section of n-heptane is the highest amongst the various fuels investigated in this project. The σ_{eff} of the mixture of n-heptane and carrier air is 9 times higher than that of hot coflow. Furthermore, the number density of the gas mixture in the fuel jet is much

higher than that in the coflow due to the temperature difference. The combination of high σ_{eff} and N results in a 30 times higher signal in the fuel jet than that in the coflow near the jet exit plane. The signal in the fuel jet is high so that the gain of the camera must be kept low, which reduces the signal-to-noise ratio (SNR), especially in the hot regions. Therefore it is very challenging to quantify Rayleigh scattering accurately under these circumstances. Hence quantification of Rayleigh scattering for prevaporised n-heptane flames carried by air, representing difficult scenarios, are described here.

The Rayleigh cross-section weakly increases with temperature due to the increased population of more energetic rotational and vibrational states at a higher temperature. Espey et al. [162] reported that the Rayleigh cross-section is estimated to increase by 2% with temperature increasing from 300 K to 1000 K. Zhao and Hiroyasu [163] estimated a 4% increase in the Rayleigh cross-section with temperature increasing from 300 K to 2000 K. Experimental measurements by Sutton and Driscoll [164] showed a 2-8% increase in the Rayleigh cross-section with temperature increasing from 295 K to 1500 K using a 355 nm laser beam, while a 5-11% increase in the Rayleigh cross-section was found with temperature increasing from 295 K to 1450 K using a 266 nm laser beam. When a 532 nm laser beam (same as the one used in this project) was used, a less than 2% variation was reported in the Rayleigh cross-section as temperature increased from 300 K to approximately 2200 K [154]. Hence, Rayleigh cross-sections are assumed to be constant throughout the whole temperature range in flames in this project.

3.6.1 Laminar Flame Calculations

The detailed information on the species concentration can be obtained from laminar flame calculations, from which σ_{eff} is deduced as a function of mixture fraction. For instance, Fuest et al. [165] applied one-dimensional (line) imaging Raman/Rayleigh

scattering as well as laminar flame calculations to quantify the temperature of a turbulent piloted flame. Laminar flame calculations are performed with the OPPDIF code in the Chemkin package, which is based on the opposed jet flame geometry. This one-dimensional opposed-flow geometry is suitable for studying the chemistry across the reaction zone.

Figure 3.9 shows a schematic of an opposed n-heptane flame. The cold mixture of n-heptane and carrier gas is modelled as the fuel stream. The temperature and composition of the hot exhaust gases produced from a lean mixture of hydrogen, natural gas, air and nitrogen are calculated with the Equilibrium package in the Chemkin, which then are input into the OPPDIF model as the oxidiser. The n-heptane chemical kinetics mechanism is provided by [166], which consists of 88 species and 387 reactions. The two opposing inlets are separated by 20 mm. The momentum of the fuel stream and the oxidiser stream are carefully balanced such that the stagnation plane is located at the midpoint between the two inlets. Calculations are performed using the multicomponent transport formulation, meanwhile the effects of thermal diffusion are accounted for.

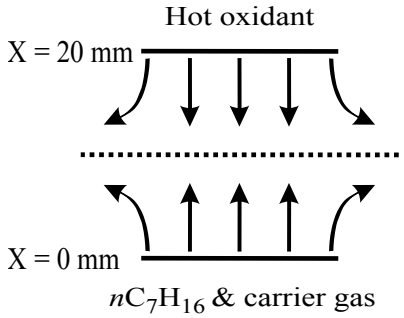

Figure 3.9: Schematic of an opposed n-heptane flame. The dashed line in the middle represents the stagnation plane.

The concentration of major species is used to calculate the effective Rayleigh cross-section of the gas mixture. In the current study, major species are defined as species whose peak mole fraction is $\gtrsim$ 1%, including $N_2, H_2, O_2, H_2O, CO, CO_2, C_2H_4, C_2H_2$, and n-heptane. Some n-heptane flames ap-

pear lifted, and many Rayleigh scattering images are taken upstream of the apparent lift-off height. Hence, no reaction occurs at some locations investigated, and these cases are referred to as non-reacting cases. In those non-reacting cases, only N_2, O_2, H_2O, CO_2, and n-heptane are considered as major species.

The Rayleigh cross-section of each major species is calculated based on the refractive indices provided by [167], which is reported as a normalised value to the Rayleigh cross-section of N_2 in this project. The mole fraction of major species is calculated with the OPPDIF code as a function of mixture fraction, from which the relationship between the effective Rayleigh cross-section and the mixture fraction is obtained. The temperature of the gas mixture as a function of the mixture fraction is also obtained from laminar flame calculations. Given these information, a relationship between T^* and σ_{eff} is readily obtained, which is displayed in Fig. 3.10. In the non-reacting case, T^* increases monotonically with the decreasing σ_{eff}, which is due to the mixing of hotter coflow of low Rayleigh cross-section with colder fuel of high Rayleigh cross-section. In the reacting case, T^* increases monotonically with the decreasing σ_{eff} when T^* is approaching its peak from the fuel-rich region. The location of the peak T^* is found to match with the location of the peak flame temperature, which is within the reaction zone. Once T^* starts declining from its peak towards the fuel-lean region, σ_{eff} is almost constant as the σ_{eff} of the combustion products produced within the reaction zone is very close to that of coflow. Hence, the curve for reacting case can be separated into two parts at the peak of T^*. One part represents the relationship between T^* and σ_{eff} in the fuel-rich region, while the other part with a small variance in σ_{eff} represents the fuel-lean region and the reaction zone.

As the OPPDIF code is normally used for non-premixed flames, it is a reasonable concern that OPPDIF is not suitable for lifted flames, therefore it cannot provide a good estimation of σ_{eff}. A partially premixed case is also performed, in which

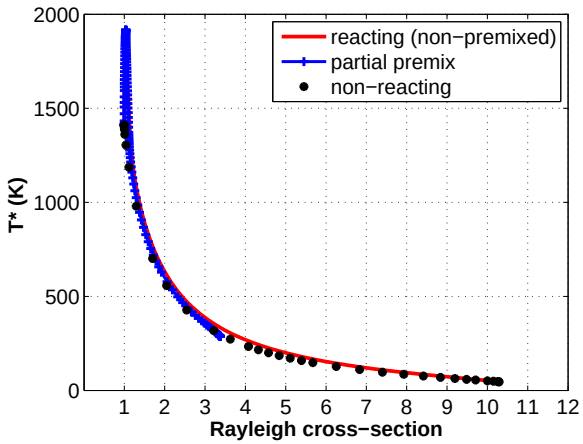

(a) $0 < \sigma_{eff} < 11$

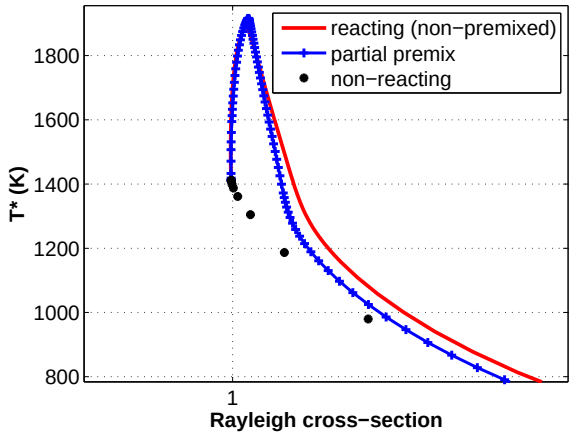

(b) $\sigma_{eff} \approx 1$

Figure 3.10: T^* as a function of the effective Rayleigh cross-section (σ_{eff}) in the reacting (non-premixed), partially-premixed, and non-reacting cases.

the fuel jet is modelled as a mixture of n-heptane, carrier gas and 50% of the total coflow by mass. This is intended to emulate the base of a lifted flame. The relationship between T^* and σ_{eff} in this partially premixed case is also plotted in Fig. 3.10. As expected, the range of σ_{eff} and T^* is narrowed due to partial mixing. Despite that, the relationship between T^* and σ_{eff} is almost identical between non-premixed flames and premixed flames. Therefore, the curve obtained from the OPPDIF calculation for the non-premixed case is applicable whether the flame is actually attached or lifted.

3.6.2 Temperature Quantification Procedure

This section describes the procedure to quantify the Rayleigh scattering results. Firstly, instantaneous Rayleigh images are corrected for dark charge, detector attenuation, background, and laser energy variations. Figure 3.11(a) displays an example of a corrected instantaneous Rayleigh scattering image. The left edge of each image coincides with the jet centreline, denoted by R/D=0. As shown in equation 3.17, the scattered Rayleigh signal is directly proportional to the effective Rayleigh cross-section, and inversely proportional to the temperature. Therefore, a relatively constant signal is collected from the hot coflow region (dark area), while the signal is very strong in the fuel-rich region (bright blue area) due to the combination of high σ_{eff} and low temperature. The signal in the fuel-rich region varies as there are different degrees of mixing between the fuel and the surrounding coflow in this region.

Secondly, according to equations (3.19) and (3.20), a T^* image displayed in Fig. 3.11(b) is generated as the product of the reciprocal of the corrected Rayleigh image and the constant H. Here, the coflow region is chosen as the reference point, the temperature of which is measured by a type-R thermocouple. Taking the 9% O_2 coflow case as an example, the effective Rayleigh cross-section of the coflow $\sigma_{eff,ref}$ is calculated to be 0.997. $I_{R,ref}$ is averaged from the total signal in the central part of the coflow region, which is away from the burner wall and the fuel-rich region.

Thirdly, to deduce the effective Rayleigh cross-section from T^* based on their relationships in different cases shown in Figure 3.10, it is necessary to determine whether a pixel corresponds to a reacting case or a non-reacting case. This information can be obtained from OH-LIF as OH is used as a flame marker [63]. As shown in Figure 3.11(c), the corresponding corrected OH-LIF images are spatially matched with the corrected Rayleigh scattering images so that each pixel in these two images represents the same physical location. The maximum signal at a given

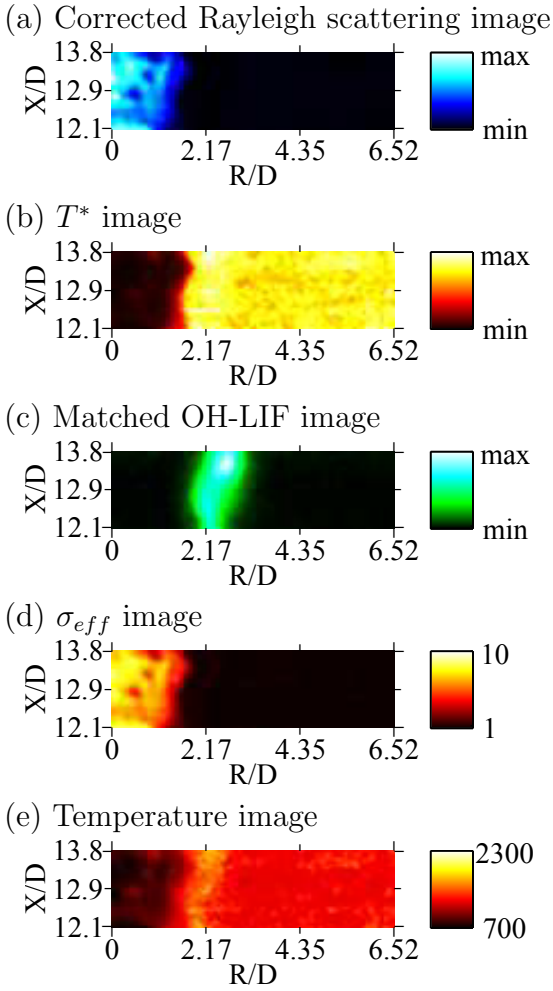

Figure 3.11: Examples of instantaneous images of n-heptane flames used during the temperature quantification process: (a) Rayleigh scattering; (b) T^*; (c) OH-LIF; (d) σ_{eff}; (e) temperature.

row in the OH-LIF image is compared to a threshold value. A signal higher than the threshold value indicates the formation of OH and the occurrence of reactions, and vice versa.

Fourthly, in the non-reacting case, the effective Rayleigh cross-section can be interpolated from T^* image directly due to their monotonic relationship. In the reacting case, the relationship between σ_{eff} and T^* in the fuel-rich region differs from that in the fuel-lean region. Figure 3.10 demonstrates that the peak T^* is the separation point between the two relationships. Laminar flame calculations show that the location of the peak T^* can be approximated as the location of the peak

number density of OH. Therefore, the location of the peak OH signal at each row of the corresponding OH-LIF image is applied to identify the boundary between the fuel-rich and the fuel-lean region. In each region, σ_{eff} is interpolated from the T^* image, based on the corresponding curve shown in Fig. 3.10. The resultant image of σ_{eff} is displayed in Fig. 3.11(d). It shows that the value of σ_{eff} decreases gradually from the fuel jet centreline to the fuel-lean region.

Finally, the instantaneous temperature image shown in Figure 3.11(e) is generated as a product of the T^* and σ_{eff} images. The temperature image demonstrates a cold fuel-rich region and a hot coflow region with a uniform temperature distribution. Between the fuel-rich region and the coflow, there is a thin strip with high temperature, indicating the location of the reaction zone.

3.6.3 Uncertainties and Accuracy

The hot coflow stream has the lowest Rayleigh scattering, hence the coflow region is the most vulnerable to low signal-to-noise ratio. The interpixel noise in the coflow stream in the averaged temperature images is close to 20 K, and the interpixel noise in the instantaneous images is around 80 to 150 K. The temporal uncertainties can be estimated from the shot-to-shot variation of the coflow temperature. Figure 3.12 displays the temperature histograms of the instantaneous images for a 1250-K coflow. The red vertical dashed line indicates the mean coflow temperature, which is averaged from 249 instantaneous images. It can be seen from this figure that the temporal (inter-shot) fluctuation from the mean temperature is mostly within 10 K. The maximum deviation from the mean temperature is approximately 30 K. The shot-to-shot standard deviation is calculated to be 8 K.

To evaluate the accuracy of the Rayleigh thermometry, the coflow temperature measured with Rayleigh scattering is compared to that measured with a type-R thermocouple. Figure 3.13 plots the mean temperature profiles of the 3% O_2 coflow

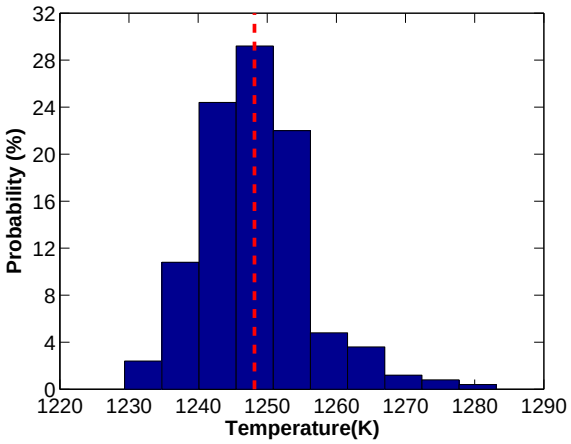

Figure 3.12: Temperature histograms for a 1250-K coflow: the red vertical dashed line indicates the mean temperature.

measured by Rayleigh scattering and the thermocouple, which are measured at 3 mm above the jet exit plane. As shown in this figure, Rayleigh temperature imaging has captured the trend in the temperature distribution quite well. The differences between the two techniques typically do not exceed 60 K. Overall, the measurements of the averaged temperatures from these two techniques are in close agreement with each other.

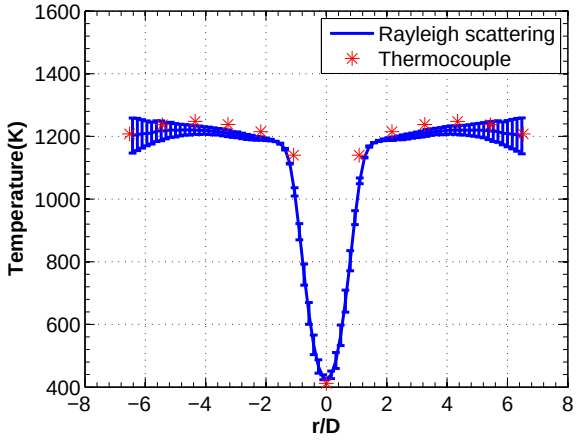

Figure 3.13: Mean temperature profiles of the 3% O_2 coflow measured by Rayleigh scattering and the thermocouple: r is the distance along the radial direction, and D is the diameter of the fuel jet.

Accurate Rayleigh scattering quantification is limited to the bottom part of a

flame as OH layers are needed to identify the boundary between fuel-rich and fuel-lean regions. As revealed by OH-LIF images, some of the OH layers are distorted due to the existence of vortex, particularly at the downstream of the flame, hence it is difficult to distinguish the fuel-rich zone from the fuel-lean zone. In this case, the appropriate relationship between σ_{eff} and T^* shown in Fig. 3.10 at a given pixel cannot be determined with confidence, hence those Rayleigh scattering images are not used in this thesis.

3.7 OH-LIF Quantification

3.7.1 Principle of OH-LIF Quantification

The OH-LIF signal is semi-quantified by calibration with a steady laminar flame in the slot burner, which is in the same field of view as the JHC burner. It is worth mentioning that OH-LIF signal is collected through a dichroic mirror with greater than 80% reflectance in the range of 270 to 340 nm, therefore emitted photons with different frequencies caused by vibrational energy transfer or rotational energy transfer are also collected. As mentioned in section 3.2.1, the fluorescence intensity in the linear regime is defined by the following equation 3.5 [150, 168]:

$$F = CB_{ij}NEf_i\frac{A_{ji}}{Q_{ji}} \qquad \text{(3.5 revisited)}$$

In the case of OH-LIF, N represents the number density of OH (n_{OH}). As OH-LIF of the measured/target flames and the calibrated flame are performed with the same laser beam, B_{ij} and A_{ji} are the same. Furthermore, signal from these flames is collected with the exact optical system, thus C is considered the same. Comparing the fluorescence signal from the target flame with that from the calibrated flame,

the above equation then becomes:

$$F/F_{cal} = \frac{n_{OH}}{n_{cal}} \frac{E}{E_{cal}} \frac{f}{f_{cal}} \frac{Q_{cal}}{Q} \tag{3.21}$$

This equation can be changed into

$$n_{OH} = n_{cal} \frac{F}{F_{cal}} \frac{E_{cal}}{E} \frac{f_{cal}}{f} \frac{Q}{Q_{cal}} \tag{3.22}$$

The term for laser energy differences $\frac{E_{cal}}{E}$ has already been solved during laser energy profile correction. The fraction of the total population existing at a given state is not the same between two flames due to the temperature difference. However, Medwell [152] found that Boltzmann population distribution of OH at X-state with v''=0 and J''=7.5 is relatively constant with the flame temperature ranging from 1000 K to 2000 K. Hence $\frac{f_{cal}}{f}$ can be approximated to one. Now the above equation can be rewritten as:

$$n_{OH} = n_{cal} \frac{F}{F_{cal}} \frac{Q}{Q_{cal}} \tag{3.23}$$

Referring back to equation 3.13 in section 3.2.1, the quenching rate at a given mixture fraction can be directly calculated given the knowledge of major collision partners:

$$Q_{ji} = \Sigma_c N_c k_c \tag{3.24}$$

A preliminary analysis identifies several species as major species in the region where OH is formed, including N_2, H_2, O_2, H_2O, CO, CO_2 and OH. The quenching rate coefficients k_c of these species as a function of temperature are listed in Table 3.3, which are obtained from a previous study by Tamura et al. [169]. The concentrations of those major species and the flame temperature at a given mixture fraction are estimated from laminar flame calculations, based on which the quenching rate Q_{ji} of OH can be calculated.

Collision partner	$\sigma_{Q\infty}$ (Å^2)	ε/mT (K)	k_c (10^{-13} cm^{3}s^{-1})
N_2	0.4	624	$4.47\sigma_Q T^{0.5}$
H_2	4.5	224	$10.88\sigma_Q T^{0.5}$
O_2	8	243	$4.37\sigma_Q T^{0.5}$
H_2O	20	434	$4.92\sigma_Q T^{0.5}$
CO	12	397	$4.47\sigma_Q T^{0.5}$
CO_2	11	488	$4.16\sigma_Q T^{0.5}$
OH	20	384	$4.99\sigma_Q T^{0.5}$

Table 3.3: Quenching rate coefficient k_c of major collision partners for OH obtained from [169]. The collision cross-section σ_Q is defined by an empirical expression: $\sigma_Q = \sigma_{Q\infty} exp(\varepsilon/mT)$ [169].

Figure 3.14(a) displays the relationship between n_{cal} and $\frac{n_{cal}}{Q_{cal}}$ (normalised by $(\frac{n_{cal}}{Q_{cal}})_{max}$) for the calibrated flame under unstrained and various strained conditions, which are obtained via laminar flame calculations. The relationship is close to linear at various strain rates. This suggests that Q_{cal} can be approximated as a constant that is independent of strain rate. Similarly, the quenching rate for each target flame is also obtained from laminar flame calculations. Figure 3.14(b) shows quenching rates for ethanol flames carried by air under various coflow conditions. It can be seen that quenching rate for each case is slightly different. A straight line is obtained for each flame condition through curve fitting, the gradient of which is the quenching rate. Equation 3.23 is then rewritten as:

$$n_{OH} = F\frac{n_{cal}}{F_{cal}}\frac{Q}{Q_{cal}} = FK \tag{3.25}$$

For each target flame, the constant K is readily obtained from images and laminar flame calculations. Specifically, the peak number density of OH in the calibrated flame is n_{cal}, the peak fluorescence signal from the calibrated flame is F_{cal}, and the quenching rate at the the peak OH number density is used as Q_{cal}. Thus the number density of OH at a given pixel for the target flame is a product of the fluorescence signal at that pixel and K.

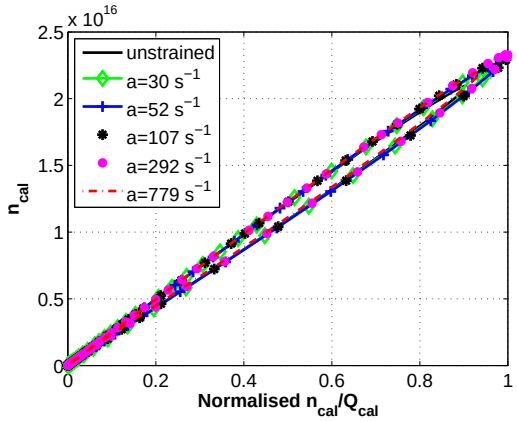

(a) Methane-air flame

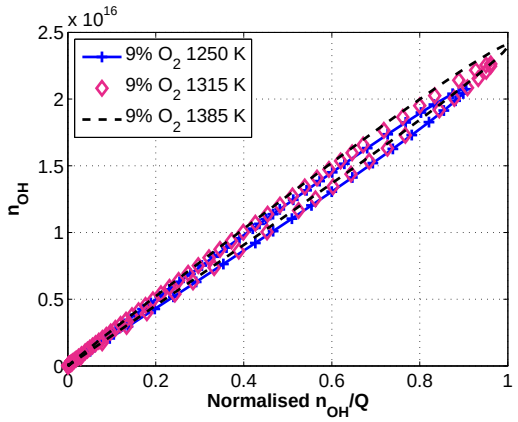

(b) Ethanol flame carried by air

Figure 3.14: The relationship between n_{cal} and $\frac{n_{cal}}{Q_{cal}}$ (normalised by $(\frac{n_{cal}}{Q_{cal}})_{max}$): (a) calibrated flame in the slot burner: partially premixed methane-air flame; (b) ethanol carried by air in coflows with 9% O_2 at various temperatures.

3.7.2 Uncertainties and Errors in OH Quantification

To evaluate the uncertainties and errors associated with quantifying the OH-LIF signal, the validity of important assumptions made in this process should be examined. The first assumption is that the experimentally determined constant C is the same for the calibrated flame and target flames. Recall that C is a combined effect of the speed of light, the linewidth of the laser beam, the overlap integral between the laser lineshape and the absorption lineshape, the fraction of fluorescence bandwidth collected, the laser path length sampled by the collection optics, and the efficiency of the optical and detection system. In reality, the overlap integral is not the same as the absorption lineshape of OH is dependent on the temperature, the pressure, and the composition of the surrounding environment. Due to the similarities between the calibrated flame and target flames, errors introduced by this effect are considered to be small.

The second assumption is that the peak OH number density obtained from laminar flame calculations can represent the actual peak OH concentration in the laminar flame in the slot burner, and it is suitable as a reference point. Using the same calculation and calibration methods, Medwell [152] found that the difference between calculated OH number density and measured OH number density of a calibrated flame is approximately 10%, indicating the suitability of these methods.

The third assumption is that the Boltzmann fraction is the same everywhere in the calibrated flame and target flames. Medwell [152] reported a 10% variation in the Boltzmann fraction with temperature ranging from 1000 K to 2000 K. Hence the maximum error introduced by this assumption is 10%.

The fourth major assumption is that the quenching rate calculated with laminar flame calculations is a good estimation. It is found that this assumption probably produces 10% error [152]. In addition, the quenching rate is assumed to be constant throughout the flame. However, as shown in Fig. 3.14, the quenching rate varies as

the temperature and composition at different locations are not the same. Laminar flame calculations reveal that 8-18% errors can be introduced due to this assumption. Due to the uncertainties and errors in the quantification process, results from OH-LIF should be only treated as semi-quantitative results.

3.8 Unsteady Laminar Flamelet Modelling

The unsteady flamelet model used in this thesis is similar to the model developed by Pitsch et al [170]. This model has previously been applied, with a two-step analysis procedure, to simulate MILD flames in the same JHC configuration by Evans et al [171]. To obtain the flow and mixture fields, non-reactive Large-Eddy Simulation (LES) is carried out. These simulations provide the temporal evolution of the flow field parameterised by the scalar dissipation rate of the mixture necessary for the second step. During the second step, unsteady flamelet equations are solved in time and mixture fraction space. The two simulation steps will be described in detail in the following sections.

3.8.1 Modelling approach - Large-Eddy Simulation

LES is carried out to obtain a solution of the turbulent flow field. The experimental configuration is simulated using a fully three-dimensional cylindrical grid with 256, 128, and 96 grid points in the axial, the radial, and the circumferential directions, respectively. The grid is stretched in the axial direction with a grid spacing of 0.5 mm at the jet exit plane. The radial grid sizing is 0.1 mm at the nozzle. The boundary conditions are set to match the experimental conditions. A well-resolved LES of the central fuel pipe upstream of the jet exit plane is run prior to the main simulations, which generates velocity data at the jet inlet boundary for the main simulations. For the inlet boundary condition of the coflow, a constant velocity

profile is prescribed. A convective outlet condition is defined for the outlet of the domain. At the radial boundary of the simulation domain, zero gradient boundary conditions are imposed for either velocities or scalars, thus there is no flux at the boundaries in the radial direction.

The parallel, finite difference code CIAO was used for the LES. It solves the filtered Navier-Stokes equations in the low Mach number limit. The momentum equations are spatially discretized with a second-order scheme [172]. Spatial gradients of the scalar equation are discretized with a third order WENO scheme [173]. Unclosed subfilter terms are closed with a dynamic Smagorinsky model [174] with Lagrangian averaging [175] for the subfilter stress term and a Smagorinsky type model [176] for the subfilter diffusivity of the scalar equation. A scalar transport equation is solved for the filtered mixture fraction $\tilde{Z}$, which locally defines the state of the fluid mixture.

The scalar dissipation rate, determined from the flow-field solution, is defined as averaged conditional scalar dissipation rate at each grid plane in the axial direction. The distance to the jet exit plane can be related to the flamelet time via a characteristic velocity u_{st}, which is the mean axial velocity at the radial position where $\tilde{Z} = Z_{st}$ [170]. The relationship between the axial distance and the flamelet time is defined by [170]

$$t = \int_0^x \frac{1}{u_{st}|\,(Z = Z_{st})} dx' \tag{3.26}$$

Fluid properties, such as density, viscosity, and diffusivity of the scalar, are obtained from an extinct flamelet solution (χ above extinction strain rate), which is tabulated and accessed during runtime. During the second step, the unsteady flamelet model simulates the ignition process based on these fluid and turbulence properties. This analysis is only focused on the onset of ignition, and it assumes that changes in the conditional scalar dissipation rates are negligible due to a small temperature increase and limited heat release in the stabilisation region. Hence,

these minor changes as a consequence of ignition are not incorporated into the LES as feedback. Jochim et al. [177] found that for diesel engine combustion, this assumption can even lead to correct predictions of the major characteristics of the entire combustion process.

3.8.2 Modelling approach - Unsteady flamelets

For the solution of chemistry, the unsteady flamelet equations [178, 179] are solved in time and mixture fraction space using the FlameMaster program [180]. The unsteady flamelet equations are

$$\rho\frac{\partial T}{\partial t} - \rho\frac{\chi}{2}\left(\frac{\partial^2 T}{\partial Z^2} + \frac{1}{c_p}\frac{\partial c_p}{\partial Z}\frac{\partial T}{\partial Z}\right) + \frac{1}{c_p}\left(\sum_{k=1}^{N} h_k \dot{m}_k - \mathcal{H}\right) = 0 \qquad (3.27)$$

where T denotes the temperature, t and Z are time and mixture fraction, respectively. χ denotes the scalar dissipation rate, ρ is the density, and c_p is the specific heat capacity at ambient pressure. N is the number of species included in the mechanism, h_k and $\mathcal{H}$ represent the enthalpy of species k and the enthalpy flux by mass diffusion, respectively.

The scalar dissipation rates and local compositions are extracted from the LES as described in the preceding section. They change with time and are coupled to the axial distance via the characteristic time.

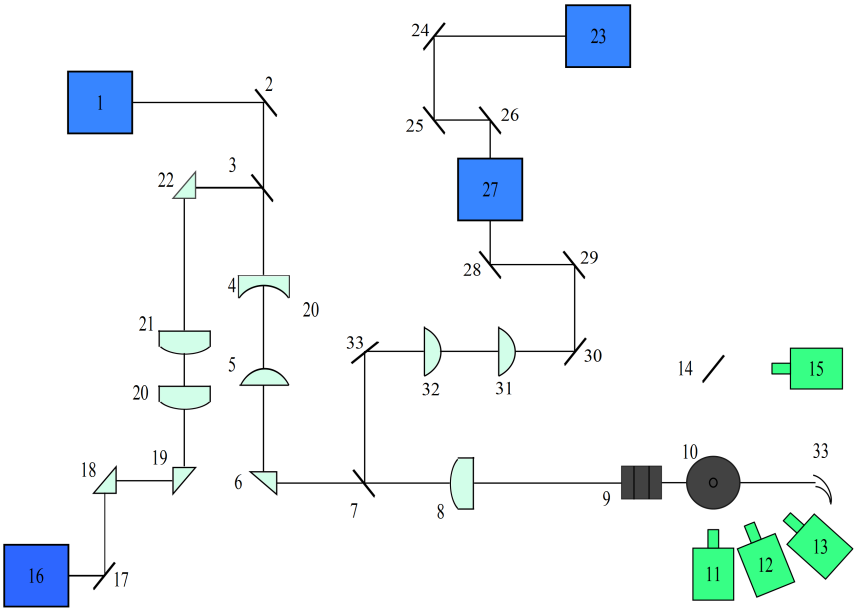

1. Quantel BrilliantB/Twins double-head Nd:YAG laser (Rayleigh Scattering)
2. High energy 532nm mirror
3. Dichroic mirror (transmit 532nm, reflect 355nm)
4. Fused silica cylindrical lens (f= -125mm)
5. Spherical lens (f= +250mm)
6. Fused silica prism
7. Dichroic mirror (transmit 355nm and 532nm, reflect 283nm)
8. Fused silica vertical cylindrical lens (f=+750mm)
9. Slot burner
10. JHC burner
11. Princeton Instruments ICCD camera for Rayleigh scattering
12. Andor iStar ICCD camera for CH_2O-LIF
13. pco.pixelfly camera for OH* chemiluminescence
14. Dichroic mirror (reflect 308nm, transmit 532nm)
15. Princeton Instruments ICCD camera for OH-LIF
16. Frequency-tripled BrilliantB Nd:YAG laser for CH_2O-LIF
17. Dichroic mirror (transmit 532, reflect 355nm)
18. Fused silica prism
19. Fused silica prism
20. Fused silica cylindrical lens (f= +300mm)
21. Fused silica cylindrical lens (f= +300mm)
22. Fused silica prism
23. Q-smart 850 single-head Nd:YAG laser for pumping the OH-LIF dye laser (#27)
24. High energy 532nm mirror
25. High energy 532nm mirror
26. High energy 532nm mirror
27. Lambda-Physik ScanMate 2E dye laser for OH-LIF
28. Silvered mirror
29. Silvered mirror
30. Silvered mirror
31. Spherical lens (f= +50)
32. Spherical lens (f=+200mm)
33. Silvered mirror
34. Beam dump

Figure 3.15: Schematic details of optical layout.

Chapter 4

An Experimental Study on MILD Combustion of Prevaporised Liquid Fuels

Statement of Authorship

Title of Paper	An experimental study on MILD combustion of prevaporised liquid fuels
Publication Status	☑ Published ☐ Accepted for Publication ☐ Submitted for Publication ☐ Unpublished and Unsubmitted w ork w ritten in manuscript style
Publication Details	J. Ye, P.R. Medwell, E. Varea, S. Kruse, B.B. Dally, H.G. Pitsch, An experimental study on MILD combustion of prevaporised liquid fuels, Appl. Energy 151 (2015) 93–101.

Principal Author

Name of Principal Author (Candidate)	Jingjing Ye		
Contribution to the Paper	Based on a thorough literature review conducted by me, and lots of discussions between me and my supervisors, several operating parameters were chosen for investigation. I decided different experimental cases with my supervisors. I setup the experiments with co-authors. I undertook the experiments and collected 80% of the experimental data independently. One co-author, Paul R. Medwell, provided me assistance while I collected the other 20% of the data. I processed, analysed, and interpreted all the experimental data. I also planned and performed all the calculations in the Chemkin software to assist the interpretation of the experimental data. I performed an analysis of the experimental and calculation results. The analysis was presented in text or figures by me. I integrated all the analysis and wrote the manuscript. I also acted as the corresponding author, and responded to the reviewers' and the editor's comments and recommendations.		
Overall percentage (%)	65		
Certification:	This paper reports on original research I conducted during the period of my Higher Degree by Research candidature and is not subject to any obligations or contractual agreements with a third party that would constrain its inclusion in this thesis. I am the primary author of this paper.		
Signature	Digitally signed by JINGJING YE Date: 2017.06.02 13:08:21 +09'30'	Date	02-June-2017

Co-Author Contributions

By signing the Statement of Authorship, each author certifies that:

i. the candidate's stated contribution to the publication is accurate (as detailed above);

ii. permission is granted for the candidate in include the publication in the thesis; and

iii. the sum of all co-author contributions is equal to 100% less the candidate's stated contribution.

Name of Co-Author	Paul R. Medwell		
Contribution to the Paper	This co-author co-designed the experiments and co-supervised the development of the work. This co-author also provided assistance during the experimental setup and part of data collection. This co-author helped to evaluate and edit the manuscript.		
Signature	Paul Medwell 2017.06.03 10:44:13 +09'30'	Date	03-JUN-2017

Name of Co-Author	Emilien Varea		
Contribution to the Paper	This co-author co-designed the experiments. This co-author also helped to set up and undertake the experiments.		
Signature	Signature numérique de Emilien Varea Date : 2017.05.30 13:33:01 +02'00'	Date	30-May-2017

Name of Co-Author	Stephan Kruse		
Contribution to the Paper	This co-author helped to design the test rig and set up the experiments.		
Signature		Date	05-June-2017

Name of Co-Author	Bassam B. Dally		
Contribution to the Paper	This co-author co-designed the experiments and co-supervised the development of the work. This co-author helped to evaluate and edit the manuscript.		
Signature	Digitally signed by Bassam Dally Date: 2017.06.05 11:30:20 +09'30'	Date	05-June-2017

Name of Co-Author	Heinz G. Pitsch		
Contribution to the Paper	This co-author co-designed the experiments. This co-author helped to evaluate and edit the manuscript.		
Signature	Digitally signed by Heinz Pitsch Location: Aachen Date: 2017.06.01 16:11:37 +02'00'	Date	01-June-2017

Please cut and paste additional co-author panels here as required.

Applied Energy 151 (2015) 93–101

Contents lists available at ScienceDirect

Applied Energy

journal homepage: www.elsevier.com/locate/apenergy

An experimental study on MILD combustion of prevaporised liquid fuels

Jingjing Ye [a,*], Paul R. Medwell [a], Emilien Varea [b], Stephan Kruse [b], Bassam B. Dally [a], Heinz G. Pitsch [b]

[a] School of Mechanical Engineering, The University of Adelaide, South Australia 5005, Australia
[b] Institute for Combustion Technology, RWTH Aachen University, Aachen 52056, Germany

HIGHLIGHTS

- MILD combustion of prevaporised liquid fuels under elevated pressure is examined.
- MILD combustion is achieved for all fuels under atmospheric pressure.
- Combustion stability is highly dependent on fuel type.
- Pressure, jet velocity and carrier gas show great impacts on NO_x emissions.

ARTICLE INFO

Article history:
Received 26 November 2014
Received in revised form 30 March 2015
Accepted 6 April 2015
Available online 29 April 2015

Keywords:
MILD combustion
Prevaporised liquid fuel
Pressurised combustion

ABSTRACT

This paper presents an experimental study on moderate or intense low oxygen dilution (MILD) combustion of prevaporised liquid fuels burning in a reverse-flow MILD combustor under elevated pressures. The influence of fuel type, equivalence ratio, carrier gas, operating pressure and air jet velocity on the combustion stability and emissions are investigated. Ethanol, acetone and *n*-heptane are vaporised and carried to the combustor using either nitrogen or air. It is found that the combustion stability is highly dependent on fuel type, with *n*-heptane being the most unstable due to its fast ignition under all high-pressure conditions studied. Measured CO emissions emitted from all fuels are very low except when the equivalence ratio approaches the lean extinction limit, and this effect is not dependent on the pressure. The joint regime of low CO and NO_x emission becomes narrower under elevated pressure as NO_x emissions emitted from all fuels increased with pressure. The enhanced NO_x formation rate via the nitrous oxide mechanism, the slower mixing, the increased flame temperature and residence time are believed to cause higher NO_x emissions as pressure increases. The NO_x emissions are reduced by increasing the air jet velocity, which is attributed to a lower peak temperature. The NO_x emissions are also reduced when the fuel is carried by nitrogen instead of air. Further research is required to understand this trend which will help in reducing NO_x emissions under these conditions, especially at elevated pressures.

1. Introduction

Moderate or intense low-oxygen dilution (MILD) combustion is a very promising technology to abate CO, NO_x and other emissions while maintaining stable combustion and high thermal efficiency [1]. As no visible flame can usually be observed in MILD combustion, it is also known as flameless oxidation (FLOX®) [1] and flameless combustion [2]. The main principle of MILD combustion is that combustion takes place with low local oxygen concentration and high reactant temperature. The local oxygen concentration of around 3–12% and the reactant temperature above the self-ignition temperature [3] lead to a moderate temperature rise across the reaction zone, suppressing the formation of NO_x, CO and soot significantly [4–6]. These features of MILD combustion are favoured in a wide range of industrial combustion systems. For instance, although the peak temperature is reduced inside a furnace, the volumetric reaction resulting from the hot and diluted mixture leads to a larger radiating volume, hence the net radiation flux from MILD combustion is increased [7]. In a gas turbine application, a higher efficiency can be achieved by increasing the mean temperature of exhaust gases without the expense of increasing NO_x formation and reducing the durability of gas-turbine components owing to a uniform temperature distribution (both spatially and temporally) with a lower peak temperature, even though a high radiant flux is not favourable. In addition, the hot mixture above autoignition temperature reduces the risk of thermo-acoustics instability associated with extinction and re-ignition especially at very lean conditions.

* Corresponding author at: School of Mechanical Engineering, The University of Adelaide, Adelaide, South Australia 5005, Australia. Tel.: +61 8313 4367.
E-mail address: jingjing.ye01@adelaide.edu.au (J. Ye).

http://dx.doi.org/10.1016/j.apenergy.2015.04.019
0306-2619/

MILD combustion belongs to the High Temperature Combustion Technology (HiCOT) domain, which denotes all the combustion technologies using high temperature reactants [8]. There are a few technologies similar to MILD combustion in this domain, such as High Temperature Air Combustion Technology (HiTAC) and Colourless Distributed Combustion (CDC), which should not be confused with MILD combustion. MILD combustion refers to a combustion process, in which the temperature of reactants is above the autoignition temperature, meanwhile the maximum allowable temperature increase is lower than the autoignition temperature of the mixture [8]. Compared to MILD combustion, HiTAC is limited to the use of highly preheated air [8]. Compared to MILD combustion, CDC is operated in a high thermal intensity combustor with a very low residence time [9].

Numerous studies have shown that the stabilisation and optimisation of MILD combustion with gaseous fuels depends on a range of operating parameters [1,8,10–14]. These include the fuel type and composition, local oxygen concentration, the initial temperature, jet momentum flow rate, residence time, degree of mixing and turbulence level. In general, the establishment of MILD combustion depends on maintaining a hot and diluted environment, leading to a delayed, but spontaneous and homogeneous ignition. In industrial combustion devices, this environment is usually created by a strong recirculation of exhaust gases, and the recirculation rate is controlled by the flow dynamics. Several designs have been proven to be effective in improving the recirculation rate, for example adopting a reverse-flow configuration [14,15] and applying high-speed jets [10,16,17]. Szegö et al. [14] reported a transition from visible flame to flameless combustion with the change in fuel/air jet momentum ratio in a parallel-jet arrangement. In their configuration, the minimum fuel/air jet momentum ratio required for stable MILD combustion determined a minimum fuel jet penetration distance, which ensures that reactants have enough time to mix well with exhaust gases separately before reaction can proceed [14]. In addition to the impact on flame stability, a higher recirculation rate created by a dominant higher air jet velocity was found to lower the emissions [10].

The preparation of a homogeneous mixture becomes challenging in the presence of a spray in MILD combustion of liquid fuels. Differing from conventional spray combustion, a spray is injected into hot vitiated air under MILD combustion conditions, where different spray–turbulence–chemistry interaction is expected. Indeed, a previous study showed that a strong spray evaporation, enhanced by a hot-diluted coflow, resulted in changes in the atomisation mechanism with an immediate liquid jet break-up near the atomiser [18]. Meanwhile, the low local oxygen concentration shifted the stoichiometric mixture fraction away from the spray axis and significantly lowered the peak flame temperature [18], which could help reduce emissions. A few researchers have explored the benefits of extending MILD combustion technology to liquid fuels. Weber et al. [19] studied MILD combustion with various fuels, such as natural gas, light fuel oil (LFO), heavy fuel oil (HFO) and coal. The performance of light fuel oil (LFO) was very close to that of natural gas when being burnt in a vitiated coflow. Nevertheless, visible flames and high NO_x emissions were found in MILD combustion of heavy fuel oil, and the contributing factors for this are not clear. Reddy et al. [20] investigated MILD combustion of biodiesel blended with standard diesel in a two-stage combustor. They found that emissions of NO_x and unburned hydrocarbon (UHC) were greatly reduced after blending biodiesel with diesel. Biodiesel has higher viscosity and boiling point than diesel, thereby evaporating more slowly, which was believed to be responsible for higher emissions. The importance of fast droplet evaporation was highlighted in their more recent study [21], in which they attempted to burn kerosene with the same combustor but under much higher thermal intensity. A longer residence time and a stronger recirculation were required to ensure that droplets evaporate completely as the droplet number density increased with the thermal intensity. Interestingly, Khalil and Gupta [22] found that butyl nonanoate generated less emissions than JP8 despite having a higher surface tension, viscosity and density in a distributed combustor with swirling air. Note that liquid fuels were injected directly into the preheated air stream (600 K) before entering the combustion chamber instead of using an atomiser in their experiments, proving great potential to extend this combustion technology to liquid fuels without modifying the combustor [22]. In a different ultra-high thermal intensity distributed combustor without any atomiser, Arghode et al. [6] studied the combustion performance of ethanol in direct-injection mode and premixed–prevaporised mode. The CO emissions from ethanol were considerably higher than those from gaseous fuel and prevaporised ethanol, which was suspected to be caused by limited residence time [6]. The NO_x emissions emitted from ethanol were less than 7 ppm regardless of the combustion mode [6].

Most previous studies [10,12,16,19] on gaseous fuels use hydrogen, methane and other short-chain alkanes. Whilst is it true that previous studies have shown that MILD combustion is not heavily dependent on the type of fuel with hydrogen addition [23] the literature is very sparse on oxygenated or long-chain hydrocarbons. This is especially true under high-pressure conditions. Hence, ethanol, acetone and *n*-heptane are considered to represent alcohol, ketone and alkane, respectively in the current study. Most of the research on MILD combustion of liquid fuels has been performed at atmospheric pressure [6,19,20,24,25]. Considerable differences in performances for various liquid fuels under MILD combustion conditions have been reported [19,20]. In particular, higher emissions were found for some fuels, such as heavy fuel oil and biodiesel fuel. It is not clear if the differences were a result of spray characteristics and/or fuel chemistry. The parameters controlling the stabilisation and optimisation of MILD combustion of liquid fuels are not fully understood. In addition, a better understanding of the impact of pressure on MILD combustion of liquid fuels is required to extend MILD combustion technology to industrial combustors operating at elevated pressure.

In this study experiments are conducted to understand the impact of various parameters on the stabilisation and optimisation of MILD combustion with three different prevaporised liquid fuels burning in a reverse-flow MILD combustor. The reverse-flow configuration applied in the present study has been proven to be effective in the establishment of MILD combustion of gaseous fuel (methane), and is well described in previous publications [26,27]. The present study is part of a two-stage project on MILD combustion of liquid fuels. As the first stage of the project, liquid fuels are vaporised before injection in this study. Hence, the mixing of reactants and surrounding hot combustion products in current study is essentially similar to that of gaseous fuels in previous studies [10,12,16,19]. The prevaporisation of liquid fuels allows the current study to ignore the complexity of spray development and focus on the impact of chemical kinetics, particularly pressure, fuel type and carrier gas. At the second stage, MILD combustion of the same type of fuels, injected as liquid sprays, will be studied. The parameters investigated in the present study are the fuel type, equivalence ratio, carrier gas, air jet velocity and operating pressure inside the combustion chamber. Measurements and observations regarding to emissions and the combustion stability under different operating conditions are presented and discussed.

2. Experimental setup

The MILD combustor includes an ignition chamber, a main combustion chamber (58 mm × 58 mm × 200 mm) and a recuperator

for preheating the air with the heat recovered from the exhaust gases. A detailed description of this MILD combustor was presented in previous studies [26,27], however a different nozzle arrangement is adopted in this study for non-premixed combustion. In brief, the preheat mode is for warming up the whole combustor, after which the combustor is switched to MILD combustion mode as shown in Fig. 1. Liquid fuels, including ethanol (purity over 96%), acetone (purity over 99.8%) and *n*-heptane (purity over 99%), are vaporised and mixed with a carrier gas in an electric heater upstream of the combustor. Among the three fuels, *n*-heptane has the highest boiling point of 371.4 K [28]. To avoid condensation along the fuel pipe, the fuel and carrier gas are heated to 443 K. Either air or nitrogen is used as carrier gas, which is injected at a rate of 0.0975 g/s and 0.0944 g/s respectively. The thermal input was 4.7 kW, giving a thermal intensity for all experiments of 7 MW/m^3.

Bypass air pipes, in which air is not preheated by the exhaust gases, are installed at the centre of the recuperator in order to control the air preheat temperature at the exit plane of the air jet. Mixing the hot primary air with a certain amount of cold bypass air helps to achieve the desired preheat temperature. The preheat temperature is set to 873 ± 50 K to ensure the autoignition of the reactants. A mixture of primary air and bypass air is injected from the air nozzle. Fuel and carrier gas are injected into the main combustion chamber from a central fuel nozzle as shown in Fig. 1. The fuel nozzle and the air nozzle are concentric, but the fuel nozzle protrudes 1.44 mm above the exit plane of the air nozzle. Two air nozzle diameters, 10 mm and 6.2 mm, are used to study the effect of air jet momentum flow rate while the fuel nozzle diameter is kept constant at 2 mm. The reverse-flow design enhances the internal recirculation of exhaust gases, which dilutes the reactants before combustion takes place. The hemispherical top inside the main combustion chamber guides the recirculation of exhaust gases. Indeed, numerical work [29] on this particular configuration demonstrates that a plateau of constant entrainment ratio is achieved close to the nozzle exit, revealing a fast and thorough mixing of reactants and hot products, which promotes MILD combustion. The combination of air preheating and strong recirculation of hot products produce MILD combustion conditions.

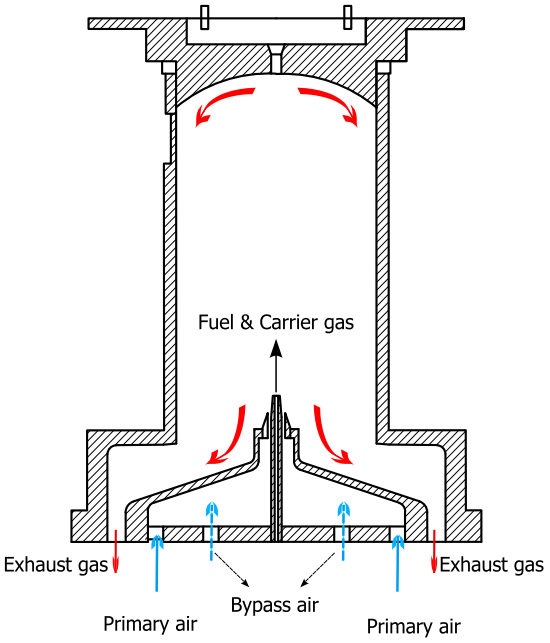

Fig. 1. MILD combustion mode.

A K-type thermocouple is placed close to the air nozzle outlet to measure the air preheat temperature. The exhaust temperature is measured by a K-type thermocouple placed at the exhaust tube. Another K-type thermocouple is used to measure the inside wall temperature of the combustor. Acetone-LIF was performed in a previous study on the same reverse-flow combustor to study the distribution of fuel for three nozzle arrangements under non-reacting conditions. The results show that premixed conditions were achieved for all three arrangements at $y/d = 4$, implying that reactants and hot products become well-mixed rapidly downstream of the nozzle exit in the current experiments. As the reactants and hot products are well-mixed, a distributed reaction with a uniform temperature distribution is expected. Hence, the temperature distribution is not measured in the current experiments. In addition, the measured exhaust temperature is typically around 1173–1273 K, and it is lower than 1373 K even when the system is operated approaching stoichiometric conditions with air preheated to 923 K. Hence, the maximum temperature increase in current experiments is less than 550 K, which shows the stabilisation of MILD combustion according to the definition given by Cavaliere and de Joannon [8].

Three windows are installed on three combustor walls at different height to allow visual observation and optical access along the centreline of the combustor. The exhaust is sampled by a Testo 350 gas analyser, averaged over a 25-min duration for each operating condition studied. The concentrations of O_2, CO, NO and NO_2 (NO_x) are measured. The estimated error for CO emission is ±2 ppm within the range of 0–39.9 ppm, and ±5% of reading in the range of 40–500 ppm. The estimated error for NO_x emission is ±5 ppm in the range of 0–99.9 ppm, and ±5% of reading in the range of 100–500 ppm. The estimated error for O_2 is ±0.2 vol.%. In order to compare the emission levels between the various dilution effects, the concentration is calculated by volume on a dry basis at 15% oxygen level (by volume) based on the following equation [30]:

$$X_{15,i} = X_i \times \frac{20.9 - 15}{20.9 - X_{O_2}} \quad (1)$$

In Eq. (1), X_i is the measured concentration of species i in the exhaust gas. X_{O_2} is the measured concentration of oxygen in the exhaust gas. $X_{15,i}$ is the corresponding concentration of species i at 15% oxygen level.

3. Results

3.1. Reference cases at atmospheric pressure

Combustion stability in the current study is determined via visual observation of the flame, monitoring the fluctuation of pressure and exhaust temperature, and the measured emission of pollutants in the exhaust gas. Specifically, optimised MILD combustion is featured by the absence of a flame, low NO_x and CO emissions. During the transition from MILD combustion to conventional combustion, in addition to the occurrence of a flame, drastic increases in NO_x and CO emissions are observed. A concentration of NO_x or CO emission lower than 10 ppm at 15% O_2 by volume is considered to be low emission for ease of comparison in this study. This threshold is adopted from regulations in parts of Southern California, which regulates stationary gas turbines to 9 ppm or less NO_x at 15% O_2 by volume [31].

Experiments of ethanol at 1 bar (absolute pressure) with nitrogen as carrier gas under a range of equivalence ratios are taken as a reference case. No visible flame is observed in combustion of ethanol under these operating conditions. The lean extinction limit at

these conditions is found to be at an equivalence ratio $\Phi = 0.25$. Fig. 2 demonstrates that CO emission is very low for a wide range of equivalence ratios. The CO mole fraction in the exhaust gas only starts to rise sharply when the equivalence ratio approaches the lean extinction limit due to incomplete combustion. Conversely, the NO_x mole fraction shows an increasing trend as the combustor approaches the stoichiometric condition. This is expected due to the higher temperatures of the system, which can be deduced from the measured higher exhaust temperatures at higher equivalence ratios. As the lean limit of the system is approached, NO_x emissions fall to levels approaching the detection limit of the gas analyser, which is consistent with excessive cooling of the combustor under these conditions. Both the concentration of CO and NO_x emissions are below 10 ppm with the equivalence ratio ranging from 0.35 to 0.72. The same responses of NO_x and CO emissions on equivalence ratio were observed in a previous study on MILD combustion of gaseous fuel (methane) using the same reverse-flow combustor by Kruse et al. [26].

3.2. Effect of pressure

Results from experiments where the operating pressure is 2.5 bar, 4 bar, and 5 bar (absolute pressure) are presented and compared to those under 1 bar in this section. The 10-mm air nozzle and 2-mm fuel nozzle are used in all of these cases. MILD combustion with ethanol is achieved under all the tested conditions. The lean extinction limit for ethanol is shifted to leaner conditions under elevated pressures. Specifically, the lean extinction limit for ethanol decreases from 0.25 at 1 bar to 0.18 at both 2.5 bar and 5 bar. Similar to that at atmospheric pressure, CO emission is close to 0 ppm until the lean extinction limit is approached while NO_x emission increases with the equivalence ratio at both 2.5 bar and 5 bar as shown in Fig. 3. Fig. 3a illustrates a substantial increase in NO_x emissions with $\Phi > 0.4$ as pressure increases. Nevertheless, similar levels of NO_x are emitted with $\Phi \leqslant 0.4$ under elevated pressure. Note that the increase in NO_x emission with pressure is also observed in experiments with air as carrier gas, which is not presented here. The range of low emissions for ethanol is shifted from $\Phi < 0.72$ at 1 bar to $\Phi < 0.46$ at 5 bar. Fig. 4 shows that a higher NO_x emission with $\Phi > 0.4$ and a narrower range of low emissions at higher pressures are also observed for acetone and *n*-heptane. Differing from ethanol, combustion of acetone becomes unstable with equivalence ratios close to stoichiometric at 5 bar, while combustion of *n*-heptane becomes unstable at 5 bar even under leaner conditions ($\Phi \approx 0.4$), therefore NO_x emissions emitted from acetone and *n*-heptane only at 4 bar are presented here. Note that measured CO emissions for acetone and *n*-heptane also approach the detection limit of the gas analyser unless the system is run near the lean extinction limit, and no clear pressure dependence is observed, which is not presented here for brevity. The positive pressure-dependence on NO_x formation with constant nozzle diameters is consistent with the previous study by Kruse et al. [26].

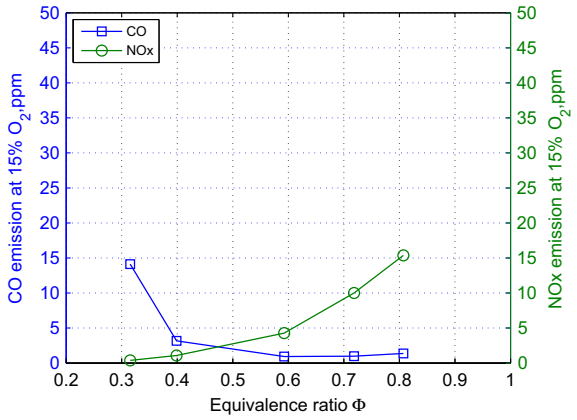

Fig. 2. Mole fraction of NO_x and CO emissions at 15% O_2 by volume for ethanol plotted against the equivalence ratio at $P = 1.0$ bar.

It is suspected that the combustion instability and higher NO_x emissions observed under elevated pressure are partially due to the inversely proportional relationship between pressure and volumetric flow rate according to the ideal gas law. The decrease in volumetric flow rate under elevated pressure results in a considerable increase in residence time, thereby increasing the available time for NO_x to be produced. However, the effect of superequilibrium O atoms and OH radicals on increasing NO_x production rate diminishes at a longer residence time [32]. The residence time here is defined as the ratio of the volume to the volumetric flow rate of reactants. Due to a decreased volumetric flow rate, the air and fuel jet velocities under 5 bar are four times lower than those under 1 bar, which can affect the mixing process, thereby affecting NO_x emissions. To investigate the impact of velocity on NO_x emissions, a parametric study of air jet velocity is performed, which is presented in the following section.

3.3. Effect of air jet velocity

To vary the air jet velocity, the 10 mm air nozzle is changed to a 6.2 mm air nozzle. The diameter of the fuel nozzle is kept at 2 mm. The corresponding air jet velocities and Reynolds numbers at different air nozzles are displayed in Table 1. The resulting air jet velocity with a 6.2 mm nozzle is around three times that with a 10 mm nozzle at a given equivalence ratio. Fig. 5a shows NO_x emissions for ethanol as a function of the equivalence ratio at different air jet velocities. NO_x emissions show similar dependencies on the equivalence ratio at different air jet velocities. However, NO_x emissions from ethanol combustion are substantially lowered as the air jet velocity is increased. In addition, NO_x emissions less than 10 ppm are achieved at all tested equivalence ratios with the higher air jet velocity. A reduction in NO_x emission at a higher jet velocity was also reported in studies on MILD combustion of gaseous fuel [10,26].

Fig. 5b compares NO_x emissions emitted from *n*-heptane at different air jet velocities at a pressure of 4 bar. It is noteworthy that combustion of *n*-heptane is unstable at both high and low air jet velocities at 5 bar, hence only NO_x emissions at 4 bar are measured and compared for *n*-heptane flames. Similar to ethanol, the range of low emissions of *n*-heptane is broadened at a higher air jet velocity. At a low air jet velocity, combustion of *n*-heptane is unstable with $\Phi \approx 0.8$ at both 2.5 bar and 4 bar. In those unstable cases a yellow flame, indicating the formation of soot, is observed, and the pressure inside the combustor is unstable. At a high air jet velocity the yellow flame is extinguished and the pressure becomes stable. However, measured CO emissions vary from 0 to 500 ppm with $\Phi \approx 0.8$, indicating the existence of combustion instabilities even with the high-speed air jet.

As the formation of NO_x, especially thermal NO, usually requires both high temperature and high local oxygen concentration, the general approach to abate NO_x is to avoid the concurrence of high temperature and high availability of oxygen, or to reduce the residence time at those favourable conditions. The increased air jet velocities promote the mixing between reactants and exhaust gases, which can be deduced from the increasing Reynolds numbers. A more homogeneous and diluted environment is produced at a better mixing, which is indicated by the disappearance of the yellow flame. This environment may produce a more uniform temperature distribution with a lower peak temperature, which restrains the formation of NO_x.

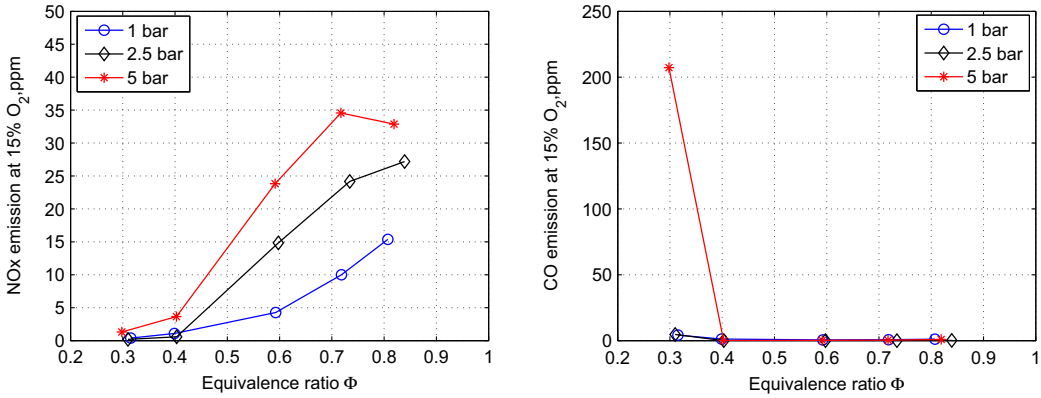

(a) mole fraction of NO_x for ethanol (b) mole fraction of CO for ethanol

Fig. 3. Mole fraction of NO_x and CO for ethanol carried by N_2 plotted against the equivalence ratio at various pressures.

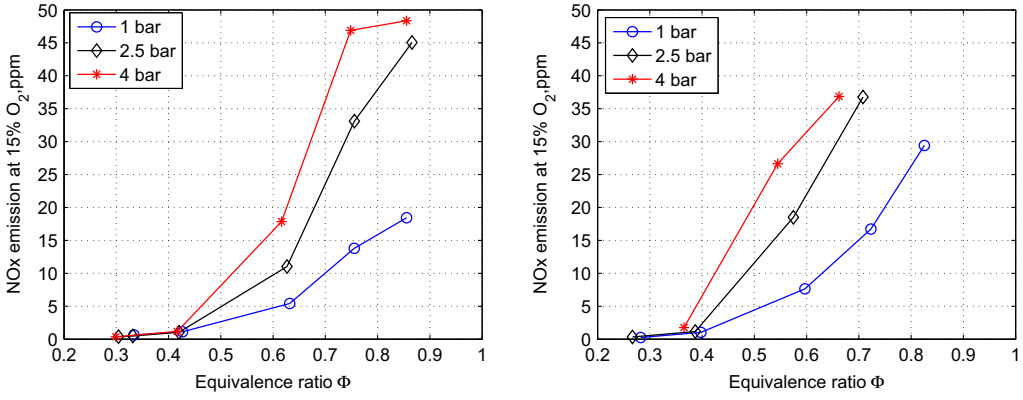

(a) acetone (b) n-heptane

Fig. 4. Mole fraction of NO_x and CO for acetone and *n*-heptane carried by N_2 plotted against the equivalence ratio at various pressures.

Table 1
Air jet velocities and Reynolds numbers for two air nozzles: D_a is the diameter of the air nozzle; U_a represents mean air jet velocity (m/s); *Re* is the Reynolds number based on the air jet diameter and mean velocity.

D_a = 10 mm			D_a = 6.2 mm		
Φ	U_a	*Re*	Φ	U_a	*Re*
Experiments of ethanol carried by N_2 at 5 bar					
0.82	12	5015	0.81	35	7422
0.72	14	5711	0.67	42	8973
0.59	17	6970	0.53	53	11344
0.4	25	10280	0.39	72	15416
0.3	34	13707	0.34	83	17683
Experiments of n-heptane carried by N_2 at 4 bar					
0.83	16	5131	0.78	47	7983
0.66	20	6453	0.68	54	9157
0.54	24	7887	0.55	66	11321
0.37	35	11510	0.36	102	17296

3.4. Effect of carrier gas

In practice, high-velocity gas is often used to assist with atomising and fuel delivery in spray combustion. It is common to use air since it is readily available. The amount of air required varies with the nozzle and burner designs, which potentially affects the mixing and flame structure. However, the impact of the type of carrier gas or atomising gas is often overlooked.

To investigate the impact of the presence of oxygen with the fuel as it is being introduced to the combustor, air and alternatively nitrogen are used as carrier gas. The carrier gas mixes with the pre-vaporised fuel in the electric heater, and delivers the fuel to the combustion chamber. Note that the mixture of the fuel and carrier air is too rich for a rich premixed flame to burn, for instance, the equivalence ratio in the mixture of ethanol and carrier air is 15.5. Experiments are referred to as nitrogen case when nitrogen is used, while the term air case is used when air is used to carry the fuel into the combustion chamber. Fig. 6 reports NO_x emissions for ethanol as a function of Φ using different carrier gases with the pressure ranging from 1 bar to 5 bar. It is shown clearly that NO_x emissions for the air cases are higher than those for the nitrogen cases, and the difference is more profound at higher pressures. Specifically, NO_x emissions for the ethanol in air case are twice as much as those for the nitrogen case at 1 bar, however, NO_x emissions for the ethanol in air case are nearly three times as much as those for the nitrogen case at 5 bar. Due to the increase in NO_x emissions, the range of low emissions becomes narrower when air is used as carrier gas instead of nitrogen as CO emissions for both cases are very low. Similar phenomena are also observed

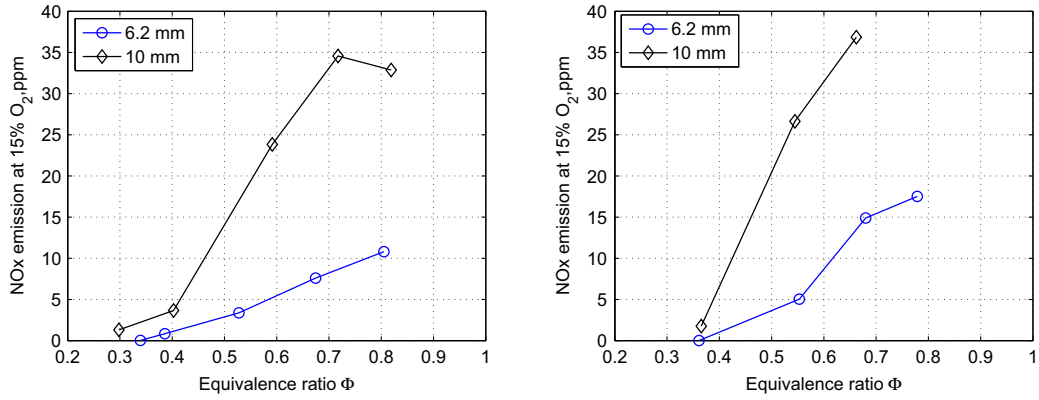

(a) mole fraction of NO_x for ethanol at 5 bar (b) mole fraction of NO_x for n-heptane at 4 bar

Fig. 5. Mole fraction of NO_x for ethanol and *n*-heptane plotted against the equivalence ratio with different air nozzles (6.2 mm and 10 mm) using N_2 as carrier gas.

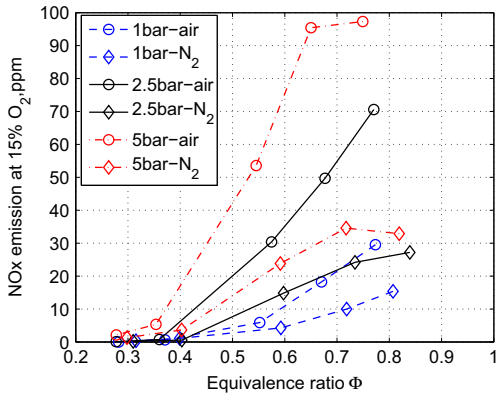

Fig. 6. NO_x emissions for ethanol with different carrier gases at various pressures.

during the combustion of acetone and *n*-heptane with different carrier gases, which are not presented here for brevity.

4. Discussion

Fig. 7 presents contour maps of CO and NO_x emissions measured for each fuel with nitrogen as carrier gas. The scale of measured values of CO emissions corresponds to the change of the colour from white to deep blue. The scale of measured values of NO_x emissions corresponds to the change of the colour from white to deep red. As indicated by the blue region at $\Phi \leqslant 0.4$, most of the CO emissions are produced at low equivalence ratios close to extinction. As shown in the red region at $\Phi \geqslant 0.6$, most of the NO_x emissions are emitted as the system approaches the stoichiometric conditions. The dependence of NO_x and CO emissions on Φ is consistent with previous studies on MILD combustion of gaseous fuels under elevated pressures [10,26]. Measured CO emissions did not show a clear pressure-dependent behaviour. The joint regime of low CO and low NO_x becomes narrower under elevated pressure as NO_x emissions increase with pressure, which are observed for all three fuels. However, it is evident in Fig. 7 that the combustion stability varies with fuel type in this particular combustor configuration, which can be seen from the unstable cases represented by yellow squares in acetone and *n*-heptane contour maps. MILD combustion of ethanol is successfully established at all of the tested conditions. No visible flame is detected during the experiments of ethanol. However, combustion of acetone is unstable with $\Phi > 0.7$ at a pressure of 5 bar. Combustion of *n*-heptane is unstable at 5 bar even under very lean conditions ($\Phi \approx 0.4$), where a yellow flame is observed. At 2.5 bar and 4 bar, MILD combustion with *n*-heptane is only established under leaner conditions ($0.4 \leqslant \Phi \leqslant 0.7$).

Fig. 7 reveals that the combustion instability only exists in cases operating under high pressures. As stated before, velocities of reactants and exhaust gases decrease linearly with pressure according to the ideal gas law, thereby increasing the flow timescale. In addition, pressure has a critical impact on chemical reaction rates, hence the Damköhler number is expected to change with pressure. It is well established that MILD combustion regime is characterised by a low Damköhler number, where both turbulence and chemistry play important roles [33]. The change in Damköhler number may shift combustion away from the MILD combustion regime, thereby leading to combustion instability.

To investigate the impact of pressure on the chemical timescale and Damköhler number, a calculation of ignition delays is performed under various pressures. The ignition delays of all three fuels are calculated in the Closed Homogeneous Batch Reactor model in the CHEMKIN software package (version 10113, x64), which is a well-accepted model for ignition delay calculation [34]. This reactor is taken to be a time-dependent adiabatic and isobaric system. The calculation is performed for a stoichiometric fuel–air mixture with inlet temperature varying from 823 K to 923 K to reflect the preheat air temperature in the current experiments. However, this calculation is only used to demonstrate the trend of ignition delays, which cannot determine the actual ignition delay times as this reverse-flow MILD combustor is much more complex than the Closed Homogeneous Batch Reactor. The ignition delays for ethanol are calculated with an ethanol chemical kinetic mechanism (57 species and 383 reactions) by Marinov [35]. Those for acetone are calculated with an acetone chemical kinetic mechanism (83 species and 419 reactions) by Pichon et al. [36], and those for *n*-heptane are calculated with an *n*-heptane chemical kinetic mechanism (654 species and 2827 reactions) by Mehl et al. [37].

The calculated ignition delays are plotted as a function of the inverse of the inlet temperature at pressures of 1 bar and 5 bar in Fig. 8. The onset of ignition is defined at the time where the maximum rate of change in OH concentration with respect to time occurs. The ignition delays are dramatically shortened with pressure for all fuels as shown in Fig. 8. This indicates that the chemistry timescale decreases greatly under elevated pressure. A combination of an increased flow timecale and a decreased

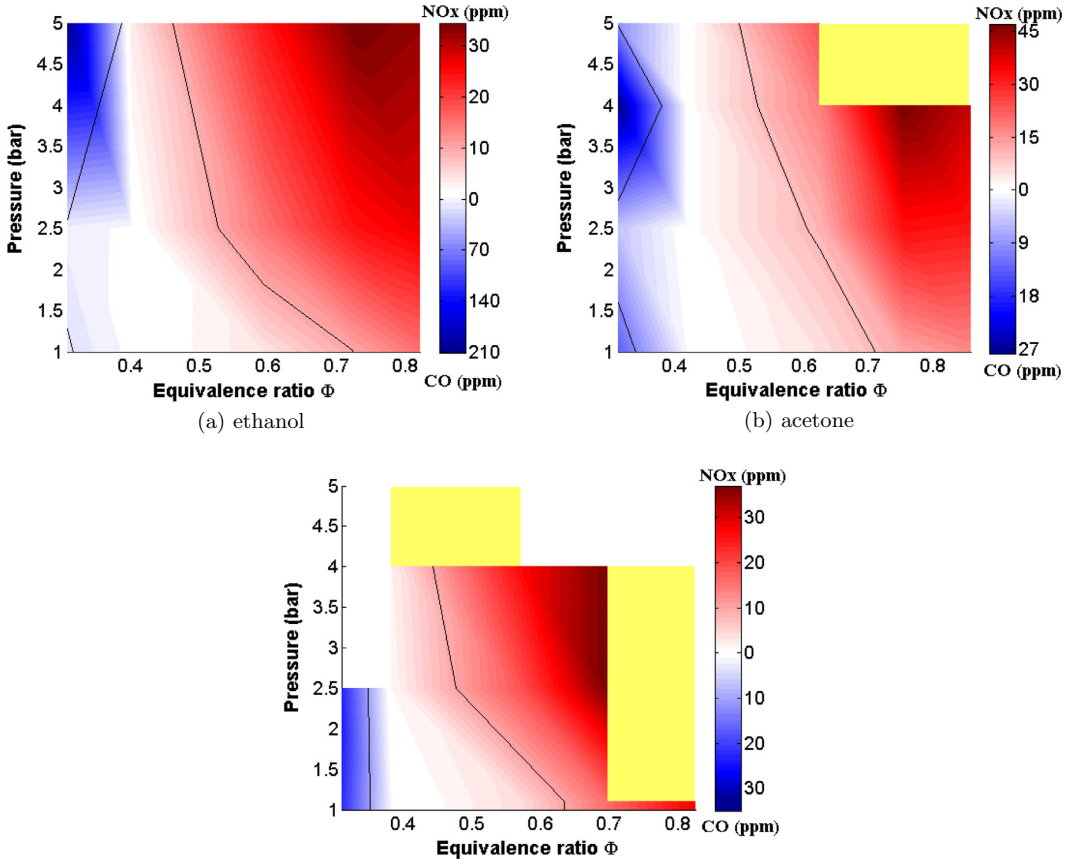

Fig. 7. Contour maps of CO and NO_x emissions for three fuels: yellow squares represent unstable cases, and blank space means no data are collected in those conditions; black lines at left are 10 ppm CO contour lines, and black lines at right are 10 ppm NO_x contour lines. (For interpretation of the references to colour in this figure legend, the reader is referred to the web version of this article.)

chemical timescale produces a higher Damköhler number. This indicates that ignition could occur before effective mixing. However, the establishment of MILD combustion relies on the preparation of a hot and diluted environment before ignition, which is controlled by mixing exhaust gases with reactants in this reverse-flow MILD combustor. Hence, it is reasonable to think that the early ignition leads to combustion instability under elevated pressure.

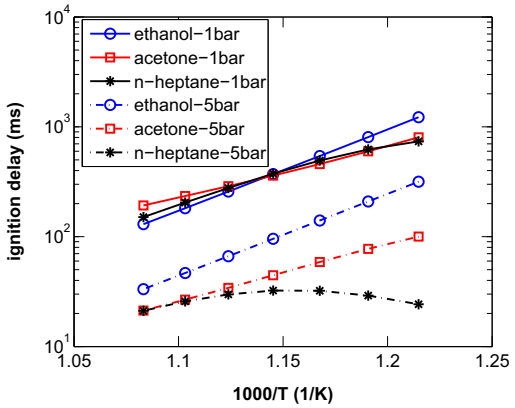

Fig. 8. Calculated ignition delays for three fuels at pressures of 1 bar and 5 bar.

The calculation of ignition delays does not show a clear difference between three fuels at 1 bar. However, we can see from Fig. 8 that the ignition delay of ethanol is the longest, followed by that of acetone and *n*-heptane with inlet temperature ranging from 823 K to 923 K at 5 bar. This trend explains the observed impact of fuel type on combustion stability as MILD combustion of ethanol is the most stable, while MILD combustion of *n*-heptane is the least stable. These results suggest that blending *n*-heptane with ethanol could prolong the ignition delay. In addition to increasing the chemical timescale by fuel blending, the flow timescale needs to be decreased to obtain a low Damköhler number, especially in a high-pressure MILD combustion device. A high-speed jet is required to promote the entrainment of the exhaust gases and enhance the dilution of reactants in this combustor design. It is also proposed that a better design will be to separate the air and fuel jet, ensuring that fuel and air mix with exhaust gases before they mix with each other.

From Fig. 7 it is clear that there is a positive dependence of NO_x emission on pressure for mixtures with $\Phi > 0.4$. To explore the direct impact of pressure on the production rate of NO_x, an analysis of NO_x formation mechanisms under the current operating conditions is performed. The importance of the thermal NO mechanism

is significantly affected by the temperature due to a large activation energy required by its primary reaction, which is not affected by pressure [38]. Current experiments are performed under fuel lean conditions, rendering the nitrous oxide mechanism important [32]. The nitrous oxide mechanism is initiated by a three body reaction $O + N_2 + M \rightleftharpoons N_2O + M$. The reaction rate of this three body reaction is known to increase with pressure [39]. In addition, Kruse et al. [26] found that the rate coefficient of this three body reaction overtakes that of thermal NO reaction as pressure increases. Therefore, it is believed that the enhanced formation rate of NO_x via the nitrous oxide mechanism contributes to the increase in NO_x under elevated pressure.

The flame temperature increases with pressure at a given equivalence ratio, which can enhance NO_x formation. NO_x formation is very sensitive to the temperature as the logarithm of rate constant is inversely proportional to the reciprocal of the temperature. The adiabatic flame temperature for ethanol–air flame varies from 1596 K to 2401 K with the equivalence ratio ranging from 0.3 to 0.82 at an inlet temperature of 873 K under 1 bar. Given the same range of equivalence ratio and inlet temperature, the adiabatic flame temperature for ethanol–air flame varies from 1596 K to 2448 K under 5 bar. The adiabatic flame temperature is calculated in the Equilibrium Reactor model in CHEMKIN. Relevant reaction rates for NO_x formation are expected to be enhanced considerably under elevated pressures due to the strong dependence of rate constants on temperature.

As volumetric flow rate decreases linearly with pressure, it is likely that the increase in residence time also contributes to the increase in NO_x emission under elevated pressure. An uncertainty analysis is performed with CHEMKIN-PRO (version 15113, x64) to reveal the impact of residence time on NO_x formation. Results show that the variance in residence time contributes to 66% of the uncertainty in NO concentration, while the same variance in pressure only contributes to 34% of the uncertainty. As the volumetric flow rate is lowered, the air and fuel jet velocities decrease, which weakens the exhaust gas recirculation, producing a less homogeneous and diluted mixture. This consequently leads to a higher peak temperature, thereby resulting in the increase in NO_x emissions. As discussed in Section 3.3, NO_x emissions decrease with the increasing air jet velocity when the chamber pressure is kept constant, which highlights the impact of velocity. In addition, Kruse et al. [26] studied the impact of pressure on NO_x emissions while maintaining the same jet velocities by changing the nozzle diameter accordingly. NO_x emissions were found to decrease with pressure at constant jet velocities, while they increased with pressure at constant nozzle diameters (decreasing velocities) [26]. Their results indicate that the decreased jet velocity probably is the major contributor for the increase in NO_x emissions as pressure increases [26].

Contradictory results have been reported on pressure dependence of NO_x emission in the literature [31,40–42]. A review on NO_x emission under gas-turbine conditions summarised that NO_x formation was independent of pressure in lean ($\Phi \leqslant 0.6$) turbulent and laminar premixed flames, while NO_x emission increased with pressure at higher equivalence ratios, where the flame temperature was beyond 1900 K [31]. The increasing absolute concentrations of equilibrium O atoms with pressure were thought to be responsible for the increase in NO_x emission [31]. The dependence of NO_x emission on pressure in current experiments is consistent with that reported in this review despite that the critical equivalence ratio in current experiments is shifted to leaner conditions ($\Phi \leqslant 0.4$). In more recent experimental and numerical studies in Jet-Stirred Reactors, a rather moderate decrease in NO_x emission was reported for a premixed and preheated mixture of methane and air with $\Phi = 0.55$ at a constant residence time and flame temperature as pressure increased [40,41]. Biagioli and Güthe [42] performed a numerical study of NO_x formation under fuel lean conditions with pressure ranging from 1 bar to 30 bar. They divided NO_x formation mechanisms into two categories according to the relative chemistry timescale: fast "prompt" NO_x produced within the flamelet region and slow "post-flame" NO_x [42]. They found that "prompt" NO_x dominated the NO_x formation at atmospheric condition, while "post-flame" NO_x became dominant at 30 bar [42]. Given a constant residence time under perfectly premixed conditions, the total NO_x emission under elevated pressure was equal to that at 1 bar at a critical adiabatic flame temperature, and the total NO_x emission under elevated pressure was higher than the atmospheric one as the adiabatic flame temperature rose beyond this critical value [42]. As the "post-flame" NO_x is greatly affected by residence time and fuel–air unmixedness, the critical flame temperature can be shifted [42]. For instance, they found the critical flame temperature at which total NO_x emission at 5 bar was equal to total NO_x emission at 1 bar dropped from 2022 K to 1818 K as the residence time increased from 5 ms to 30 ms [42]. In addition, experimental results from Fric [43] showed that both the temporal and spatial unmixedness lead to an increase in NO_x emission. These results suggest that the conflicting pressure dependence of NO_x may result from differences in flame temperature, residence time and the degree of mixing. These results also show that low-NO_x under elevated pressure is achievable by modifying the operating conditions.

The type of carrier gas shows a strong impact on emissions in this study. Lower NO_x emissions are produced when fuels are carried by nitrogen instead of air. The stoichiometric mixture fraction Z_{st} of ethanol is 0.1 without carrier gas. The use of N_2 as a carrier gas increases Z_{st} to 0.148, while using air as the carrier gas increases it further to 0.15. A previous study has shown that shifting the stoichiometric mixture fraction toward the fuel-rich side through dilution with N_2 or CO_2 shifts the reaction zone to a region with a higher dissipation rate [44]. A higher dissipation rate restrains the formation of flame and NO_x emission [44]. However, the shift in the stoichiometric mixture fraction in the current experiments is relatively small to cause such an effect. Stårner et al. [45] observed that a spray flame with carrier air behaved more like a premixed flame with burning occurring at the jet centreline, while diffusion flame behaviour was observed when nitrogen was used as carrier gas. This has been confirmed by the temperature distribution of a spray flame carried by air with non-linear excitation regime two-line atomic fluorescence imaging (NTLAF) [46]. Noteworthy is that the equivalence ratio of the mixture of carrier air and fuel in the fuel jet in their experiments was around 1.2–3.2 [45]. In addition, there was no recirculation of the exhaust gases to dilute the reactants in their experiments. The equivalence ratio in the mixture of carrier air and ethanol is 15.5 in the current experiments, which indicates that the flame carried by air is unlikely to behave as premixed flame. It is speculated that some parcels of flammable mixture with higher local oxygen concentration formed when air is used as carrier gas, leading to a higher peak temperature, which could be responsible for the increase in NO_x emission. Imaging the distribution of the OH radical should be performed to investigate this hypothesis in future experiments.

5. Conclusions

MILD combustion of prevaporised ethanol, acetone and *n*-heptane was successfully established in a MILD combustor with a reverse-flow configuration over a broad range of equivalence ratios with the chamber pressure ranging from 1 bar to 5 bar. The combustion stability is affected by fuel type, even though similar levels of emissions are measured from different fuels in this particular combustor configuration. It was found that ethanol burns well under the test conditions while combustion of acetone

and *n*-heptane become unstable at higher equivalence ratios and higher pressures. Calculations reveal that the ignition delay is greatly shortened when the chamber pressure increases from 1 bar to 5 bar. This indicates that early ignition is likely to occur before effective mixing, especially for *n*-heptane. In addition to increasing the chemical timescale to improve combustion stability, the flow timescale needs to be decreased to guarantee fast mixing, especially in a high-pressure MILD combustion device, which can be achieved by a high-speed jet.

CO emission does not show a clear dependence on pressure, while NO_x emission increases with pressure. Hence, the joint regime of low CO and low NO_x emission becomes narrower under elevated pressure. The enhanced NO_x formation rate via the nitrous oxide mechanism, the slower mixing, the increased flame temperature and residence time are believed to cause higher NO_x emission as pressure increases. NO_x emission is reduced by increasing the air jet velocity, which is attributed to a more uniform temperature distribution with a lower peak temperature. NO_x emission is reduced when the fuel is carried by nitrogen instead of air, and the reduction is more profound under higher pressures. Further research is required to understand this trend which will help in achieving low NO_x emission from these flames even under elevated pressures.

Acknowledgements

The authors wish to acknowledge the support of The University of Adelaide and Institute for Combustion Technology in RWTH Aachen University. The authors wish to thank the assistance of Veronika Wassmuth in operating the laboratory. This research is funded by the China Scholarship Council and The University of Adelaide through a joint postgraduate scholarship. Funding from the Australian Research Council (ARC) and United States Air Force Asian Office of Aerospace Research and Development (AOARD) is gratefully acknowledged.

References

[1] Wünning J, Wünning J. Flameless oxidation to reduce thermal NO-formation. Prog Energy Combust Sci 1997;23(1):81–94.
[2] Sánchez M, Cadavid F, Amell A. Experimental evaluation of a 20 kW oxygen enhanced self-regenerative burner operated in flameless combustion mode. Appl Energy 2013;111:240–6.
[3] Rao A, Levy Y. A new combustion methodology for low emission gas turbine engines. In: 8th International symposium on high temperature air combustion and gasification, Poznań, Poland; 2010. p. 177–85.
[4] Derudi M, Rota R. Experimental study of the mild combustion of liquid hydrocarbons. Proc Combust Inst 2011;33(2):3325–32.
[5] Medwell PR, Kalt PAM, Dally BB. Imaging of diluted turbulent ethylene flames stabilized on a jet in hot coflow JHC burner. Combust Flame 2008;152(1):100–13.
[6] Arghode VK, Khalil AEE, Gupta AK. Fuel dilution and liquid fuel operational effects on ultra-high thermal intensity distributed combustor. Appl Energy 2012;95:132–8.
[7] Weber R, Orsino S, Lallemant N, Verlaan A. Combustion of natural gas with high-temperature air and large quantities of flue gas. Proc Combust Inst 2000;28(1):1315–21.
[8] Cavaliere A, de Joannon M. Mild combustion. Prog Energy Combust Sci 2004;30(4):329–66.
[9] Arghode VK, Gupta AK, Bryden KM. High intensity colorless distributed combustion for ultra low emissions and enhanced performance. Appl Energy 2012;92:822–30.
[10] Sadanandan R, Lückerath R, Meier W, Wahl C. Flame characteristics and emissions in flameless combustion under gas turbine relevant conditions. J Propul Power 2011;27(5):970–80.
[11] Li P, Dally BB, Mi J, Wang F. MILD oxy-combustion of gaseous fuels in a laboratory-scale furnace. Combust Flame 2013;160(5):933–46.
[12] Medwell PR, Kalt PAM, Dally BB. Reaction zone weakening effects under hot and diluted oxidant stream conditions. Combust Sci Technol 2009;181(7):937–53.
[13] Effuggi A, Gelosa D, Derudi M, Rota R. Mild combustion of methane-derived fuel mixtures: natural gas and biogas. Combust Sci Technol 2008;180(3):481–93.
[14] Szegö GG, Dally BB, Nathan GJ. Operational characteristics of a parallel jet MILD combustion burner system. Combust Flame 2009;156(2):429–38.
[15] Arghode VK, Gupta AK. Investigation of reverse flow distributed combustion for gas turbine application. Appl Energy 2011;88(4):1096–104.
[16] Cavigiolo A, Galbiati MA, Effuggi A, Gelosa D, Rota R. Mild combustion in a laboratory-scale apparatus. Combust Sci Technol 2003;175(8):1347–67.
[17] Arghode VK, Gupta AK. Investigation of forward flow distributed combustion for gas turbine application. Appl Energy 2011;88(1):29–40.
[18] Rodrigues HC, Tummers MJ, van Veen EH, Roekaerts DJ. Spray flame structure in conventional and hot-diluted combustion regime. Combust Flame 2015;162(3):759–73.
[19] Weber R, Smart JP, Kamp Wv. On the (MILD) combustion of gaseous, liquid, and solid fuels in high temperature preheated air. Proc Combust Inst 2005;30(2):2623–9.
[20] Reddy VM, Biswas P, Garg P, Kumar S. Combustion characteristics of biodiesel fuel in high recirculation conditions. Fuel Process Technol 2014;118:310–7.
[21] Reddy VM, Katoch A, Roberts WL, Kumar S. Experimental and numerical analysis for high intensity swirl based ultra-low emission flameless combustor operating with liquid fuels. Proc Combust Inst 2015;35(3):3581–9.
[22] Khalil AE, Gupta AK. Clean combustion in gas turbine engines using Butyl Nonanoate biofuel. Fuel 2014;116:522–8.
[23] Medwell PR, Dally BB. Effect of fuel composition on jet flames in a heated and diluted oxidant stream. Combust Flame 2012;159(10):3138–45.
[24] Reddy VM, Kumar S. Development of high intensity low emission combustor for achieving flameless combustion of liquid fuels. Propul Power Res 2013;2(2):139–47.
[25] Reddy VM, Sawant D, Trivedi D, Kumar S. Studies on a liquid fuel based two stage flameless combustor. Proc Combust Inst 2013;34(2):3319–26.
[26] Kruse S, Kerschgens B, Berger L, Varea E, Pitsch H. Experimental and numerical study of MILD combustion for gas turbine applications. Appl Energy 2015;148:456–65.
[27] Varea E, Kruse S, Pitsch H, Albin T, Abel D. Actuation studies for active control of MILD combustion for gas turbine application. In: ASME Turbo Expo 2014: Turbine Technical Conference and Exposition, vol. 4B. Düsseldorf, Germany: Combustion, Fuels and Emissions, American Society of Mechanical Engineers; 2014. p. GT2014–27138.
[28] O'Loughlin W, Masri A. A new burner for studying auto-ignition in turbulent dilute sprays. Combust Flame 2011;158(8):1577–90.
[29] Varea E, Berger L, Kruse S, Pitsch H. Entrainment rate and mixing process in a confined counterflow reactor. In: Proceedings of the European combustion meeting; 2015.
[30] Electronic code of federal regulations. <http://www.ecfr.gov/cgi-bin/ECFR?SID=242f99cc8c3086c21fd59d5256ce127e&page=browse>; 2014 [access 22.08.14].
[31] Correa SM. A review of NO_x formation under gas-turbine combustion conditions. Combust Sci Technol 1993;87(1–6):329–62.
[32] Turns SR. An introduction to combustion. New York: McGraw-Hill; 1996.
[33] Galletti C, Parente A, Tognotti L. Numerical and experimental investigation of a mild combustion burner. Combust Flame 2007;151(4):649–64.
[34] Liu S, Hewson JC, Chen JH, Pitsch H. Effects of strain rate on high-pressure nonpremixed *n*-heptane autoignition in counterflow. Combust Flame 2004;137(3):320–39.
[35] Marinov NM. A detailed chemical kinetic model for high temperature ethanol oxidation. Int J Chem Kinet 1999;31:183–220.
[36] Pichon S, Black G, Chaumeix N, Yahyaoui M, Simmie J, Curran H, et al. The combustion chemistry of a fuel tracer: measured flame speeds and ignition delays and a detailed chemical kinetic model for the oxidation of acetone. Combust Flame 2009;156(2):494–504.
[37] Mehl M, Pitz WJ, Westbrook CK, Curran HJ. Kinetic modeling of gasoline surrogate components and mixtures under engine conditions. Proc Combust Inst 2011;33(1):193–200.
[38] Smith GP, Golden DM, Frenklach M, Moriarty NW, Eiteneer B, Goldenberg M, et al. <http://www.me.berkeley.edu/gri_mech/> [accessed 08.10.14].
[39] Warnatz J, Maas U, Dibble RW. Combustion: physical and chemical fundamentals, modeling and simulation, experiments, pollutant formation. Springer; 2006.
[40] Shuman TR. NO_x and CO formation for lean-premixed methane–air combustion in a jet-stirred reactor operated at elevated pressure. PhD thesis, University of Washington; 2000.
[41] Rutar T, Malte PC. NO_x formation in high-pressure jet-stirred reactors with significance to lean-premixed combustion turbines. J Eng Gas Turbines Power 2002;124(4):776–83.
[42] Biagioli F, Güthe F. Effect of pressure and fuel–air unmixedness on NO_x emissions from industrial gas turbine burners. Combust Flame 2007;151(1):274–88.
[43] Fric TF. Effects of fuel–air unmixedness on NO_x emissions. J Propul Power 1993;9(5):708–13.
[44] Dally B, Riesmeier E, Peters N. Effect of fuel mixture on moderate and intense low oxygen dilution combustion. Combust Flame 2004;137(4):418–31.
[45] Stärner SH, Gounder J, Masri AR. Effects of turbulence and carrier fluid on simple, turbulent spray jet flames. Combust Flame 2005;143(4):420–32.
[46] Medwell PR, Masri AR, Pham PX, Dally BB, Nathan GJ. Temperature imaging of turbulent dilute spray flames using two-line atomic fluorescence. Exp Fluids 2014;55(11):1–11.

Chapter 5

The Transition of Ethanol Flames from Conventional to MILD Combustion

Statement of Authorship

Title of Paper	The transition of ethanol flames from conventional to MILD combustion
Publication Status	☑ Published ☐ Accepted for Publication ☐ Submitted for Publication ☐ Unpublished and Unsubmitted w ork w ritten in manuscript style
Publication Details	J. Ye, P. R. Medwell, B. B. Dally, M. J. Evans, The transition of ethanol flames from conventional to MILD combustion, Combust. Flame 171 (2016) 173-184.

Principal Author

Name of Principal Author (Candidate)	Jingjing Ye		
Contribution to the Paper	I co-designed the experiments, including choosing different operating parameters and performing calculations for various experimental cases. I setup the experiments with co-authors. I undertook the experiments, and performed digital photography and imaging of OH* chemiluminescence with two of my co-authors. I processed, analysed, and interpreted all the experimental data. I also planned and performed all the calculations with the OPPDIF code in the Chemkin software to assist the interpretation of the experimental data. I performed an analysis of the experimental and calculation results. The analysis was presented in text or figures by me. I integrated all the analysis and wrote the manuscript. I also acted as the corresponding author, and responded to the reviewers' and the editor's comments and recommendations.		
Overall percentage (%)	75		
Certification:	This paper reports on original research I conducted during the period of my Higher Degree by Research candidature and is not subject to any obligations or contractual agreements with a third party that would constrain its inclusion in this thesis. I am the primary author of this paper.		
Signature	Digitally signed by JINGJING YE Date: 2017.06.03 10:07:14 +09'30'	Date	03-June-2017

Co-Author Contributions

By signing the Statement of Authorship, each author certifies that:

i. the candidate's stated contribution to the publication is accurate (as detailed above);

ii. permission is granted for the candidate in include the publication in the thesis; and

iii. the sum of all co-author contributions is equal to 100% less the candidate's stated contribution.

Name of Co-Author	Paul R. Medwell		
Contribution to the Paper	This co-author co-designed the experiments and co-supervised the development of the work. This co-author also provided assistance and supervision during the experimental setup and data collection. This co-author helped to evaluate and edit the manuscript.		
Signature	Paul Medwell 2017.06.03 10:45:10 +09'30'	Date	03-JUN-2017

Name of Co-Author	Bassam B. Dally		
Contribution to the Paper	This co-author co-supervised the development of the work. This co-author helped to evaluate and edit the manuscript.		
Signature	Digitally signed by Bassam Dally Date: 2017.06.05 11:31:18 +09'30'	Date	05-June-2017

Name of Co-Author	Michael J. Evans		
Contribution to the Paper	This co-author co-designed and undertook experiments. This co-author also helped to evaluate and edit the manuscript.		
Signature	Digitally signed by Michael Evans Date: 2017.06.04 18:37:02 +09'30'	Date	04-June-2017

Please cut and paste additional co-author panels here as required.

Combustion and Flame 171 (2016) 173–184

Contents lists available at ScienceDirect

Combustion and Flame

journal homepage: www.elsevier.com/locate/combustflame

The transition of ethanol flames from conventional to MILD combustion

Jingjing Ye*, Paul R. Medwell, Bassam B. Dally, Michael J. Evans

School of Mechanical Engineering, The University of Adelaide, Adelaide, South Australia 5005, Australia

ARTICLE INFO

Article history:
Received 4 January 2016
Revised 28 February 2016
Accepted 24 May 2016

Keywords:
MILD combustion
Prevaporised ethanol
Carrier gas

ABSTRACT

The present paper is focused on prevaporised ethanol flames in the transition from conventional combustion to the MILD combustion regime. Photographs and imaging of OH* chemiluminescence reveal a distinctive flame structure when ethanol carried by air burns in a 3% O_2 coflow (typical of MILD combustion), differing from that at higher oxygen levels. In comparison to flames carried by air in a 9% O_2 coflow, the spatial gradient and the peak in the OH* signal profile are significantly reduced in the 3% O_2 coflow, indicating a more uniform distribution of heat release and temperature. The use of N_2 as a carrier gas renders the OH* profile for the 6% O_2 coflow case similar to that of flames carried by air in the 3% O_2 coflow. The experimental results indicate a transition from conventional combustion to MILD combustion with the decrease of coflow O_2 level and/or the use of N_2 as a carrier gas. Calculations reveal that a substantial drop in the peak heat release rate and/or overall net heat release rate might contribute to the lack of luminosity of flames in the 3% O_2 coflow, suggesting a need for threshold values of these two in defining MILD combustion. A series of laminar flame calculations are performed to identify the MILD combustion regime based on the absence of a negative heat release region. The absence of a negative heat release region is found to be strain rate dependent at a given temperature and O_2 level of the oxidant stream. This is mainly a result of the enhanced transportation of O_2 across the reaction zone at a higher strain rate. At low strain rates, the negative heat release region is more likely to disappear in a 3% O_2 oxidant flow due to a combination of low flame temperature and high availability of O_2.

1. Introduction

A large body of work has been published on Moderate or Intense Low-oxygen Dilution (MILD) combustion due to its capacity to reduce emissions and maintain high thermal efficiency [1–5]. In practice, MILD combustion is achieved through enhanced mixing of hot exhaust gases with reactants, which creates a hot oxygen-deficient environment. According to a MILD combustion regime map summarised by Rao and Levy [6], the local oxygen concentration is around 3–12%, and the temperature of the reactants is above the autoignition temperature. This environment creates a semi-uniform temperature distribution with a lower peak flame temperature, which significantly reduces the emissions of NO_x and soot [5,7,8]. These characteristics of MILD combustion are highly desired in many industrial applications. For instance, a larger radiating volume and a higher net radiation flux, resulting from volumetric reactions under MILD combustion conditions, are favoured in furnaces and boilers [2]. This high radiant flux is not necessarily advantageous when it comes to application in gas turbines, where excessive heating of the walls may lead to material degradation. However, due to a semi-uniform temperature distribution with a lower peak temperature under MILD combustion conditions, a higher efficiency can be achieved by raising the mean temperature of products, while maintaining low NO_x formation and the durability of gas-turbine components.

A configuration of a jet in a hot and diluted coflow is commonly adopted to facilitate the experimental study of MILD combustion as the temperature and oxygen concentration of the coflow can be adjusted independently to mimic MILD combustion conditions [9,10]. However, several differences in the flame structure and behaviour on simple gaseous fuels were reported in previous studies [7,9–14], even though those experiments were all defined as MILD combustion based on the regime map by Rao and Levy [6]. For instance, the liftoff heights of jet flames in various hot and diluted coflow responded differently to changes in the same parameter, indicating differences in the jet stabilisation mechanism [10–12]. Particularly, Oldenhof et al. [10,11] reported that the liftoff height initially reduced with increasing jet velocity or Reynolds number in a hot coflow with 7.6–8.8% O_2 by mass, which was consistent with experimental studies in the Jet in Hot Coflow (JHC) burner [7].

* Corresponding author.
E-mail address: jingjing.ye01@adelaide.edu.au (J. Ye).

http://dx.doi.org/10.1016/j.combustflame.2016.05.020
0010-2180/

These measurements contradict measurements of liftoff heights reported by Cabra et al. [12], which is probably caused by a higher O_2 level in the coflow ($X_{O_2} \geq 12\%$). Another phenomenon observed in flames burning in the JHC burner, differing from conventional lifted flames, was that liftoff heights increased with coflow temperature or oxygen level [13]. This unusual behaviour was attributed to the transition from MILD combustion regime to the conventional combustion regime [13]. Indeed, significant differences in the jet stabilisation mechanism occur as coflow O_2 concentration changes. Gordon et al. [14] proposed that lifted flames in a hot coflow are stabilised by a build-up of ignition kernels. They classified the evolution of autoignition for methane flames in a hot coflow with 11–12% O_2 by volume into three stages: CH_2O only, OH formation, CH_2O consumption and formation of a steady lifted flame [14]. In particular, CH_2O reached its maximum before ignition, then it was consumed after ignition [14]. However, the formation of OH peaked at ignition, and those peaks were maintained in the lifted flame [14]. When the mole fraction of O_2 was reduced to 3%, CH_2O was found to play the same role as an ignition precursor, while an OH tail was found to extend to the jet exit plane, indicating an attached flame [7]. Similar phenomenon was reported in a numerical study by Sidey et al. [15]. They found that as the mixture became more diluted, the initial pre-ignition reaction merged with the primary ignition reaction such that the sharp rise in the temperature profile disappeared [15].

To understand the transition from conventional combustion to MILD combustion, Medwell et al. [13] performed comprehensive experiments on methane- and ethylene-based flames, including a wide range of jet Reynolds number, coflow oxygen concentration and temperature. The present study is a follow-up study on this topic, which is part of a larger programme. Instead of alkanes, the present study investigates ethanol flames. Ethanol can be produced from renewable energy sources, such as sugar-cane and corn. It has a low tendency to generate soot and particulate matter. In addition, ethanol can be burnt at very lean conditions because of its high flame speed [16], which produces a lower flame temperature, thereby reducing NO_x and CO emissions. Moreover, a previous study by Rodrigues et al. [17] found that the occurrence of high ethanol flame temperature was significantly suppressed under MILD combustion conditions in comparison to that in conventional combustion conditions, which could help abate NO_x and CO emissions further.

In the present study, ethanol is prevaporised before injection to avoid the complicated coupling effects of fuel chemistry and spray characteristics. In this case, heated gas is required as a carrier to help deliver prevaporised ethanol and prevent it from condensing. The choice of carrier gas, such as air or N_2, has been reported to affect the temperature distribution and the flame structure in spray burners [18,19], and change the NO_x formation in a reverse-flow MILD combustor [20]. In addition, previous work [21] has shown that the enhanced O_2 diffusion towards the fuel-rich side through "reaction zone weakening" is a key feature of MILD combustion flames, leading to an increasing formation of important intermediates. The build-up of those intermediates is responsible for the stabilisation of the flames [21]. Adding a small amount of O_2 to the fuel stream is suspected to produce similar effects. Although N_2 is unlikely to be used for fuel atomisation or delivery in industrial applications, part of the hot exhaust gases are expected to provide the preheating and dilution of liquid fuels when MILD combustion of liquid fuels is commercialised. The exhaust gas is composed of oxidiser and inert, which is represented by air and N_2, respectively. It is important to understand the impact of those species in the exhaust gas. By switching air and N_2 alternatively as a carrier gas in a JHC burner, this issue can be explored in a controlled and simplified environment.

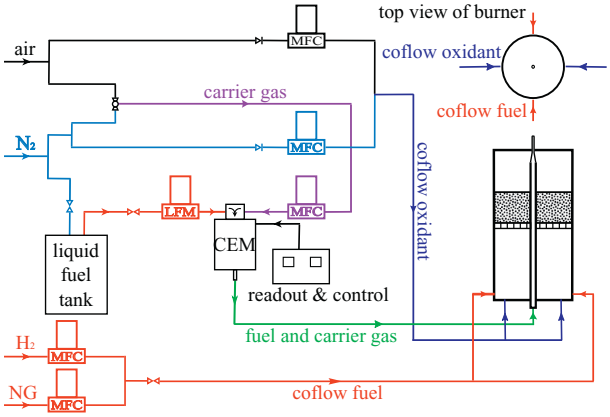

Fig. 1. Experimental Setup: CEM is the Controlled Evaporator and Mixer, MFC is the mass flow controller for gases, and LFM is the liquid flow meter.

In summary, this paper aims to improve the understanding of the transition from conventional combustion to MILD combustion. Due to the potential advantages of applying MILD combustion to ethanol flames, this paper is focused on the transition of prevaporised ethanol flames in a hot diluted coflow, the understanding of which can provide guidance to establish MILD combustion of ethanol when it is commercialised. Images of OH^* chemiluminescence are collected from prevaporised ethanol flames issuing into a JHC burner to reveal the impact of carrier gas, jet velocity and coflow oxygen concentration. A series of laminar flame calculations are performed to provide additional insights into the experimental observations.

2. Experimental details

2.1. Experimental setup and operating conditions

The basic configuration and operation of this JHC burner shown in Fig. 1 are the same as a previous study [7]. The JHC burner consists of an air-cooled central fuel jet (ID = 4.6 mm) in a coflow of hot exhaust products from a secondary porous-bed burner (ID = 82 mm) located 90 mm upstream of the jet exit plane. The hot coflow is produced from the combustion of a lean mixture of natural gas, air, H_2 and N_2. The mole fractions of natural gas, air, H_2 and N_2 are manipulated to generate 3–11% oxygen by volume in the hot coflow, while the C/H ratio is kept constant. The temperature for the various coflow conditions (T_{coflow}) varies from 1250 K to 1385 K. To obtain fully developed turbulent pipe flow, the length of the central fuel jet is more than 100 times the jet diameter. The burner is wrapped with ceramic fibre insulation to minimise heat losses and maintain a constant temperature of the coflow.

As shown in Fig. 1, ethanol is heated and mixed with carrier gas in a Controlled Evaporator and Mixer (CEM). The temperature of the heater inside the CEM is set by the Bronkhorst control unit, which also controls the mass flow rates of ethanol and carrier gas. The preheat temperature is set to 413 K, which is higher than the boiling point of ethanol to prevent condensation along the pipeline. After prevaporisation, the mixture of ethanol and carrier gas is fed into the JHC burner via the central fuel jet. Note that when switching between air and N_2 as a carrier gas, the flow rates of ethanol and carrier gas are kept constant. For the baseline case (F10-A1), the jet Reynolds number and the bulk jet velocity are kept around 10,000 and 44 m/s, respectively. Due to the lower viscosity and density of N_2, the jet Reynolds number of ethanol carried by N_2 is 1% higher than that of ethanol carried by air, while

Table 1
List of fuel jet conditions: $X_{carrier}$ indicates the mole fraction of carrier gas in the fuel jet.

	Re_{jet}	Carrier gas	$X_{carrier}$
F10-A1	10,000	Air	0.59
F30-A1	30,000	Air	0.59
F10-A3	10,000	Air	0.67
F10-N3	10,000	N_2	0.67

Table 2
Stoichiometric mixture fraction (Z_{st}) for various fuel jets in the coflow with 3–11% O_2 by volume.

O_2 in the coflow (%)	F10-A1	F10-A3	F10-N3
3	0.0342	0.0427	0.0362
6	0.0669	0.0828	0.0706
9	0.0964	0.1184	0.1015
11	0.1138	0.1392	0.1198

the bulk jet velocity is 2% higher. Table 1 shows all the fuel jet conditions investigated in the present paper. As shown in Table 1, low (F10-A1) and high jet Reynolds number cases (F30-A1) are performed to investigate the impact of jet Reynolds number. Cases denoted by F10-A3 and F10-N3 are performed to study the impact of carrier gas. The mole fraction of carrier gas in the fuel jet is 0.67 in F10-A3 and F10-N3 cases, which is higher than that in the baseline case to magnify the differences caused by carrier gases. It is worth mentioning that though air is added to the fuel jet, those flames are not partially premixed flames. A plethora of literature, for example, a study by Stårner et al. [22], has shown that flames with air dilution of the fuel up to 77% by volume behave like non-premixed flames. Hence, the comparison between these different carrier gases cases is valid. In addition, it has been validated by simulations that no reactions occur before the fuel stream is fed to the burner. Table 2 shows the stoichiometric mixture fraction (Z_{st}) for a given combination of coflow and fuel jet conditions.

Imaging of the flames is achieved both through conventional photography and OH* chemiluminescence, which is detected with an electronically gated pco.pixelfly camera equipped with a Lambert Instruments intensifier. The camera system is coupled to a 50 mm f/3.5 UV transmissive lens and a 310 nm bandpass optical filter with a bandwidth of 10 nm. The photographs of the flames are taken using a Canon EOS 60D SLR camera with a standard 50 mm f/1.8 lens.

2.2. The use of OH* chemiluminescence in MILD combustion

The chemiluminescence of OH* is a natural emission of light within the flame when excited OH relaxes from an upper electronic state to a lower electronic state. It is known that OH* has a short lifetime and its formation requires high energy [23]. Previous studies [24,25] have shown that the intensity of OH* chemiluminescence can be used as an indicator of the reaction zone and the heat release rate in lean premixed flames.

In order to interpret the intensity of OH* chemiluminescence confidently under MILD combustion conditions, laminar flame calculations are performed for ethanol flames with the OPPDIF code in the Chemkin software. The full multi-component formulation as well as thermal diffusion are included in calculations. As most previous studies using OH* imaging were performed for premixed flames [24,25], a non-premixed case with pure ethanol in the fuel stream is included in calculations to account for non-premixed flames in the current experiments. A partial premixed case is performed for comparison, in which the fuel jet is modelled as 50% of ethanol and 50% of air (by volume). The stoichiometric mixture fraction in the non-premixed case and partially premixed case is 0.0164 and 0.0283, respectively. Calculations are performed for various oxygen concentrations and inlet velocities (strain rates), which show the same trend. Hence, only results for flames in the oxidant stream with 3% O_2 at a fuel inlet velocity of 0.8 m/s and an oxidiser inlet velocity of 1.68 m/s are presented here. Note that the velocities of the two opposed flows are set in a way that their jet momentum flow rates balance at the midpoint between the two inlets in all the laminar flame calculations in this paper. The distance between the two opposed nozzles is 20 mm. The chemical kinetic mechanism used includes the ethanol chemical kinetic mechanism developed by Marinov [26] and OH* kinetics provided in [27] and [28].

Figure 2 displays the profiles of normalised temperature, number density of OH* (n_{OH^*}) and heat production rate (HPR) in mixture fraction space for ethanol flames burning in a 1250-K oxidiser, in which the location of the stoichiometric mixture fraction is indicated by a vertical dotted line. Note that a previous study found that the number density of OH* obtained from laminar flame calculations agreed well with the measured chemiluminescence of OH* [29]. The heat production rate here is defined as the net heat production rate from gas-phase reactions per unit volume. It can be seen that OH* and most of the heat is produced within the high temperature region, which falls on the oxidiser side. In addition, the location of the peak n_{OH^*} and HPR closely matches with the location of peak flame temperature. The correlation between OH* and HPR was also reported in a simulation of non-premixed methane flames in hot diluted coflow [30]. However, it is shown in Fig. 3 that the location of peak n_{OH^*} fails to coincide with the location of peak n_{OH}. This is supported by OH-PLIF measurements in MILD combustion of methane in a cross-flow configuration, which demonstrates that OH was formed in the absence of heat release, as indicated by the lack of OH* chemiluminescence [31]. The phenomena described above are observed in both the partially premixed and non-premixed cases. Therefore, OH* chemiluminescence can be used as an indicator of high temperature and heat production rate region, though it does not necessarily correlate with the number density of OH particularly well.

3. Results

3.1. Impact of coflow oxygen concentration

To investigate the impact of coflow oxygen concentration on the transitional behaviour, experiments are performed with ethanol carried by air (F10-A1) in a 1250-K coflow. Figure 4 displays photographs of the ethanol flames carried by air under the four coflow conditions (3, 6, 9, and 11% O_2 by volume). The bottom edge of all the photographs coincides with the jet exit plane. All the photographs in this section are taken with an ISO sensitivity of 1600, exposure time of 1 ms and an f-number of 2.

The surrounding air entrainment has an effect on the flame above 100 mm downstream the jet exit plane ($X/D = 22$, where X is the axial distance above the jet and D is the jet diameter) [32]. The impact of cold air entrainment on the reaction zone has been discussed in a previous study [32], hence the present study only focuses on the region shielded by the hot coflow. Flames in the 9% O_2 and 11% O_2 coflow are very similar, which appear as typical lifted jet flames. Those flames in 9% O_2 and 11% O_2 coflow show a clear flame base, and a continuous flame sheet downstream of the base. The luminosity of flames, within the region controlled by the hot coflow, reduces significantly with coflow oxygen level. Particularly, the luminosity of ethanol flame in the 3% O_2 coflow is so low that it appears lifted in the photograph. However, a previous study on the same JHC burner [7] has reported the existence of OH and CH_2O kernels in ethylene flames in a 3% O_2 coflow, though photographs of those flames also suggested that they were

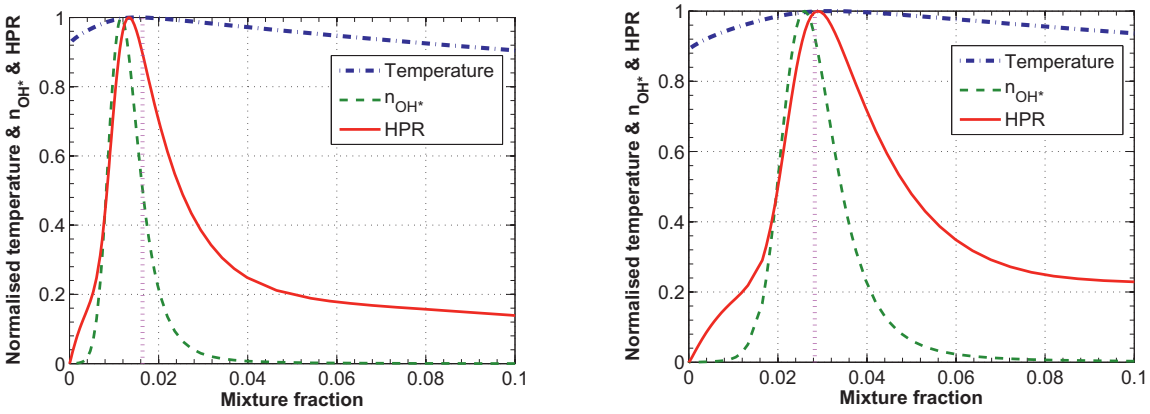

(a) non-premixed case (b) partially premixed case

Fig. 2. Normalised temperature, number density of OH^* (n_{OH^*}) and heat production rate (HPR) as a function of mixture fraction for ethanol flames in a 1250-K oxidiser with 3% O_2: (a) non-premixed case; (b) partially premixed case. The vertical dotted line indicates the location of the stoichiometric mixture fraction.

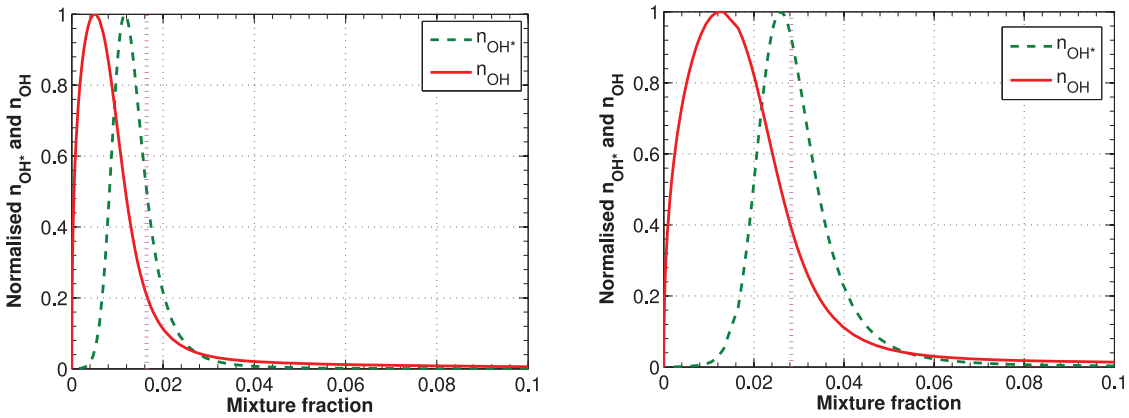

(a) non-premixed case (b) partially premixed case

Fig. 3. Normalised number density of OH^* (n_{OH^*}) and OH (n_{OH}) as a function of mixture fraction for ethanol flames in a 1250-K oxidiser with 3% O_2: (a) non-premixed case; (b) partially premixed. The vertical dotted line indicates the location of the stoichiometric mixture fraction.

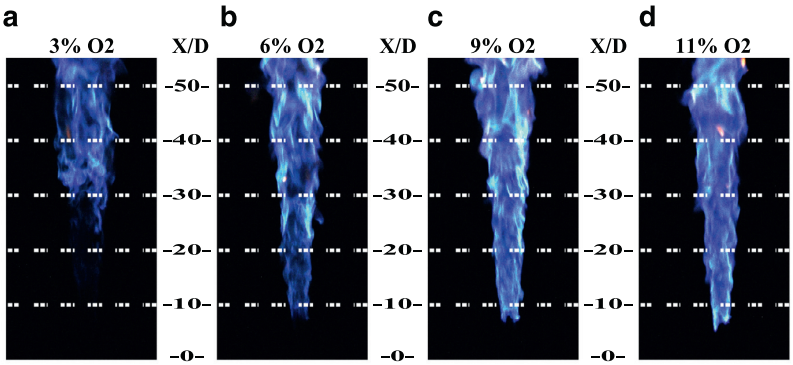

Fig. 4. Photographs of ethanol flames carried by air (F10-A1) at a 1250-K coflow with 3–11% O_2 by volume. The region shielded by coflow is up to $X/D = 22$, where X is the axial distance above the jet and D is the jet diameter.

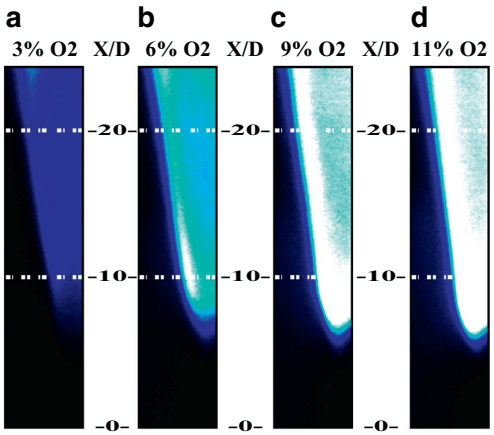

Fig. 5. Averaged OH* images (left-hand side of jet centreline) of ethanol flames carried by air (F10-A1) at a 1250-K coflow with 3–11% O_2 by volume.

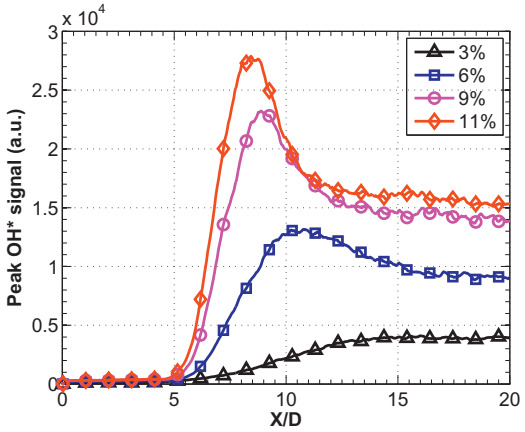

Fig. 6. The peak OH* signal from ethanol flames carried by air (F10-A1) as a function of X/D in the coflow with 3%, 6%, 9% and 11% O_2 by volume.

lifted. In addition, the detection of OH* chemiluminescence in the apparently lifted region ($X/D < 20$) of ethanol flames in the current experiments suggest reactions in fact occurs, which is shown in Fig. 5. The lack of luminosity is in line with the common observation that MILD combustion is "flameless" [2,5,33]. The flame base in the 6% O_2 coflow is less clear in comparison to that in the 9% O_2 coflow, though it is much more discernible than that in the 3% O_2 coflow.

The differences in the flame structure under various coflow conditions are also observed in OH* images. Figure 5 displays the OH* chemiluminescence images. The intensity of the OH* chemiluminescence from ethanol flames in a 3% O_2 coflow is fairly weak, and it gradually reduces towards the jet exit plane. However, a clear base is discernible for flames in 9% O_2 and 11% O_2 coflow. Figure 6 presents the peak OH* signal for various coflow conditions. The peak OH* signal presented refers to the maximum OH* signal at a given height in the averaged image after background correction, which is in arbitrary units.

The intensity of OH* chemiluminescence in the flame increases significantly with the coflow oxygen level. This observation is different from a previous study on MILD combustion in jets in crossflow [31], which reported that the oxygen level had little impact on the intensity of OH* chemiluminescence. However, these two

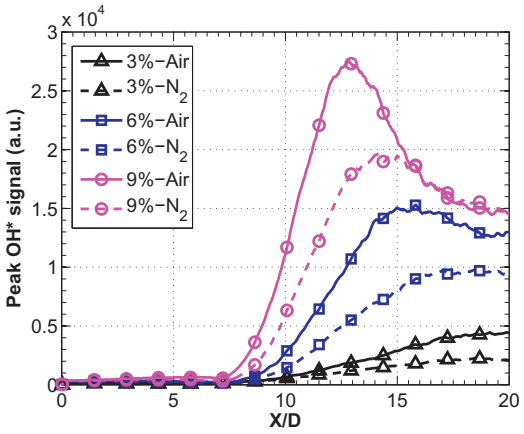

Fig. 7. The peak OH* signal from ethanol flames carried by air (F10-A3) or N_2 (F10-N3) as a function of X/D in the coflow with 3%, 6% and 9% O_2 by volume.

findings are not contradictory as at a lower oxygen level, the adiabatic flame temperature of the coflow was increased in the previous study rather than being kept constant. The build-up of OH* also changes significantly with the coflow oxygen level. For flames carried by air in the 9% and 11% O_2 coflow, three distinguishable regions are formed: in the first region no chemiluminescence is produced; in the second region a rapid production of OH* occurs, where the intensity of OH* chemiluminescence peaks; in the third region a decline in the intensity of OH* chemiluminescence is apparent. However, in a 3% O_2 coflow, there is neither a rapid build-up of OH* nor a decrease in the intensity of OH* chemiluminescence. Instead, the intensity of OH* chemiluminescence increases gradually with the axial distance in the 3% O_2 coflow. This suggests that the flame temperature becomes more spatially distributed in a more diluted coflow. Moreover, heat is produced more distributively in the 3% O_2 coflow due to the close correlation of OH* and heat production rate. The OH* profile for flames in the 6% O_2 coflow show features in between the 3% O_2 coflow and the 9% O_2 coflow. Due to the distributed nature of MILD combustion, the OH* profile in the 6% O_2 coflow signals a transition from MILD combustion to conventional combustion, which is consistent with experimental observation in the previous study of gaseous fuels [13].

3.2. Impact of carrier gas

In order to investigate the impact of carrier gas, air or nitrogen is used as a carrier gas to deliver prevaporised ethanol. The mole fraction of carrier gas in the fuel jet is 0.67 in this set of experiments (F10-A3/F10-N3). Figure 7 presents the peak OH* signal against X/D for various coflow conditions. Given the same coflow condition, the intensity of OH* chemiluminescence is higher when the flame is carried by air. In addition, the spatial gradient of OH* in the axial direction is greater when carrier air is used instead of N_2.

As described in Section 3.1, the OH* profile changes significantly with the coflow oxygen level. The intensity of OH* chemiluminescence increases gradually with the axial distance in the 3% O_2 coflow, while a peak in OH* is observed in the 6% O_2 coflow when air is used as a carrier gas. The peak in the OH* intensity disappears when N_2 is used as a carrier gas instead of air in the 6% O_2 coflow as shown in Fig. 7. Despite the higher (6%) coflow oxygen level, flames carried by N_2 behaves closer to flames issuing into a 3% O_2 coflow. Hence, the use of N_2 as a carrier gas produces a similar impact to diluting the coflow, which also leads to a more

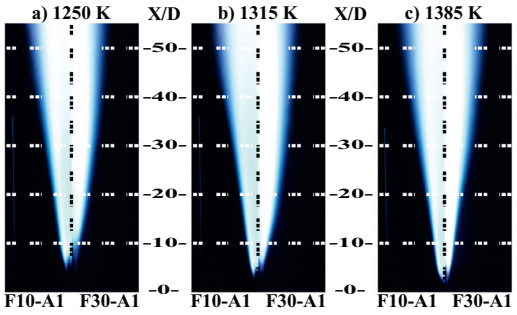

Fig. 8. Photographs of ethanol flames carried by air with low (left:F10-A1) and high jet velocities (right:F30-A1) in 9% O_2 coflow with the coflow temperature varying from 1250 K to 1385 K.

uniform thermal field. The stoichiometric mixture fraction (Z_{st}) is calculated to be 0.0706 for ethanol flames carried by N_2 in a 6% O_2 coflow, while it is 0.0828 in the flames carried by air. It is suspected that the more uniform OH* distribution is not only caused by the fuel dilution effect, but also caused by the actual changes in the flame structure, which will be discussed later. It is worth noting that the instantaneous OH* images display the same trends mentioned above for the averaged images, despite the turbulent fluctuations in the flames.

3.3. Impact of jet velocity

To investigate the impact of jet velocity on lifted flames in a hot diluted coflow, experiments are performed using ethanol with two jet velocities in 9% O_2 coflow with the coflow temperature varying from 1250 K to 1385 K. Figure 8 shows ethanol flames carried by air at various coflow conditions with low (left:F10-A1) and high jet velocities (right:F30-A1). All the photographs are taken with an ISO sensitivity of 1600, exposure time of 4 s and an f-number of 16. The low jet velocity is 44 m/s, while the high jet velocity is 112 m/s. The bulk jet Reynolds numbers for low velocity case and high velocity case are 10,000 and 30,000, respectively. The Reynolds number does not increase proportionally with the jet velocity as the CEM fails to maintain the jet temperature at 413 K due to the higher flow rate. All the ethanol flames shown here are blue in colour. No smoke or particulates are observed even in a 1385-K coflow during the experiments, suggesting the absence of soot particulates. This is consistent with the MILD combustion characteristics, where the distributed reaction zone suppresses soot production. Neither the flame shape nor the luminosity changes with increasing jet velocity. Despite the much higher velocity, the liftoff heights do not change significantly either. Specifically, the ethanol flame in the 1250-K coflow is slightly more visually lifted at the higher jet velocity, while the differences in the liftoff heights are negligible in the hotter coflows. A previous study on this burner with methane- and ethylene- based fuels has also reported minor impact of jet Reynolds number on the liftoff height [13].

The experimental results show an unusual relationship between liftoff heights and jet velocity/Reynolds number for flames in the JHC burner. For a cold-fuel-hot-oxidant configuration, a large body of work reported that autoignition occurs at the most reactive mixture fraction (Z_{MR}) instead of the stoichiometric mixture fraction [34]. The existence of the most favourable mixture fraction Z_{MR} for combustion results from the balance between high temperature at low mixture fraction, and high fuel concentration at high mixture fraction [34]. The ignition delay time is largely determined by the minimum value of the scalar dissipation rate along the most-reactive isolevel, and the first ignition kernel always occurs at the position with the minimum scalar dissipation rate along this isolevel [35,36]. The minimum scalar dissipation rate was found to be independent of the Reynolds number [35,36]. Several competing effects on ignition are expected to happen at an increasing turbulence level. The autoignition can be prolonged due to higher mean scalar dissipation rates. However, a low local scalar dissipation rate is more likely to occur due to the enhanced fluctuation in the scalar dissipation rate [34]. Meanwhile, an enhanced mixing of reactants at the shear layer can accelerate the ignition [7]. The nearly constant lift-off heights at different jet Reynolds number are likely to be the combined results of all those possibilities due to the existence of the hot oxidiser.

4. Discussion

Experimental results suggest a transition from conventional combustion to MILD combustion as the coflow O_2 mole fraction drops from 9% to 3%. In order to identify the transition boundary with confidence, differences between these flames should be carefully examined according to the definitions and characteristics of MILD combustion.

As illustrated in Figs. 4 and 7, based on the "flameless" characteristic of MILD combustion, flames burning in a 3% O_2 hot coflow fit into the MILD combustion category, while flames burning in a 9% O_2 hot coflow do not. To better understand how coflow O_2 level changes the intensity and distribution of OH*, laminar flame calculations are performed in Chemkin for ethanol flames carried by air fed toward a 1250-K oxidant flow with 3–9% O_2. Figure 9(a) shows the distribution of OH* in mixture fraction space at a strain rate of 270 s^{-1}, and ground-state OH is included for comparison. The location of peak OH is shifted to smaller mixture fraction with a reduced peak OH number density as the O_2 level in the oxidant stream decreases. Interestingly, the peaks in OH number density for the three oxidant streams fall onto a straight line, as indicated by a thick dash-dot line.

Figure 9 (b) presents Z_{pOH}, Z_{pOH^*}, scaled peak temperature (T_p) and peak heat release rate (H_p) as a function of Z_{st} for three oxidant streams. Given a more diluted oxidiser, Z_{st} is shifted to smaller mixture fraction. Figure 9(b) shows that the location of peak OH number density Z_{pOH} is linearly proportional to Z_{st} for each oxidant stream, so is the location of peak OH* number density Z_{pOH^*}. However, the peak OH* number density does not change linearly with the O_2 level in the oxidant flow, as indicated by the thin dash-dot line in Fig. 9(a). The number density of OH* reduces greatly with the O_2 level decreasing from 6% to 3%, which is in agreement with experimental results displayed in Fig. 7. Hence, the shift in Z_{pOH^*} is determined by the diluting effect on Z_{st}, while some factors other than that account for the change in the peak OH* number density. As described in Section 2.2, OH* is closely related with temperature and heat release rate. Hence, the peak temperature and peak heat release rate, scaled to fit in one figure, are plotted against Z_{st} in Fig. 9(b). The decrease in the peak temperature is linear to the shift in Z_{st}. However, the peak heat release in the 3% O_2 case does not fit onto the dash-dot line generated by the peak heat release rates in the 6% and 9% O_2 cases. Note that the gradient of the dash-dot line is almost identical to that of Z_{pOH^*}. The overall net heat release rate is also found to decrease non-linearly as the oxidant stream becomes more diluted. The disproportional drop in the peak heat release rate and/or the overall net heat release rate could be the cause of the "flameless" characteristics in MILD combustion, suggesting a need for threshold limits of them in defining MILD combustion regime.

In addition to the absence of visible flames, MILD combustion is characterised by a semi-uniform temperature distribution with low emissions of NO_x and soot in previous experimental studies

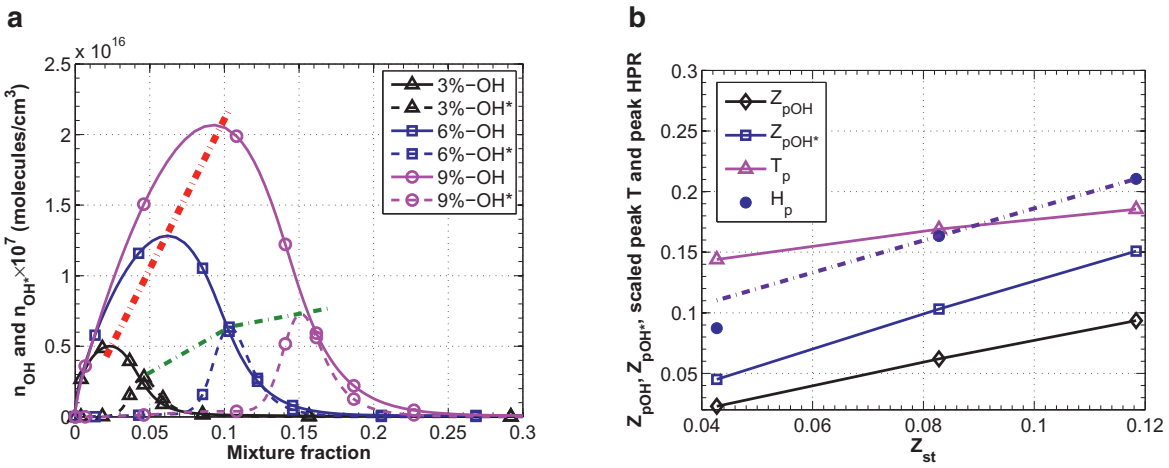

Fig. 9. (a) Number density of OH* (multiplied by 10^7) and OH as a function of mixture fraction for ethanol flames in 1250-K oxidisers with different O_2 levels (3%, 6% and 9%); (b) Z_{pOH}, Z_{pOH^*}, scaled peak temperature (T_p) and peak heat release rate (H_p) as a function of Z_{st} for three oxidant streams. The dash-dot line is generated by the peak heat release rate in the 6% and 9% O_2 cases only.

[5,7,8]. The suppression of soot precursors under MILD combustion conditions was suggested to associate with particular features in the heat release profile by de Joannon et al. [37]. They performed numerical studies with OPPDIF code in the Chemkin software, in which MILD combustion of methane are simulated in three different configurations: Hot-Fuel-Diluted-Fuel, Hot-Oxidant-Diluted-Fuel and Hot-Diluted-Oxidant [37–39]. They identified MILD combustion regime in terms of heat release in mixture fraction space [38]. Two common signatures are associated with the MILD combustion in the three configurations. First, the fuel pyrolysis was suppressed at a high level of dilution, as indicated by the absence of a negative heat release region [38]. In this pyrolytic region, endothermic reactions, such as methane decomposition or methyl radical recombination and dehydrogenation, exceed the oxidation reactions [39]. The suppression of this pyrolytic region is of great importance as soot is most likely to form in this region in practical combustion appliances [40]. Second, the location of the peak heat production rate (Z_{hmax}) mismatched with the location of stoichiometric mixture fraction (Z_{st}) [38]. They found that up to a certain level of fuel dilution, Z_{hmax} was very close to Z_{st} [39]. Once the fuel dilution was beyond that particular limit, the heat production region started to shift backward toward the lean side [39]. Hence, Z_{hmax} shifted toward the lean side, meanwhile Z_{st} shifted towards the fuel rich side due to the fuel dilution [39]. Notably, Hilbert and Thévenin [36] found that Z_{hmax} corresponded to Z_{MR} at the ignition time in a counterflow system of hot air and cold hydrogen diluted in nitrogen, in both laminar and turbulent regimes. Those MILD combustion characteristics reported by de Joannon et al. [37–39] are also applicable to n-heptane flames [41]. It is interesting to see if those findings can be extrapolated to ethanol, therefore the boundary between MILD combustion and traditional combustion can be defined on the heat release profile only.

Laminar flame calculations for pure ethanol flames are performed with the fuel inlet temperature set to 413 K. The oxidiser inlet is modelled as the 1250-K experimental coflow with 3%, 6% and 9% O_2. The separation of the two inlets is 20 mm, and the stagnation plane is at 10 mm. The strain rate varies from 64 s^{-1} to 7400 s^{-1}. Note that the impact of strain rate on the negative heat release region is considered in the present study, which has not been reported in literature.

Figure 10(a) shows the profiles of heat production rate for ethanol flames in the 1250-K oxidiser with 3% O_2 at three strain rates. Note that calculations are performed with a series of strain rates, three of which are presented here to represent typical heat production rate profiles. The heat production rate at the stoichiometric mixture fraction for each strain rate is marked with an asterisk on the line plots. At a strain rate of 64 s^{-1}, a narrow oxidative region exists at the lean side, which is followed by a negative heat release region. A single peak heat release rate exists at a given strain rate. A mismatch of Z_{hmax} and Z_{st} is evident at the three strain rates, though the location of peak heat release is shifted to the fuel rich side at the highest strain rate, the underlying factors for which are not clear. On the lean side of Z_{hmax}, there exists an inflection point upon which the gradient of the curve changes. This inflection point becomes less apparent as the strain rate increases. Note that the negative heat release region caused by pyrolytic reactions is suppressed at higher strain rates. Particularly, the minimum heat release rate becomes zero at a strain rate of 131 s^{-1}, which is referred to as the critical strain rate. The critical strain rate is much higher at the 6% and 9% O_2 level, however the general features remain the same. Those results at higher O_2 levels are not presented here for brevity.

In order to have a full picture of the transition from conventional combustion to MILD combustion, the role of temperature is also taken into account in the laminar flame calculations. The temperature of the oxidiser investigated in the calculations ranges from 1250 K to 1550 K. The two signatures in heat production rate profiles found by de Joannon et al. [38] are used to identify MILD combustion regime. Figure 10(b) shows the critical strain rate, where the transition from conventional combustion to MILD combustion happens, given a combination of temperature and O_2 mole fraction in the oxidant stream. As the mismatch of Z_{hmax} and Z_{st} is independent of strain rate, the critical strain rate is solely determined by the absence of a negative heat release region. Taking a 1250-K oxidiser with 3% O_2 as an example, the critical strain rate is 131 s^{-1}. Given a strain rate lower than 131 s^{-1}, conventional combustion occurs. In contrast, MILD combustion takes place with a strain rate higher than that critical value. The critical strain rate for the negative heat release region to disappear increases with the temperature and O_2 level of the oxidiser. Particularly, at a high O_2 level, the required strain rate to diminish the negative heat release region increases substantially with the temperature of the oxidiser varying from 1400 K to 1550 K. However, for ethanol flame in the oxidant stream with 3% O_2, MILD combustion can be

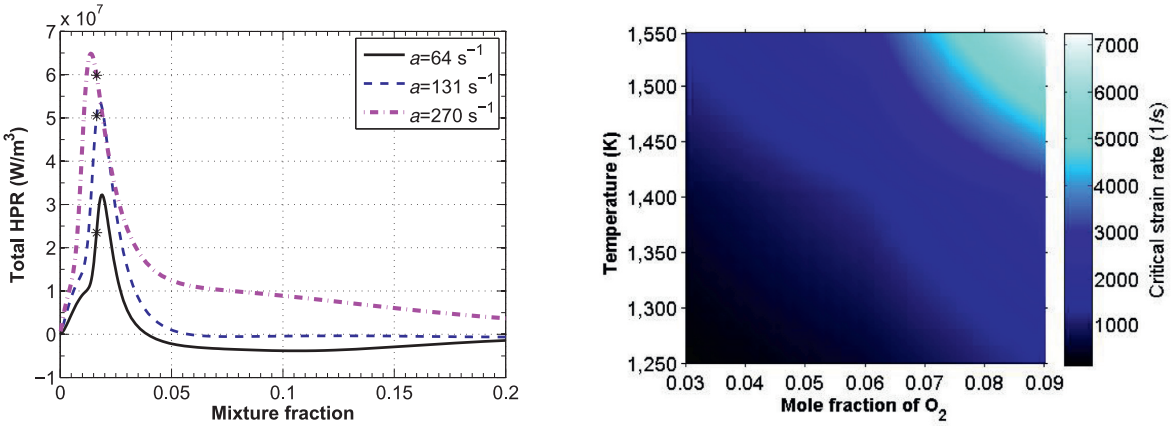

(a) X_{O_2}=3% (b) Critical strain rate

Fig. 10. (a) Heat production rate profiles of ethanol flames in a 1250-K oxidiser with 3% O_2: the heat production rate at the stoichiometric mixture fraction is marked with an asterisk; (b) The critical strain rate required for the transition from conventional combustion to MILD combustion to occur in a given oxidant stream.

achieved with relatively moderate strain rate even at a temperature of 1550 K.

Experimental results in Section 3.3 show that the jet Reynolds number has negligible impact on the apparent lift-off height and luminosity of flames in 9% O_2 coflow with various temperature, which seems to differ from results provided by laminar flame calculations. Taking flames in the 9% O_2 1250-K oxidant stream as an example, calculations show that a negative heat release region still exists as the strain rate increases from 64 s^{-1} to 1200 s^{-1}, which is an almost 20-fold increase. However, the jet Reynolds numbers only ranges from 10,000 to 30,000 in current experiments. It is suspected that the jet Reynolds numbers in the current experiments correspond to strain rates within a small range, which is not sufficient to make a difference.

Figure 10(b) demonstrates that the absence of a negative heat release region is strain rate dependent at a given temperature and O_2 mole fraction of the oxidant stream. To understand the impact of strain rate on the heat production, a brief analysis on the ethanol chemistry is essential. In ethanol-air combustion, CH_3CH_2OH is first converted to three C_2H_5O isomers via H-atom abstraction reactions, including CH_3CH_2O, CH_2CH_2OH, and CH_3CHOH [26]. Most of the three isomers are oxidised to CH_3HCO, and then further oxidised to CO or CO_2 [26]. Besides oxidation, the pyrolysis of ethanol generally occurs at the coexistence of low local oxygen concentration and high temperature. During the pyrolysis, ethanol is decomposed to smaller hydrocarbons in the absence of oxygen, which removes heat from the system. A preliminary analysis is performed to identify key contributing reactions to the total heat release rate, taking ethanol flames in a 1250-K oxidiser with 3% O_2 as an example. One of the major contributors identified among all the endothermic reactions is the reaction $CH_3CH_2OH(+M) \rightleftharpoons CH_3+CH_2OH(+M)$. Figure 11(a) shows that the heat subtraction from the decomposition of CH_3CH_2OH initially increases, then decreases with the strain rate. At a higher strain rate, the residence time is reduced, meanwhile the reactants are supplied to the reaction zone at a faster rate. The non-linear relationship between the heat subtraction from this reaction and strain rate is suspected to result from these two competing factors. Of the exothermic reactions, the most striking trend is found in reaction $CH_3CHOH+O_2 \rightleftharpoons CH_3HCO+HO_2$ as illustrated in Fig. 11(b). There is a six-fold increase in the heat addition from the oxidation of CH_3CHOH with strain rate increasing from 64 s^{-1} to 270 s^{-1}.

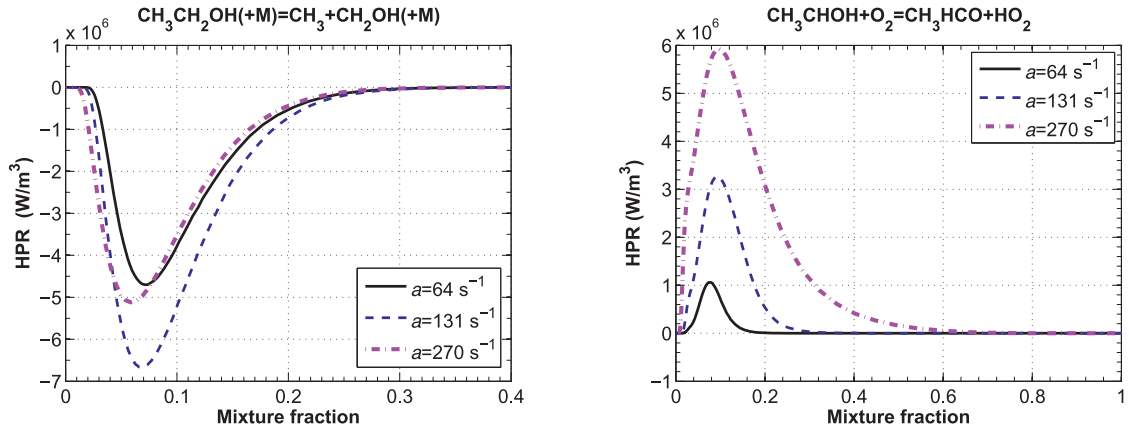

(a) Endothermic (b) Exothermic

Fig. 11. Heat production rate profiles of particular reactions for ethanol flames in a 1250-K oxidiser with 3% O_2.

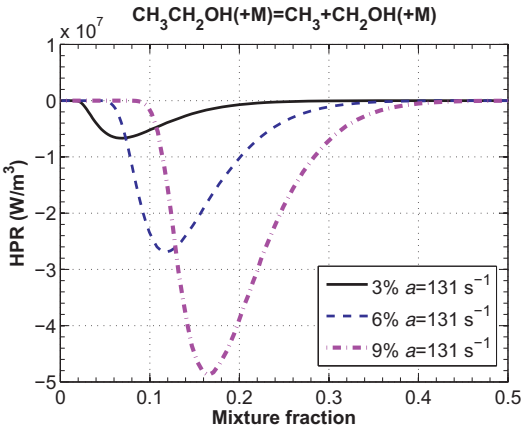

Fig. 12. Heat production rate profile for ethanol decomposition as a function of mixture fraction at three oxidant streams.

It is understood that the strong increase in the heat addition from this reaction overcompensates the heat subtraction, which explains the absence of a negative heat release region at a higher strain rate. The significant increase in this reaction is suspected to result from an enhanced transportation of O_2 across the reaction zone at a higher strain rate, particularly at a low coflow O_2 level [21], which is confirmed by the calculation of mass flux of O_2 at these strain rates.

Figure 10(b) demonstrates that, at low strain rates, the negative heat release region is more likely to disappear as the O_2 level in the oxidant stream decreases. This is because the reaction $CH_3CH_2OH(+M) \rightleftharpoons CH_3+CH_2OH(+M)$ is greatly suppressed at a lower O_2 level, which is shown in Fig. 12. As mentioned previously, the occurrence of fuel pyrolysis requires the coexistence of low local oxygen concentration and high temperature. Hence, there are two possible reasons for the depression of fuel pyrolysis in the oxidant stream with 3% O_2: low temperature and/or increased availability/concentration of O_2.

Figure 12 shows that reaction $CH_3CH_2OH(+M) \rightleftharpoons CH_3+CH_2OH(+M)$ initiates at around Z=0.4 for the oxidant stream with 9% O_2, at which the flame temperature is around 1100 K as indicated by Fig. 13(a). This reaction only starts at Z=0.2 for the oxidiser with 3% O_2 due to lower flame temperature.

Comparing to the distribution of OH in mixture fraction space as shown in Fig. 15, laminar flame calculations reveal that this reaction mostly takes place on the fuel-rich side of the reaction zone. Figure 13(b) shows the concentration of O_2 for three oxidisers in the range of interest. The concentration of O_2 on the fuel-rich side in the 3% case is higher than that in the 6% and 9% case despite a lower initial O_2 concentration in the oxidiser. The O_2 concentration on the fuel-rich side results from two competing factors: the consumption of O_2 and the transportation of O_2 across the reaction zone [21]. Calculations reveal that the mass flux of O_2 on the fuel-rich side of the reaction zone is higher in the 3% O_2 stream than that in the 9% O_2 stream as shown in Fig. 15. The lower consumption rate of O_2 in the 3% O_2 stream, resulted from a lower system reactivity, also contributes to the higher local O_2 concentration as reported in a previous study [21]. Hence, the combined effects of low temperature and higher local concentration of O_2 greatly suppresses the fuel pyrolysis in the oxidant stream with 3% O_2. MILD combustion is characterised with low soot emissions [7,8], which essentially requires the suppression of this pyrolytic region. This makes ethanol flames in the oxidiser with 3% O_2 more likely to fall into the MILD combustion category.

Imaging of OH* chemiluminescence revealed that the use of N_2 as a carrier gas produces a more uniform distribution of OH*, which makes flames in a 6% O_2 coflow behave more like flames in a 3% O_2 coflow. It is interesting to investigate the impact of carrier gas on the heat production rate profile, particularly on the absence of a negative heat release region. Parametric studies are performed for pure ethanol flames (no dilution), ethanol diluted with pure N_2, and ethanol diluted with pure O_2 in a 1250-K oxidiser with 3% O_2 in the Chemkin software. To directly compare the oxidiser with the inert, O_2 is used to mix with ethanol instead of air. Laminar flame calculations are performed for various amounts of carrier gas and strain rates. It should be noted that these conditions are not the same as the experiments, however they are chosen to exacerbate the effects of carrier gas/fuel dilution. At low strain rates, a negative heat release region exists when ethanol is not mixed with carrier gas. When ethanol is mixed with carrier gas, this negative heat release region starts to disappear as the amount of N_2 or O_2 in the fuel stream increases. For example, at a strain rate of 64 s^{-1}, in order to make the minimum heat release rate non-negative, the mole fraction of O_2 in the fuel stream should be greater than 0.3 when ethanol is mixed with pure O_2. As for ethanol diluted with pure N_2, a mole fraction of N_2 greater than 0.7 is required to diminish the negative heat release region. The

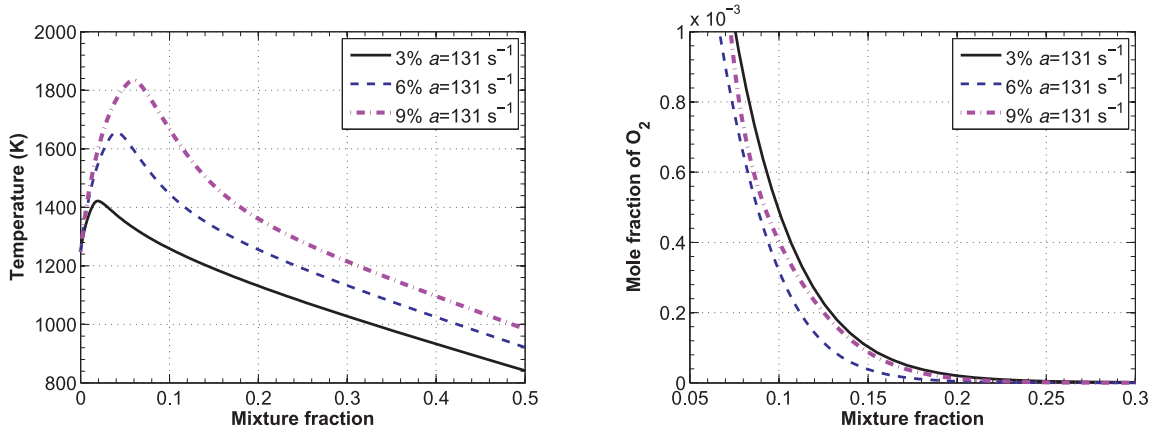

(a) Temperature (b) Mole fraction of O_2

Fig. 13. Temperature and mole fraction of O_2 as a function of mixture fraction at three oxidant streams.

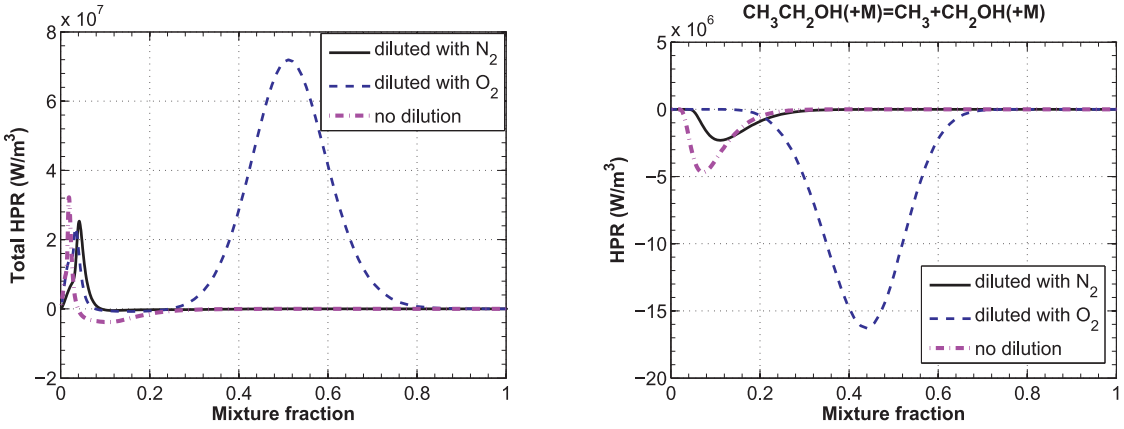

(a) Total HPR (b) Ethanol decomposition

Fig. 14. Heat production rate profiles as a function of mixture fraction for three cases: pure ethanol flames (no dilution), ethanol diluted with pure N_2, and ethanol diluted with pure O_2 in a 1250-K oxidiser with 3% O_2.

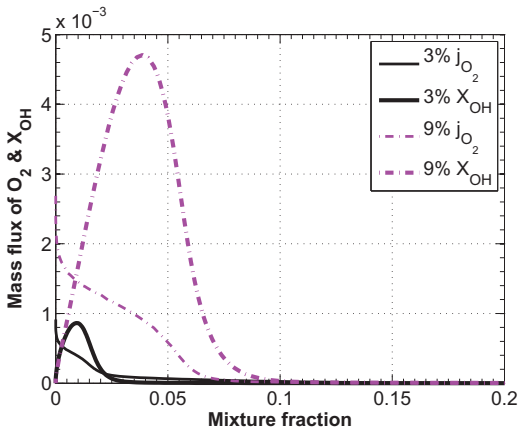

Fig. 15. Mass flux of O_2 (j_{O_2}) and mole fraction of OH (X_{OH}) as a function of mixture fraction at two oxidant streams.

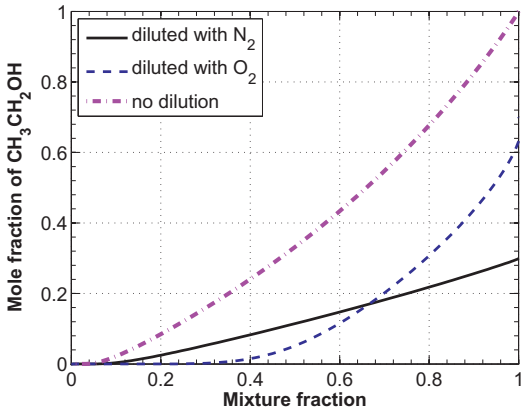

Fig. 16. The distribution of ethanol in mixture fraction space for three cases: pure ethanol flames (no dilution), ethanol diluted with pure N_2, and ethanol diluted with pure O_2 in a 1250-K oxidiser with 3% O_2.

heat production rate profiles for the pure ethanol flame (X_{EtOH}=1), ethanol mixed with N_2 (X_{N_2}=0.7, X_{EtOH}=0.3), and ethanol mixed with O_2 (X_{O_2}=0.3, X_{EtOH}=0.7) at a strain rate of 64 s^{-1} are shown in Figure 14(a). To explain the absence of a negative heat release region in those cases, heat subtraction from ethanol decomposition is investigated due to its importance. As shown in Fig. 14(b), heat subtraction from ethanol decomposition is lowered when ethanol is diluted with N_2, which is likely to result from lower flame temperature. The heat subtraction from the decomposition of ethanol, shifting to a richer region, is greatly increased when O_2 is mixed with ethanol. Comparing the total heat production rate profile with the profile for ethanol decomposition, it is clear that this reaction takes place within the strong oxidative region at the fuel rich side. Hence the heat subtraction from ethanol decomposition is overtaken by the heat release from oxidative reactions when ethanol is diluted with O_2. In addition, Fig. 16 shows that for ethanol mixed with O_2 case, ethanol is largely consumed at $Z > 0.2$, which is consistent with the location of ethanol decomposition in this case (see Fig. 14(b)).

The heat production rate profile changes significantly when ethanol is diluted with O_2. A wide oxidative region exists at the fuel rich side due to the existence of O_2 in the fuel stream, which contributes to most of the heat release. A narrow oxidative region exists at $Z < 0.1$, the shape of which is similar to that for ethanol mixed with N_2. In addition to two heat-release regions, Fig. 17 demonstrates that OH exists at $0 \leq Z \leq 0.05$ and $0.2 \leq Z \leq 0.8$, suggesting the existence of a double-reaction zone when ethanol is mixed with O_2. Previous work [21] has shown that the enhanced O_2 diffusion towards the fuel-rich side through "reaction zone weakening" is a key feature of MILD combustion flames, leading to an increasing formation of important intermediates. The build-up of those intermediates is responsible for the stabilisation of the flames [21]. Figure 17 suggests that adding O_2 to the fuel stream directly also produces this effect.

5. Conclusions

The present paper was focused on the transition of prevaporised ethanol flames from conventional combustion to MILD combustion. Ethanol flames in the 3% O_2 coflow appear "flameless" in the region controlled by coflow such that the flame base is difficult to identify. Imaging of OH^* chemiluminescence shows that

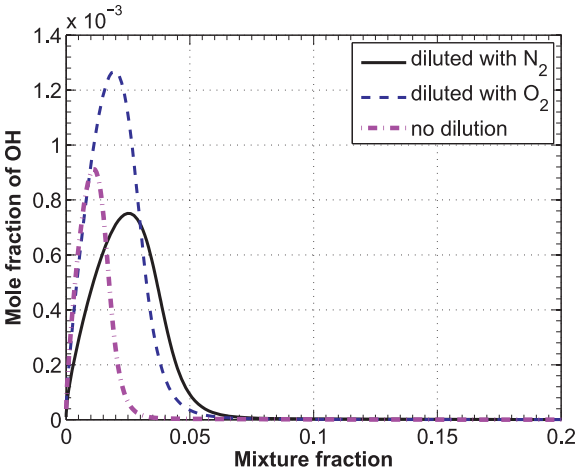

(a) $0 \leq Z \leq 0.2$

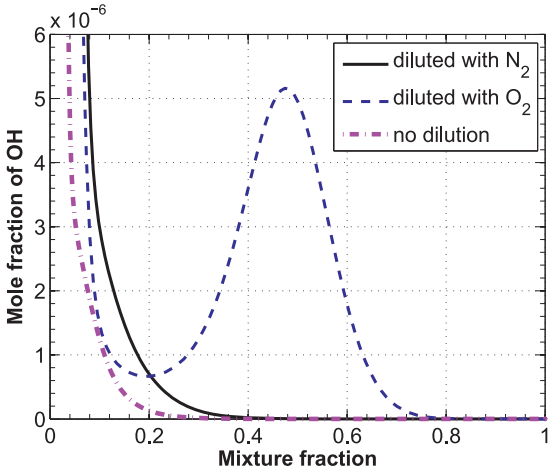

(b) $0 \leq Z \leq 1$

Fig. 17. The distribution of OH in mixture fraction space for three cases: pure ethanol flames (no dilution), ethanol diluted with pure N_2, and ethanol diluted with pure O_2 in a 1250-K oxidiser with 3% O_2.

the spatial gradient and the peak in the OH* signal profile are significantly reduced in the 3% O_2 coflow, indicating a more uniform distribution of heat release and temperature. The use of N_2 as a carrier gas renders the OH* profile for the 6% O_2 coflow case similar to that of ethanol flame carried by air in the 3% O_2 coflow. Experimental results suggest a transition from conventional combustion to MILD combustion with the decrease of coflow O_2 level or the use of N_2 as a carrier gas. In order to clarify this transition, a series of laminar flame calculations are performed to examine the flame structure in details. Several key findings are summarised as follows:

- The location of peak OH* in mixture fraction space is shifted proportionally to the O_2 level in the oxidant stream as it is determined by the shift in Z_{st}. However, the change in the peak OH* number density is not linear with the O_2 level, which might result from the disproportional change in the peak heat release rate and/or the overall net heat release rate. This suggests a need to define threshold limits of them to achieve "flameless" MILD combustion.
- The absence of a negative heat release region is used to identify MILD combustion regime. The negative heat release region is more likely to disappear at a higher strain rate given a constant O_2 level in the oxidiser. The main reason for this is that the transportation of O_2 across the reaction zone is enhanced at a higher strain rate, which promotes the oxidative reactions instead of fuel decomposition.
- At relatively low strain rates, the negative heat release region has a higher potential to disappear at a low O_2 level in the oxidant flow. In comparison to the oxidant streams with 6% and 9% O_2, a combined effect of lower flame temperature and higher local concentration of O_2 is found to inhibit the decomposition of ethanol at the 3% O_2 oxidant stream.
- The impact of carrier gas on the presence/absence of a negative heat release region is investigated. It is found that using either O_2 or N_2 as a carrier gas helps to diminish the negative heat release region, and more N_2 is needed to achieve the same result. The absence of a negative heat release region is believed to result from lower flame temperature when N_2 is used as a carrier gas. When O_2 is used, a strong oxidation on the fuel rich side overtakes the endothermic reactions, diminishing the negative heat release region.

Acknowledgments

This research is funded by the China Scholarship Council and The University of Adelaide through a joint postgraduate scholarship. Funding from the Australian Research Council (ARC) and United States Air Force Asian Office of Aerospace Research and Development (AOARD) is gratefully acknowledged.

References

[1] J. Wünning, J. Wünning, Flameless oxidation to reduce thermal NO-formation, Prog. Energy Combust. 23 (1) (1997) 81–94.
[2] R. Weber, S. Orsino, N. Lallemant, A. Verlaan, Combustion of natural gas with high-temperature air and large quantities of flue gas, Proc. Combust. Inst. 28 (1) (2000) 1315–1321.
[3] B.B. Dally, S.H. Shim, R.A. Craig, P.J. Ashman, G.G. Szegö, On the burning of sawdust in a MILD combustion furnace, Energy Fuels 24 (6) (2010) 3462–3470.
[4] C. Galletti, A. Parente, M. Derudi, R. Rota, L. Tognotti, Numerical and experimental analysis of (NO) emissions from a lab-scale burner fed with hydrogen-enriched fuels and operating in mild combustion, Int. J. Hydrogen Energy 34 (19) (2009) 8339–8351.
[5] M. Saha, B.B. Dally, P.R. Medwell, E.M. Cleary, Moderate or intense low oxygen dilution (MILD) combustion characteristics of pulverized coal in a self-recuperative furnace, Energy Fuels 28 (9) (2014) 6046–6057.
[6] A. Rao, Y. Levy, A new combustion methodology for low emission gas turbine engines, 8th International Symposium on High Temperature Air Combustion and Gasification, Poznań, Poland (2010), pp. 177–185.
[7] P.R. Medwell, P.A.M. Kalt, B.B. Dally, Imaging of diluted turbulent ethylene flames stabilized on a jet in hot coflow (JHC) burner, Combust. Flame 152 (1) (2008) 100–113.
[8] M. Derudi, R. Rota, Experimental study of the mild combustion of liquid hydrocarbons, Proc. Combust. Inst. 33 (2) (2011) 3325–3332.
[9] B.B. Dally, A.N. Karpetis, R.S. Barlow, Structure of turbulent non-premixed jet flames in a diluted hot coflow, Proc. Combust. Inst. 29 (1) (2002) 1147–1154.
[10] E. Oldenhof, M. Tummers, E. Van Veen, D. Roekaerts, Ignition kernel formation and lift-off behaviour of jet-in-hot-coflow flames, Combust. Flame 157 (6) (2010) 1167–1178.
[11] E. Oldenhof, M. Tummers, E. Van Veen, D. Roekaerts, Role of entrainment in the stabilisation of jet-in-hot-coflow flames, Combust. Flame 158 (8) (2011) 1553–1563.
[12] R. Cabra, J.Y. Chen, R.W. Dibble, A.N. Karpetis, R.S. Barlow, Lifted methane-air jet flames in a vitiated coflow, Combust. Flame 143 (4) (2005) 491–506.
[13] P.R. Medwell, B.B. Dally, Experimental observation of lifted flames in a heated and diluted coflow, Energy Fuels 26 (9) (2012) 5519–5527.
[14] R.L. Gordon, A.R. Masri, E. Mastorakos, Simultaneous Rayleigh temperature, OH-and CH_2O-LIF imaging of methane jets in a vitiated coflow, Combust. Flame 155 (1) (2008) 181–195.
[15] J. Sidey, E. Mastorakos, R. Gordon, Simulations of autoignition and laminar premixed flames in methane/air mixtures diluted with hot products, Combust. Sci. Technol. 186 (4–5) (2014) 453–465.

[16] A.H. Lefebvre, D.R. Ballal, Gas turbine combustion : alternative fuels and emissions, Taylor and Francis, Hoboken, 2010.
[17] H.C. Rodrigues, M.J. Tummers, E.H. van Veen, D.J. Roekaerts, Spray flame structure in conventional and hot-diluted combustion regime, Combust. Flame 162 (3) (2015) 759–773.
[18] S.H. Stårner, J. Gounder, A.R. Masri, Effects of turbulence and carrier fluid on simple, turbulent spray jet flames, Combust. Flame 143 (4) (2005) 420–432.
[19] W. O'Loughlin, A.R. Masri, The structure of the auto-ignition region of turbulent dilute methanol sprays issuing in a vitiated co-flow, Flow Turbul. Combust. 89 (1) (2012) 13–35.
[20] J. Ye, P.R. Medwell, E. Varea, S. Kruse, B.B. Dally, H.G. Pitsch, An experimental study on MILD combustion of prevaporised liquid fuels, Appl. Energy 151 (2015) 93–101.
[21] P.R. Medwell, P.A.M. Kalt, B.B. Dally, Reaction zone weakening effects under hot and diluted oxidant stream conditions, Combust. Sci. Technol. 181 (7) (2009) 937–953.
[22] S.H. Stårner, R. Bilger, M. Long, J. Frank, D. Marran, Scalar dissipation measurements in turbulent jet diffusion flames of air diluted methane and hydrogen, Combust. Sci. Technol. 129 (1–6) (1997) 141–163.
[23] R. Lückerath, W. Meier, M. Aigner, FLOX® combustion at high pressure with different fuel compositions, J. Eng. Gas Turbines Power 130 (1) (2008) 011505.
[24] J. Lee, D. Santavicca, Experimental diagnostics for the study of combustion instabilities in lean premixed combustors, J. Propulus. Power 19 (5) (2003) 735–750.
[25] L.C. Haber, U. Vandsburger, W.R. Saunders, V.K. Khanna, An examination of the relationship between chemiluminescent light emissions and heat release rate under non-adiabatic conditions, ASME Turbo Expo 2000: Power for Land, Sea, and Air, American Society of Mechanical Engineers (2000). V002T02A041–V002T02A041
[26] N.M. Marinov, A detailed chemical kinetic model for high temperature ethanol oxidation, Int. J. Chem. Kinet. 31 (1999) 183–220.
[27] C. Panoutsos, Y. Hardalupas, A. Taylor, Numerical evaluation of equivalence ratio measurement using OH∗ and CH∗ chemiluminescence in premixed and non-premixed methane-air flames, Combust. Flame 156 (2) (2009) 273–291.
[28] J.M. Hall, E.L. Petersen, An optimized kinetics model for OH chemiluminescence at high temperatures and atmospheric pressures, Int. J. Chem. Kinet. 38 (12) (2006) 714–724.
[29] M. De Leo, A. Saveliev, L.A. Kennedy, S.A. Zelepouga, OH and CH luminescence in opposed flow methane oxy-flames, Combust. Flame 149 (4) (2007) 435–447.
[30] J.A. Sidey, E. Mastorakos, Simulations of laminar non-premixed flames of methane with hot combustion products as oxidiser, Combust. Flame 163 (2015a) 1–11.
[31] J. Sidey, E. Mastorakos, Visualization of MILD combustion from jets in cross-flow, Proc. Combust. Inst. 35 (3) (2015b) 3537–3545.
[32] P.R. Medwell, P.A.M. Kalt, B.B. Dally, Simultaneous imaging of OH, formaldehyde, and temperature of turbulent nonpremixed jet flames in a heated and diluted coflow, Combust. Flame 148 (1) (2007) 48–61.
[33] B. Dally, E. Riesmeier, N. Peters, Effect of fuel mixture on moderate and intense low oxygen dilution combustion, Combust. Flame 137 (4) (2004) 418–431.
[34] E. Mastorakos, Ignition of turbulent non-premixed flames, Prog. Energy Combust. 35 (1) (2009) 57–97.
[35] E. Mastorakos, T. Baritaud, T. Poinsot, Numerical simulations of autoignition in turbulent mixing flows, Combust. Flame 109 (1) (1997) 198–223.
[36] R. Hilbert, D. Thévenin, Autoignition of turbulent non-premixed flames investigated using direct numerical simulations, Combust. Flame 128 (1) (2002) 22–37.
[37] M. de Joannon, P. Sabia, G. Cozzolino, G. Sorrentino, A. Cavaliere, Pyrolitic and oxidative structures in hot oxidant diluted oxidant (HODO) MILD combustion, Combust. Sci. Technol. 184 (7–8) (2012) 1207–1218.
[38] M. de Joannon, P. Sabia, G. Sorrentino, A. Cavaliere, Numerical study of mild combustion in hot diluted diffusion ignition (HDDI) regime, Proc. Combust. Inst. 32 (2) (2009) 3147–3154.
[39] M. de Joannon, G. Sorrentino, A. Cavaliere, MILD combustion in diffusion-controlled regimes of hot diluted fuel, Combust. Flame 159 (5) (2012) 1832–1839.
[40] C. Esarte, M. Peg, M.P. Ruiz, A. Millera, R. Bilbao, M.U. Alzueta, Pyrolysis of ethanol: gas and soot products formed, Ind. Eng. Chem. Res. 50 (8) (2011) 4412–4419.
[41] M. de Joannon, P. Sabia, A. Cavaliere, Alternative ignition systems, ProcessEng Engineering GmbH, pp. 133–150.

Chapter 6

Characteristics of Turbulent *n*-Heptane Jet Flames in a Hot and Diluted Coflow

Statement of Authorship

Title of Paper	Characteristics of Turbulent *n*-Heptane Jet Flames in a Hot and Diluted Coflow
Publication Status	☐ Published ☑ Accepted for Publication ☐ Submitted for Publication ☐ Unpublished and Unsubmitted w ork w ritten in manuscript style
Publication Details	J. Ye, P. R. Medwell, M. J. Evans, B. B. Dally, Characteristics of Turbulent *n*-Heptane Jet Flames in a Hot and Diluted Coflow, accepted on 23rd May 2017, Combust. Flame, DOI: 10.1016/j.combustflame.2017.05.027

Principal Author

Name of Principal Author (Candidate)	Jingjing Ye		
Contribution to the Paper	I co-designed the experiments. Based on discussions between me and one of my supervisors, several operating parameters were chosen for investigation. I decided different experimental cases with my supervisors. I setup the experiments with co-authors. I undertook the experiments with my co-authors. We performed digital photography, imaging of OH* chemiluminescence, and OH-LIF together. I processed, analysed, and interpreted all the experimental data. I also planned and performed all the calculations and analyses in the Chemkin software to assist the interpretation of the experimental data. I performed an analysis of the experimental and calculation results. The analysis was presented in text or figures by me. I integrated all the analysis and wrote the manuscript. I also acted as the corresponding author, and responded to the reviewers' and the editor's comments and recommendations.		
Overall percentage (%)	70		
Certification:	This paper reports on original research I conducted during the period of my Higher Degree by Research candidature and is not subject to any obligations or contractual agreements with a third party that would constrain its inclusion in this thesis. I am the primary author of this paper.		
Signature	Digitally signed by JINGJING YE Date: 2017.06.03 10:12:00 +09'30'	Date	03-June-2017

Co-Author Contributions

By signing the Statement of Authorship, each author certifies that:

i. the candidate's stated contribution to the publication is accurate (as detailed above);

ii. permission is granted for the candidate in include the publication in the thesis; and

iii. the sum of all co-author contributions is equal to 100% less the candidate's stated contribution.

Name of Co-Author	Paul R. Medwell		
Contribution to the Paper	This co-author co-designed the experiments and co-supervised the development of the work. This co-author also provided assistance and supervision during the experimental setup and data collection. This co-author helped to evaluate and edit the manuscript.		
Signature	Paul Medwell 2017.06.03 10:46:12 +09'30'	Date	03-JUN-2017

Name of Co-Author	Michael J. Evans		
Contribution to the Paper	This co-author co-designed and undertook experiments. This co-author also helped to evaluate and edit the manuscript.		
Signature	Digitally signed by Michael Evans Date: 2017.06.04 18:38:16 +09'30'	Date	04-June-2017

Name of Co-Author	Bassam B. Dally		
Contribution to the Paper	This co-author co-supervised the development of the work. This co-author helped to evaluate and edit the manuscript.		
Signature	Igitally signed by Bassam Dally ate: 2017.06.05 11:32:39 +09'30'	Date	05-June-2017

Please cut and paste additional co-author panels here as required.

Elsevier Editorial System(tm) for Combustion and Flame

Manuscript Draft

Manuscript Number: CNF-D-17-00149R2

Title: Characteristics of Turbulent n-Heptane Jet Flames in a Hot and Diluted Coflow

Article Type: Full Length Article

Keywords: MILD combustion; prevaporised n-heptane; OH-LIF; lift-off; net negative heat release rate

Corresponding Author: Ms. JJ Ye,

Corresponding Author's Institution: The University of Adelaide

First Author: JJ Ye

Order of Authors: JJ Ye; Paul R Medwell; Michael J Evans; Bassam B Dally

Abstract: Distinctive behaviour of turbulent n-heptane jet flames is revealed by conventional photography and laser-induced fluorescence of the hydroxyl radical (OH-LIF) performed in a Jet in Hot Coflow (JHC) burner. Prevaporised n-heptane, carried by air, issues into a hot vitiated coflow at two temperatures (1250 K and 1315 K) with three coflow oxygen levels (XO_2=3%, 6% and 9%), mimicking moderate or intense low oxygen dilution (MILD) combustion conditions. Results for n-heptane flames are compared to those for ethylene, ethanol and natural gas flames, and two main discrepancies are found: firstly, the apparent lift-off height of n-heptane flames decreases gradually with the increasing coflow oxygen level, while the apparent lift-off height of other fuels exhibit a non-monotonic trend; secondly, a transitional flame structure of n-heptane occurs in a coflow with XO_2=3%, while this structure occurs in a coflow with $XO_2 \geq 9\%$ for other fuels. Calculations using a closed homogeneous reactor model support the interpretation of the experimental data, namely that the temporal profiles of OH in the n-heptane flames are similar for the 3% and 9% O_2 cases, differing from the behaviour of other fuels. A comparative analysis of n-heptane and ethanol chemistry, focused on the fuel pyrolysis and net negative heat release regions, suggests that it is more difficult for n-heptane than ethanol to meet one of the criteria of MILD combustion.

Detailed Response to Reviewers

Characteristics of Turbulent *n*-Heptane Jet Flames in a Hot and Diluted Coflow

Jingjing Ye[a,*], Paul R. Medwell[a], Michael J. Evans[a], Bassam B. Dally[a]

[a] *Centre for Energy Technology, School of Mechanical Engineering, The University of Adelaide, South Australia 5005, Australia*

Abstract

Distinctive behaviour of turbulent *n*-heptane jet flames is revealed by conventional photography and laser-induced fluorescence of the hydroxyl radical (OH-LIF) performed in a Jet in Hot Coflow (JHC) burner. Prevaporised *n*-heptane, carried by air, issues into a hot vitiated coflow at two temperatures (1250 K and 1315 K) with three coflow oxygen levels (X_{O_2} = 3%, 6% and 9%), mimicking moderate or intense low oxygen dilution (MILD) combustion conditions. Results for *n*-heptane flames are compared to those for ethylene, ethanol and natural gas flames, and two main discrepancies are found: firstly, the apparent liftoff height of *n*-heptane flames decreases gradually with the increasing coflow oxygen level, while the apparent liftoff height of other fuels exhibit a non-monotonic trend; secondly, a transitional flame structure of *n*-heptane occurs in a coflow with X_{O_2} = 3%, while this structure occurs in a coflow with $X_{O_2} \geq 9\%$ for other fuels. Calculations using a closed homogeneous reactor model support the interpretation of the experimental data, namely that the temporal profiles of OH in the *n*-heptane flames are similar for the 3% and 9% O_2 cases, differing from the behaviour of other fuels. A comparative analysis of *n*-heptane and ethanol chemistry, focused on the fuel pyrolysis and net negative heat release regions, suggests that it is more difficult for *n*-heptane than ethanol to meet one of the criteria of MILD combustion.

Keywords: MILD combustion, prevaporised *n*-heptane, OH-LIF, liftoff, net negative heat release rate

1. Introduction

Moderate or Intense Low-oxygen Dilution (MILD) combustion has attracted extensive research interest [1, 2, 3, 4, 5, 6, 7, 8, 9, 10, 11, 12], driven by a long-term goal to provide energy in a more efficient and sustainable way. MILD combustion occurs in a hot and diluted environment, typically achieved by strong preheating and dilution of reactants by hot exhaust gases.

The enhanced recirculation or entrainment of hot exhaust gases under MILD combustion conditions can be achieved through various means, such as a reverse-flow design [13] or with the use of high momentum fuel jets [14]. In these configurations, the characteristic timescale of the fluid flow is intentionally shortened [6]. More importantly, the enhanced recirculation dilutes the fresh reactants and reduces the local oxygen concentration, thereby increasing the chemical timescale. The combined effects of short fluid timescale

*Corresponding author
Email address: jingjing.ye01@adelaide.edu.au (Jingjing Ye)

and long chemical timescale lead to a strong interaction between turbulence and chemistry under MILD combustion conditions, which has been reported in previous studies [15, 16]. This dominant turbulence-chemistry interaction further complicates the already complex combustion processes, hence it is essential to isolate different parameters through carefully designed experiments in order to enable a deeper understanding of the effect of these parameters on the combustion process. One method of separating these parameters is through the use of a laboratory-scale Jet in Hot Coflow (JHC) burner [17], which consists of a cold jet issuing into a hot and vitiated coflow, emulating MILD combustion conditions. This configuration provides control over the boundary conditions and allows optical access for *in situ* measurements.

A large body of research work has been conducted to improve the understanding of the flame stabilisation mechanisms and the resultant characteristics in MILD combustion [7, 8, 10, 15, 16, 18, 19, 20, 21, 22, 23, 24, 25]. The vast majority of these studies were focused on simple gaseous fuels, such as hydrogen and methane. For instance, Dally et al. [16] investigated the establishment of MILD methane flames, and reported the necessity of a high scalar dissipation rate in the vicinity of the jet exit plane in order to prevent early ignition caused by flame propagation from downstream before the fresh mixture is well diluted by hot exhaust gases. This finding agrees with a study by Katsuki and Hasegawa [15] who found that a rapid dilution of reactants via a shearing motion with high speed air was required to ensure reactions proceed in highly vitiated conditions. Nevertheless, it is worth noting that laminar MILD flames of various methane- and ethylene-based fuels have also been established under low-strain conditions in many experimental configurations consisting of a jet issuing into a hot and diluted coflow [26, 27].

Minamoto and Swaminathan [24] investigated the often-cited "homogeneous" characteristic of MILD combustion in a three-dimensional direct numerical simulation (DNS) study of methane flames in a near-uniform mixture-fraction-field, with variations of approximately $\pm 5\%$ of the mean value. Thin regions of intense reactions were revealed by their analysis, which indicated the existence of flamelets [24]. These flamelets interacted with each other frequently in space and time, leading to the thickening of the reaction zone and the appearance of non-flamelets behaviour [24, 28]. This is consistent with an experimental study on MILD methane flames by Sidey and Mastorakos [25], where thin flame fronts were revealed by instantaneous imaging of OH.

Previous numerical studies of methane by de Joannon et al. [29, 30, 31] demonstrated that the MILD combustion regime is associated with several common signatures in the heat production rate profile: the broadening of the heat production profile with a single peak in mixture fraction space, the lack of correlation between the location of the peak heat production rate (Z_{hmax}) and the stoichiometric mixture fraction, and the absence of a net negative heat release region. The absence of a net negative heat release region is attributed to the suppression of pyrolytic reactions, which is also responsible for low soot formation, an important feature of MILD combustion [9].

Compared to studies of methane-based flames, published results are sparse on more complex fuels, such as oxygenated fuels and long-chain alkanes. Although previous work has indicated that MILD combustion is insensitive to fuel type when simple hydrocarbons are mixed with hydrogen [32], the role of fuel structure on the flame stabilisation mechanism and the typical MILD combustion characteristics should not be

underestimated. For instance, Oldenhof et al. [33] investigated the ignition event and liftoff behaviour of various jet-in-hot-coflow flames via high-speed imaging. They found that the addition of higher alkanes, such as ethane and propane, to methane flames significantly affects the chemical timescale, thus the liftoff height [33]. Another study on a reverse-flow MILD combustor [13] reported that the combustion stability was strongly dependent on the fuel type: unstable combustion of n-heptane was observed at higher equivalence ratios under elevated pressures, meanwhile MILD combustion of ethanol with invisible flame and low emissions were established under the same conditions. Identifying the reasons for the difference in stability between the two flames was not possible because of limited control over the mixing process inside the combustor. Reddy et al. [34] studied combustion of biodiesel and biodiesel blended with standard diesel in a two-stage combustor under MILD combustion conditions. Lower emissions of NO_x and unburned hydrocarbons (UHCs) were produced from biodiesel blended with standard diesel than pure biodiesel. This was thought to be caused by a faster evaporation of standard diesel due to its lower viscosity and boiling point [34], further highlighting the potential sensitivity of MILD combustion to the fuel type.

The impact of fuel type has also been investigated for solid fuels in the furnace environment. Saha et al. [7] investigated MILD combustion of pulverised brown and black coal in a self-recuperative furnace: NO_x emissions from black coal were measured to be much higher than those from brown coal combustion, which was explained by a higher nitrogen content in black coal [7]. Weber et al. [18] compared the combustion performance of various fuels, including natural gas, light fuel oil (LFO), heavy fuel oil (HFO) and coal, in a refractory lined furnace. When natural gas and LFO were burnt, the whole furnace was illuminated while no visible flame was observed [18]. In contrast, visible flames with high NO_x emissions were always observed when HFO and coal were fired instead, though NO_x emissions were still lower than those generated in the normal air-fuel combustion in the same furnace [18]. Hence they pointed out that even though exhaust gas recirculation is not effective in reducing NO_x formation via the fuel-NO mechanism, it helps reduce NO_x through the enhanced NO reburning mechanism by providing locally sub-stoichiometric conditions [18].

A limited number of experimental studies [35, 36, 37] on the flame structure of complex fuels have been performed in a well-controlled environment, where operating parameters can be controlled and changed independently. Rodrigues et al. [35] investigated ethanol flame structure in both a hot diluted coflow and air. They found that the mixing with a hot diluted coflow, along with an enhanced evaporation of droplets, provided a richer gaseous mixture towards the spray axis and reduced the peak flame temperature [35]. They also investigated the effects of coflow temperature and dilution level, though the two parameters were not varied independently [36]. It was found that the coflow temperature and composition had little impact on the droplet mean size and velocity distribution, however it affected the flame liftoff heights by changing the droplet vaporisation timescale and the chemical timescale [36]. O'Loughlin et al. [37] performed planar imaging of OH and CH_2O of methanol spray flames in a hot and diluted coflow to understand the autoignition process. Similar to gaseous fuels, CH_2O was detected upstream of OH, reinforcing its important role as an ignition precursor [37]. Different from gaseous fuels, a double-flame-front was commonly found in methanol flames, which may be formed by local ignitable mixtures due to droplet evaporation [37].

Previous work [7, 13, 18, 34] has shown that complex fuels burning under MILD combustion conditions

exhibit distinct features to simpler fuels, such as hydrogen and methane. This is manifested in higher pollutant emissions [7, 18, 34], the existence of visible flames [13, 18] and combustion instabilities [13]. Part of the dissimilarities were ascribed to different physical properties of the fuels, however, because most of the previous work was not conducted in a well-controlled environment, the understanding of the underlying fundamentals is limited. In particular, prominent combustion instabilities reported for n-heptane flames in a pressurised MILD combustor [13] are not well understood. In order to provide more insights to the different behaviour of n-heptane flames, the present study is focused on prevaporised n-heptane to isolate the chemical effects. Moreover, results for n-heptane are directly compared to those for natural gas, ethylene and ethanol to demonstrate the distinctive characteristics of n-heptane. It is worth mentioning that n-heptane is of interest to a wide combustion community as it is a primary reference fuel for octane rating and is widely used as a surrogate fuel for diesel fuel in studies [38, 39, 40]. Experiments in the present study are conducted in a JHC burner as it provides a well-defined environment, emulating MILD combustion conditions. Visualisation of n-heptane flames is performed with conventional photography and laser-induced fluorescence of OH (OH-LIF) to reveal the flame structure, and an in-depth chemical analysis is performed to assist the explanation of the observed flame characteristics.

2. Experimental Details

2.1. Experimental Setup and Operating Conditions

Presented in Fig. 1 is the experimental setup of the current study, which is the same as a previous study [41]. A controlled evaporator and mixer (CEM) is used to preheat and premix n-heptane with carrier air. The temperature of the heater inside the CEM was set to 473 K by a control unit, which is higher than the boiling temperature (T_{boil} = 371 K) of n-heptane. The pipeline conveying the mixture between the CEM and the JHC burner was wrapped with insulation to minimise the heat loss and prevent the condensation. The temperature near the jet exit plane was measured to be 412 K, indicating that the entire line is above the vaporisation temperature. The equivalence ratio in the fuel jet was kept at 9.8, and the jet Reynolds number was maintained around 10,000. Turbulence properties of the JHC burner can be inferred from measurements in a previous study by Oldenhof et al. [11]. They performed two-component Laser Doppler Anemometry (LDA) to measure the flow field in the Delft jet-in-hot coflow (DJHC) burner [11], which has the same dimensions as the JHC burner in the present study.

[Figure 1 about here.]

The prevaporised mixture of fuel and carrier air is fed into the JHC burner through the central jet (ID = 4.6 mm), surrounded by a hot and vitiated coflow. The hot coflow was produced from combustion of a lean mixture of natural gas, hydrogen, air and nitrogen in a secondary porous-bed burner (ID = 82 mm), located 90 mm upstream of the jet exit plane. In order to create a coflow with different oxygen levels and temperature, the ratio of air/nitrogen was varied, meanwhile the ratio of natural gas/hydrogen was held constant. The resultant temperature and composition of hot coflow are given in Table 1. The mean

	Mole fraction of species in coflow			
T_{cofl} (K)	O_2	H_2O	CO_2	N_2
1250	0.091	0.107	0.036	0.766
1250	0.061	0.107	0.036	0.797
1250	0.030	0.107	0.036	0.827
1315	0.091	0.117	0.039	0.752
1315	0.061	0.117	0.039	0.783
1315	0.030	0.117	0.039	0.813

Table 1: List of coflow conditions: T_{cofl} is the coflow temperature measured by a thermocouple after correction for radiation. The mole fractions were determined by equilibrium calculations, and confirmed with measurements with a gas analyser.

coflow temperature was measured by a thermocouple and corrected for heat losses. The mole fractions were determined by equilibrium calculations, and confirmed with measurements with a gas analyser.

2.2. Optical Setup and Image Processing

Flames were visualised with conventional photography and laser-induced fluorescence of OH (OH-LIF). The photography was performed with a Canon EOS 60D SLR camera equipped with a standard 50 mm f/1.8 lens. The present study is focused on the region controlled by the hot coflow, where no soot was observed. Only the blue channel of each photograph is presented to indicate the intensity of CH* chemiluminescence near 430 nm [42] in the coflow-controlled region.

The OH radical was excited with the A-X (1,0) $Q_1(7)$ line (283.222 nm) as this excitation wavelength has a relatively constant ground-state population distribution throughout the expected range of the flame temperature [43]. Moreover, signal from this excitation wavelength is strong with reduced interference from the stray light [44]. The OH-LIF signal was detected using a 16-bit Princeton Instruments ICCD camera, equipped with a 78 mm f/3.8 standard UV fixed focal length lens. In front of this lens, a dichroic mirror was mounted at a 45 degree angle to the laser sheet. This mirror has a greater than 80% reflectance in the range of 270 to 340 nm, but transmits other wavelengths, thereby acting as a broadband filter. Each instantaneous image was corrected for dark charge, detector attenuation, background and laser power variations. The OH-LIF signal was semi-quantified using a method previously reported by Medwell et al. [43].

3. Results and Discussion

3.1. Liftoff heights

The liftoff height is an important parameter of a flame, which has been investigated extensively in both conventional combustion and MILD combustion regimes [8, 21, 33, 45, 46]. Under conventional combustion conditions the liftoff height is expected to decrease with the increase of oxygen level in the oxidant stream

Fuel	Re	V_{jet} (m/s)	T_{cofl} (K)	T_{jet} (K)	$X_{carrier}$
n-heptane	10,000	50	1250	412	0.84
ethanol	10,000	44	1250	412	0.60
ethylene[a]	10,000	17	1300	320	none
natural gas[a]	4000	10	1400	320	none

Table 2: Experimental conditions for various flames compared in Fig. 2: Re is the bulk jet Reynolds number; V_{jet} is the jet exit velocity; T_{cofl} is the coflow temperature; T_{jet} is the jet temperature; $X_{carrier}$ is the mole fraction of carrier gas in the jet. Data for the cases superscripted with "a" is provided by a previous study [45]. It should be noted that pure natural gas flames cannot be sustained at Re = 10,000 in a coflow with 3% O_2 [45].

due to enhanced reactivity. However, previous studies of methane- and ethylene-based flames [8, 45] reported that the apparent liftoff height changed non-monotonically as the oxygen level increased. These studies [8, 45] investigated five coflow levels, including 3%, 4.5%, 6%, 7.5%, and 9% by volume. Particularly, as shown in Fig. 2, natural gas and ethylene flames are the most lifted in the coflow with 6% O_2, and the liftoff height in the 3% O_2 case is shorter than that in the 9% O_2 case. The largest liftoff height at the 6% O_2 case was ascribed to the transition away from MILD combustion regime with the increase of the coflow oxygen level [45].

Due to the uncertainty associated with identifying the apparent liftoff heights, the previous study used a range of identifiable positions estimated from CH* chemiluminescence (SNR 30:1) to define the liftoff height [45]. As some flames in a hot and diluted coflow show very low flame luminosity and gradual ignition processes, this approach is considered to be more appropriate than using a single cut-off value [45]. In order to be consistent with previous measurements and enable the comparison of various fuels, the blue channel of the photograph (Fig. 3) is used to estimate a range of liftoff heights in the present study. The lowest and highest identifiable liftoff positions are used to define the mean liftoff height. The mean liftoff height of each fuel is then normalised to their maximum liftoff height amongst three coflow cases. The variation in the two positions are plotted as error bars in Fig. 2, however they indicate the uncertainty rather than an inherent error with the measurements. The conditions of various flames compared in Fig. 2 are listed in Table 2.

[Figure 2 about here.]

To investigate the liftoff behaviour of *n*-heptane flames under conditions relevant to MILD combustion, experiments were conducted with prevaporised *n*-heptane, carried by air, injected into a 1250-K coflow with various oxygen concentrations (X_{O_2} = 3-9%). Photographs of *n*-heptane flames under the three coflow conditions are displayed in Fig. 3, and photographs of ethanol flames under the same coflow conditions are included for comparison. The jet Reynolds number of ethanol flames was also kept around 10,000. The bottom edge of all the photographs (Fig. 3) indicates the location of the jet exit plane. All the photographs in this section were taken with an ISO sensitivity of 1600, exposure time of 1/15 second and an f-number of 2. The same colour scale is applied to all the photographs in Fig. 3, which is chosen to emphasise the low

signal near the flame base, hence much of the photographs appear saturated.

[Figure 3 about here.]

The liftoff heights of n-heptane flames show a different trend to that of ethanol flames under the same coflow conditions. As displayed in Fig. 3, the apparent liftoff height of n-heptane flames monotonically decreases as the coflow oxygen level increases from 3% to 9%. This matches with the expectation of conventional combustion, where the increasing oxygen level improves the reactivity, thereby reducing the liftoff height.

The apparent liftoff height of ethanol flames in the coflow with 3% O_2 is the shortest, closely followed by the 9% O_2 case, then the 6% O_2 case. This non-monotonic trend is consistent with previous observations of natural gas and ethylene flames in the same JHC burner: the largest liftoff height also occurred within the coflow with 6% oxygen as shown in Fig. 2.

The non-monotonic change in the liftoff heights is likely to be a product of competing effects of local scalar dissipation rate and mixture reactivity. A change in the coflow oxygen level results in a shift in the ignition location, thereby changing its relative position to the jet shear layer. Indeed, transient flamelet simulation results [46] suggested that when the coflow oxygen level increases from 3% to 9% by volume, the ignition location shifts to a higher scalar dissipation rate region, whilst the reactivity of flames is enhanced. It is logical to expect that the coflow oxygen level at which the maximum liftoff height occurs is fuel dependent as the change in the flame reactivity is determined by the fuel chemistry. Nonetheless, this coflow oxygen level was reported to be 6% for methane-, ethylene-based flames [45] and ethanol flames surrounding by hot diluted coflows. The same trend in methane- and ethylene-based flames may be attributed to the increased importance of H_2/O_2 chemistry in their oxidation pathway due to a higher reactant temperature [47, 48]. A sensitivity analysis [49] revealed that the oxidation rate of ethanol is most sensitive to the following reactions in general:

$CH_3+HO_2 \leftrightharpoons CH_4+O_2$

$H+HO_2 \leftrightharpoons H_2+O_2$

$CH_3CH_2O+M \leftrightharpoons CH_3+CH_2O+M$

$CH_3+CH_3(+M) \leftrightharpoons C_2H_6(+M)$

The sensitivity analysis indicates the importance of hydrogen oxidation and methyl recombination channels in ethanol oxidation, which may lead to the similarities between ethanol, methane- and ethylene-based flames.

A detailed sensitivity analysis by Curran et al. [38] found that the following types of reactions promote the overall oxidation rate of n-heptane most in general:

$xC_7H_{14}OOH\text{-}yO_2 \leftrightharpoons nC_7\text{ket } xy+OH$

$nC_7H_{16}+OH \leftrightharpoons \text{heptyl radical}+H_2O$

In $xC_7H_{14}OOH\text{-}yO_2$, x is the number of the carbon attached by the OOH group, and y refers to the site where the O_2 group is attached [38]. As for nC_7ket xy (ketohydroperoxide), x is the number of the carbon attached by the keto group, and y indicates the site where the hydroperoxy group is attached [38]. Subsequently, nC_7ket xy is decomposed to oxygenated species and OH radical, which increases the system

reactivity via chain branching [38]. It is also pointed out that as temperature increases, the sensitivity coefficients of the above reactions decrease. This is because the decomposition of hydroperoxy-heptyl and heptyl radicals, such as C_7H_{15}, preferentially goes through unimolecular reactions instead of successive O_2 addition [38].

The following types of reactions are very effective in inhibiting the overall oxidation process [38]:

$xC_7H_{14}OOH\text{-}y \leftrightharpoons C_7H_{14}+HO_2$

alkyl radical $\leftrightharpoons$ olefin+methyl or smaller alkyl radical

These two types of reactions inhibit the overall oxidation of *n*-heptane as they produce stable olefins and less reactive radicals like HO_2 [38]. This sensitivity analysis suggests that the overall oxidation of *n*-heptane is very sensitive to its fuel-specific decomposition reactions, which are different from the hydrogen oxidation and methyl recombination channels seen in other fuels.

3.2. Spatial evolution of OH—laser-induced fluorescence of OH

The photographs in the preceding section demonstrate a different liftoff trend for *n*-heptane flames compared to fuels studied previously. In order to reveal the flame structure of *n*-heptane, instantaneous imaging of OH was performed using the laser-induced fluorescence (LIF) technique. The concentration and distribution of OH have been frequently investigated in literature due to its importance. For example, location of OH was used to identify the location of flame front in a jet-in-cross-flow burner [25], and its intensity variation indicated the relative distribution of temperature in a FLOX® burner [50]. Similarly, the evolution of OH was used to understand the autoignition process and flame stabilisation mechanism in a vitiated coflow burner [22].

Representative instantaneous OH-LIF images for *n*-heptane jet flames surrounded by the 1250 K coflow and the 1315 K coflow are presented in Fig. 4(a)-(d). In the vertical direction, the centre of each image is at X/D = 3.2 (15 mm), X/D = 6.4 (29 mm) and X/D = 12.9 (59 mm) above the jet exit plane. The left edge of each image is coincident with the jet centreline (R/D = 0, and R is the radial distance from the jet centreline). The same color scale was chosen across all the images to emphasise low OH signal, causing some images to appear saturated. Images presented here were smoothed by median filtering to improve the signal-to-noise ratio. Time-averaged OH-LIF images showed the same trend as instantaneous images, but are not presented here for brevity.

A faint OH signal was captured from the *n*-heptane flame in the 1250 K coflow with 3% oxygen as shown in the image centred at X/D = 3.2 (Fig. 4(a)), however, no discernible OH signal was observed in the corresponding 9% O_2 case at the same height. This contradicts the visual appearance of *n*-heptane flames shown in the photographs, where the flame is apparently more lifted in the 3% O_2 case than the 9% O_2 case. It is worth mentioning that the *n*-heptane flame also appears more lifted in the 3% O_2 case in simultaneously recorded OH^* chemiluminescence images (not shown for brevity). Given the close correlation between heat release rate and chemiluminescence intensity [41], and the strong dependence of radiation on the temperature, it can be inferred that reactions contributing to the main heat release and temperature rise take place further downstream in the 3% O_2 case than the 9% O_2 case. Previous studies for hydrogen-

and ethylene-based flames in a hot coflow also reported a build-up of OH upstream of the base of apparently lifted flames [8, 22, 51]. It was found that the formation and transportation of ignition precursors play a significant role in stabilising jet flames in a highly heated and diluted environment [23].

At X/D = 6.4, the structure of OH in the *n*-heptane flames become similar regardless of the oxygen level in the coflow (Fig. 4(a) and (b)). In particular, a well-defined region of high level OH, connecting with a thinner "tail" of lower level OH, exists in both the 3% and 9% O_2 cases. A similar OH structure, referred to as a transitional flame structure, has been reported previously for ethylene flames within a hot coflow with X_{O_2} = 9% but not within a coflow with X_{O_2} = 3% [8, 32]. The same phenomenon was also reported for a hydrogen flame in a hot coflow with $X_{O_2} \approx 15\%$ [51]: a transitional flame structure, with a weak OH contour upstream of the main OH mass fraction field, was simulated by a probability density function (PDF) transport combustion coupled with the standard k-ε turbulence model [51]. A similar transitional flame structure has also been identified in computational models of different methane- and ethylene-based flames in a coflow with Y_{O_2} = 11.4% [52] and in a coflow with X_{O_2} = 9% [53]. The occurrence of this transitional flame structure was used to indicate the transition away from the MILD combustion regime [53]. Amongst the previous studies and the present results, *n*-heptane is the only fuel that demonstrates a transitional flame structure in a 3% O_2 coflow.

Instantaneous images of OH-LIF for *n*-heptane flames in 1315 K coflows with 3% and 9% O_2 are presented in Fig. 4(c) and Fig. 4(d), respectively. At X/D = 3.2, the OH level increased drastically due to the increased reactivity in the 1315 K coflow, compared to that in the 1250 K coflow. Moreover, as the coflow temperature increased to 1315 K, the formation of OH occurred further upstream.

Typical instantaneous OH images of ethanol flames, issuing into the 1250 K coflow (Fig. 4(e)-(f)) and the 1315 K coflow (Fig. 4(g)-(h)) with 3% and 9% O_2, are included in this section for comparison. Discernible OH-LIF signal was observed in the ethanol flame for the 3% O_2 case as shown in the image centred at X/D = 3.2 (Fig. 4(e)), stronger than that in the *n*-heptane flame under the same condition.

Very little OH was produced in the ethanol flame in the 9% O_2 case at X/D = 3.2, which is consistent with photographs of ethanol flames where they appear more lifted in the 9% O_2 case than the 3% O_2 case. At the image centred at X/D = 6.4, faint OH signal upstream of a region of strong OH (transitional flame structure) was observed in the 9% O_2 case.

The OH level in the ethanol flames increased significantly when the coflow temperature increased from 1250 K to 1315 K. More importantly, the structure and evolution of OH in the ethanol flames also became similar between the 3% and 9% O_2 cases. At X/D = 3.2, a rapid transition from weak to strong OH is apparent in the ethanol flames in the 3% and 9% O_2 coflow, which was only observed in the 9% O_2 case in the 1250 K coflow. In other words, the flame structure for ethanol flame is different between the 3% and 9% O_2 cases in the 1250 K coflow, however these differences disappear in the 1315 K coflow. This indicates that the flame stabilisation mechanism changes with both the coflow oxygen level and temperature.

Imaging of OH-LIF did not show the formation of ignition kernels for either ethanol or *n*-heptane flames in the present study. A previous experimental study by Oldenhof et al. [33] reported that ignition kernels of OH were first observed at approximately 80 mm above the jet exit plane, which were then transferred

Fuel	T(K)	Z_{st}	X_{O_2}	X_{fuel}	X_{N_2}	X_{H_2O}	X_{CO_2}
n-heptane	1250/1222/950	0.0098	0.030	0.0027	0.82	0.11	0.036
n-heptane	1250/1174/950	0.0288	0.090	0.0082	0.76	0.10	0.036
ethanol	1250/1210/950	0.0164	0.030	0.0099	0.82	0.10	0.036
ethanol	1250/1144/950	0.0477	0.088	0.029	0.74	0.10	0.035
ethylene	1250/1223/950/934	0.01	0.030	0.0099	0.82	0.10	0.036
ethylene	1250/1176/950/903	0.0296	0.089	0.029	0.74	0.10	0.035

Table 3: Inputs for various cases in the closed homogeneous reactor model. The mole fractions of minor species for various cases are provided in supplemental material.

downstream while growing in size. In the previous study the maximum coflow temperature varied from 1460 K to 1540 K, and the mass fraction of coflow oxygen varied from 8.5% to 9.5%. However, in the present study the investigated hot coflow is at two temperatures (1250 K and 1315 K) with the coflow oxygen level varying from 3% to 9% by volume. As suggested by OH-LIF results presented in this section, the coflow temperature and oxygen level affect the jet flames substantially, and they are likely to cause differences in the ignition processes observed between the two studies.

[Figure 4 about here.]

3.3. Temporal evolution of OH—closed homogeneous reactor

Compared to smaller hydrocarbons studied previously, turbulent *n*-heptane flames demonstrate distinctive characteristics in terms of the liftoff heights and the structure of the hydroxyl radical (OH) as discussed in Sections 3.1 and 3.2. In order to have a more complete picture of the ignition process of *n*-heptane flames, calculations were performed using a closed homogeneous reactor model with the AURORA solver in Chemkin. The chemical kinetics mechanism used for the different fuels are: *n*-heptane [39], consisting of 88 species and 387 reactions; ethanol [49], consisting of 53 species and 383 reactions; ethylene[54], consisting of 57 species and 325 reactions. The required inputs for calculations in the closed homogeneous reactor model are summarised in Table 3.

Stoichiometric mixtures, rather than the most reactive mixtures, for the various fuels are investigated in this section. Though the minimum ignition delay occurs at the most reactive mixture fraction (Z_{mr}) in a cold-fuel-hot-coflow configuration, previous studies [46, 55] have shown that the differences in the ignition delay between Z_{st} and Z_{mr} are small. The first ignition event occurs at a mixture fraction leaner than Z_{st} due to the competing effects of high temperature at a leaner mixture fraction and high fuel concentration at a richer mixture fraction. One of the objectives of the present calculations is to investigate these competing effects. Hence, results for stoichiometric mixtures at constant temperatures, neglecting the impact of mixing cold fuel with hot oxidant on the temperature, will be presented. Meanwhile, results at variable temperatures determined from mixing will also be discussed.

The temporal profiles of OH calculated using Chemkin are presented in Fig. 5 to provide more insight to the ignition processes. The temperature of all the stoichiometric mixtures investigated was kept at 1250 K

(same as the coflow temperature used in the experiments) neglecting the impact of mixing cold fuel with hot oxidant on the temperature. It should be noted that major species in the hot oxidant were kept the same as coflows in the experiments (shown in Table 1), and equilibrium levels of minor species were included because the inclusion of minor species in the oxidant has previously been reported to considerably affect the reactivity of MILD flames and reduce the ignition delays [27, 56]. It should be noted that the stoichiometric mixture fraction is reported here instead of equivalence ratio to reveal the difference in the mixture composition among all the fuels.

For *n*-heptane flames, a more rapid build-up of OH radical is shown in the 9% O_2 case than the 3% O_2 case, suggesting a faster ignition at a higher oxygen level. A common feature between the 9% and 3% O_2 cases is a single continuous increase in the OH mole fraction before it reaches its maximum concentration.

The impact of oxygen level is more evident in ethanol flames than *n*-heptane flames. Particularly the gradient of the OH profile is significantly steeper in the 9% O_2 case than that in the 3% O_2 case. Moreover, in the 3% O_2 case there is a period of almost constant OH concentration between 0.6 ms and 1.6 ms. Compared to the temporal profile of OH in the 9% O_2 case, the profile in the 3% O_2 case reflects a prolonged two-stage ignition event.

The effect of oxygen level is more pronounced in ethylene flames in comparison to *n*-heptane and ethanol flames. A two-stage ignition is clearly shown in the temporal profile of OH in the 3% O_2 case, which was also observed in a stoichiometric mixture of ethylene and hot oxidant at 1100 K [56]. Notably, the increase of OH at each stage of ignition in the 3% O_2 case is much smoother and slower than that in the 9% O_2 case. The gradual accumulation of OH temporally, together with a more uniform spatial distribution of OH radical as revealed by OH-LIF of ethylene flames in previous studies [8, 56], suggests that reducing the oxygen level from 9% to 3% shifts a fast reacting flame to a more gradual and slowly igniting flame, which then conceptually agrees more closely with the distributed nature of MILD combustion.

[Figure 5 about here.]

A prolonged ignition process at a lower oxygen level can also be achieved for *n*-heptane flames but at a much lower temperature as shown in Fig. 6. Results at 950 K are presented as the temporal profile of OH for *n*-heptane starts resembling that for ethanol given the same oxidant composition. At 1250 K, it takes 1.6 ms for OH to reach the peak value in the 9% O_2 case, while it takes 3.2 ms in the 3% O_2 case. At 950 K, this time increases from 173 ms to 558 ms when the oxygen level decreases from 9% to 3%. As expected, the differences in the growth of OH between the 3% and 9% O_2 cases are more prominent for ethanol and ethylene flames at 950 K, though additional features appear in the OH profile for the ethylene flame.

[Figure 6 about here.]

In the configuration of a cold fuel jet issuing into a hot and diluted coflow, the temperature of a mixture is determined by the energy balance at a given composition. Considering the impact of mixing on the resultant temperature, calculations were also performed for *n*-heptane, ethanol and ethylene flames at a temperature determined from mixing at the stoichiometric mixture fraction (Z_{st}) in the closed homogeneous reactor.

It is worth noting that the oxidant compositions in all the calculations were kept the same as the coflow compositions in the experiments.

Interestingly, for both *n*-heptane and ethanol flames the OH profiles in the 3% and 9% O_2 cases are not dissimilar as shown in Fig. 7(a). In fact, the growth in the hydroxyl radical concentration is slightly faster in the 3% O_2 case than the 9% O_2 case. When the oxygen level changes from 9% to 3%, the stoichiometric mixture fraction is smaller meanwhile the temperature of the mixture considerably increases. Taking *n*-heptane flames as examples, Z_{st} changes from 0.0288 to 0.0098, and the initial temperature of the mixture increases from 1174 K to 1222 K. The effect of a lower fuel concentration at a smaller Z_{st} is overcompensated by the effect of a higher temperature, rendering a faster ignition in the 3% O_2 case than the 9% O_2 case. It is worth pointing out that the effect of strain rate is neglected in the current calculations, however, in practical combustion systems, a higher strain rate is expected at a larger Z_{st} due to turbulence, which will retard the ignition in the 9% O_2 case even further.

When the oxygen level decreases from 9% to 3%, the changes in the mixture fraction and the resultant temperature of the stoichiometric mixture are similar between ethylene and *n*-heptane. The gradient of the OH profile in the 9% O_2 case is reduced when considering the resultant temperature, however the increase in the OH concentration is still more rapid in the 9% O_2 case than that in the 3% O_2 case. As can be seen in Fig. 7(b), the ethylene mixture is very reactive even at a lower temperature, leading to negligible changes in the ignition process. In order to examine the impact of the mixture temperature, calculations for ethylene mixed with a 950 K hot oxidant at two oxygen levels were performed, results from which are presented in Fig. 8. After considering the difference in the temperature after mixing, the growth rate of OH radical becomes similar between the 3% and 9% O_2 cases, consistent with *n*-heptane and ethanol mixing with a 1250 K oxidant (Fig. 7(a)).

[Figure 7 about here.]

Overall, given the same temperature, the temporal evolution of OH profiles demonstrates strong fuel-dependent ignition characteristics under conditions relevant to MILD combustion. This phenomenon can be related to homogeneous charge compression ignition (HCCI) engines, in which well-mixed fuel and air are compressed sufficiently to auto ignite. The performance of an HCCI engine was found to be highly sensitive to the fuel properties as a consequence of ignition being kinetically controlled [57]. Given the shared similarities between HCCI engines and MILD combustion (albeit with differences in pressure), the importance of fuel type on the flame structure and behaviour under MILD combustion conditions is to be expected. For conventional combustion, ignition can be defined as a rapid growth of temperature and chain carriers, initiated by chain-branching reactions [47]. Chain carriers are active radicals, such as atomic H and O, OH, HO_2 and CH_3 [47]. The dominating chain-branching reactions and chain carriers during the ignition process are significantly affected by the temperature of a given mixture. At higher temperatures, above approximately 1200 K, it is recognised that the reaction $H + O_2 \rightarrow O + OH$ dominates hydrocarbon ignition [47, 58, 59]. The decomposition of ethyl, vinyl and other radicals produces atomic H, while the recombination of methyl radicals produces relatively inert C_2H_6, which terminates the chain-branching reaction [47].

[Figure 8 about here.]

When the temperature ranges from 850 K to 1200 K, a reacting system can undergo two-stage ignition [47]. For most hydrocarbons, the second-stage ignition or the thermal runaway of ignition, is dominated by the high-temperature ignition mechanism mentioned in the preceding paragraph. The first-stage ignition or cool ignition is featured with a modest temperature increase, in which a complex fuel-dependent low temperature oxidation mechanism comes into play [60]. Previous studies show that fuel is partially consumed, and H_2O_2 builds up steadily during the first-stage ignition [47]. The decomposition of H_2O_2 initiates at a temperature around 1000 to 1100 K, producing a large amount of OH radicals and triggering the second-stage ignition [47]. Gibson et al. [61] found that formaldehyde (CH_2O) is an important precursor for the second-stage ignition, meanwhile the decomposition of H_2O_2 at sufficiently high temperature augments the chain-branching reaction. In previous studies, the temperature of a MILD combustion system ranged from 800 K to 1600 K [26, 45], where two-stage ignition may occur. Hence it can be deduced that the impact of fuel type cannot be overlooked under MILD combustion conditions, and its importance is dependent on the coflow temperature.

3.4. Fuel chemistry analysis

Experimental results in the preceding sections suggest that *n*-heptane flames behave differently from ethanol and ethylene flames issuing into the 1250 K coflow with 3% O_2, emulating MILD combustion conditions. This is consistent with previous experimental results in a pressurised reverse-flow MILD combustor, in which MILD combustion of *n*-heptane failed to be established at high equivalence ratios under elevated pressures, meanwhile stable ethanol flames were stabilised under all the conditions investigated [13]. A further analysis on the fuel chemistry is performed in this section to investigate the discrepancies observed in the experiments.

According to the classifications of MILD combustion regime based on some common features on the heat production rate profiles [29, 30, 31] (discussed in Section 1), previous work [41] has found that the heat production rate profiles of ethanol flames show two important features when the MILD combustion regime is reached. Firstly, the location of the peak heat production rate mismatches with the location of stoichiometric mixture fraction [41]. Secondly, the transition of ethanol flames from conventional combustion regime to MILD combustion regime is associated with a net negative heat release region, which is more likely to disappear at a high strain rate [41]. At a low strain rate, this regime can only be established in an oxidant stream with a low O_2 level [41].

Experimental results from the JHC burner in the present study and in a pressurised reverse-flow MILD combustor [13] reveal that *n*-heptane flames did not exhibit typical MILD combustion characteristics, in contrast to ethanol flames under the same conditions. Hence it is hypothesised that *n*-heptane flame does not share the two common MILD combustion signatures with ethanol in the heat production rate profile under the same conditions. As the disappearance of a net negative heat release region is relevant to pyrolytic reactions, it is necessary to first analyse and compare the chemical kinetics of ethanol and *n*-heptane.

Primary kinetic pathways in the combustion of ethanol are illustrated in Fig. 9(a). It has been demonstrated that ethanol (CH_3CH_2OH) goes through H-atom abstraction reactions first, producing three C_2H_5O isomers [49]. These isomers are mostly converted to acetaldehyde (CH_3HCO), a majority of which is in turn converted to CH_2HCO and CH_3CO through dehydrogenation. As also seen in methane oxidation, these two species are then decomposed to CH_3 and CO. When the available oxygen is limited and the temperature is high, pyrolysis of ethanol takes place, subtracting heat from the system [41]. Smaller hydrocarbons such as CH_3, C_2H_5 are produced by the decomposition of ethanol. This, in turn, is followed by methane pyrolysis mechanism, involving recombination of methyl radicals and dehydrogenation of vinyl radicals [49].

As shown in Fig. 9(b), the unimolecular decomposition of *n*-heptane produces one of the four C_7H_{15} isomers and one H atom, or two alkyl radicals, such as pC_4H_9 and nC_3H_7. Some C_7H_{15} isomers react with O_2 and produce C_7H_{14} isomers. The decomposition of C_7H_{15} and C_7H_{14} isomers produces smaller alkyl radicals and olefins, subsequently producing even smaller hydrocarbons, such as C_2H_4, through secondary fuel pyrolysis. Afterwards, similar to ethanol chemistry, these smaller hydrocarbons go through a series of reactions and produce CO, eventually being converted to CO_2 in the end.

[Figure 9 about here.]

It is demonstrated in Fig. 9 that in comparison to ethanol, the pyrolysis of *n*-heptane can proceed through more possible reaction channels, such as the decomposition of the parent fuel, various alkyl radicals and olefins. An analysis of heat production profiles of *n*-heptane flames was performed to show how pyrolytic reactions behave at conditions relevant to MILD combustion. Laminar flame calculations for *n*-heptane flames were performed with the oxidiser inlet modelled as the 1250 K experimental coflow with 3% and 9% O_2. The *n*-heptane chemical kinetic mechanism used in the present study is from Yoo et al. [39]. Results for ethanol flames under the same conditions, using a chemical kinetic mechanism from Marinov et al. [49], were included for comparison. The separation of the two inlets was 20 mm, and the stagnation plane was at 10 mm.

The heat production profiles of ethanol flames in the oxidant stream with 9% and 3% O_2 at three strain rates are shown in Fig. 10. Laminar flame calculations were performed with a range of strain rates, and results at three strain rates were selected to show the typical structure. The heat production rate at the stoichiometric mixture fraction for each strain rate is marked with a diamond on the line plots. The heat production rate profiles of ethanol flames in the 9% O_2 oxidiser show similar features to that in the 3% O_2 case. The peak heat production rate does not occur at Z_{st} at any of the strain rates investigated for any of the cases. For the 9% O_2 case, the net negative heat release region disappears at a strain rate of 1510 s^{-1} (referred to hereafter as the critical strain rate).

[Figure 10 about here.]

When the oxygen level reduces to 3%, the critical strain rate, at which the net negative heat release region is eliminated, reduces dramatically to a strain rate of 131 s^{-1} (as shown in Fig. 10). As identified in a previous study [41], one of the major contributors for heat subtraction in ethanol flames in the 3% and 9% oxidisers is $CH_3CH_2OH(+M) \rightleftharpoons CH_3+CH_2OH(+M)$ in the forward direction. This reaction is strongly dependent on the

flame temperature as it has a high activation energy. Hence this reaction is greatly suppressed in the oxidant stream with lower oxygen level due to a much lower flame temperature. In addition, the concentration of O_2 is higher in the pyrolytic region in the 3% O_2 case than that in the 9% O_2 case [41]. As fuel pyrolysis generally takes place in an environment with low local oxygen concentration and high temperature, it was concluded that the suppression of the pyrolytic reactions is a result of a higher local availability of oxygen and lower flame temperature [41].

The heat production profiles of n-heptane flames display features very different from ethanol flames. For n-heptane flames in the oxidant stream with 9% O_2, an inflection point, where the gradient of the heat production profile changes, exists at the lean side of the peak production rate Z_{hmax}. At a strain rate of 80 s^{-1}, the inflection point occurs very close to Z_{st}. As the strain rate increases, the location of the inflection point shifts away from Z_{st}. Though Z_{hmax} and Z_{st} are not matched at all the strain rates investigated, the net negative heat release region does not vanish, even at a strain rate approaching extinction. It should be noted that calculations for n-heptane flames were performed with strain rates spanning from 80 s^{-1} to 2900 s^{-1}, and representative results at three strain rates are presented in Fig. 11 for clarity.

As depicted in Fig. 11(b), the heat production profiles of n-heptane flames in the 3% O_2 case differ from those in the 9% O_2 case. An inflection point can only be seen vaguely at a strain rate of 80 s^{-1}, and the peak production rate occurs very close to Z_{st}. The location of the peak production rate shifts away from Z_{st} with the increasing strain rate. The net negative heat release rate is reduced at a higher strain rate, however, different from ethanol, this net negative heat release region still exists at a high strain rate even in the oxidant stream with low O_2 level. The heat production rate profiles of n-heptane flames in Hot Oxidant Diluted Fuel configuration were investigated at 10 bar by de Joannon et al. [62]. In this configuration, n-heptane diluted with N_2 was injected into heated air. They found that the mismatch of Z_{hmax} and Z_{st}, and the absence of a net negative heat release region only occurred when n-heptane was diluted with 99% N_2 by volume [62].

[Figure 11 about here.]

Figure 11 indicates that the net negative heat release region of n-heptane flames does not disappear as the O_2 level decreases, dissimilar to ethanol flames. However, similar to ethanol flames, there is a significant decrease in the flame temperature as the O_2 level changes from 9% to 3% (as shown in Fig. 12(a)). In addition, Fig. 12(b) shows that the concentration of O_2 is higher in the 3% O_2 case than that in the 9% O_2 case in the pyrolytic region (where the net heat release region is in Fig. 11), although the initial O_2 level in the oxidiser is lower. Therefore, the amount of O_2 in the oxidiser has the same impact on the flame temperature and O_2 availability in n-heptane flames as ethanol flames, nevertheless, its impact on the heat release seems to be different. To understand this difference, a more detailed analysis was performed and identified important reactions contributing to $\gtrsim$ 60% of the total heat subtraction at the location of minimum net heat release. These major endothermic reactions for the 3% and 9% O_2 cases are summarised in Table 4.

[Figure 12 about here.]

The most prominent change comes from reaction $C_2H_5(+M) \rightleftharpoons H+C_2H_4(+M)$, the contribution of which to the total heat subtraction increases by nearly 11% as the O_2 level reduces. It is worth noting that this

reactions	activation energy (cal/mole)	importance in the 9% case	importance in the 3% case
15. $C_2H_5(+M) \rightleftharpoons H+C_2H_4(+M)$	1.00E+04	20.8%	31.7%
124. 1-$C_4H_8 \rightleftharpoons C_3H_5$-a+$CH_3$	7.10E+04	13.2%	5.0%
241. $C_3H_2+H_2O \rightleftharpoons C_3H_3+OH$	1.57E+04	10.1%	0.1%
284. $nC_7H_{16} \rightleftharpoons pC_4H_9+nC_3H_7$	1.21E+05	8.0%	5.5%
148. 1-$C_5H_{10} \rightleftharpoons C_2H_5+C_3H_5$-a	7.40E+04	7.8%	4.4%
106. $nC_3H_7 \rightleftharpoons CH_3+C_2H_4$	2.84E+04	5.7%	9.4%
133. $pC_4H_9 \rightleftharpoons C_2H_5+C_2H_4$	2.96E+04	5.2%	9.2%
327. 2-$C_7H_{15} \rightleftharpoons pC_4H_9+C_3H_6$	3.01E+04	3.8%	8.4%

Table 4: Important endothermic reactions of n-heptane flames in the oxidant stream with 3% and 9% O_2 level. The importance of each reaction is represented by their contribution to the total heat subtraction in percentage.

reaction has the lowest activation energy among all the listed reactions. The contribution of reaction 106, 133, 327 increases in the 3% O_2 case, and the activation energy of these reactions also falls to the low end of the primary reactions. In contrast, reaction 124, 284 and 148, which have much higher activation energy, contribute less to the total heat subtraction when the coflow oxygen level decreases from 9% to 3%.

When the oxygen level reduces from 9% to 3%, the importance of endothermic reactions with relatively high activation energy reduces, meanwhile endothermic reactions with low activation energy are enhanced, indicating a higher reactivity of the system in terms of fuel pyrolysis. Therefore, in comparison to ethanol flames, the impact of lowered flame temperature caused by a low oxygen level on suppressing pyrolytic reactions is significantly dampened as the pyrolysis of n-heptane can proceed through alternative channels favouring lower activation energy.

The analysis presented suggests that compared to ethanol, it is more difficult for n-heptane to meet the MILD combustion criteria in terms of heat production profiles. This agrees with the analysis on the temporal evolution of OH for n-heptane flames, which helps explain the distinctive characteristics of n-heptane flames under conditions relevant to MILD combustion conditions.

4. Conclusions

In order to improve the understanding of the behaviour of n-heptane flames under conditions relevant to MILD combustion, an experimental study was performed with prevaporised n-heptane flames in a JHC burner. Imaging of flames through conventional photography and OH-LIF revealed that n-heptane flames failed to demonstrate MILD combustion characteristics typically seen in other fuels such as ethanol, methane-, and ethylene-based flames.

Flame liftoff heights of the various flames were determined through visual observations using photography. The results revealed that the liftoff height for n-heptane flames decreases gradually with an increase in the

oxygen level in the coflow. In contrast, the liftoff height for ethanol, ethylene and natural gas flames initially increases when the coflow oxygen level rises to 6%, then decreases as it rises to 9%. This non-monotonic trend in liftoff height is likely to result from opposing effects of local scalar dissipation rate and mixture reactivity. Specifically, a change in the coflow oxygen level shifts the ignition location, consequently changing its relative position to the jet shear layer. The same response in liftoff heights for ethanol, ethylene and methane-based flames is attributed to similarities in their oxidation pathway, while a distinct and complex chemistry is suspected to be responsible for the differences in the *n*-heptane flames.

The occurrence of the transitional flame structure, a change from weak to strong OH at the apparent liftoff height, was found to correlate with the transition away from MILD combustion regime in previous studies [8, 53]. The OH-LIF images of the *n*-heptane flames show a well-defined region of high level OH, followed by a thinner "tail" of lower level OH in both the 3% and 9% O_2 cases. However, this transitional flame structure was only observed in the coflow with $X_{O_2} \geq 9\%$ for ethanol, methane- and ethylene-based flames. This again demonstrates that the coflow oxygen level affects *n*-heptane flames differently in comparison to other fuels.

The absence of a net negative heat release region, one of the common signatures in MILD combustion regime, indicates the suppression of pyrolytic reactions and thus the soot abatement in MILD combustion [29, 30, 31]. For ethanol flames, this net negative heat release region disappears in an oxidiser with low O_2 level or at a high strain rate. In contrast, a net negative heat release region exists in *n*-heptane flames despite the low O_2 level and high strain rates. It was found that the pyrolysis of *n*-heptane proceeds through many possible reaction channels as a consequence of its complex chemistry. When the oxygen level is reduced, the *n*-heptane flame temperature decreases, and the importance of endothermic reactions, with much lower activation energy, increases. Hence the reactivity of the system in terms of pyrolysis is enhanced, which explains the difficulties in diminishing the net negative heat release region and meeting one of the criteria of MILD combustion.

In addition to soot reduction, MILD combustion is also associated with a distributed reaction with a small temperature gradient [6]. In the present study, temporal evolution of OH was investigated to demonstrate any discrepancy in the ignition process temporally. When the temperature of stoichiometric mixtures is maintained at 1250 K, a reduction in the oxygen level from 9% to 3% makes the ignition process more prolonged and steady for ethanol and ethylene flames, however it does not have profound effects on the ignition process for *n*-heptane flames. When the mixture temperature is reduced to 950 K, a slow and steady build-up of OH is found in the 3% O_2 case for *n*-heptane flames, which conceptually agrees more closely with the distributed nature of MILD combustion. This is also consistent with previous experimental results in a pressurised reverse-flow MILD combustor: MILD combustion of *n*-heptane was more difficult to stabilise than ethanol under the same conditions [13]. Hence, it can be inferred from the above results that changing the initial conditions, such as lowering the mixture temperature, can help achieve a more distributed MILD combustion of *n*-heptane.

5. Acknowledgements

This research is funded by the China Scholarship Council and The University of Adelaide through a joint postgraduate scholarship. Funding from the Australian Research Council (ARC) and United States Air Force Asian Office of Aerospace Research and Development (AOARD) is gratefully acknowledged. The assistance provided by Mr. Chia Xiong Thong and Ms. Kathleen Lask in the laboratory is greatly appreciated.

6. References

[1] J. Wünning, J. Wünning, Flameless oxidation to reduce thermal NO-formation, Prog. Energ. Combust. 23 (1) (1997) 81–94.

[2] S. Kumar, P. Paul, H. Mukunda, Prediction of flame liftoff height of diffusion/partially premixed jet flames and modeling of mild combustion burners, Combust. Sci. Technol. 179 (10) (2007) 2219–2253.

[3] B. B. Dally, S. H. Shim, R. A. Craig, P. J. Ashman, G. G. Szegö, On the burning of sawdust in a MILD combustion furnace, Energy Fuels 24 (6) (2010) 3462–3470.

[4] C. Galletti, A. Parente, M. Derudi, R. Rota, L. Tognotti, Numerical and experimental analysis of NO emissions from a lab-scale burner fed with hydrogen-enriched fuels and operating in MILD combustion, Int. J. Hydrogen Energ. 34 (19) (2009) 8339–8351.

[5] P. Li, B. B. Dally, J. Mi, F. Wang, Mild oxy-combustion of gaseous fuels in a laboratory-scale furnace, Combust. Flame 160 (5) (2013) 933–946.

[6] A. Cavaliere, M. de Joannon, Mild combustion, Prog. Energ. Combust. 30 (4) (2004) 329–366.

[7] M. Saha, B. B. Dally, P. R. Medwell, E. M. Cleary, Moderate or intense low oxygen dilution (MILD) combustion characteristics of pulverized coal in a self-recuperative furnace, Energy Fuels 28 (9) (2014) 6046–6057.

[8] P. R. Medwell, P. A. M. Kalt, B. B. Dally, Imaging of diluted turbulent ethylene flames stabilized on a jet in hot coflow (JHC) burner, Combust. Flame 152 (1) (2008) 100–113.

[9] M. Derudi, R. Rota, Experimental study of the mild combustion of liquid hydrocarbons, Proc. Combust. Inst. 33 (2) (2011) 3325–3332.

[10] O. Lammel, H. Schütz, G. Schmitz, R. Lückerath, M. Stöhr, B. Noll, M. Aigner, M. Hase, W. Krebs, FLOX® combustion at high power density and high flame temperatures, J. Eng. Gas Turb. Power 132 (12) (2010) 121503.

[11] E. Oldenhof, M. Tummers, E. Van Veen, D. Roekaerts, Role of entrainment in the stabilisation of jet-in-hot-coflow flames, Combust. Flame 158 (8) (2011) 1553–1563.

[12] J. Sidey, E. Mastorakos, R. Gordon, Simulations of Autoignition and Laminar Premixed Flames in Methane/Air Mixtures Diluted with Hot Products, Combust. Sci. Technol. 186 (4-5) (2014) 453–465.

[13] J. Ye, P. R. Medwell, E. Varea, S. Kruse, B. B. Dally, H. G. Pitsch, An experimental study on MILD combustion of prevaporised liquid fuels, Appl. Energy 151 (2015) 93–101.

[14] G. G. Szegö, B. B. Dally, G. J. Nathan, Operational characteristics of a parallel jet MILD combustion burner system, Combust. Flame 156 (2) (2009) 429–438.

[15] M. Katsuki, T. Hasegawa, The science and technology of combustion in highly preheated air, in: Symp. (Int.) Combust., Vol. 27, 1998, pp. 3135–3146.

[16] B. Dally, E. Riesmeier, N. Peters, Effect of fuel mixture on moderate and intense low oxygen dilution combustion, Combust. Flame 137 (4) (2004) 418–431.

[17] B. B. Dally, A. N. Karpetis, R. S. Barlow, Structure of turbulent non-premixed jet flames in a diluted hot coflow, Proc. Combust. Inst. 29 (1) (2002) 1147–1154.

[18] R. Weber, J. P. Smart, W. vd Kamp, On the (MILD) combustion of gaseous, liquid, and solid fuels in high temperature preheated air, Proc. Combust. Inst. 30 (2) (2005) 2623–2629.

[19] R. Sadanandan, R. Lückerath, W. Meier, C. Wahl, Flame characteristics and emissions in flameless combustion under gas turbine relevant conditions, J. Propul. Power 27 (5) (2011) 970–980.

[20] S. Kruse, B. Kerschgens, L. Berger, E. Varea, H. Pitsch, Experimental and numerical study of MILD combustion for gas turbine applications, Appl. Energy 148 (2015) 456–465.

[21] R. Cabra, J. Y. Chen, R. W. Dibble, A. N. Karpetis, R. S. Barlow, Lifted methane-air jet flames in a vitiated coflow, Combust. Flame 143 (4) (2005) 491–506.

[22] R. L. Gordon, A. R. Masri, E. Mastorakos, Simultaneous Rayleigh temperature, OH-and CH_2O-LIF imaging of methane jets in a vitiated coflow, Combust. Flame 155 (1) (2008) 181–195.

[23] P. R. Medwell, D. L. Blunck, B. B. Dally, The role of precursors on the stabilisation of jet flames issuing into a hot environment, Combust. Flame 161 (2) (2013) 465–474.

[24] Y. Minamoto, N. Swaminathan, Scalar gradient behaviour in MILD combustion, Combust. Flame 161 (4) (2013) 1063–1075.

[25] J. Sidey, E. Mastorakos, Visualization of MILD combustion from jets in cross-flow, Proc. Combust. Inst. 35 (3) (2015) 3537–3545.

[26] B. C. Choi, S. H. Chung, Autoignited laminar lifted flames of methane/hydrogen mixtures in heated coflow air, Combust. Flame 159 (4) (2012) 1481–1488.

[27] M. Evans, P. Medwell, Z. Tian, J. Ye, A. Frassoldati, A. Cuoci, Effects of oxidant stream composition on non-premixed laminar flames with heated and diluted coflows, Combust. Flame 178 (2016) 297–310.

[28] Y. Minamoto, T. Dunstan, N. Swaminathan, R. Cant, DNS of EGR-type turbulent flame in MILD condition, Proc. Combust. Inst. 34 (2) (2013) 3231–3238.

[29] M. de Joannon, P. Sabia, G. Sorrentino, A. Cavaliere, Numerical study of mild combustion in hot diluted diffusion ignition (HDDI) regime, Proc. Combust. Inst. 32 (2) (2009) 3147–3154.

[30] M. de Joannon, G. Sorrentino, A. Cavaliere, MILD combustion in diffusion-controlled regimes of hot diluted fuel, Combust. Flame 159 (5) (2012) 1832–1839.

[31] M. de Joannon, P. Sabia, G. Cozzolino, G. Sorrentino, A. Cavaliere, Pyrolitic and Oxidative Structures in Hot Oxidant Diluted Oxidant (HODO) MILD Combustion, Combust. Sci. Technol. 184 (7-8) (2012) 1207–1218.

[32] P. R. Medwell, B. B. Dally, Effect of fuel composition on jet flames in a heated and diluted oxidant stream, Combust. Flame 159 (10) (2012) 3138–3145.

[33] E. Oldenhof, M. Tummers, E. Van Veen, D. Roekaerts, Ignition kernel formation and lift-off behaviour of jet-in-hot-coflow flames, Combust. Flame 157 (6) (2010) 1167–1178.

[34] V. M. Reddy, P. Biswas, P. Garg, S. Kumar, Combustion characteristics of biodiesel fuel in high recirculation conditions, Fuel Process. Technol. 118 (2014) 310–317.

[35] H. C. Rodrigues, M. J. Tummers, E. H. van Veen, D. Roekaerts, Spray flame structure in conventional and hot-diluted combustion regime, Combust. Flame 162 (3) (2015) 759–773.

[36] H. C. Rodrigues, M. Tummers, E. van Veen, D. Roekaerts, Effects of coflow temperature and composition on ethanol spray flames in hot-diluted coflow, Int. J. Heat. Fluid Fl. 51 (2015) 309–323.

[37] W. O'Loughlin, A. R. Masri, The structure of the auto-ignition region of turbulent dilute methanol sprays issuing in a vitiated co-flow, Flow Turbul. Combust. 89 (1) (2012) 13–35.

[38] H. Curran, P. Gaffuri, W. J. Pitz, C. K. Westbrook, A Comprehensive Modeling Study of n-Heptane Oxidation, Combust. Flame 114 (1-2) (1998) 149–177.

[39] C. S. Yoo, T. Lu, J. H. Chen, C. K. Law, Direct numerical simulations of ignition of a lean n-heptane/air mixture with temperature inhomogeneities at constant volume: Parametric study, Combust. Flame 158 (9) (2011) 1727–1741.

[40] D. A. Rothamer, J. A. Snyder, R. K. Hanson, R. R. Steeper, R. P. Fitzgerald, Simultaneous imaging of exhaust gas residuals and temperature during HCCI combustion, Proc. Combust. Inst. 32 (2) (2009) 2869–2876.

[41] J. Ye, P. R. Medwell, B. B. Dally, M. J. Evans, The transition of ethanol flames from conventional to MILD combustion, Combust. Flame 171 (2016) 173–184.

[42] J. Kojima, Y. Ikeda, T. Nakajima, Basic aspects of OH (A), CH (A), and C_2 (d) chemiluminescence in the reaction zone of laminar methane-air premixed flames, Combust. Flame 140 (1) (2005) 34–45.

[43] P. R. Medwell, P. A. M. Kalt, B. B. Dally, Simultaneous imaging of OH, formaldehyde, and temperature of turbulent nonpremixed jet flames in a heated and diluted coflow, Combust. Flame 148 (1) (2007) 48–61.

[44] V. Sick, N. Wermuth, Single-shot imaging of OH radicals and simultaneous OH radical/acetone imaging with a tunable Nd: YAG laser, Applied Physics B 79 (2) (2004) 139–143.

[45] P. R. Medwell, B. B. Dally, Experimental observation of lifted flames in a heated and diluted coflow, Energy Fuels 26 (9) (2012) 5519–5527.

[46] M. Evans, P. Medwell, H. Wu, A. Stagni, M. Ihme, Classification and lift-off height prediction of non-premixed mild and autoignitive flames, Proc. Combust. Inst. 36 (2017) 4297-4304.

[47] C. K. Westbrook, Chemical kinetics of hydrocarbon ignition in practical combustion systems, Proc. Combust. Inst. 28 (2) (2000) 1563–1577.

[48] P. Sabia, M. d. Joannon, A. Picarelli, R. Ragucci, Methane auto-ignition delay times and oxidation regimes in MILD combustion at atmospheric pressure, Combust. Flame 160 (1) (2013) 47–55.

[49] N. M. Marinov, A detailed chemical kinetic model for high temperature ethanol oxidation, Int. J. Chem. Kinet. 31 (1999) 183–220.

[50] R. Lückerath, W. Meier, M. Aigner, FLOX® combustion at high pressure with different fuel compositions, J. Eng. Gas Turb. Power 130 (1) (2008) 011505.

[51] R. Cabra, T. Myhrvold, J. Y. Chen, R. W. Dibble, A. N. Karpetis, R. S. Barlow, Simultaneous laser Raman-Rayleigh-LIF measurements and numerical modeling results of a lifted turbulent H_2/N_2 jet flame in a vitiated coflow, Proc. Combust. Inst. 29 (2) (2002) 1881–1888.

[52] C. Duwig, M. J. Dunn, Large eddy simulation of a premixed jet flame stabilized by a vitiated co-flow: Evaluation of auto-ignition tabulated chemistry, Combust. Flame 160 (12) (2013) 2879–2895.

[53] M. Evans, P. Medwell, Z. Tian, Modeling lifted jet flames in a heated coflow using an optimized eddy dissipation concept model, Combust. Sci. Technol. 187 (7) (2015) 1093–1109.

[54] G. P. Smith, D. M. Golden, M. Frenklach, N. W. Moriarty, B. Eiteneer, M. Goldenberg, C. T. Bowman, R. K. Hanson, S. Song, W. C. G. Jr., V. V. Lissianski, Z. Qin, Gri-mech 3.0, 2000, Mechanism available from `http://www.me.berkeley.edu/gri_mech/`.

[55] M. J. Evans, P. R. Medwell, Z. F. Tian, A. Frassoldati, A. Cuoci, A. Stagni, Ignition characteristics in spatially zero-, one- and two-dimensional laminar ethylene flames, AIAA Journal (2016) 3255–3264.

[56] P. R. Medwell, M. J. Evans, Q. N. Chan, V. R. Katta, Laminar flame calculations for analyzing trends in autoignitive jet flames in a hot and vitiated coflow, Energy Fuels 30 (10) (2016) 8680–8690.

[57] P. L. Kelly-Zion, J. E. Dec, A computational study of the effect of fuel type on ignition time in homogenous charge compression ignition engines, Proc. Combust. Inst. 28 (1) (2000) 1187–1194.

[58] M. Frenklach, H. Wang, M. J. Rabinowitz, Optimization and analysis of large chemical kinetic mechanisms using the solution mapping method - combustion of methane, Prog. Energ. Combust. 18 (1) (1992) 47–73.

[59] H. Curran, J. M. Simmie, P. Dagaut, D. Voisin, M. Cathonnet, The ignition and oxidation of allene and propyne: Experiments and kinetic modeling, Symp. (Int.) Combust. 26 (1) (1996) 613–620.

[60] H. Yamada, K. Suzaki, H. Sakanashi, N. Choi, A. Tezaki, Kinetic measurements in homogeneous charge compression of dimethyl ether: role of intermediate formaldehyde controlling chain branching in the low-temperature oxidation mechanism, Combust. Flame 140 (1) (2005) 24–33.

[61] C. Gibson, P. Gray, J. Griffiths, S. Hasko, Spontaneous ignition of hydrocarbon and related fuels: A fundamental study of thermokinetic interactions, Symp. (Int.) Combust. 20 (1) (1985) 101–109.

[62] M. de Joannon, P. Sabia, A. Cavaliere, Alternative ignition systems, Verlag ProcessEng Engineering GmbH, 2009, Ch. HDDI mild combustion, pp. 133–150.

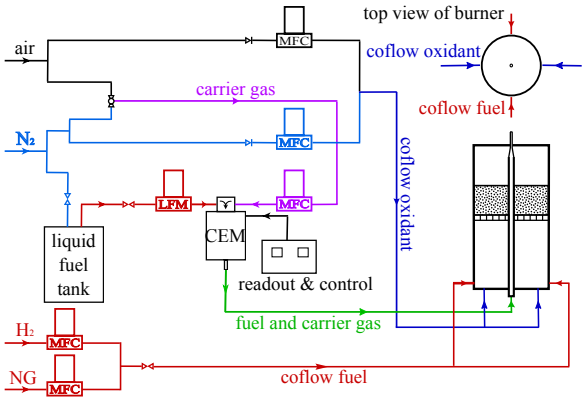

Figure 1: Experimental Setup: CEM is the Controlled Evaporator and Mixer, MFC is the mass flow controller for gases, and LFM is the liquid flow meter.

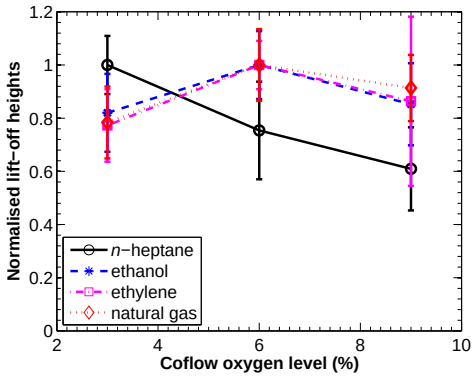

Figure 2: A comparison of normalised liftoff heights of n-heptane flames to ethanol, ethylene and natural gas flames. The lowest and highest identifiable liftoff positions in CH* chemiluminescence or the blue channel of the photograph are used to define the mean liftoff height. The variation in the two positions are plotted as error bars to indicate the uncertainty.

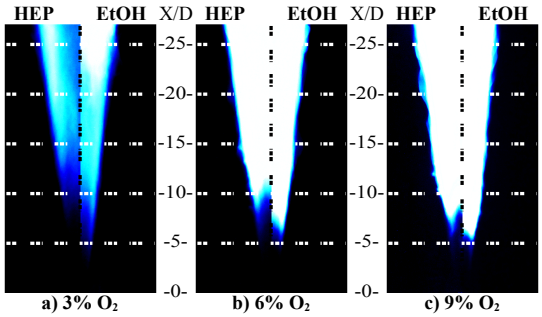

Figure 3: Photographs of n-heptane (HEP) and ethanol (EtOH) flames carried by air at a 1250-K coflow with 3-9% O_2 by volume. The region shielded by the coflow is up to X/D = 22 [43], where X is the axial distance above the jet and D is the jet diameter.

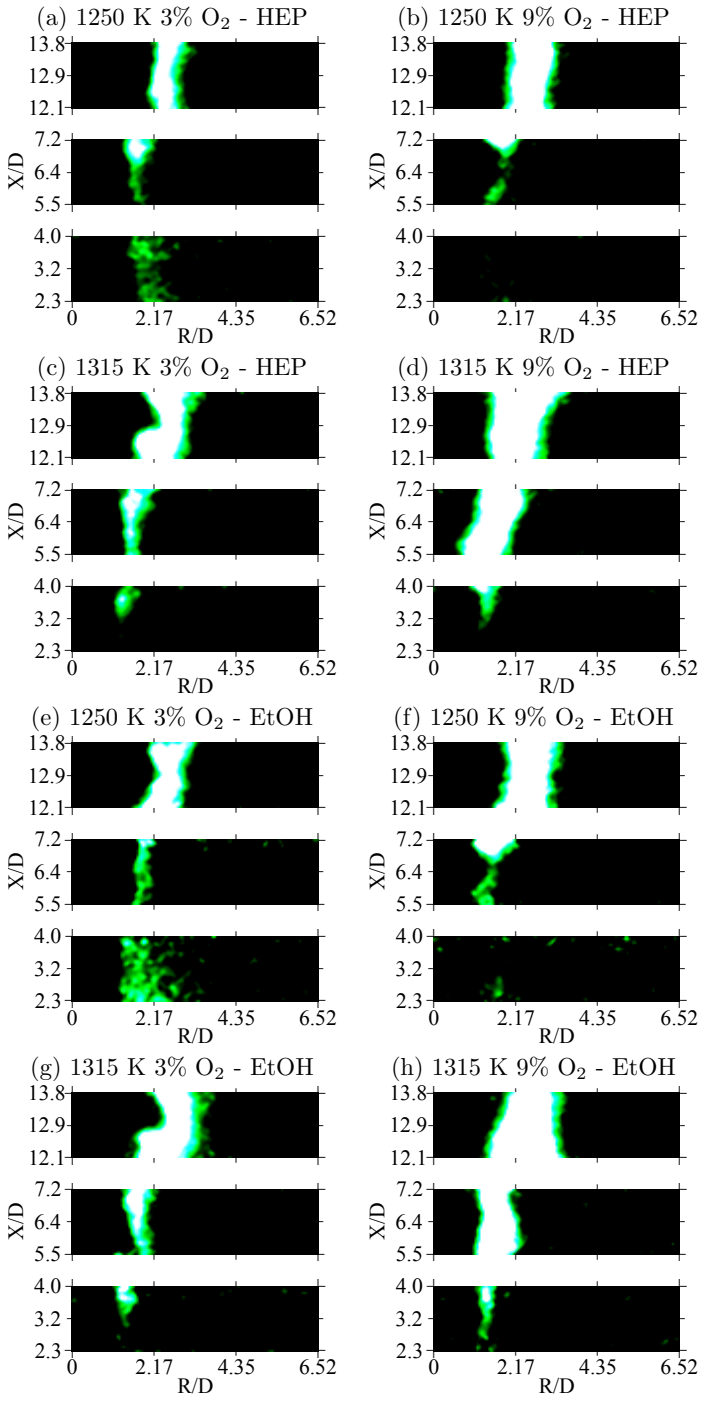

Figure 4: A selection of instantaneous OH images for *n*-heptane (HEP) and ethanol (EtOH) flames in various coflows. These images are centred at X/D = 3.2 (15 mm), X/D = 6.4 (29 mm) and X/D = 12.9 (59 mm) above the jet exit plane, respectively. The left edge of each image is coincident with the jet centreline, and R is the radial distance from the jet centreline. Each image is 8 × 30 mm.

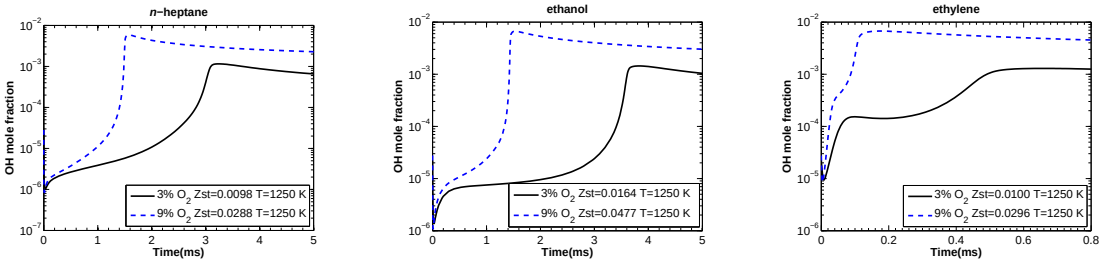

Figure 5: Temporal evolution of OH for n-heptane, ethanol and ethylene mixing with hot oxidant with 3% and 9% O_2 at stoichiometric mixture fractions at 1250 K.

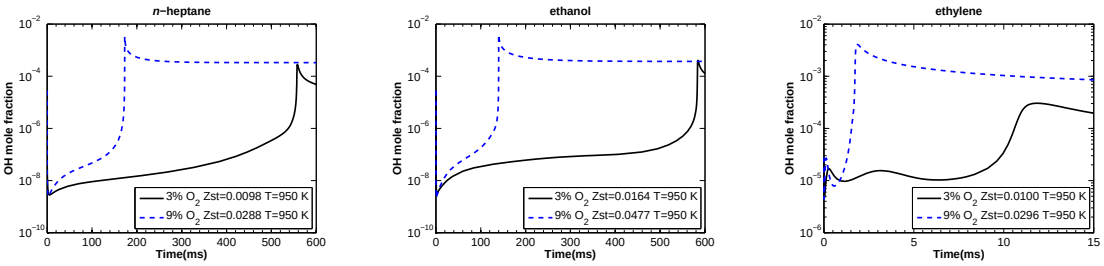

Figure 6: Temporal evolution of OH for n-heptane, ethanol and ethylene mixing with hot oxidant with 3% and 9% O_2 at stoichiometric mixture fractions at 950 K.

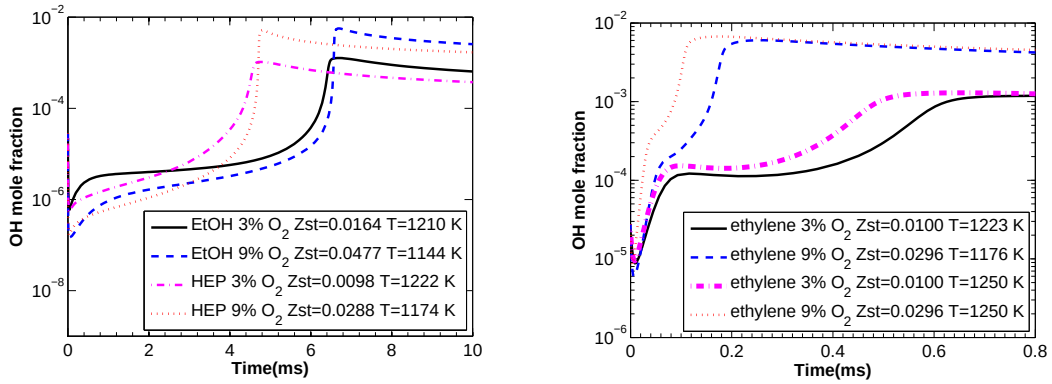

(a) (b)

Figure 7: Temporal evolution of OH for n-heptane, ethanol and ethylene mixing with hot oxidant with 3% and 9% O_2 in stoichiometric conditions (a) n-heptane and ethanol flames; (b) ethylene flames.

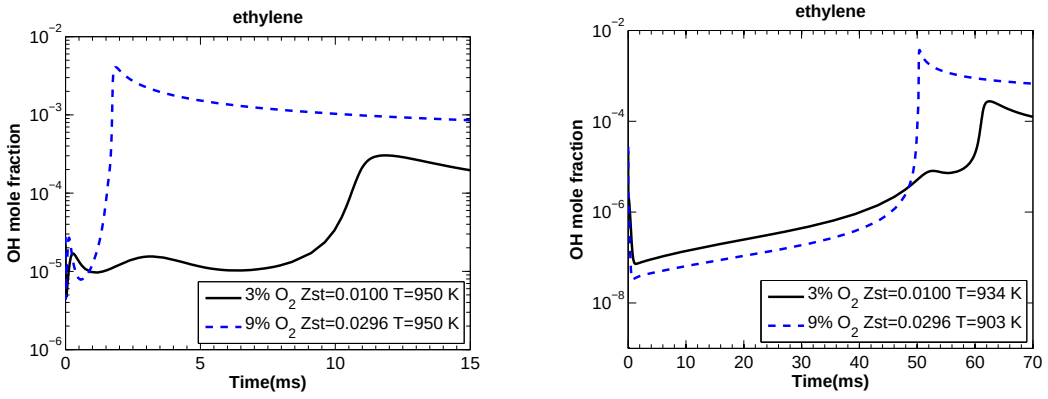

(a) (b)

Figure 8: Temporal evolution of OH for ethylene mixing with a 950-K hot oxidant in stoichiometric conditions (a) constant temperature; (b) resultant temperature from mixing.

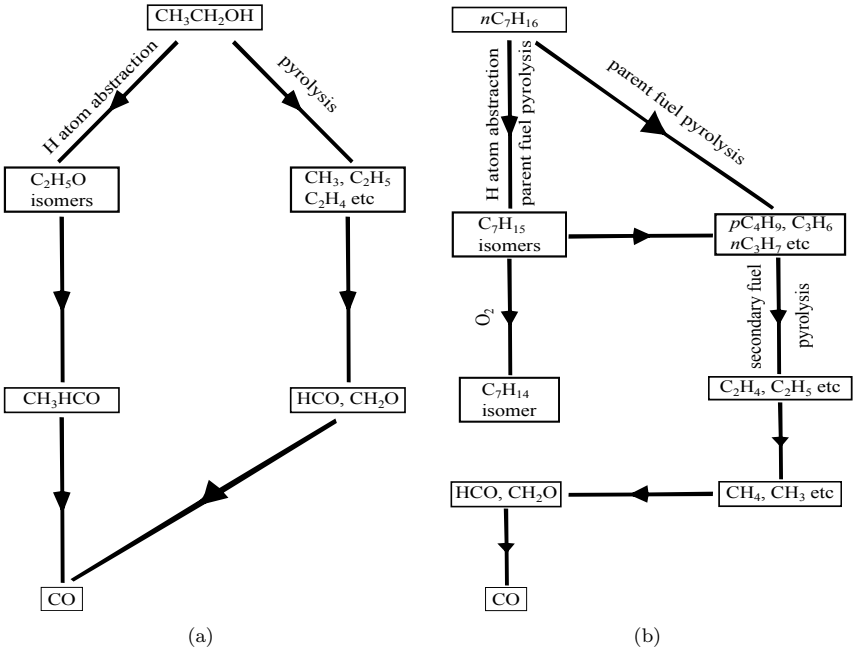

Figure 9: General scheme of primary kinetic pathways for ethanol and n-heptane flames.

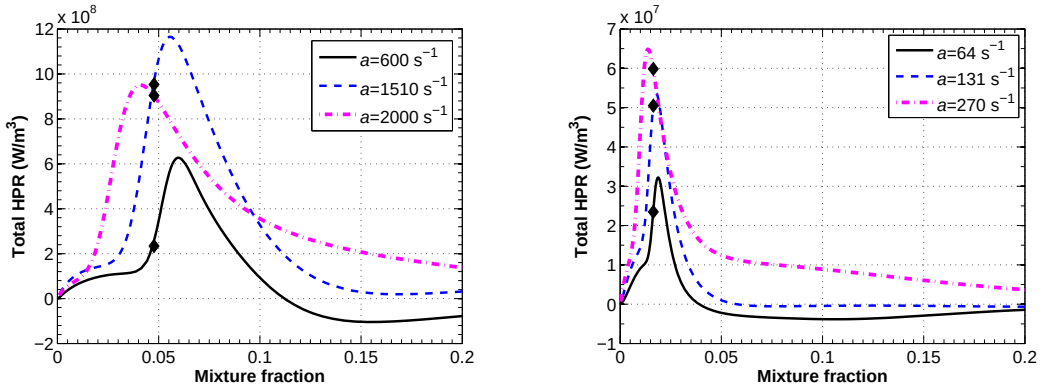

(a) 9% O_2 (b) 3% O_2

Figure 10: Heat production rate (HPR) profiles of ethanol flames in a 1250-K oxidiser with 9% and 3% O_2 at three strain rates (a). The heat production rate at the stoichiometric mixture fraction is marked with a diamond.

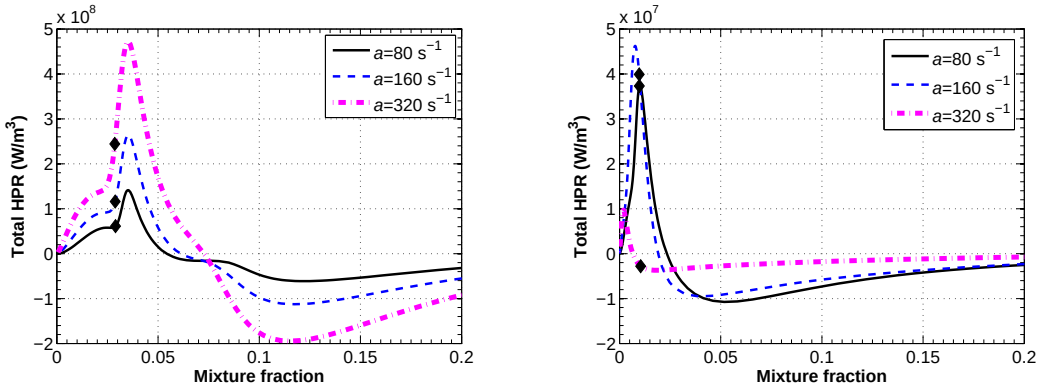

(a) 9% O_2 (b) 3% O_2

Figure 11: Heat production rate (HPR) profiles of n-heptane flames in a 1250-K oxidiser with 9% and 3% O_2 at three strain rates (a). The heat production rate at the stoichiometric mixture fraction is marked with a diamond.

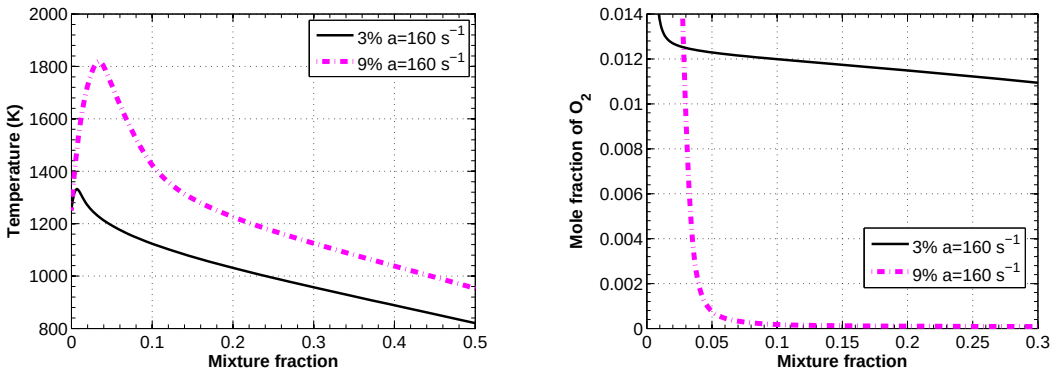

(a) (b)

Figure 12: Temperature (a) and mole fraction of O_2 (b) as a function of mixture fraction for n-heptane flames in the 3% and 9% oxidant stream.

Supplementary Material

Click here to download Supplementary Material: supplemental_material.pdf

LaTeX Source Files

Click here to download LaTeX Source Files: LaTeX source file.zip

Chapter 7

Structural Differences of Ethanol and DME Jet Flames in a Hot Diluted Coflow

Statement of Authorship

Title of Paper	Structural Differences of Ethanol and DME Jet Flames in a Hot Diluted Coflow
Publication Status	☐ Published ☐ Accepted for Publication ☑ Submitted for Publication ☐ Unpublished and Unsubmitted w ork w ritten in manuscript style
Publication Details	J. Ye, P. R. Medwell, K. Kleinheinz, M. J. Evans, B. B. Dally, H. G. Pitsch, Structural Differences of Ethanol and DME Jet Flames in a Hot Diluted Coflow, submitted to Combust. Flame

Principal Author

Name of Principal Author (Candidate)	Jingjing Ye		
Contribution to the Paper	Based on discussions between me and one of my supervisors, several operating parameters were chosen for investigation. I decided different experimental cases with my supervisors. I setup the experiments with two co-authors. I undertook the experiments with two co-authors. We performed digital photography, imaging of OH* chemiluminescence, OH-LIF, CH_2O-LIF, and Rayleigh scattering together. I processed, analysed, and interpreted all the experimental data. I also planned and performed all the reaction flux analyses with the OPPDIF code in the Chemkin software to assist the interpretation of the experimental data. I also co-planned the laminar flamelet analysis. I analysed the results from the laminar flamelet analysis. I integrated all the numerical and experimental analysis and wrote the manuscript. I also acted as the corresponding author, and responded to the reviewers' and the editor's comments and recommendations.		
Overall percentage (%)	60		
Certification:	This paper reports on original research I conducted during the period of my Higher Degree by Research candidature and is not subject to any obligations or contractual agreements with a third party that would constrain its inclusion in this thesis. I am the primary author of this paper.		
Signature	Digitally signed by JINGJING YE Date: 2017.06.02 13:04:04 +09'30'	Date	02-June-2017

Co-Author Contributions

By signing the Statement of Authorship, each author certifies that:

i. the candidate's stated contribution to the publication is accurate (as detailed above);

ii. permission is granted for the candidate in include the publication in the thesis; and

iii. the sum of all co-author contributions is equal to 100% less the candidate's stated contribution.

Name of Co-Author	Paul R. Medwell		
Contribution to the Paper	This co-author co-designed the experiments and co-supervised the development of the work. This co-author also provided assistance and supervision during the experimental setup and data collection. This co-author helped to evaluate and edit the manuscript.		
Signature	Paul Medwell 2017.06.03 10:47:27 +09'30'	Date	03-JUN-2017

Name of Co-Author	Konstantin Kleinheinz		
Contribution to the Paper	This co-author performed the laminar flamelet analysis. This co-author also helped to evaluate and edit the manuscript.		
Signature		Date	02-June-2017

Name of Co-Author	Michael J. Evans		
Contribution to the Paper	This co-author co-designed and undertook experiments. This co-author also helped to evaluate and edit the manuscript.		
Signature	Digitally signed by Michael Evans Date: 2017.06.04 18:39:09 +09'30'	Date	04-June-2017

Name of Co-Author	Bassam B. Dally		
Contribution to the Paper	This co-author co-supervised the development of the work. This co-author helped to evaluate and edit the manuscript.		
Signature	Digitally signed by Bassam Dally Date: 2017.06.05 11:33:36 +09'30'	Date	05-June-2017

Name of Co-Author	Heinz G. Pitsch		
Contribution to the Paper	This co-author co-supervised the development of the work. This co-author helped to evaluate and edit the manuscript.		
Signature	Digitally signed by Heinz Pitsch Location: Aachen Date: 2017.06.01 16:10:43 +02'00'	Date	01-June-2017

Please cut and paste additional co-author panels here as required.

Elsevier Editorial System(tm) for Combustion and Flame

Manuscript Draft

Manuscript Number:

Title: Structural Differences of Ethanol and DME Jet Flames in a Hot Diluted Coflow

Article Type: Full Length Article

Keywords: MILD combustion; ethanol; dimethyl ether (DME); Jet in Hot Coflow (JHC)

Corresponding Author: Ms. JJ Ye,

Corresponding Author's Institution: The University of Adelaide

First Author: JJ Ye

Order of Authors: JJ Ye; Paul R Medwell; Konstantin Kleinheinz; Michael J Evans; Bassam B Dally; Heinz G Pitsch

Abstract: This study compares the flame structure of ethanol and dimethyl ether (DME) in a hot and diluted oxidiser experimentally and computationally. Experiments were conducted on a Jet in Hot Coflow (JHC) burner, with the fuel jet issuing into a 1250-K coflow at three oxygen levels. For both the ethanol and the DME flames, a transitional flame structure was revealed by laser-induced fluorescence (LIF) of OH, as the coflow oxygen level increased from 3% to 9% indicating deviation from the MILD combustion regime. Planar measurements using OH-LIF, CH2O-LIF, and Rayleigh scattering images reveal that the overall spatial distribution and evolution of OH, CH2O, and temperature were quite similar for the two fuels. Reaction flux analyses of ethanol and DME were performed with the OPPDIF code, and ethane (C2H6) was also included in the analyses for comparison. These analyses reveal that each of the three fuels is decomposed via different chemical pathways, leading to the differences in the intermediate species pool. However, temperature sensitivity analysis indicates that these differences play a minor role in the overall oxidation processes in the 3% O2 cases. Under these conditions, the H2/O2 pathways are very important for both ethanol and DME. In contrast, the importance of fuel-specific reactions overtakes that of H2/O2 reactions when fuels are burnt in the cold air or in the vitiated oxidant stream with 9% O2. Unsteady laminar flamelet analyses were performed to investigate the ignition processes with a two-step approach. This approach utilises non-reactive Large-Eddy Simulation (LES) to obtain temporal evolution of the flow field parameterised by the scalar dissipation rate of the mixture, necessary for the unsteady laminar flamelet analysis as a second step. Results indicate that the ignition of DME requires a lower scalar dissipation rate and a higher initial temperature than ethanol, reflecting a lower reactivity of DME at the conditions investigated in this paper. This could explain why the DME flames always appeared more lifted than the ethanol flames in the experiments.

Suggested Reviewers: Jenni A.M. Sidey
Department of Engineering, University of Cambridge

jams4@cam.ac.uk
Expert in laser diagnostics and MILD combustion

Sudarshan Kumar
Indian Institute of Technology Bombay
sudar@aero.iitb.ac.in;sudar4@gmail.com
Expert on MILD combustion

Mark J. Tummers
Delft University of Technology
M.J.Tummers@tudelft.nl
Expert in combustion, particularly interested in flames in a hot coflow

Katharina Kohse-Höinghaus
Bielefeld University
kkh@uni-bielefeld.de
Expert in chemistry and alternative fuels

Tiziano Faravelli
Department of Chemistry, Materials, and Chemical Engineering, Politecnico di Milano
tiziano.faravelli@polimi.it
Expert in chemical engineering and numerical modelling

Structural differences of ethanol and DME jet flames in a hot diluted coflow

Jingjing Ye[a,*], Paul R. Medwell[a], Konstantin Kleinheinz[b], Michael J. Evans[a], Bassam B. Dally[a], Heinz G. Pitsch[b]

[a]*School of Mechanical Engineering, The University of Adelaide, South Australia 5005, Australia*
[b]*Institute for Combustion Technology, RWTH Aachen University, Aachen 52056, Germany*

Abstract

This study compares the flame structure of ethanol and dimethyl ether (DME) in a hot and diluted oxidiser experimentally and computationally. Experiments were conducted on a Jet in Hot Coflow (JHC) burner, with the fuel jet issuing into a 1250-K coflow at three oxygen levels. For both the ethanol and the DME flames, a transitional flame structure was revealed by laser-induced fluorescence (LIF) of OH, as the coflow oxygen level increased from 3% to 9% indicating deviation from the MILD combustion regime. Planar measurements using OH-LIF, CH_2O-LIF, and Rayleigh scattering images reveal that the overall spatial distribution and evolution of OH, CH_2O, and temperature were quite similar for the two fuels. Reaction flux analyses of ethanol and DME were performed with the OPPDIF code, and ethane (C_2H_6) was also included in the analyses for comparison. These analyses reveal that each of the three fuels is decomposed via different chemical pathways, leading to the differences in the intermediate species pool. However, temperature sensitivity analysis indicates that these differences play a minor role in the overall oxidation processes in the 3% O_2 cases. Under these conditions, the H_2/O_2 pathways are very important for both ethanol and DME. In contrast, the importance of fuel-specific reactions overtakes that of H_2/O_2 reactions when fuels are burnt in the cold air or in the vitiated oxidant stream with 9% O_2. Unsteady laminar flamelet analyses were performed to investigate the ignition processes with a two-step approach. This approach utilises non-reactive Large-Eddy Simulation (LES) to obtain temporal evolution of the flow field parameterised by the scalar dissipation rate of the mixture, necessary for the unsteady laminar flamelet analysis as a second step. Results indicate that the ignition of DME requires a lower scalar dissipation rate and a higher initial temperature than ethanol, reflecting a lower reactivity of DME at the conditions investigated in this paper. This could explain why the DME flames always appeared more lifted than the ethanol flames in the experiments.

Keywords: MILD combustion, ethanol, dimethyl ether (DME), Jet in Hot Coflow (JHC)

1. Introduction

The ever-rising concern for the environment has increased efforts to improve energy efficiency and reduce pollutant emissions. Amongst advanced combustion technologies, Moderate or Intense Low-oxygen Dilution

*Corresponding author
Email address: jingjing.ye01@adelaide.edu.au (Jingjing Ye)

(MILD) combustion is a promising technology because of its potential to reduce emissions while maintaining a high thermal efficiency [1]. In practical devices, MILD combustion is usually established through a strong recirculation of hot exhaust gases, leading to volumetric reactions without visible flames under some conditions [1, 2]. Hence it is also referred to as flameless oxidation (FLOX®) [1]. Under MILD combustion conditions the peak flame temperature is reduced due to a larger total volume of gases and the altered chemistry at a lower local oxygen concentration. Consequently, this causes a drastic reduction in emissions, particularly in nitrogen oxides [3, 4].

Previous studies of MILD combustion [5, 6, 7, 8, 9] have mostly focused on common fossil fuels. There are limited studies that investigate MILD combustion of renewable fuels [10, 11]. Experimental measurements performed on the Jet in Hot Coflow (JHC) burner revealed a similar reaction zone structure of natural gas, ethylene, and LPG flames when hydrogen was added to the three fuels. This suggests different types of fuels are interchangeable under MILD combustion conditions [12]. Supporting this, Derudi and Rota [4] have reported that the averaged flame temperature and pollutants emissions were similar for methane and LPG flames when they were burnt in MILD combustion mode. Whilst it is true that some previous studies have shown that for simple fuels the flame characteristics under MILD combustion conditions are very similar [4, 12], this is not true for more complex fuels [8, 13, 14]. For instance, visible flames and high NO_x emissions were reported as distinctive features when heavy fuel oil was used instead of light fuel oil in a furnace [8]. Reddy et al. [13] found that lower NO_x and unburned hydrocarbon emissions were produced when a combustor was fired with a mixture of biodiesel and diesel rather than pure biodiesel. Ye et al. [14] performed a comparative study of ethanol, acetone, and *n*-heptane in a reverse-flow MILD combustor. They found that combustion of acetone and *n*-heptane became unstable at equivalence ratios of 0.7-0.8 and elevated pressures, where visible flames and high emissions were observed [14]. Meanwhile stable combustion of ethanol was established under all the investigated conditions [14].

A better understanding of the impact of fuel type on the flame structure is required, particularly for fuels that are more complex than methane and hydrogen. Due to increasing interest in reducing the dependence on petroleum-derived fuels and diversifying the energy supply, alternative fuels have received great attention. Combining alternative fuels with MILD combustion would exploit the benefits of both, leading to more efficient combustion with lower emissions. Ethanol (CH_3CH_2OH) and dimethyl ether (CH_3OCH_3), isomers of C_2H_6O, are very promising fuels. Comparing them also provides an opportunity to explore the impact of molecular structure on the flame behaviour under vitiated coflow conditions.

Ethanol (EtOH), a type of alcohol, has a low tendency to generate soot and particulate-matter [15]. Due to its high flame speed it can be burnt at very lean conditions with a relatively low flame temperature [16]. As a consequence, NO_x emissions are suppressed. Ethanol can be produced from a wide range of renewable raw materials. Second generation bio-ethanol is derived from lignocellulosic biomass like wood, which is not in competition with food chain [17]. Its renewable nature, low emissions, and reduced production costs make it an attractive alternative fuel [18].

Dimethyl ether (DME), the simplest ether, is an excellent alternative fuel for transportation and power generation [19]. For instance, DME can be used as a substitute for diesel fuels due to its capacity to abate

soot emissions [20]. The existence of an O atom and absence of any C-C bonds in DME contribute to its smoke-free nature [21]. It is also an ideal ignition promoter in engines not only because of its low auto-ignition temperature and high cetane number, but also because of its rapid vaporisation upon injection [20]. It can be manufactured from a variety of resources such as natural gas, wastes, and biomass [20].

Due to the potential utility of DME in gas turbine applications, the comparison between DME and methane (main component of natural gas) has attracted great interest. Lee and Yoon [22] tested DME in a gas turbine, and they reported that lower NO_x emissions were produced from DME than methane. Chen et al. [23] investigated the impact of adding DME to methane-air flames on the ignition characteristics. They found that the ignition delay times of the methane-air mixture were significantly shortened due to a rapid build-up of CH_3 and HO_2 radicals with the presence of DME [23].

Limited comparative studies [24, 25, 26, 27, 28, 29, 30, 31, 32] have been performed to investigate the effect of molecular structure on the combustion behaviour of DME and ethanol flames. Most of these studies were focused on the role of the structure of oxygenated fuels in reducing soot precursors and soot particulates.

Previous studies have investigated the autoignition and extinction characteristics of ethanol and DME [25, 33]. Wang et al. [25] reported that DME flames were more resilient to extinction than ethanol flames, though this difference decreased as the fuel jet became more diluted with N_2 [25]. Tingas et al. [33] performed an analytical analysis of the autoignition characteristics of ethanol/air and DME/air homogeneous mixtures at an initial pressure of 5 MPa and an initial temperature of 1100 K. This analysis revealed an overall shorter ignition delay in the ethanol/air case. They found that the C-C bond in ethanol is maintained and the hydrogen chemistry plays a dominant role at the early stage of autoignition [33]. In contrast, the autoignition of DME/air is initiated by single-carbon chemistry [33]. As the reaction progresses, similar hydrogen chemistry pathways dominate in both fuels [33]. Formaldehyde was reported to be insignificant in the autoignition dynamics of ethanol/air mixtures, while adding formaldehyde can promote or retard the ignition of DME/air mixtures depending on the initial temperature [34].

There is a paucity of information on ethanol and DME flames under conditions relevant to MILD combustion. Kang et al. [10] investigated NO_x emissions of DME flames in a MILD burner. They found that the NNH-intermediate pathway was the major route for NO_x formation in DME flames under MILD combustion conditions [10]. Rodrigues et al. [11, 35] studied the ethanol spray flame structure in a hot and vitiated coflow. An enhanced spray evaporation in the presence of hot coflow led to changes in the atomisation mechanism, with an immediate liquid jet break-up near the atomiser [11]. Moreover, the reduced local oxygen concentration shifted the stoichiometric mixture fraction away from the spray axis, consequently reducing the peak flame temperature [11]. The liftoff heights of the ethanol spray flames were found to be dependent on the droplet convective, vaporisation, and chemical time scales before ignition [35].

The present paper aims to improve the understanding of the impact of fuel structure on MILD flames by performing a combined experimental and computational investigation of ethanol and DME. In order to control parameters independently, a JHC burner was used to emulate a MILD furnace environment where the gas mixture inside the combustion chamber is hot and diluted, with a fuel stream injecting into it. In this configuration, DME or prevaporised ethanol was issued into a hot and diluted coflow with the O_2 level

T_{cofl} (K)	X_{O_2}	X_{H_2O}	X_{CO_2}	X_{N_2}	Z_{st}
1250	0.091	0.107	0.036	0.766	0.0863
1250	0.061	0.107	0.036	0.797	0.0597
1250	0.030	0.107	0.036	0.827	0.0305

Table 1: List of coflow conditions: T_{cofl} is the coflow temperature measured by a thermocouple after correction for radiation. The mole fractions of species in the coflow were determined by equilibrium calculations, and confirmed with measurements with a gas analyser.

varying from 3%-9% (by volume). To reveal the flame structure of the two fuels, the distributions of OH, CH_2O, and temperature have been measured instantaneously and simultaneously. Digital photographs and images of OH^* chemiluminescence have also been recorded. Detailed analyses of the reaction pathways and the temporal ignition processes have been performed for ethanol and DME to explain the differences observed in the experiments.

2. Experimental Details

2.1. Experimental Setup and Operating Conditions

The basic configuration and operation of this JHC burner shown in Fig. 1 are the same as in a previous study [36]. The JHC burner consists of an insulated central fuel jet (ID = 4.6 mm) surrounded by an annular coflow (ID = 82 mm). This coflow is generated from a secondary porous-bed burner located 90 mm upstream of the jet exit plane. The hot vitiated coflow was produced from the combustion of a lean mixture of natural gas (92% methane by volume), hydrogen, air, and nitrogen. The mole fractions of natural gas, hydrogen, air and nitrogen were manipulated to vary the coflow oxygen level from 3% to 9% by volume, while the temperature and C/H ratio were kept constant. The temperature of various coflows (T_{coflow}) was kept at 1250 K. The three hot coflow conditions are summarised in Table 1. To obtain a fully developed turbulent pipe flow, the length of the central fuel jet is more than 100 times the jet diameter. The burner was wrapped with ceramic fibre insulation to minimise heat losses and maintain a constant temperature of the coflow.

As shown in Fig. 1, ethanol was heated and mixed with carrier gas in a Controlled Evaporator and Mixer (CEM). The temperature of the heater inside the CEM was set by the Bronkhorst control unit, which also controlled the mass flow rates of ethanol and carrier gas. The preheat temperature was around 413 K, which is higher than the boiling point of ethanol (T_{boil} = 352 K). Furthermore, the pipeline was wrapped with insulation to minimise heat losses and prevent condensation. After prevaporisation, ethanol was carried by N_2 into the JHC burner via the central fuel jet. Dimethyl ether was mixed with N_2 and injected to the JHC burner directly. The jet Reynolds number for both ethanol and DME flames was kept around 10,000. It should be noted that the mole fraction of N_2 in the fuel jet was maintained at 0.59 for both fuels. In this case, due to the same chemical formula, the stoichiometric mixture fractions (Z_{st}) for both fuels are the same in a given coflow. The value of Z_{st} is 0.0305, 0.0597, and 0.0863 in the 3%, 6%, and 9% O_2 coflow, respectively.

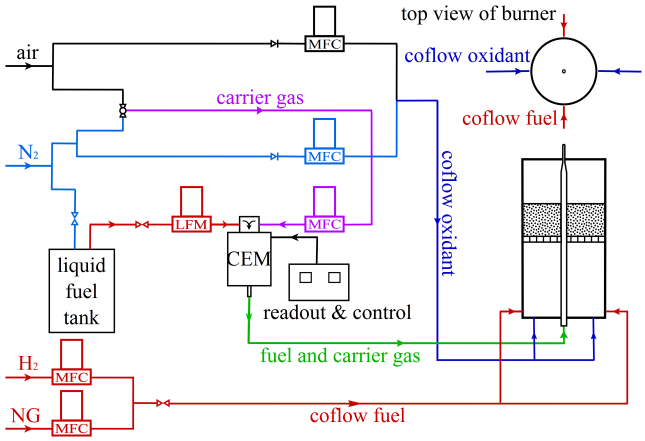

Figure 1: Experimental Setup: CEM is the Controlled Evaporator and Mixer, MFC is the mass flow controller for gases, and LFM is the liquid flow meter.

A slot burner was mounted in the same field of view as the JHC burner to provide reference and calibration for image processing. The rectangular slot burner consists of a central fuel slot with an air slot on each side. Partially-premixed natural gas and air were fed through the central slot at a low velocity, coflowing by two streams of low-velocity air. This setup produced a straight and laminar flame. Hence, variations in the signal of this laminar flame can be considered solely due to the laser energy fluctuations.

2.2. Optical Setup

Imaging of flames was achieved through conventional photography, OH^* chemiluminescence, Rayleigh scattering, and laser-induced fluorescence of OH (OH-LIF) and CH_2O (CH_2O-LIF). The photographs of the flames were taken using a Canon EOS 60D SLR camera with a standard 50 mm f/1.8 lens. The chemiluminescence of OH^* was detected with an electronically-gated pco.pixelfly camera, equipped with a Lambert Instruments intensifier. The camera system was coupled with a 50 mm f/3.5 UV transmissive lens and a 310 nm bandpass optical filter with a bandwidth of 10 nm.

Rayleigh scattering was used to determine the temperature distribution of the flames. A frequency-doubled Nd:YAG laser was used to generate a 532 nm laser beam. The measured output energy was approximately 90 mJ/pulse before the slot burner. The detection of Rayleigh scattering signal was via a Princeton Instruments intensified CCD (ICCD) camera equipped with a 50 mm f/1.4 lens, which was mounted normal to the laser sheets. No visible particulate matter and soot were observed during the experiments. Thus in order to maximise the collected Rayleigh signal, no filter was mounted in front of the collecting lens.

The A-X (1,0) $Q_1(7)$ line (283.222 nm) was chosen to excite OH due to its low sensitivity to ground-state population distribution in the expected temperature range [37]. A Q-smart 850 pulsed Nd:YAG laser was used to pump a Lambda-Physik ScanMate 2E dye laser at 532 nm with Rhodamine 6G dye. The output of the dye laser was frequency doubled to match the A-X (1,0) $Q_1(7)$ line. The energy of the OH laser was measured to be 0.9 mJ/pulse before the slot burner. The OH-LIF signal was detected with a Princeton Instruments ICCD camera, fitted with a 78 mm f/3.8 standard UV lens. This camera was mounted parallel

to the laser sheets. A dichroic mirror was mounted in front of the lens of the OH camera at a 45 degree angle to the laser sheets. This mirror has a greater than 80% reflectance in the range of 270 to 340 nm, thus acting as a bandpass filter.

A frequency-tripled Nd:YAG laser was used to generate a 355 nm beam to excite CH_2O. The measured output energy was approximately 32 mJ/pulse before the slot burner. The CH_2O-LIF signal was collected with an Andor iStar ICCD camera, equipped with a 50 mm f/1.4 lens. Detection of formaldehyde was through a combination of long-wave-pass Andover Optics 395 FG03-50 and short-wave-pass Andover Optics 450 FL07-50 filters. The 532 nm, the 283.222 nm and the 355 nm laser sheets overlapped with each other and formed co-planar laser sheets. The heights of the 532 nm and 355 nm laser sheets were approximately 20 mm, while the 283.222 nm laser sheet height was slightly shorter. Imaging from the central 8 mm of the laser sheets is presented in this paper.

2.3. Image Processing

Each instantaneous image from the three ICCD cameras was corrected for dark charge, detector attenuation, background, and laser energy variations. To correlate the information on the three images to each other, the three images were matched such that each corresponding pixel in them represents the exact same physical location. After spatial matching, the in-plane resolution of all three ICCD cameras was around 250 μm.

Rayleigh scattering and OH-LIF signal were semi-quantified using the same method as reported in a previous study [37]. Specifically, laminar flame calculations using the OPPDIF code of the Chemkin package were performed to estimate the mixture composition, thereby the effective Rayleigh cross-section in mixture fraction space. The effective Rayleigh cross-section was found to be independent of strain rate. As for the quantification of OH, Boltzmann population distribution of OH at X-state with $v'' = 0$ and $J'' = 7.5$ was found to be relatively constant with the flame temperature ranging from 1000 K to 2000 K [38]. The collisional cross-section and quenching rate coefficient as a function of temperature were obtained from a previous study by Tamura et al. [39], and the temperature distribution in mixture fraction space was estimated through laminar flame calculations. The calculated quenching rate for each flame was found to be constant across the reaction zone at various strain rates, hence a single value was used for each case. The peak OH number density of the steady laminar flame in the slot burner was calculated to be 2.1×10^{16} molecules/cm^3, which was used to calibrate the OH number density in the ethanol and DME flames.

It should be noted that the CH_2O signal was not quantified in the present study. However, because of the same geometry and facility, and the small temperature change in the fuel-rich region, the CH_2O signal is expected to reflect the relative quantity of CH_2O in various cases. Furthermore, previous studies [40, 41] reported that the temperature dependence of the CH_2O partition function and its quenching rate partially compensate for each other within a temperature range of 500 K to 1600 K. Therefore the CH_2O-LIF signal is considered to be proportional to the number density of CH_2O within 15%–25% [40, 41].

3. Experimental Results and Discussion

3.1. Visual Observations

Figure 2 presents photographs of DME (left) and ethanol (right) flames carried by nitrogen under the three coflow conditions (3%, 6%, and 9% O_2 by volume). These photographs were taken with the same camera settings and presented with the same colour scale. None of the investigated flames emitted smoke or particulates during the experiments. All the photographs were split into red, green, and blue channels, and only the blue channel is displayed, indicating the CH* chemiluminescence near 430 nm [42]. The bottom edge of all the photographs coincides with the jet exit plane. Parts of the photographs appear saturated as this universal colour scale is chosen to emphasise the low signal from the flames in the 3% O_2 coflow. It is worth mentioning that a previous study on the same JHC burner [37] reported that the entrainment of the surrounding air starts to affect the jet flame at approximately 100 mm above the jet exit plane (X/D = 22, where X is the axial distance above the jet exit plane and D is the jet diameter), and the present study is only focused on the coflow-controlled region.

In a given coflow, DME flames always appear more lifted than ethanol flames. For both fuels, the flame shape and appearance are similar between the 6% and 9% O_2 coflows, despite minor differences in the flame luminosity. When the coflow O_2 level reduces to 3%, the flame luminosity is drastically lower, especially near the flame base, therefore the exact liftoff height cannot be identified without ambiguity. Natural gas and ethylene flames issuing into a hot coflow with lower oxygen concentration were also reported to have faint flame bases [43, 44].

Under conventional combustion, an increase in the oxygen level in the oxidant stream is expected to cause a decrease in the liftoff height as the reactivity of the mixture is enhanced. However, as shown in Fig 2, the apparent liftoff heights of the ethanol flames are comparable under three coflow conditions. The liftoff height of the DME flame in the 3% O_2 coflow is also similar to that in the 6% O_2 case. The flame in the 9% O_2 case was slightly less lifted. This unusual trend in the liftoff height indicates that the flame stabilisation mechanism under conditions relevant to MILD combustion may be different from that in conventional combustion.

3.2. OH chemiluminescence*

A mean image of OH* chemiluminescence is averaged from 140 images taken with a gate time of 1 ms. The maximum OH* signal at a given height in the mean image after correcting for background is referred to as the peak intensity of OH* chemiluminescence. This is presented as a function of X/D for the ethanol and the DME flames in Fig. 3.

The peak intensity of OH* chemiluminescence increases substantially with the coflow O_2 level for both fuels. This is consistent with the increased flame luminosity shown in Fig. 2. A previous study on MILD combustion of methane using a jet-in-cross-flow burner reported that minor changes were found in the intensity of OH* chemiluminescence as the oxygen level increased [45]. The coflow temperature and oxygen level were strongly coupled in the previous study, however they are independent of each other in the current work. This may account for the discrepancy in the trend of OH* chemiluminescence.

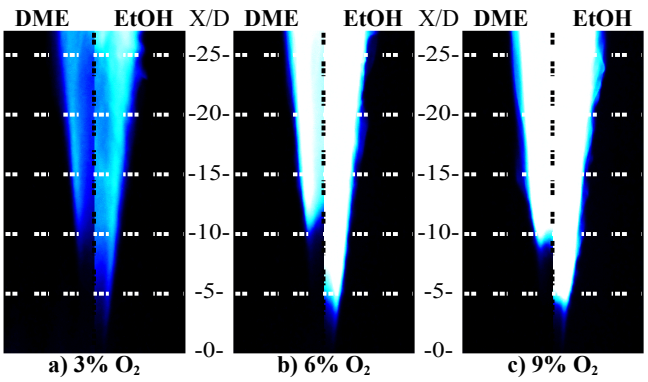

Figure 2: Photographs of DME and ethanol (EtOH) flames carried by nitrogen in the 1250-K coflow with various oxygen concentrations (3%, 6%, and 9% O_2 by volume). The jet flames were shield by the surrounding coflow until approximately X/D=22, where X is the axial distance above the jet exit plane and D is the jet diameter.

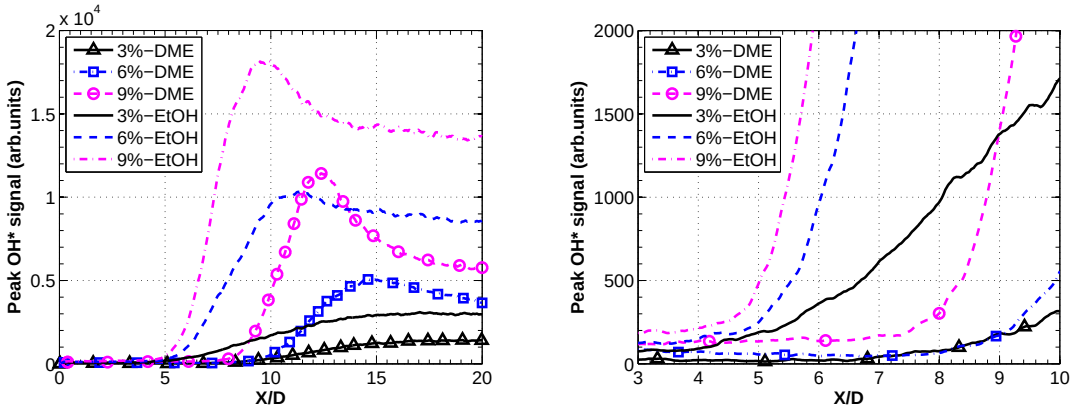

(a) X/D = 0 - 20

(b) X/D = 3 - 10

Figure 3: The peak intensity of OH* chemiluminescence at each axial distance in the mean images of ethanol and DME flames carried by N_2

Figure 3(b) displays the OH* profiles in the region between X/D = 3 - 10. It shows that given the same fuel, the growth in the OH* chemiluminescence is initiated nearly at the same axial location under the three coflow conditions. For instance, the signal of OH* chemiluminescence started to increase approximately at X/D = 5 for ethanol in various coflow cases.

The coflow O_2 level also affects the evolution of the build-up of the OH* chemiluminescence. For the ethanol flames in the 6% and 9% O_2 coflow, the peak intensity of OH* chemiluminescence increases rapidly over a small distance until it reaches its maximum, which is then followed by a decline in the intensity. In contrast, the peak intensity of OH* chemiluminescence from the ethanol flame in the 3% O_2 coflow increases gradually along the axial direction with a much smaller spatial gradient. The peak OH* chemiluminescence has been found to correlate to the peak temperature and the peak heat release rate in methane [46] and ethanol flames [47]. Therefore, in comparison with flames in the 6% and 9% O_2 coflows, a more spatially

distributed temperature and heat release can be deduced from the OH^* profile in the 3% O_2 case. Based on the distributed nature of MILD combustion [1, 48, 49], flames in the 3% O_2 coflow agree better with MILD combustion conceptually than flames in the coflow with a higher oxygen level.

The coflow O_2 level shows the same impact on the build-up of OH^* chemiluminescence for the DME flames. However, in comparison with the ethanol flames, the rapid increase in the peak intensity of OH^* chemiluminescence initiates further downstream in the DME flames. For instance, in the 6% O_2 coflow the OH^* chemiluminescence signal starts to increase around X/D = 10, where the flame base is located in the photograph shown in Fig. 2. Under the same coflow conditions, the peak intensity of OH^* chemiluminescence in the DME flames is considerably lower than that in the ethanol flames.

3.3. Instantaneous images: impact of coflow O_2 level

A selection of instantaneous OH (top), CH_2O (middle), and temperature (bottom) image triplets for the ethanol flames in the 3% and the 9% O_2 coflow are displayed in Fig. 4. The centre of the images is at X/D = 3.15 (14.5 mm), X/D = 4.89 (22.5 mm), and X/D = 6.41 (29.5 mm) above the jet exit plane. The color scale is chosen to emphasise the low OH and CH_2O signals, hence some images with strong signals appear saturated. The instantaneous OH, CH_2O and temperature images were smoothed with a median filter to enhance the apparent signal-to-noise ratio.

At X/D = 3.15 above the jet exit plane, a faint OH signal, approaching the detection limit of the current setup, is observed from ethanol flames in the 3% O_2 coflow. This indicates a small quantity of OH was formed at this height. At X/D = 4.89 and X/D = 6.41, a higher level of OH was produced at approximately R/D = 2 in the ethanol flame in the 3% O_2 coflow. The OH layer was uniformly distributed across the entire laser sheet vertically.

The OH structure of the ethanol flame in the 9% O_2 coflow displays subtle, but important, differences in comparison with that in the 3% O_2 coflow. A similar level of faint OH signal is also observed at X/D = 3.15, however the OH level becomes significantly higher at X/D = 4.89 and X/D = 6.41 in the 9% O_2 case, suggesting a higher spatial gradient of OH than the 3% O_2 case. This agrees with a sharp increase in the OH^* chemiluminescence in the 9% O_2 case, as shown in Fig. 3. Figures 4(e) and (f) also show that a thin region of weak OH "tail" exists upstream of a wide and defined region of strong OH. The occurrence of this kind of structure, referred to as a transitional flame structure, has been reported for ethylene-based flames in a coflow with 9% but not with 3% O_2 by volume [12]. This feature has previously been utilised to identify the transition away from the MILD combustion regime as the coflow oxygen level increases [50].

Along with a small quantity of OH, a considerable amount of CH_2O is measured in the fuel-rich region in the 3% and 9% O_2 cases. This further supports that reactions have already started at X/D = 3.15. This is in accordance with the common observation that CH_2O is the ignition precursor in flames issuing into a hot vitiated coflow [51, 52]. The CH_2O signal increases substantially with the axial distance, meanwhile its spatial distribution is broadened downstream.

The CH_2O signals of flames within the 9% O_2 coflow are lower than those in the 3% O_2 coflow, particularly near the jet exit plane. Typical of stable intermediates, the evolution of CH_2O is subject to convective-

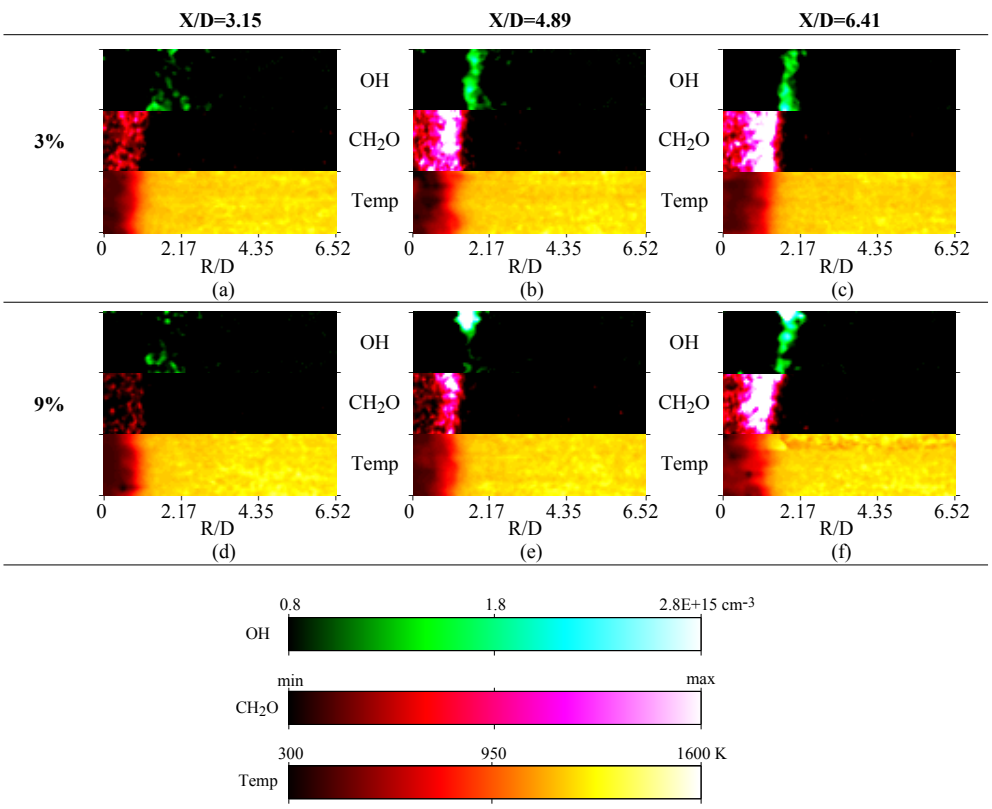

Figure 4: A selection of instantaneous OH (top), CH_2O (middle), and temperature (bottom) image triplets for ethanol flames in the 3% and the 9% O_2 coflow. These images are centred at X/D = 3.15 (14.5 mm), X/D = 4.89 (22.5 mm), and X/D = 6.41 (29.5 mm) above the jet exit plane, respectively. The left edge of each image is coincident with the jet centreline. Each image 8 × 30 mm.

diffusive transport effects, as well as chemical kinetics effects [53]. A previous study on methane flames found that an increase in the O_2 concentration at the location of peak CH_2O led to an increase in CH_2O production [6]. In addition, a higher O_2 concentration at the location of peak CH_2O was reported in a 3% O_2 coflow than that in a 9% O_2 coflow, resulting from an enhanced transport of O_2 to the fuel-rich side [6]. This could be responsible for a higher CH_2O signal in the 3% than the 9% O_2 case, although it is acknowledged that the chemical kinetics impacts of O_2 levels on CH_2O formation might be dissimilar between ethanol and methane flames.

The temperature distribution of flames in the 3% and the 9% O_2 coflow is similar. The temperature images show a cold fuel-rich region and a hot coflow region with a uniform distribution of temperature. The temperature in the fuel-rich region increased gradually with the axial distance as more fuel was mixed with the hot coflow along the axial direction. At X/D = 4.89 and X/D = 6.41, a well-defined region of OH is observed, and there is no noticeable temperature increase at the corresponding locations. The lack of correlation between the OH formation and the temperature increase was also reported in ethylene flames in a previous study on the same JHC burner [36].

3.4. Instantaneous images: impact of fuel type

Ethanol (CH_3-CH_2-OH) and DME (CH_3-O-CH_3) have the same number of C, H and O atoms, but different chemical structure. Their distinct chemical structure is expected to cause differences in the flame structure.

Figures 5 and 6 display a selection of instantaneous OH (top), CH_2O (middle), and temperature (bottom) image triplets for the ethanol and the DME flames in the 3% and the 9% O_2 coflows, respectively. A higher CH_2O-LIF signal is observed in the DME flames than in the ethanol flames at a given axial distance. On average, the CH_2O signal in the DME flames is twice that in ethanol flames under the same coflow conditions. A previous study by Gabet et al. [54] also reported a strong CH_2O-LIF signal in DME flames in comparison with the methane-based flames.

The OH signal is slightly higher in the DME flames than in the ethanol flames at X/D = 3.15. Further downstream, the coflow oxygen level produced the same effects on the OH structure in the DME flames as in the ethanol flames. Specifically, a spatially distributed OH layer is observed approximately at R/D = 2 in the DME flame issuing into the 3% O_2 coflow. As for the 9% O_2 case, the OH level increases rapidly with the axial distance, and a transitional flame structure is shown at X/D = 6.41.

In summary, the coflow oxygen level shows the same impact on the distribution and build-up of OH and CH_2O for the ethanol and the DME flames. However, the intensity of OH-LIF and CH_2O-LIF signals vary between these two fuels, indicating different levels of OH and CH_2O were produced. Particularly, the OH and CH_2O signals in the DME flames are higher than those in the ethanol flames upstream of the apparent lift-off height, despite that the DME flames appeared more lifted than the ethanol flames. These phenomena are further investigated via numerical studies later in this paper.

4. Reaction flux analysis with the OPPDIF code

A limited number of previous studies have focused on a direct comparison of DME and ethanol flames [24, 25, 26, 27, 28, 29, 30, 31, 55], most of which were for laminar and/or premixed flames. A few studies [25, 27] were performed on a counter-flow burner configuration in order to investigate the extinction and autoignition characteristics for the two fuels. Autoignition of ethanol flames was found to be delayed by the addition of DME, and the magnitude of this effect is dependent on strain rate [27]. It was also reported that DME flames were less prone to extinction than ethanol flames due to differences in the kinetics of intermediate species, such as formyl and methyl radicals [25]. However, experimental results in the present study show that these two fuels behave similarly under MILD combustion conditions in general. It is hypothesised that the H_2/O_2 pathways become dominant in the oxidation of both DME and ethanol due to a higher reactant temperature under MILD combustion conditions, resulting in their similarities.

In order to investigate this hypothesis and better understand the effect of fuel chemistry and interpret the experimental results, reaction path and sensitivity analyses should be performed. The oxidation of the fuels is initiated via fuel decomposition, including unimolecular decomposition and H atom abstraction reactions. It is necessary to analyse the fuel decomposition reactions in order to reveal differences in the initiation of the

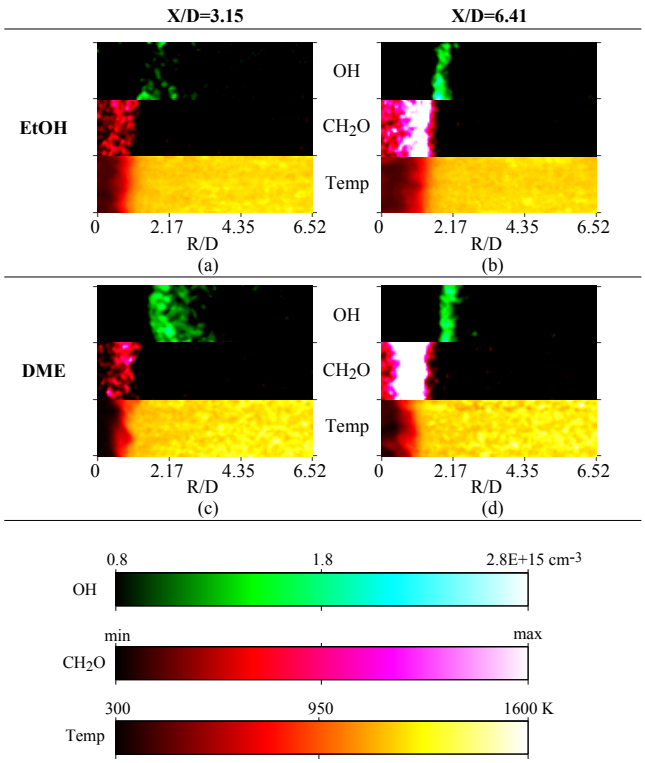

Figure 5: A selection of typical instantaneous OH (top), CH_2O (middle), and temperature (bottom) image triplets for ethanol and DME flames in the 3% O_2 coflow. These images are centred at X/D = 3.15 (14.5 mm) and X/D = 6.41 (29.5 mm) above the jet exit plane, respectively. The left edge of each image is coincident with the jet centreline. Each image 8 × 30 mm.

oxidation processes amongst the three fuels. Hence, primary kinetic pathways and sensitivity analysis should be performed at the mixture fraction where the peak fuel consumption rate occurs. To complement these results, analysis on the sensitivity of temperature to reaction rates across the whole mixture fraction domain is also required to demonstrate important features in the overall pyrolysis and oxidation processes. The Chemkin software is chosen for these reaction flux analyses as it provides built-in reaction path and sensitive analysis tools. In order to focus on the fuel chemistry and avoid the complexity of turbulence-chemistry interaction, laminar flame calculations of non-premixed flames at atmospheric pressure are performed with the OPPDIF code in the Chemkin software. These calculations are performed for steady flames, thus they are only relevant downstream of the stabilisation point.

A schematic of the opposed-flow flame setup is shown in Fig. 7. The fuel inlet is modelled as a cold mixture of N_2 (same concentration as the carrier N_2 in the experiments) and fuel: CH_3OCH_3, C_2H_5OH or ethane. Ethane (C_2H_6) is considered here for comparison to identify if a particular feature in a flame is caused by the existence of the O atom or by the different fuel structure. To reveal the impact of the presence of a hot and diluted coflow, the oxidiser inlet is modelled as cold air, a hot experimental coflow with 3% or 9% O_2 by volume, which is referred to as air case, 3% O_2 case, and 9% O_2 case, respectively. The two opposing inlets are separated by 20 mm, and the momentum of the two inlets are balanced such that the

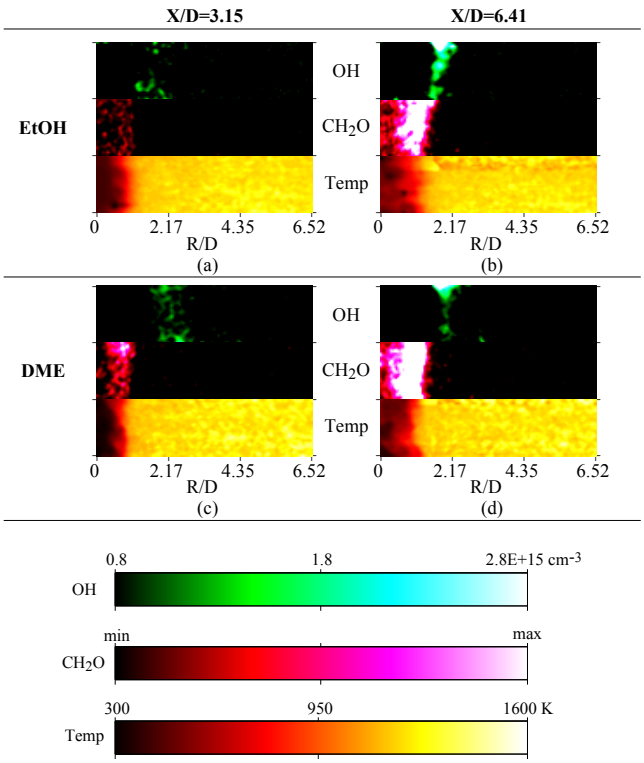

Figure 6: A selection of typical instantaneous OH (top), CH_2O (middle), and temperature (bottom) image triplets for ethanol and DME flames in the 9% O_2 coflow. These images are centred at X/D = 3.15 (14.5 mm) and X/D = 6.41 (29.5 mm) above the jet exit plane, respectively. The left edge of each image is coincident with the jet centreline. Each image 8 × 30 mm.

stagnation plane is at X = 10 mm. Only results at a strain rate of 150 s^{-1} are presented in this subsection for brevity; however it is worth noting that the general trends are independent of strain rate.

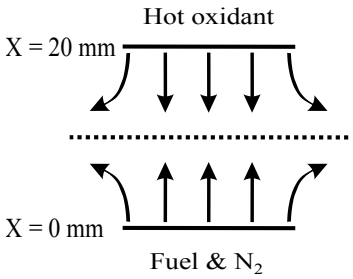

Figure 7: Schematic of the opposed-flow flame setup.

All the calculations and analyses were carried out using a mechanism developed by Zhao et al. [56], consisting of 55 species and 290 reversible reactions. This mechanism consists of DME-related reactions and a baseline H_2/C_1-C_2 submodel developed for fuels like C_2H_5OH [56], which has been tested in previous studies [54, 55, 57, 58]. A multicomponent transport formulation is adopted while considering the effects of thermal diffusion in all the calculations.

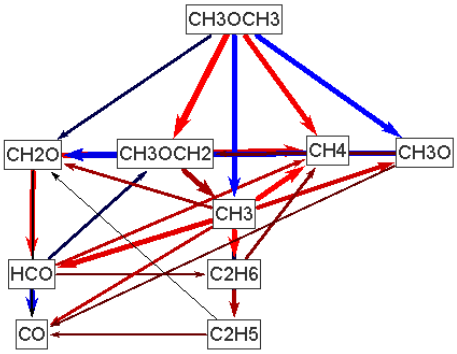

(a) CH_3OCH_3 decomposition at Z = 0.11

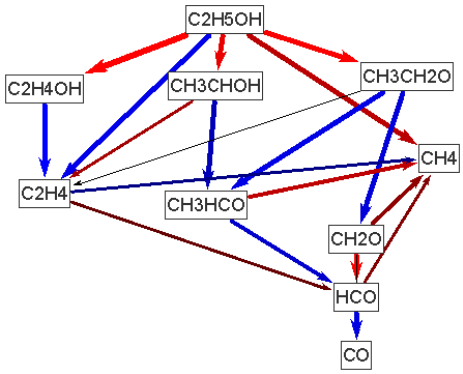

(b) C_2H_5OH decomposition at Z = 0.15

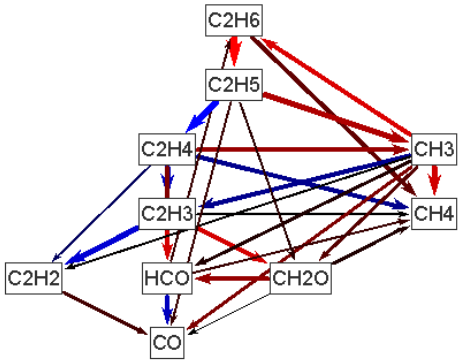

(c) C_2H_6 decomposition at Z = 0.07

Figure 8: The fuel decomposition pathways at the mixture fraction where the peak fuel consumption rate occurs in the 3% O_2 case. The pathways start with the fuel, followed by the nine most important species containing carbon. The thickness of arrows corresponds to the absolute rate of production/destruction. Arrows are coloured by heat, where brown to red indicates the increasing magnitude of positive heat release, and dark to blue indicates the increasing magnitude of negative heat release.

4.1. Fuel chemistry comparison for the 3% O_2 case

Figure 8 illustrates primary kinetic pathways at the mixture fraction where the peak fuel consumption rate occurs in the 3% O_2 case. This demonstrates the major routes of fuel decomposition at that mixture fraction. The pathways start with the fuel, followed by the nine most important species containing carbon.

The existence of O atom is preserved during the decomposition of DME. Figure 8(a) demonstrates that the destruction of DME produces CH_2O, CH_3OCH_2, CH_3, CH_4, and CH_3O. One of the major intermediate species in the DME consumption path is CH_2O. The production of CH_2O is predominantly via β-scission after H-abstraction reactions: $CH_3OCH_3 \rightarrow CH_3OCH_2 \rightarrow CH_3+CH_2O$. Most of CH_2O is converted to formyl radical (HCO), subsequently converted to CO. The importance of CH_2O can also be inferred from its concentration. As displayed in Fig. 9(a), the concentration of CH_2O in the DME flames is significantly higher than the ethanol and the ethane flames. This is in accordance with imaging of CH_2O-LIF in the current experiments, where a higher CH_2O-LIF signal was collected from the DME flames than the ethanol flames at the same axial location.

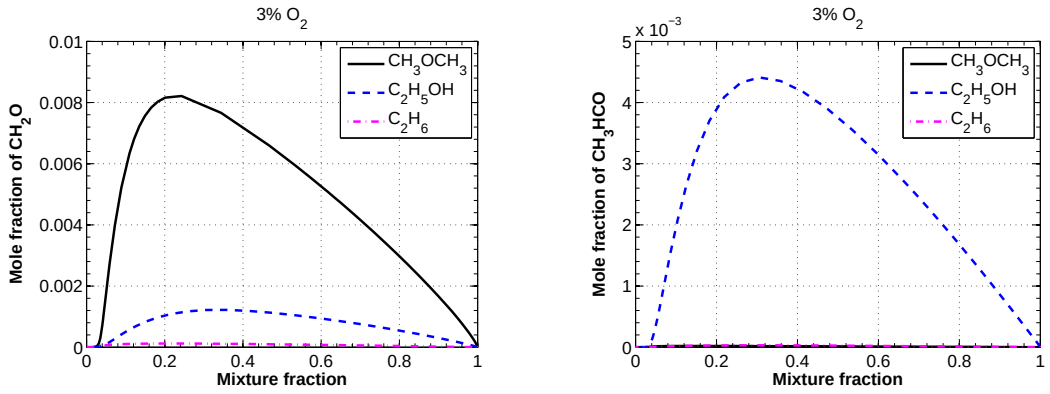

(a) (b)

Figure 9: Mole fraction of CH_2O and CH_3HCO as a function of mixture fraction for three fuels with a 3% O_2 hot oxidant.

The O atom is also retained during the consumption of ethanol. Figure 8(b) demonstrates that five main species, including C_2H_4OH, CH_3CHOH, CH_3CH_2O, C_2H_4, and CH_4, are formed following the destruction of ethanol. Some of these species are further converted to CH_3HCO mainly via hydrogen atom abstraction reactions. The vast production of CH_3HCO is an important feature in ethanol chemistry, which has been reported in previous studies [28, 30]. As shown in Fig. 9(b), the mole fraction of CH_3HCO in the ethanol flame is remarkably higher than that in the DME and the ethane flames.

In comparison with DME and ethanol, ethane is mainly converted to C_2H_5 via H-abstraction by H. Hence, the amount of unsaturated C_2 species in the ethane flame is expected to be considerably higher than that in the ethanol and the DME flames. Figure 10 displays a reduction in the concentrations of C_2H_4 and C_2H_2 in flames of oxygenated fuels, particularly DME. Higher yields of unsaturated C_2 species in the ethanol flame than the DME flame can be attributed to the formation of C_2H_4OH, which is subsequently decomposed to C_2H_4 and OH. In addition, due to the absence of a C-C bond, CH_3OCH_3 decomposes to CH_2O and CH_3 directly. This leads to a higher production of CH_4, as shown in Fig. 10(c).

The difference in the production of unsaturated C_2 species is not of great importance in the combustion of pure ethanol or DME. However, this should be taken into account when they are used as a fuel blend to reduce soot emissions. For instance, emissions of soot and particulates produced from heavy fuel oil were still high even when it was burnt in flameless combustion mode [8, 59]. The addition of oxygenated fuels to heavy fuel oil may help reduce these emissions.

More information regarding the fuel decomposition can be obtained from sensitivity analysis of the fuel concentration. This quantitatively shows how sensitive the fuel concentration is to the reaction rate of a particular reaction. As displayed in Fig. 11, for all three fuels the destruction of the fuel is most sensitive to the chain branching reaction $H+O_2 \rightleftharpoons O+OH$ (R1). The other common feature amongst the three fuels is that their concentration is sensitive to $CO+OH \rightleftharpoons CO_2+H$ (R29), which is one of the main contributors for heat release, thus promoting the consumption of the fuel. In comparison with ethanol and ethane, the concentration of DME is more sensitive to reactions involving methyl radical as shown in Fig. 11(a). Further

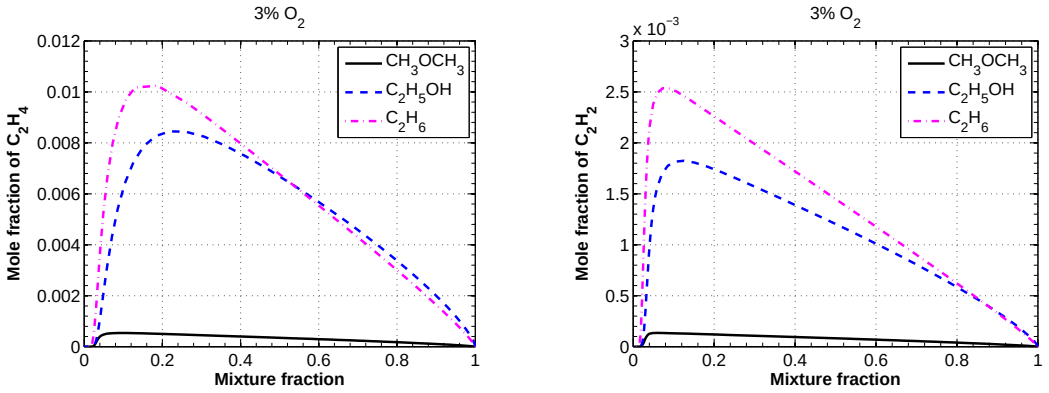

(a)

(b)

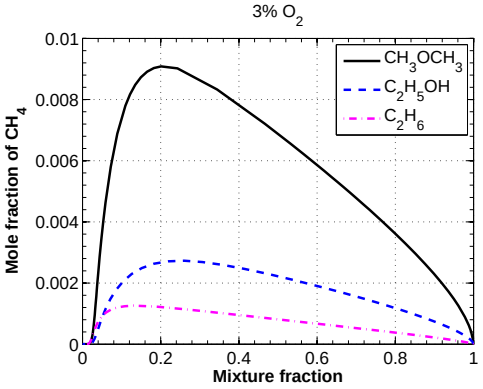

(c)

Figure 10: Mole fraction of C_2H_4, C_2H_2, and CH_3 as a function of mixture fraction for three fuels with a 3% O_2 hot oxidant.

analysis reveals that the production of methyl radical is significantly influenced by reaction R1 in the DME flame, contributing to the dominant importance of R1 in the fuel decomposition.

Results of temperature sensitivity are presented in Fig. 12. These results quantitatively demonstrate how sensitive temperature is to the reaction rate of a particular reaction. For all three fuels, reaction $H+O_2 \rightleftharpoons O+OH$ (R1) has the largest positive sensitivity coefficient, indicating the largest effect on increasing the temperature of the system. Reaction $CH_3+H(+M) \rightleftharpoons CH_4(+M)$ (R53) has the largest negative sensitivity coefficient and affects the temperature decrease the most. Consistent with the sensitivity analysis of the fuel consumption, temperature is also very sensitive to $CO+OH \rightleftharpoons CO_2+H$ (R29) for all three fuels.

To summarise, the differences in the fuel decomposition pathways in the 3% O_2 case affect the intermediate species pool considerably. This is reflected in the relative importance of intermediates, such as CH_2O, CH_3HCO, and CH_4. However, these differences in the chemical kinetics seem to play a minor role in the overall ignition and oxidation process as suggested by temperature sensitivity analysis. This analysis indicates the importance of H_2/O_2 pathways for all three fuels burning in a hot oxidiser with 3% O_2, which helps explain the similarities between the ethanol and the DME flames observed in the current experiments.

4.2. Fuel chemistry comparison for the air case

In order to better understand the impact of a hot and diluted oxidiser, calculations and sensitivity analyses were also performed for the three fuels burning in cold air (air case). Figure 13 shows that the peak flame temperature decreases by nearly 600 K as the oxidiser changes from the cold air to the 3% O_2 hot coflow. This matches with the usual observation of MILD flames with a reduced temperature increase. However, the temperature reduction is less than 200 K in the 9% O_2 case. The peak flame temperature of the three fuels is very close to each other when they are burning under the same oxidiser.

One interesting difference between the 3% O_2 case with the air case is found in the relative concentration of unsaturated C_2 species. To better depict the difference, the mole fractions of C_2H_4 and C_2H_2 are normalised to their peak mole fractions in the ethane flame at each case, as shown in Fig. 14. When oxygenated fuels are burnt instead of ethane, the reduction in the amount of unsaturated C_2 species is less significant in the air cases than the 3% O_2 cases. This indicates how intermediate species kinetics change with the oxidants. Fig. 14(b) and 14(e) also show the profiles of C_2H_4 and C_2H_2 in the 9% O_2 case, which resemble more closely the profiles in the air case rather than those in the 3% O_2 case. The fuel chemistry at the 9% O_2 case will be discussed in more detail in the following section.

Figure 15 presents the sensitivity analysis results of the destruction of each fuel at the mixture fraction, at which the peak fuel consumption rate occurs in the air cases. In contrast to the 3% O_2 cases, the concentration of each fuel does not show the largest sensitivity to $H+O_2 \rightleftharpoons O+OH$ (R1), but becomes more sensitive to fuel-specific reactions. For instance, the destruction of ethanol is most sensitive to $C_2H_5OH \rightleftharpoons C_2H_4+H_2O$ (R204).

The temperature sensitivity analysis also reflects differences between the 3% O_2 case and the air case. As shown in Fig. 16, reaction $H+O_2 \rightleftharpoons O+OH$ (R1) no longer has the largest positive impact on temperature. For all three fuels in the air case, temperature is mostly influenced by $H+OH+M \rightleftharpoons H_2O+M$ (R12), closely followed by $H+O_2(+M) \rightleftharpoons HO_2(+M)$ (R13). This shifted importance is suspected to result from a much

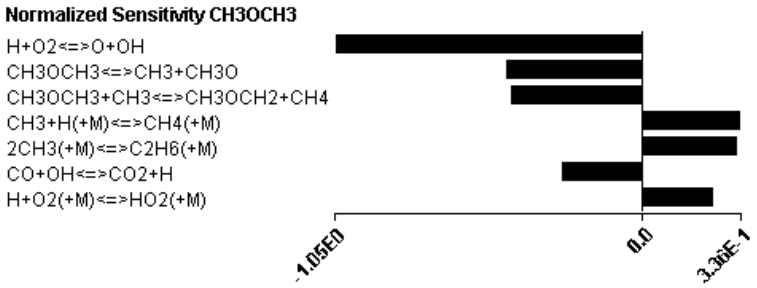

(a) Sensitivity coefficient of CH_3OCH_3 at Z = 0.11

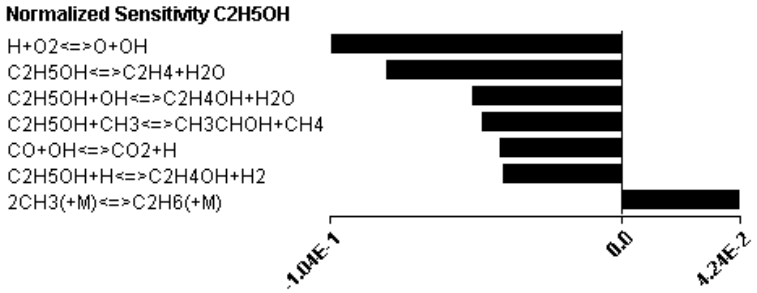

(b) Sensitivity coefficient of C_2H_5OH at Z = 0.15

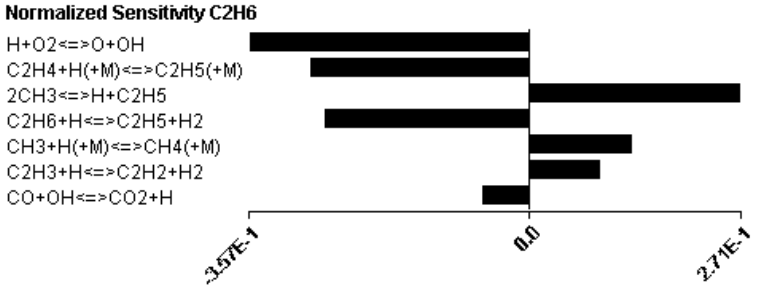

(c) Sensitivity coefficient of C_2H_6 at Z = 0.07

Figure 11: Sensitivity coefficients for the fuel at the mixture fraction where the peak fuel consumption rate occurs for three fuels with a 3% O_2 hot oxidant.

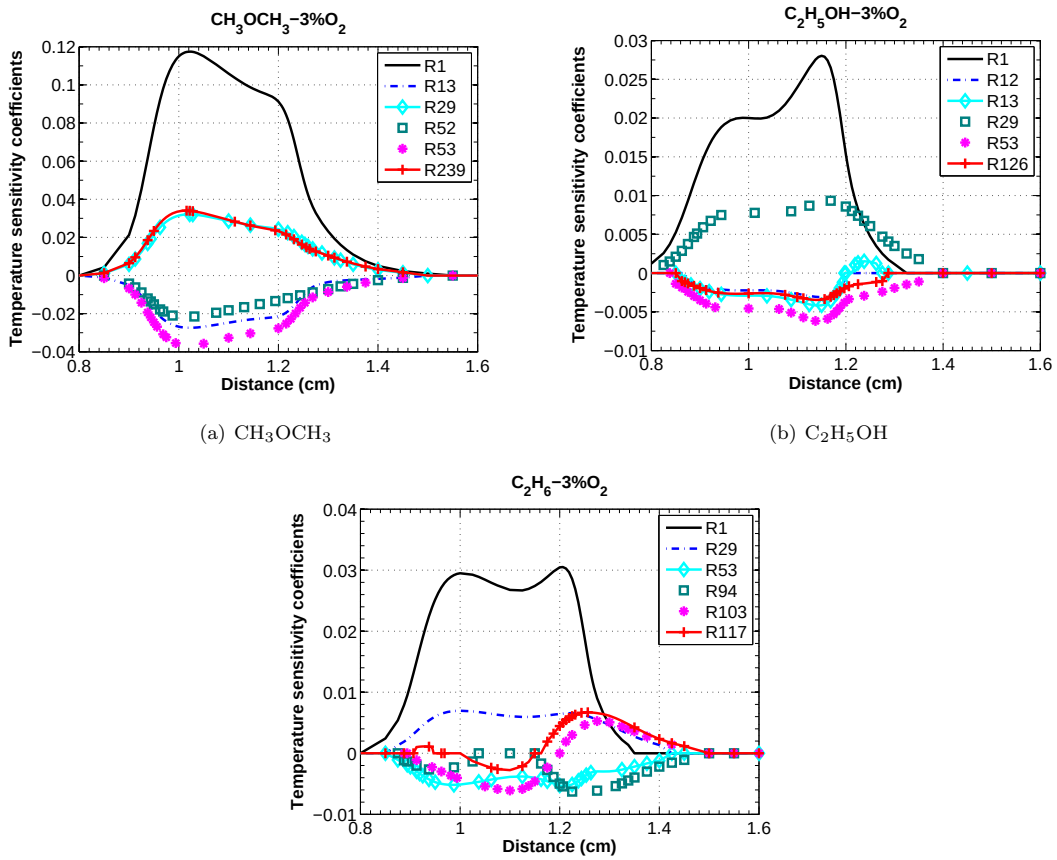

(a) CH_3OCH_3

(b) C_2H_5OH

(c) C_2H_6

Figure 12: Temperature sensitivity to reaction rates as a function of distance for three fuels with a 3% O_2 hot oxidant.

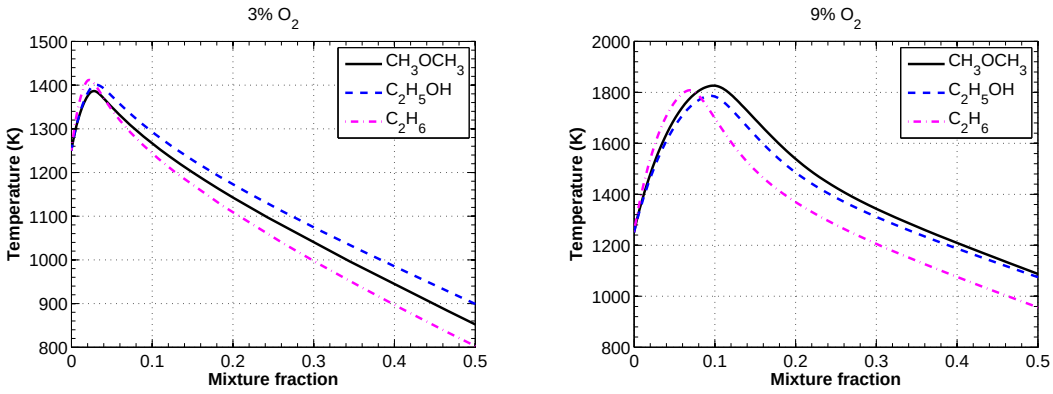

(a) CH_3OCH_3 (b) C_2H_5OH

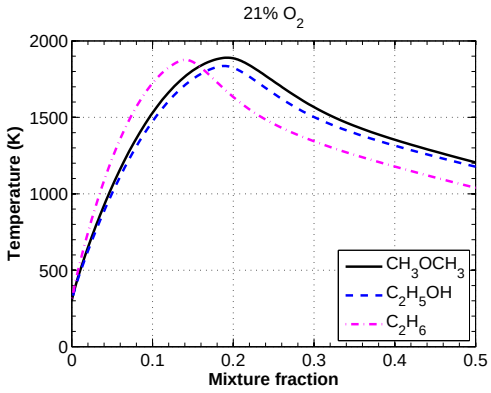

(c) C_2H_6

Figure 13: Temperature as a function of mixture fraction for CH_3OCH_3, C_2H_5OH, and C_2H_6 flames burning in a vitiated oxidiser with 3% or 9% O_2 and in a cold air (O_2 = 21%).

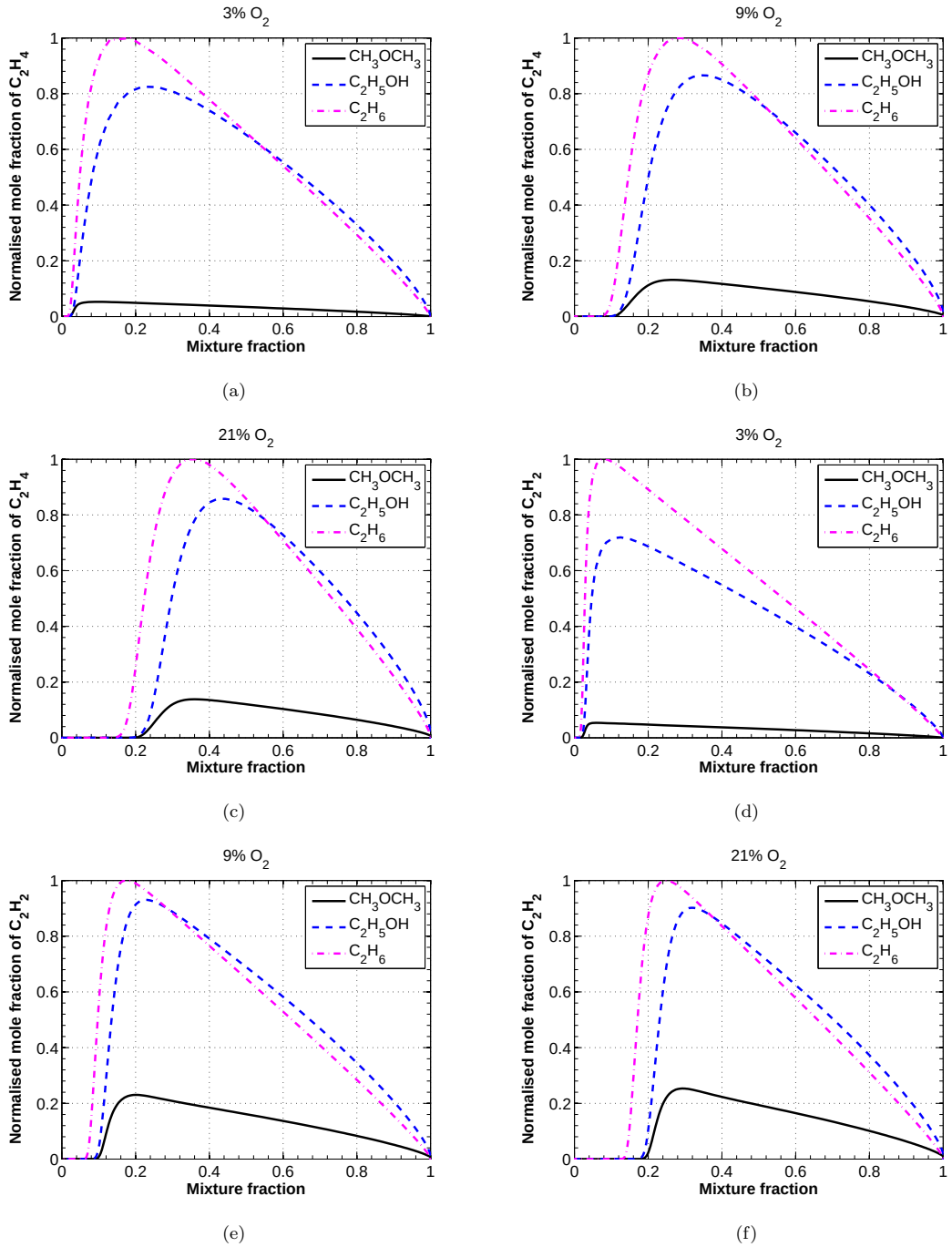

Figure 14: Normalised mole fraction of C_2H_4 and C_2H_2 for CH_3OCH_3, C_2H_5OH, and C_2H_6 flames burning in a vitiated oxidiser with 3% or 9% O_2 and in a cold air ($O_2 = 21\%$). The mole fractions of these species are normalised to their peak mole fractions in the ethane flame at each case.

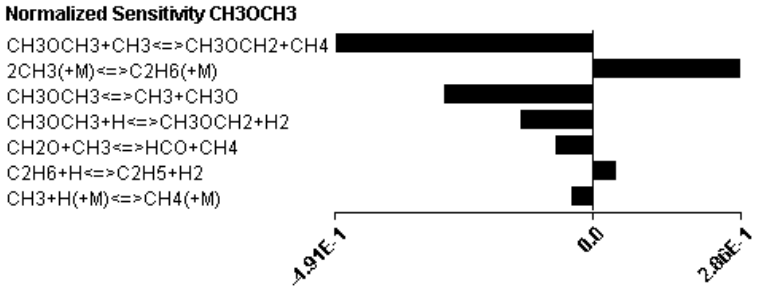

(a) Sensitivity coefficient of CH_3OCH_3 at Z = 0.37

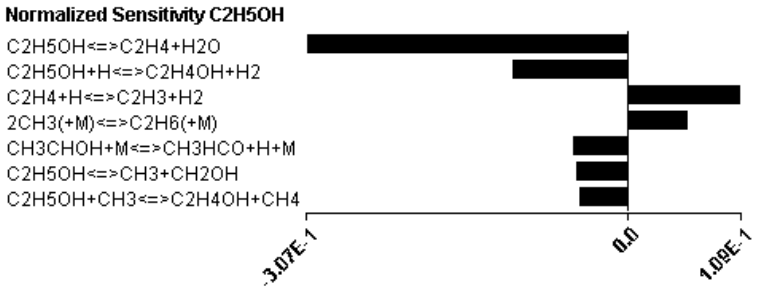

(b) Sensitivity coefficient of C_2H_5OH at Z = 0.33

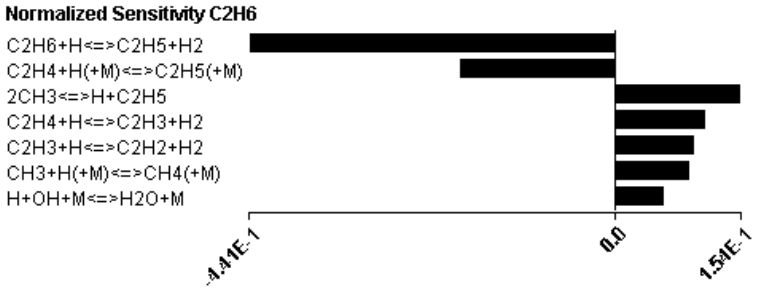

(c) Sensitivity coefficient of C_2H_6 at Z = 0.25

Figure 15: Sensitivity coefficients for the fuel at the mixture fraction where the peak fuel consumption rate occurs for three fuels with cold air as the oxidiser.

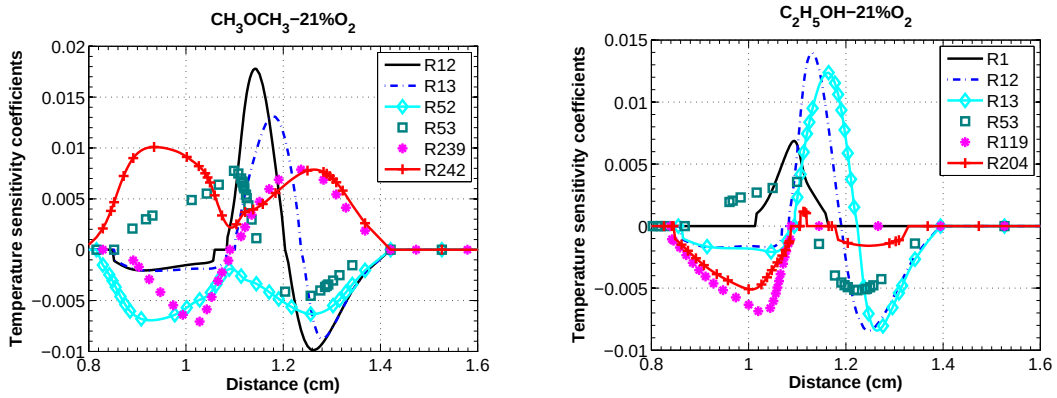

(a) CH_3OCH_3

(b) C_2H_5OH

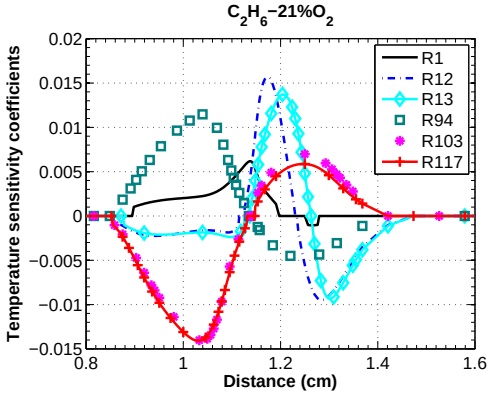

(c) C_2H_6

Figure 16: Temperature sensitivity to reaction rates as a function of distance for three fuels with cold air as the oxidiser.

lower initial temperature in the air case than the 3% O_2 case. Pellett et al. [60] reported that the reaction rates of R1 and R13 are balanced at the cross-over temperature approximately at 925 K at 1 atm. Hence, the lower temperature of air shifts the local temperature below the cross-over temperature, thereby promoting R13 over R1.

Important reactions become more different among the three fuels in the air case with respect to the 3% O_2 case, particularly in the fuel-rich region. In this region, reactions that have the largest positive/negative temperature sensitivities are mostly fuel-specific reactions with little shared similarities, such as $CH_3OCH_3 \rightleftharpoons CH_3+CH_3O$ (R239) in the DME flame, and $C_2H_4+H \rightleftharpoons C_2H_3+H_2$ (R119) in the ethanol flame.

The sensitivity analyses of the temperature and the fuel concentration suggest that the chemical pathways of three fuels become more different in the air case. Hence, ethanol and DME flames may be more dissimilar to each other when they are burnt in cold air instead of a hot oxidiser with 3% O_2.

4.3. Fuel chemistry comparison for the 9% O_2 case

Figure 17 shows a list of reactions that strongly affect the concentration of each fuel at the mixture fraction where the peak fuel consumption rate occurs in the 9% O_2 case. Interestingly, similar to the air case, these results indicate that fuel related reactions play a dominant role during the fuel decomposition process. Specifically, the concentrations of the three fuels are not very sensitive to $H+O_2 \rightleftharpoons O+OH$ (R1) and $CO+OH \rightleftharpoons CO_2+H$ (R29), different from results in the 3% O_2 case.

The reduced importance of reaction $H+O_2 \rightleftharpoons O+OH$ (R1) in the 9% O_2 case is also revealed by temperature sensitivity analysis, as shown in Fig. 18. Despite a very high initial temperature of the oxidiser, reactions of lower activation energy ($H+OH+M \rightleftharpoons H_2O+M$ (R12) and $H+O_2(+M) \rightleftharpoons HO_2(+M)$ (R13)) become more important than R1. Moreover, reactions that affect temperature the most in the 9% O_2 case are nearly the same as in the air case, regardless of large differences in the temperature and oxygen concentration of the oxidiser between these two cases.

In summary, sensitivity analysis results indicate that a three-fold increase in the oxygen concentration causes fundamental changes in the chemical kinetics of these fuels between the 3% and the 9% O_2 case. This can be used to explain why the ethanol and the DME flames shifted away from the MILD combustion regime as the oxygen concentration in the hot coflow increased from 3% to 9% in the current experiments.

5. Unsteady Flamelet Analysis

Reaction flux analyses in the preceding section were performed for steady opposed-flow laminar flames. However, the ignition of fuels is a time-varying process. Hence, an unsteady laminar flamelet analysis is presented to compare the transient ignition processes of the ethanol and the DME flames.

The unsteady flamelet model used here is similar to the model developed by Pitsch et al [61]. This model has previously been applied, with a two-step analysis procedure, to simulate MILD flames in the same JHC configuration by Evans et al [44]. To obtain the flow and mixture fields, non-reactive Large-Eddy Simulation (LES) was carried out. These simulations provided the temporal evolution of the flow field parameterised by the scalar dissipation rate of the mixture necessary for the second step. During the second step, unsteady flamelet equations were solved in time and mixture fraction space. The two simulation steps will be described in detail in the following sections.

5.1. Modelling approach - Large-Eddy Simulation

LES was carried out to obtain a solution of the turbulent flow field. The experimental configuration was simulated using a fully three-dimensional cylindrical grid with 256, 128, and 96 grid points in the axial, the radial, and the circumferential directions, respectively. The grid is stretched in the axial direction with a grid spacing of 0.5 mm at the jet exit plane. The radial grid sizing is 0.1 mm at the nozzle. The boundary conditions were set to match the experimental conditions. A well-resolved LES of the central fuel pipe upstream of the jet exit plane was run prior to the main simulations, which generates velocity data at the jet inlet boundary for the main simulations. For the inlet boundary condition of the coflow, a constant velocity profile is prescribed. A convective outlet condition is defined for the outlet of the domain. At the radial

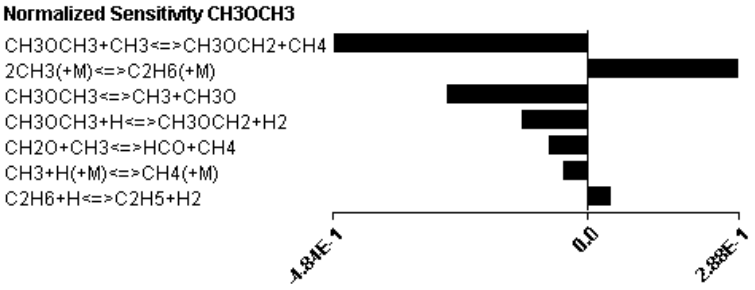

(a) Sensitivity coefficient of CH_3OCH_3 at Z = 0.28

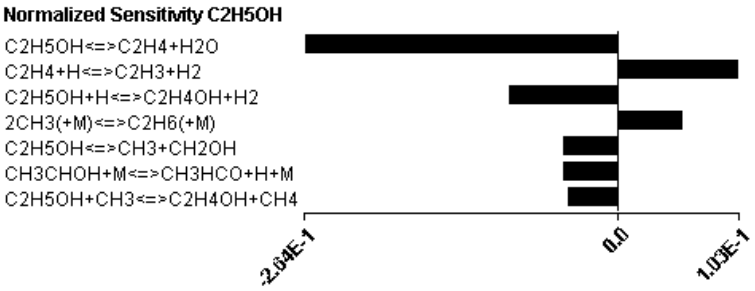

(b) Sensitivity coefficient of C_2H_5OH at Z = 0.25

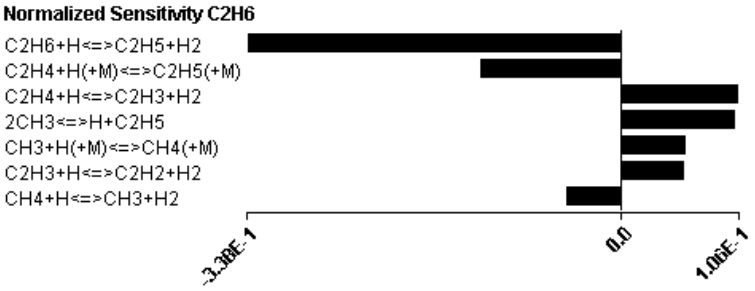

(c) Sensitivity coefficient of C_2H_6 at Z = 0.18

Figure 17: Sensitivity coefficients for the fuel at the mixture fraction where the peak fuel consumption rate occurs for three fuels with a 9% O_2 hot oxidant.

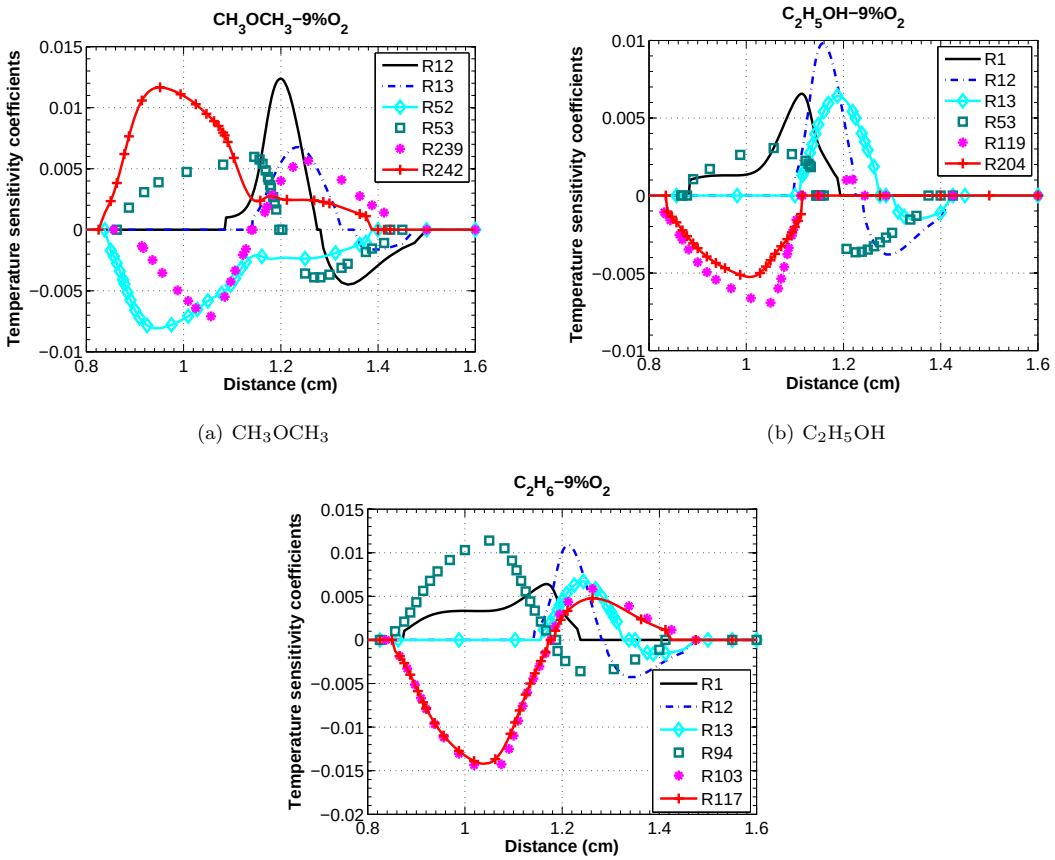

(a) CH_3OCH_3

(b) C_2H_5OH

(c) C_2H_6

Figure 18: Temperature sensitivity to reaction rates as a function of distance for three fuels with a 9% O_2 hot oxidant.

boundary of the simulation domain, zero gradient boundary conditions are imposed for either velocities or scalars, thus there is no flux at the boundaries in the radial direction.

The parallel, finite difference code CIAO was used for the LES. It solves the filtered Navier-Stokes equations in the low Mach number limit. The momentum equations are spatially discretized with a second-order scheme [62]. Spatial gradients of the scalar equation are discretized with a third order WENO scheme [63]. Unclosed subfilter terms are closed with a dynamic Smagorinsky model [64] with Lagrangian averaging [65] for the subfilter stress term and a Smagorinsky type model [66] for the subfilter diffusivity of the scalar equation. A scalar transport equation is solved for the filtered mixture fraction $\tilde{Z}$, which locally defines the state of the fluid mixture.

The scalar dissipation rate, determined from the flow-field solution, is defined as averaged conditional scalar dissipation rate at each grid plane in the axial direction. The distance to the jet exit plane can be related to the flamelet time via a characteristic velocity u_{st}, which is the mean axial velocity at the radial position where $\tilde{Z} = Z_{st}$ [61]. The relationship between the axial distance and the flamelet time is defined by [61]

$$t = \int_0^x \frac{1}{u_{st}|\,(Z = Z_{st})} dx' \tag{1}$$

Fluid properties, such as density, viscosity, and diffusivity of the scalar, are obtained from an extinct flamelet solution (χ above extinction strain rate), which is tabulated and accessed during runtime. During the second step, the unsteady flamelet model simulates the ignition process based on these fluid and turbulence properties. This analysis is only focused on the onset of ignition, and it assumes that changes in the conditional scalar dissipation rates are negligible due to a small temperature increase and limited heat release in the stabilisation region. Hence, these minor changes as a consequence of ignition are not incorporated into the LES as feedback. Jochim et al. [67] found that for diesel engine combustion, this assumption can even lead to correct predictions of the major characteristics of the entire combustion process.

5.2. Modelling approach - Unsteady flamelets

For the solution of chemistry, the unsteady flamelet equations [68, 69] are solved in time and mixture fraction space using the FlameMaster program [70]. The unsteady flamelet equations are

$$\rho\frac{\partial T}{\partial t} - \rho\frac{\chi}{2}\left(\frac{\partial^2 T}{\partial Z^2} + \frac{1}{c_p}\frac{\partial c_p}{\partial Z}\frac{\partial T}{\partial Z}\right) + \frac{1}{c_p}\left(\sum_{k=1}^{N} h_k \dot{m}_k - \mathcal{H}\right) = 0 \tag{2}$$

where T denotes the temperature, t and Z are time and mixture fraction, respectively. χ denotes the scalar dissipation rate, ρ is the density, and c_p is the specific heat capacity at ambient pressure. N is the number of species included in the mechanism, h_k and $\mathcal{H}$ represent the enthalpy of species k and the enthalpy flux by mass diffusion, respectively.

The scalar dissipation rates and local compositions are extracted from the LES as described in the preceding section. They change with time and are coupled to the axial distance via the characteristic time. The mechanism used in the unsteady flamelets model is the same as in Section 4 [56].

5.3. Results and discussion

Figure 19 shows the peak temperature from the flamelet solution as a function of time for ethanol and DME flames in the 3% and 9% O_2 cases. The mixture fraction where the peak temperature occurs is denoted as Z_{Tpeak}. Temperature profiles at Z_{st} and the most reactive mixture fraction (Z_{mr}) are also included for comparison. The most reactive mixture fraction is a result of the competing effects of high temperature at a leaner mixture fraction and high fuel concentration at a richer mixture fraction [71].

The maximum peak temperature is very close for the two fuels. However, given the same oxidant stream, a rapid increase in the peak temperature takes place earlier in the ethanol flames, indicating a much faster ignition in comparison with the DME flames. In the current experiments, DME flames always appeared more lifted than ethanol flames, as revealed by digital photography and imaging of OH* chemiluminescence. The larger liftoff heights are likely to result from longer ignition delay times of DME flames at the conditions corresponding to the most reactive mixture fraction.

As the oxygen level reduces from 9% to 3%, the ignition process becomes prolonged with a reduced temperature increase for both ethanol and DME. This change is most prominent at Z_{st}, where the gradient of the temperature profile is considerably sharper in the 9% O_2 case than the 3% O_2 case. Thus, flames in the 3% O_2 case agree better with the definition of MILD flame being distributed with a low temperature increase [1, 48, 49].

The flame propagation process is reflected by the change in Z_{Tpeak} with time. As demonstrated in Fig. 19, the peak temperature initially occurs at a very low mixture fraction with a low scalar dissipation rate for both fuels. As the ignition process proceeds, the temperature increase slowly propagates to a higher mixture fraction region where the corresponding scalar dissipation rate (χ) is higher.

The peak flame temperature occurs at a relatively leaner condition in the DME flames than the ethanol flames, particularly at the onset of temperature rise. The scalar dissipation rates at a given peak temperature for the DME flames are lower than those in the ethanol flames. For instance, at the location where the peak temperature reaches 1600 K, the scalar dissipation rate is 0.8 1/s for DME, but it is 1.5 1/s for ethanol in the 9% O_2 case. Mastorakos [71] reported that the ignition delay time is mainly determined by the scalar dissipation rate at the most reactive mixture fraction in the cold-fuel-hot-oxidant configuration. The ignition of the DME flames occurs later and at a leaner condition than in the ethanol flames. This also means that the initial temperature of the flammable mixture is higher in the DME flames than the ethanol flames. As shown in Fig. 19 (the bottom figure), the scalar dissipation rate at a given mixture fraction decreases with time, and the scalar dissipation rate is lower in the leaner conditions at a given time. These results indicate that the ignition of DME requires a lower scalar dissipation rate and a higher initial temperature than ethanol, reflecting a lower reactivity of DME at the conditions investigated here. A series of steady flamelets calculations is performed to produce a S-curve of scalar dissipation rate and the corresponding maximum temperature for the various cases investigated. These results show that, given the same oxidant stream, the scalar dissipation rate of ignition on the lower branch of S-curve for DME is lower than that for ethanol. This agrees with a previous study by Loukou et al. [27], who found that autoignition of ethanol was retarded by the addition of DME.

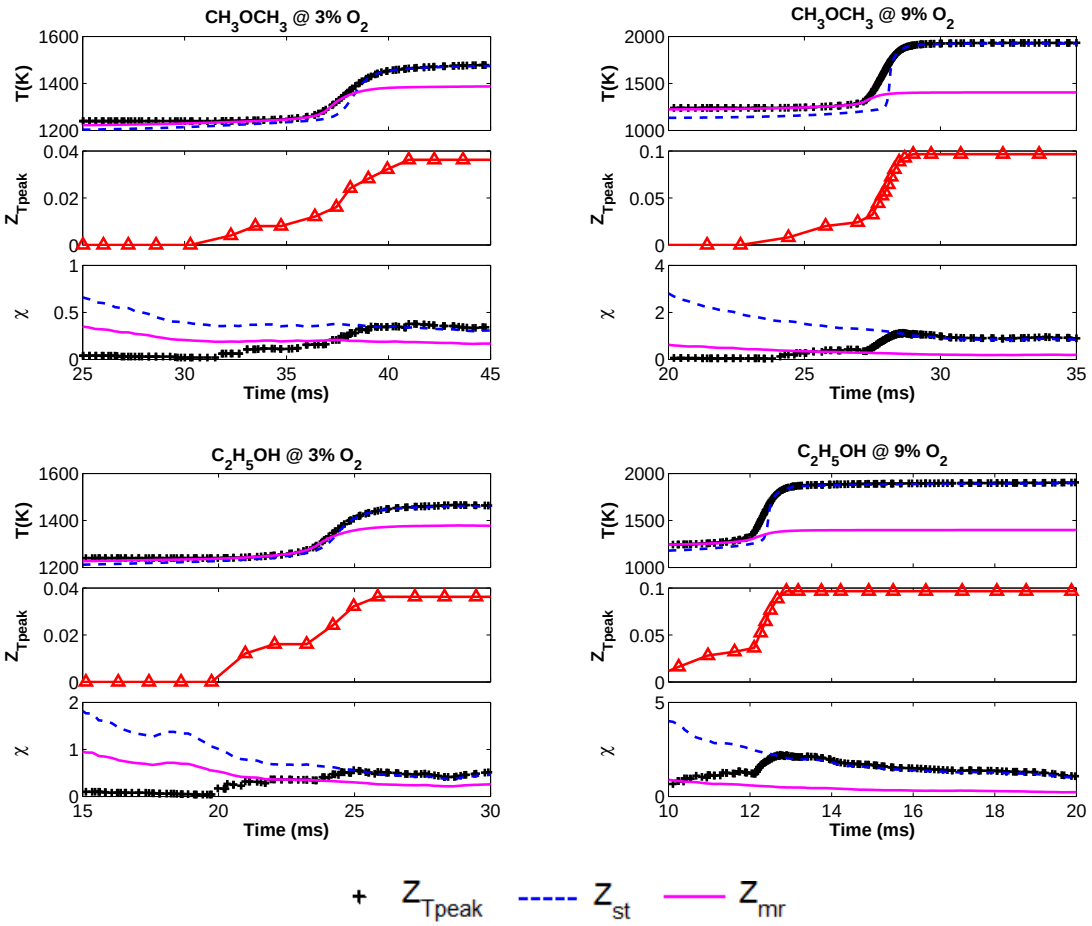

Figure 19: The mixture fraction where the peak temperature occurs is denoted as Z_{Tpeak}. The temperature and the scalar dissipation rate (χ) for ethanol and DME flames at Z_{Tpeak}, Z_{st}, and Z_{mr} in the 3% and 9% O_2 cases are presented as a function of time.

In order to better depict the temporal evolution process, Fig. 20 presents temperature as a function of mixture fraction at four time steps, including when the temperature increase (ΔT) reaches 10 K, when ΔT = 100 K, when the most rapid change in temperature ($(dT/dt)_{max}$) occurs, and when the maximum peak temperature occurs. The temperature increase (ΔT) is defined as the difference between the peak temperature in the whole mixture fraction domain and the initial temperature of the oxidiser. In the case of the DME flame burning in the 3% O_2 case, the peak temperature occurs at Z = 0.00805, Z = 0.0201, Z = 0.0201, and Z = 0.0362 at the four time steps, respectively. In the case of the DME flame burning in the 9% O_2 case, the peak temperature occurs at Z = 0.0161, Z = 0.0201, Z = 0.0564, and Z = 0.0926 at the four time steps, respectively. This shift in the mixture fraction at the four time steps in the ethanol flames is the same as the DME flames. The stoichiometric mixture fractions for both fuels are 0.0305 and 0.0863 in the 3% and 9% O_2 cases, respectively. Figure 20 shows that for both fuels, though the maximum temperature eventually occurs at a slightly richer mixture fraction than Z_{st}, the first temperature increase occurs at a

much leaner condition, corresponding to the most reactive mixture fraction. The value of Z_{mr} indicates the dominant role of the hot oxidant temperature over the fuel concentration in the mixture reactivity.

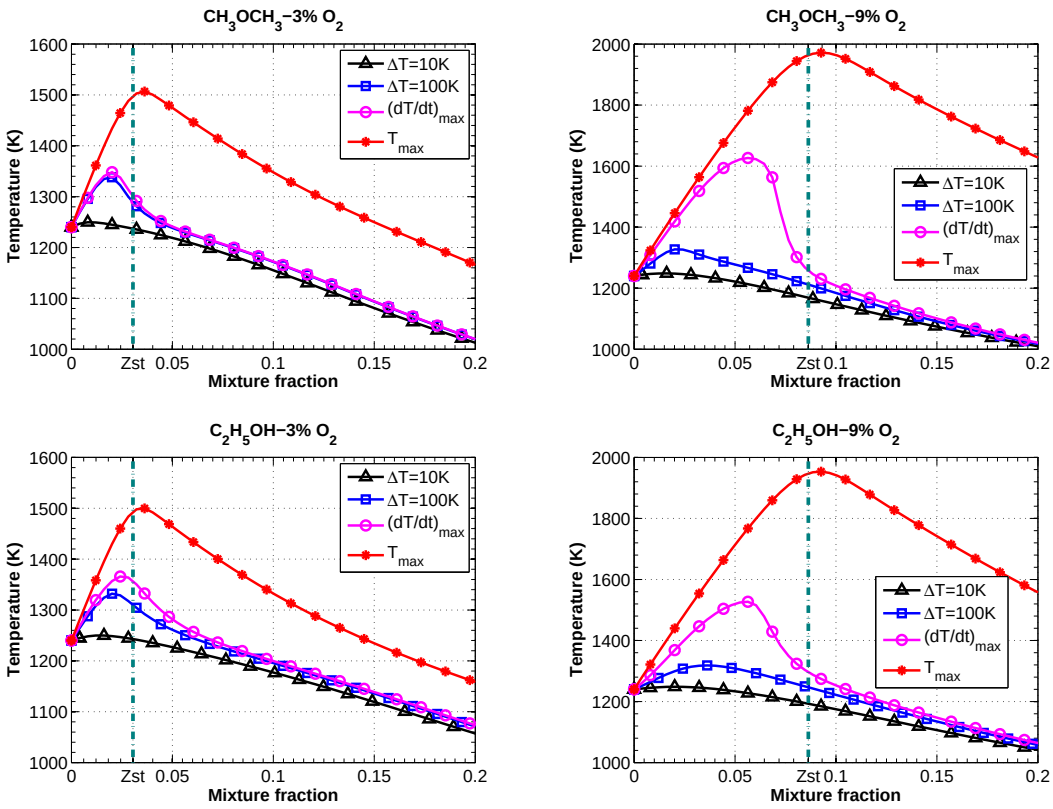

Figure 20: Temperature as a function of mixture fraction at four time steps, including when the temperature increase (ΔT) reaches 10 K, when ΔT = 100 K, when the most rapid change in temperature ($(dT/dt)_{max}$) occurs, and when the maximum peak temperature occurs.

Figure 21 shows the mole fractions of OH, HO_2, CH_3, CH_3OCH_2, and C_2H_4OH, which are normalised to their maximum mole fractions at Z_{mr}. Profiles of CH_3OCH_2 and C_2H_4OH are presented as these species are amongst the first products when the parent fuel is consumed via H-atom abstraction reactions. Normalised temperature profiles at Z_{mr} are also included to indicate the stage of the ignition process.

The species profiles show that the ethanol and the DME flames undergo different processes prior to the main ignition event. Here the main ignition event refers to the most rapid change in temperature ($(dT/dt)_{max}$). For instance, there is a steady build-up of HO_2 radicals during the early phase of ignition featured with a moderate temperature increase in the DME flames. In the meantime, the concentrations of both CH_3 and CH_3OCH_2 change very slowly, particularly in the 3% O_2 case. For instance, during t = 5 ms to t = 25 ms, the concentration of CH_3OCH_2 is almost constant, while CH_3 is formed slowly in the 3% O_2 case. The consumption of HO_2 initiates at t = 33 ms and t = 26 ms in the 3% and 9% O_2 case, respectively. This process promotes chain-branching reactions and triggers the main ignition event.

The onset of ignition is initiated more rapidly in the ethanol flames than in the DME flames. In addition,

during the early phase of ignition, the concentrations of HO_2, CH_3, and CH_3OCH_2 in the ethanol flames change much faster than in the DME flames. The steady opposed-flow flame analysis in Section 4 highlights the distinct fuel decomposition processes of ethanol and DME, which are related to the differences in the temporal evolution of intermediate species produced before the main ignition event. During the main ignition event, there is a rapid consumption of HO_2 and CH_3, in addition to a fast build-up of OH, in both the ethanol and the DME flames. Results from this unsteady flamelet model also show that the growth in the OH concentration occurs earlier in the ethanol flames than in the DME flames in the whole mixture fraction domain. This cannot explain the lower OH-LIF signals observed in the ethanol flames than in the DME flames at the same axial location in the current experiments, and a further study is required to understand this.

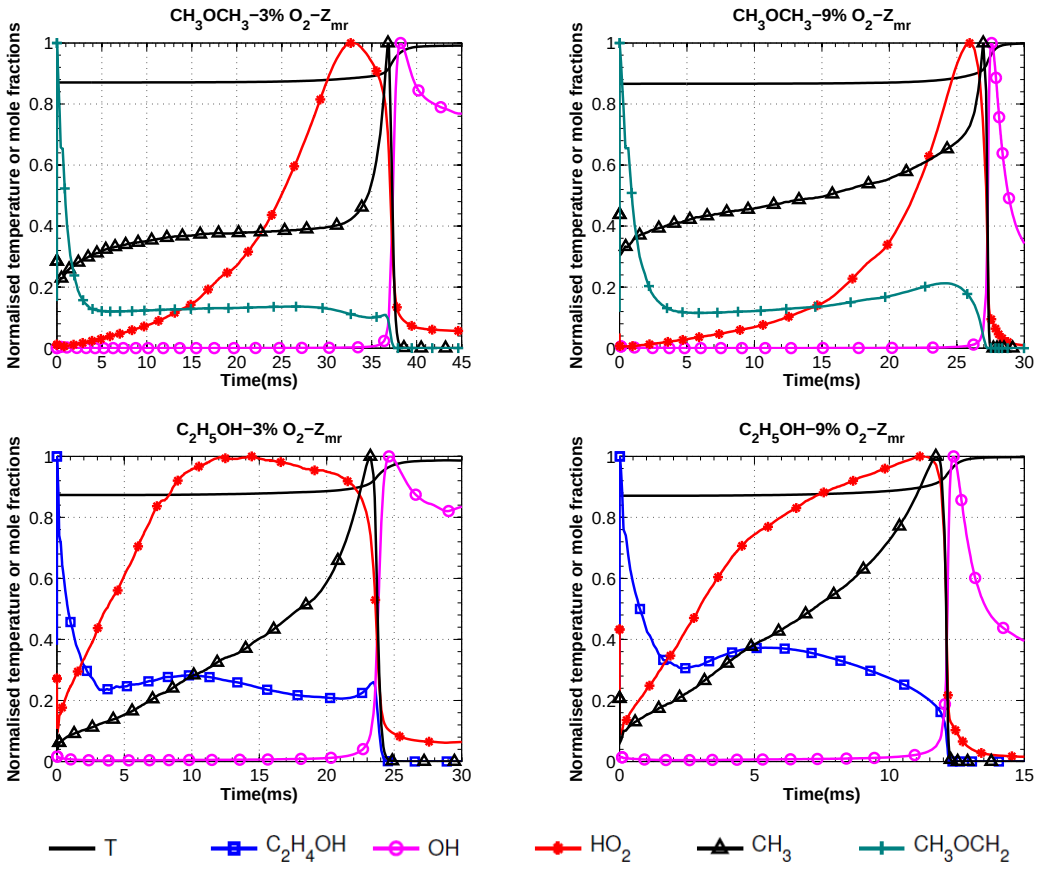

Figure 21: Normalised temperature and mole fractions of some species as a function of time for all cases at the most reactive mixture fraction.

6. Conclusions

This paper presents a combined experimental and computational investigation of ethanol and DME flames under conditions relevant to MILD combustion. The distributions of OH, CH_2O, and temperature were

recorded instantaneously and simultaneously. Imaging of OH^* chemiluminescence and digital photography were also performed to reveal the flame structure and the apparent liftoff heights. Steady laminar flame calculations using the OPPDIF code and an unsteady laminar flamelet analyses were conducted to help shed more light on the effect of the operating parameters on the chemical pathways and ignition process. The key findings arising from this study are:

- A transitional flame structure revealed by OH-LIF was observed in the ethanol and the DME flames issuing into the 9% O_2 coflow but not in the 3% O_2 coflow. The occurrence of this transitional flame structure suggests that the ethanol and the DME flames deviated away from the MILD combustion regime as the coflow oxygen level increased from 3% to 9%.

- The initiation of the ignition of both fuels is characterised by a moderate temperature increase and a steady build-up of radicals. In comparison with DME, the onset of ignition of ethanol occurs much earlier and with a more rapid build-up of radicals. It also occurs under relatively richer conditions with a higher scalar dissipation rate than DME. This indicates that ethanol is more reactive than DME at the conditions investigated here, which could explain why the DME flames always appeared more lifted than the ethanol flames in the experiments.

- Ethanol and DME are destroyed via different pathways, leading to differences in the intermediate species pool. However, temperature sensitivity analysis indicates that the differences in the fuel decomposition pathways play a minor role in the overall oxidation processes in the 3% O_2 cases. Under these conditions, the H_2/O_2 pathways are very important for both fuels, contributing to the similarities between them.

- When air and a vitiated oxidant stream with 9% O_2 are used instead of a vitiated oxidiser with 3% O_2, the flame temperature becomes more sensitive to fuel-specific reactions for each fuel. These results suggest that the chemical kinetics may change fundamentally due to a three-fold increase in the oxygen concentration. This explains why experimental ethanol and DME flames shifted away from the MILD combustion regime as the hot coflow oxygen level increased from 3% to 9%.

7. Acknowledgements

This research is funded by the China Scholarship Council and The University of Adelaide through a joint postgraduate scholarship. Funding from the Australian Research Council (ARC) and United States Air Force Asian Office of Aerospace Research and Development (AOARD) is gratefully acknowledged. The assistance provided by Mr. Chia Xiong Thong and Dr. Kathleen Lask in the laboratory is greatly appreciated.

8. References

[1] J. Wünning, J. Wünning, Flameless oxidation to reduce thermal NO-formation, Prog. Energ. Combust. 23 (1) (1997) 81–94.

[2] G. G. Szegö, B. B. Dally, G. J. Nathan, Operational characteristics of a parallel jet MILD combustion burner system, Combust. Flame 156 (2) (2009) 429–438.

[3] I. Özdemir, N. Peters, Characteristics of the reaction zone in a combustor operating at mild combustion, Exp. Fluids 30 (6) (2001) 683–695.

[4] M. Derudi, R. Rota, Experimental study of the mild combustion of liquid hydrocarbons, Proc. Combust. Inst. 33 (2) (2011) 3325–3332.

[5] R. Sadanandan, R. Lückerath, W. Meier, C. Wahl, Flame characteristics and emissions in flameless combustion under gas turbine relevant conditions, J. Propul. Power 27 (5) (2011) 970–980.

[6] P. R. Medwell, P. A. M. Kalt, B. B. Dally, Reaction zone weakening effects under hot and diluted oxidant stream conditions, Combust. Sci. Technol. 181 (7) (2009) 937–953.

[7] A. Cavigiolo, M. A. Galbiati, A. Effuggi, D. Gelosa, R. Rota, Mild combustion in a laboratory-scale apparatus, Combust. Sci. Technol. 175 (8) (2003) 1347–1367.

[8] R. Weber, J. P. Smart, W. vd Kamp, On the (MILD) combustion of gaseous, liquid, and solid fuels in high temperature preheated air, Proc. Combust. Inst. 30 (2) (2005) 2623–2629.

[9] P. Li, B. B. Dally, J. Mi, F. Wang, Mild oxy-combustion of gaseous fuels in a laboratory-scale furnace, Combust. Flame 160 (5) (2013) 933–946.

[10] Y. Kang, T. Lu, X. Lu, Q. Wang, X. Huang, S. Peng, D. Yang, X. Ji, Y. Song, Study on combustion characteristics of dimethyl ether under the moderate or intense low-oxygen dilution condition, Energy Convers. Manage. 108 (2016) 549–565.

[11] H. C. Rodrigues, M. J. Tummers, E. H. van Veen, D. Roekaerts, Spray flame structure in conventional and hot-diluted combustion regime, Combust. Flame 162 (3) (2015) 759–773.

[12] P. R. Medwell, B. B. Dally, Effect of fuel composition on jet flames in a heated and diluted oxidant stream, Combust. Flame 159 (10) (2012) 3138–3145.

[13] V. M. Reddy, P. Biswas, P. Garg, S. Kumar, Combustion characteristics of biodiesel fuel in high recirculation conditions, Fuel Process. Technol. 118 (2014) 310–317.

[14] J. Ye, P. R. Medwell, E. Varea, S. Kruse, B. B. Dally, H. G. Pitsch, An experimental study on MILD combustion of prevaporised liquid fuels, Appl. Energy 151 (2015) 93–101.

[15] C. Esarte, M. Peg, M. P. Ruiz, A. Millera, R. Bilbao, M. U. Alzueta, Pyrolysis of ethanol: gas and soot products formed, Ind. Eng. Chem. Res. 50 (8) (2011) 4412–4419.

[16] A. H. Lefebvre, D. R. Ballal, Gas Turbine Combustion: Alternative Fuels and Emissions, Hoboken: Taylor and Francis, 2010.

[17] M. Balat, H. Balat, Recent trends in global production and utilization of bio-ethanol fuel, Appl. Energy 86 (11) (2009) 2273–2282.

[18] W. Leitner, J. Klankermayer, S. Pischinger, H. Pitsch, K. Kohse-Höinghaus, Advanced biofuels and beyond: Chemistry solutions for propulsion and production, Angewandte Chemie 129 (20) (2017) 5500–5544.

[19] D. Cocco, V. Tola, G. Cau, Performance evaluation of chemically recuperated gas turbine (CRGT) power plants fuelled by di-methyl-ether (DME), Energy 31 (10) (2006) 1446–1458.

[20] C. Arcoumanis, C. Bae, R. Crookes, E. Kinoshita, The potential of di-methyl ether (DME) as an alternative fuel for compression-ignition engines: A review, Fuel 87 (7) (2008) 1014–1030.

[21] H. Curran, W. Pitz, C. Westbrook, P. Dagaut, J. Boettner, M. Cathonnet, A wide range modeling study of dimethyl ether oxidation, Int. J. Chem. Kinet. 30 (3) (1998) 229–241.

[22] M. C. Lee, Y. Yoon, Development of a gas turbine fuel nozzle for DME and a design method thereof, Fuel 102 (2012) 823–830.

[23] Z. Chen, X. Qin, Y. Ju, Z. Zhao, M. Chaos, F. L. Dryer, High temperature ignition and combustion enhancement by dimethyl ether addition to methane-air mixtures, Proc. Combust. Inst. 31 (1) (2007) 1215–1222.

[24] C. S. McEnally, L. D. Pfefferle, The effects of dimethyl ether and ethanol on benzene and soot formation in ethylene nonpremixed flames, Proc. Combust. Inst. 31 (1) (2007) 603–610.

[25] Y. L. Wang, P. S. Veloo, F. N. Egolfopoulos, T. T. Tsotsis, A comparative study on the extinction characteristics of non-premixed dimethyl ether and ethanol flames, Proc. Combust. Inst. 33 (1) (2011) 1003–1010.

[26] K. H. Song, P. Nag, T. A. Litzinger, D. C. Haworth, Effects of oxygenated additives on aromatic species in fuel-rich, premixed ethane combustion: a modeling study, Combust. Flame 135 (3) (2003) 341–349.

[27] A. Loukou, J. Reiter, R. Gehmlich, C. Hasse, D. Trimis, E. Pucher, K. Seshadri, Autoignition and extinction of mixtures of ethanol and dimethyl ether, in: Proceedings of the European Combustion Meeting, 2015.

[28] A. Frassoldati, T. Faravelli, E. Ranzi, K. Kohse-Höinghaus, P. R. Westmoreland, Kinetic modeling study of ethanol and dimethyl ether addition to premixed low-pressure propene-oxygen-argon flames, Combust. Flame 158 (7) (2011) 1264–1276.

[29] T. Kitamura, T. Ito, J. Senda, H. Fujimoto, Extraction of the suppression effects of oxygenated fuels on soot formation using a detailed chemical kinetic model, JSAE review 22 (2) (2001) 139–145.

[30] J. Wang, U. Struckmeier, B. Yang, T. A. Cool, P. Osswald, K. Kohse-Höinghaus, T. Kasper, N. Hansen, P. R. Westmoreland, Isomer-specific influences on the composition of reaction intermediates in dimethyl ether/propene and ethanol/propene flame, J. Phys. Chem. A 112 (39) (2008) 9255–9265.

[31] B. A. V. Bennett, C. S. McEnally, L. D. Pfefferle, M. D. Smooke, M. B. Colket, Computational and experimental study of the effects of adding dimethyl ether and ethanol to nonpremixed ethylene/air flames, Combust. Flame 156 (6) (2009) 1289–1302.

[32] P. Pepiot-Desjardins, H. Pitsch, R. Malhotra, S. Kirby, A. Boehman, Structural group analysis for soot reduction tendency of oxygenated fuels, Combust. Flame 154 (1) (2008) 191–205.

[33] E. A. Tingas, D. C. Kyritsis, D. A. Goussis, Autoignition dynamics of DME/air and EtOH/air homogeneous mixtures, Combust. Flame 162 (9) (2015) 3263–3276.

[34] E. A. Tingas, D. C. Kyritsis, D. A. Goussis, Ignition delay control of DME/air and EtOH/air homogeneous autoignition with the use of various additives, Fuel 169 (2016) 15–24.

[35] H. C. Rodrigues, M. Tummers, E. van Veen, D. Roekaerts, Effects of coflow temperature and composition on ethanol spray flames in hot-diluted coflow, Int. J. Heat. Fluid Fl. 51 (2015) 309–323.

[36] P. R. Medwell, P. A. M. Kalt, B. B. Dally, Imaging of diluted turbulent ethylene flames stabilized on a jet in hot coflow (JHC) burner, Combust. Flame 152 (1) (2008) 100–113.

[37] P. R. Medwell, P. A. M. Kalt, B. B. Dally, Simultaneous imaging of OH, formaldehyde, and temperature of turbulent nonpremixed jet flames in a heated and diluted coflow, Combust. Flame 148 (1) (2007) 48–61.

[38] P. R. Medwell, Laser diagnostics in MILD combustion, Ph.D. thesis (2007).

[39] M. Tamura, P. A. Berg, J. E. Harrington, J. Luque, J. B. Jeffries, G. P. Smith, D. R. Crosley, Collisional quenching of CH (A), OH (A), and NO (A) in low pressure hydrocarbon flames, Combust. Flame 114 (3) (1998) 502–514.

[40] D. C. Kyritsis, V. S. Santoro, A. Gomez, The effect of temperature correction on the measured thickness of formaldehyde zones in diffusion flames for 355 nm excitation, Exp. Fluids. 37 (5) (2004) 769–772.

[41] C. Brackmann, J. Bood, M. AldÉn, G. Pengloan, O. Andersson, Quantitative measurements of species and temperature in a DME-air counterflow diffusion flame using laser diagnostic methods, Combust. Sci. Technol. 178 (6) (2006) 1165–1184.

[42] J. Kojima, Y. Ikeda, T. Nakajima, Basic aspects of OH (A), CH (A), and C_2 (d) chemiluminescence in the reaction zone of laminar methane-air premixed flames, Combust. Flame 140 (1) (2005) 34–45.

[43] P. R. Medwell, B. B. Dally, Experimental observation of lifted flames in a heated and diluted coflow, Energy Fuels 26 (9) (2012) 5519–5527.

[44] M. Evans, P. Medwell, H. Wu, A. Stagni, M. Ihme, Classification and lift-off height prediction of non-premixed MILD and autoignitive flames, Proc. Combust. Inst. 36 (3) (2017) 4297-4304.

[45] J. Sidey, E. Mastorakos, Visualization of MILD combustion from jets in cross-flow, Proc. Combust. Inst. 35 (3) (2015) 3537–3545.

[46] J. Sidey, E. Mastorakos, R. Gordon, Simulations of Autoignition and Laminar Premixed Flames in Methane/Air Mixtures Diluted with Hot Products, Combust. Sci. Technol. 186 (4-5) (2014) 453–465.

[47] J. Ye, P. R. Medwell, B. B. Dally, M. J. Evans, The transition of ethanol flames from conventional to MILD combustion, Combust. Flame 171 (2016) 173–184.

[48] S. Kumar, P. Paul, H. Mukunda, Prediction of flame liftoff height of diffusion/partially premixed jet flames and modeling of mild combustion burners, Combust. Sci. Technol. 179 (10) (2007) 2219–2253.

[49] C. Duwig, B. Li, Z. Li, M. Aldn, High resolution imaging of flameless and distributed turbulent combustion, Combust. Flame 159 (1) (2012) 306–316.

[50] M. Evans, P. Medwell, Z. Tian, Modeling lifted jet flames in a heated coflow using an optimized eddy dissipation concept model, Combust. Sci. Technol. 187 (7) (2015) 1093–1109.

[51] P. R. Medwell, D. L. Blunck, B. B. Dally, The role of precursors on the stabilisation of jet flames issuing into a hot environment, Combust. Flame 161 (2) (2013) 465–474.

[52] R. L. Gordon, A. R. Masri, E. Mastorakos, Simultaneous Rayleigh temperature, OH- and CH_2O-LIF imaging of methane jets in a vitiated coflow, Combust. Flame 155 (1) (2008) 181–195.

[53] C. Fotache, T. Kreutz, C. Law, Ignition of counterflowing methane versus heated air under reduced and elevated pressures, Combust. Flame 108 (4) (1997) 442–470.

[54] K. N. Gabet, H. Shen, R. A. Patton, F. Fuest, J. A. Sutton, A comparison of turbulent dimethyl ether and methane non-premixed flame structure, Proc. Combust. Inst. 34 (1) (2013) 1447–1454.

[55] H. Xu, C. Yao, T. Yuan, K. Zhang, H. Guo, Measurements and modeling study of intermediates in ethanol and dimethy ether low-pressure premixed flames using synchrotron photoionization, Combust. Flame 158 (9) (2011) 1673–1681.

[56] Z. Zhao, M. Chaos, A. Kazakov, F. L. Dryer, Thermal decomposition reaction and a comprehensive kinetic model of dimethyl ether, Int. J. Chem. Kinet. 40 (1) (2008) 1–18.

[57] F. Herrmann, B. Jochim, P. Oβwald, L. Cai, H. Pitsch, K. Kohse-Höinghaus, Experimental and numerical low-temperature oxidation study of ethanol and dimethyl ether, Combust. Flame 161 (2) (2014) 384–397.

[58] Z. Chen, C. Tang, J. Fu, X. Jiang, Q. Li, L. Wei, Z. Huang, Experimental and numerical investigation on diluted DME flames: Thermal and chemical kinetic effects on laminar flame speeds, Fuel 102 (2012) 567–573.

[59] R. Weber, S. Orsino, A. L. Verlaan, N. Lallemant, Combustion of light and heavy fuel oils in high-temperature air, Journal of the Institute of Energy 74 (499) (2001) 38–47.

[60] G. Pellett, C. Bruno, W. Chinitz, Review of air vitiation effects on scramjet ignition and flameholding combustion processes, in: 38th AIAA/ASME/SAE/ASEE Joint Propulsion Conference & Exhibit, 2002, p. 3880.

[61] H. Pitsch, M. Chen, N. Peters, Unsteady flamelet modeling of turbulent hydrogen-air diffusion flames, Symp. (Int.) Combust. 27 (1) (1998) 1057–1064.

[62] O. Desjardins, G. Blanquart, G. Balarac, H. Pitsch, High order conservative finite difference scheme for variable density low Mach number turbulent flows, J. Comput. Phys. 227 (15) (2008) 7125–7159.

[63] G.-S. Jiang, C.-W. Shu, Efficient implementation of weighted ENO schemes, J. Comput. Phys. 126 (1) (1996) 202–228.

[64] M. Germano, U. Piomelli, P. Moin, W. H. Cabot, A dynamic subgrid-scale eddy viscosity model, Physics of Fluids A: Fluid Dynamics 3 (7) (1991) 1760–1765.

[65] C. Meneveau, T. S. Lund, W. H. Cabot, A Lagrangian dynamic subgrid-scale model of turbulence, J. Fluid Mech. 319 (1996) 353–385.

[66] C. D. Pierce, P. Moin, A dynamic model for subgrid-scale variance and dissipation rate of a conserved scalar, Phys. Fluids 10 (12) (1998) 3041.

[67] B. Jochim, M. Korkmaz, H. Pitsch, Scalar dissipation rate based multi-zone model for early-injected and conventional diesel engine combustion, Combust. Flame 175 (2017) 138–154.

[68] N. Peters, Laminar diffusion flamelet models in non-premixed turbulent combustion, Symp. (Int.) Combust. 10 (3) (1984) 319-339.

[69] N. Peters, Laminar flamelet concepts in turbulent combustion, Symp. (Int.) Combust. 21 (1) (1988) 1231-1250.

[70] H. Pitsch, FlameMaster A C++ computer program for 0D combustion and 1D laminar flame calculations. (1998).

[71] E. Mastorakos, Ignition of turbulent non-premixed flames, Prog. Energ. Combust. 35 (1) (2009) 57–97.

Chapter 8

Conclusions

This thesis improved the understanding of MILD combustion of prevaporised liquid fuels through a combined experimental and computational investigation. It investigated the transition of a flame from the conventional combustion regime to the MILD combustion regime. The key outcomes from this investigation are summarised in this chapter.

The first part of experiments were conducted in a pressurised reverse-flow MILD combustor. Prevaporised ethanol, acetone, and n-heptane were used to represent different classes of hydrocarbons, namely, an alcohol, a ketone, and a long-chain alkane. This investigation was focused on the pollutant formation and the combustion stability, based on which several key operating parameters were identified. These parameters included fuel type, equivalence ratio, carrier gas, air jet velocity, and operating pressure inside the combustion chamber. From this set of experimental results, a series of regime maps were generated to describe the combustor behaviour as a function of operating parameters.

The operating pressure inside the combustion chamber was varied from 1 to 5 bar (absolute) in the reverse-flow MILD combustor. It had the same impact on the pollutant formation for all the fuels investigated. Particularly, the operating pressure showed a minor impact on CO emissions for all the fuels. However, NO_x

emissions were found to increase considerably with pressure, leading to a narrower operating regime of low CO and NO_x emissions under elevated pressures. Since the operating pressure is inversely proportional to the volumetric flow rate and velocity of reactants, the increased NO_x emissions at higher pressures were partly attributed to a slower mixing process and a longer residence time. Furthermore, NO_x formation via the nitrous oxide mechanism was found to be enhanced under elevated pressures. The abatement of NO_x emissions at higher pressures was achieved via increasing the air jet velocity or replacing air with nitrogen as a carrier gas.

Many of the controlling parameters, including pressure, jet velocity, and local temperature and oxygen concentration, are coupled in the reverse-flow combustor. Isolating these parameters require a different system, which can provide a better control over the initial and boundary conditions. Hence the second endeavour of this work was to perform parametric studies on a Jet in Hot Coflow (JHC) burner, in order to examine the effect of important parameters independently. Turbulent jet flames of prevaporised ethanol, acetone, *n*-heptane, and dimethyl ether (an isomer of ethanol) were investigated. Simultaneous and instantaneous imaging of OH, CH_2O, and temperature was performed. Digital photography and imaging of OH^* chemiluminescence were also recorded to reveal the flame structure.

The coflow oxygen level in the JHC burner was found to affect the flame appearance and structure considerably. The luminosity of ethanol and DME flames in the 1250-K coflow with 3% O_2 was very low such that it was difficult to identify the flame base in these cases. These flames agreed better with the often-cited "flameless" appearance in comparison with higher oxygen level cases. Moreover, a more uniform distribution of heat release and temperature, indicated by the OH^* profiles, was achieved by either lowering the coflow oxygen level or diluting the fuel with an inert (N_2). As the coflow oxygen level increased from 3% to 9%, a transitional flame structure revealed by OH-LIF (a strong OH layer connected with a weaker

"tail") was observed in both the ethanol and the DME flames. The occurrence of this transitional flame structure is associated with the deviation from the MILD combustion regime. These experimental results suggested that ethanol and DME flames shifted away from the MILD combustion regime as the coflow oxygen level increased from 3% to 9%.

Temperature sensitivity analyses of ethanol and DME revealed that the differences in their decomposition pathways have no strong impact on the overall oxidation processes when they are burning in an oxidant stream with 3% O_2. Under that condition, the H_2/O_2 pathways play an important role for both fuels. When they are burnt in cold air or an oxidiser with 9% O_2, temperature become more sensitive to fuel-specific reactions. These analyses indicate that the chemical kinetics become fundamentally different as the oxygen level increases from 3% to 9%. This may be responsible for the transition of ethanol and DME flames away from the MILD combustion regime as the coflow oxygen level varied from 3% to 9% in the experiments.

Under the same experimental conditions as ethanol and DME flames, *n*-heptane flames demonstrated distinct behaviour. A transitional flame structure revealed by OH-LIF was observed in *n*-heptane flames burning in a coflow with 3% O_2. This structure had only been observed in the coflow with equal to or more than 9% O_2 for ethanol, DME, methane- and ethylene-based flames. Furthermore, combustion of *n*-heptane became unstable at high equivalence ratios and pressures in the reverse-flow combustor. However, stable combustion of ethanol without a visible flame was established under all the tested conditions. Calculations suggested that ignition delay times of *n*-heptane flames are shorter than ethanol flames under elevated pressures. This may cause ignition of *n*-heptane to occur before fresh reactants were well mixed with hot exhaust gases, leading to the unsuccessful establishment of MILD combustion.

One criteria of MILD combustion, based on heat release profiles, is adopted to investigate the distinctive behaviour of *n*-heptane and the transition away from the MILD combustion regime. This analysis was focused on two unique features identified in MILD flames: the mismatch between the location of the peak net heat release rate (Z_{hmax}) and the location of stoichiometric mixture fraction (Z_{st}); the absence of a net negative heat release region. The mismatch between Z_{hmax} and Z_{st} was found in heat release profiles of ethanol flames regardless of the coflow oxygen level and strain rate. However, the absence of a net negative heat release region was more likely to occur at a higher strain rate. This was ascribed to an enhanced transportation of O_2 across the reaction zone, promoting oxidative reactions over fuel pyrolysis reactions in the fuel-rich region. At a low strain rate, only ethanol flames burning in an oxidant stream with 3% O_2 did not show a net negative heat release region, resulting from combined effects of a lower flame temperature and a higher availability of O_2.

The *n*-heptane flames were found to differ from the ethanol flames in terms of the heat release profiles. It was demonstrated that a net negative heat release region always occurs in the *n*-heptane flames despite a low oxygen level and a high strain rate. Reaction flux analysis revealed that the pyrolysis of *n*-heptane can proceed through many possible reaction channels due to its complex chemistry. At a lower flame temperature caused by a reduced oxygen level, the importance of endothermic reactions with much lower activation energy increases. This means that the reactivity of the system in terms of pyrolysis is enhanced and offsets the impact of a lower temperature. This explains the difficulties of *n*-heptane in diminishing the net negative heat release region and meeting one of the criteria of MILD combustion.

Another criteria of MILD combustion, a distributed reaction with a small temperature gradient, was also used to examine *n*-heptane against other fuels. Given a temperature of the stoichiometric mixtures of various fuels and hot oxidant at

1250 K, the build-up of OH radical in ethanol and ethylene flames becomes more steady and prolonged as the oxygen level reduces from 9% to 3%. However, this slow and steady build-up of OH radical is not seen in *n*-heptane flames in the 3% O_2 case until the mixture temperature is reduced to 950 K. These results suggested that changing the initial conditions, such as lowering the mixture temperature, can help achieve a more distributed MILD combustion of *n*-heptane.

The outcomes achieved by this investigation contribute to a better understanding of MILD combustion of more complex fuels. The advancements in the fundamental aspects, particularly the impact of fuel structure on the transition to MILD combustion, will help extend MILD combustion to wider areas and explore its great potential.

Chapter 9

Future Work

A better understanding on the fundamental aspects of MILD combustion of more complex fuels has been accomplished by this study. As with any finite piece of work, there remain some issues that are worth of further investigation. The following recommendations are made to advance the understanding of this topic beyond this thesis:

- The impact of fuel structure and chemistry has been highlighted by this thesis. In particular, it was more difficult to establish MILD combustion of *n*-heptane than ethanol under the same conditions. It was found that in comparison with ethanol, *n*-heptane has a shorter ignition delay and more alternative channels for pyrolysis, contributing to the unsuccessful establishment of MILD combustion. However, the role of the presence of oxygen atoms in a fuel on the stabilisation of MILD combustion is not well understood. In order to have a complete picture of the impact of the fuel, similar experimental and numerical studies are required for more fuels, such as ethane (C_2H_6), octane (C_8H_{18}), and 1-Octanol ($C_8H_{17}OH$). Particularly, the comparison of octane and 1-Octanol to *n*-heptane will help better understand the impact of oxygen atoms in a long-chain hydrocarbon. Following these studies, a further investigation should be

performed to explore the impact of fuel blend on the establishment of MILD combustion.

- The operating pressure inside the combustion chamber was found to affect the pollutant formation and the combustion stability in the reverse-flow combustor significantly. However, the operating pressure was only varied from 1 to 5 bar (absolute) in this study. It would be beneficial to perform further experiments in a modified system, which allows higher operating pressures and provides better optical access.

- Detailed measurements of the flow field of the JHC burner would be beneficial. These measurements can help understand the transport of scalars and the mixing between the cold fuel and the hot coflow. The comparison of different cases would also reveal the impact of downstream chemical reactions on the flow field near the jet exit.

- Computational methods like direct numerical simulation (DNS) that takes account of the complexity of turbulent flow field should be utilised to model various flames investigated in this project. This can potentially explain the strong influence of strain rate on the establishment of MILD combustion, which was revealed by the laminar flame calculations in this thesis.

- Spray flames burning under MILD combustion conditions should be investigated to assess the impact of spray characteristics. The droplet size distribution and key scalars within a spray flame should be measured. Particularly, pointwise laser diagnostic techniques used by Rodrigues et al. [113, 181] should be performed to resolve the droplet field. Planar imaging techniques, including non-linear excitation regime two-line atomic fluorescence (NTLAF) [182], OH-LIF and CH_2O-LIF, should be used to measure the gas-phase temperature, and the distribution of OH and CH_2O. The combined results would be invaluable

in understanding the interaction of spray, turbulence, and chemistry.

Bibliography

[1] World Energy Focus 2016/2017, Tech. rep., World Energy Council (November 2016).

[2] International Energy Outlook 2016, Report DOE/EIA-0484(2016), U.S. Energy Information Administration (May 2016).

[3] World Energy Perspectives 2016, Tech. rep., World Energy Council (November 2016).

[4] D. Gust, T. A. Moore, A. L. Moore, Solar fuels via artificial photosynthesis, Acc. Chem. Res. 42 (12) (2009) 1890–1898.

[5] Ethanol in australia, `http://biofuelsassociation.com.au/biofuels/ethanol/ethanol-in-australia/`, access: 2017-05-03.

[6] M. Balat, H. Balat, Recent trends in global production and utilization of bio-ethanol fuel, Appl. Energy 86 (11) (2009) 2273–2282.

[7] O. J. Sánchez, C. A. Cardona, Trends in biotechnological production of fuel ethanol from different feedstocks, Bioresour. Technol. 99 (13) (2008) 5270–5295.

[8] R. Santoro, T. Yeh, J. Horvath, H. Semerjian, The transport and growth of soot particles in laminar diffusion flames, Combust. Sci. Technol. 53 (2-3) (1987) 89–115.

[9] M. Frenklach, Reaction mechanism of soot formation in flames, Phys. Chem. Chem. Phys. 4 (11) (2002) 2028–2037.

[10] P. Pandey, B. Pundir, P. Panigrahi, Hydrogen addition to acetylene-air laminar diffusion flames: Studies on soot formation under different flow arrangements, Combust. Flame 148 (4) (2007) 249–262.

[11] H. Böhm, D. Hesse, H. Jander, B. Lers, J. Pietscher, H. Wagner, M. Weiss, The influence of pressure and temperature on soot formation in premixed flames, in: Symposium (International) on Combustion, Vol. 22, Elsevier, 1988, pp. 403–411.

[12] A. Cavaliere, M. de Joannon, Mild combustion, Prog. Energ. Combust. 30 (4) (2004) 329–366.

[13] R. C. Flagan, J. H. Seinfeld, Fundamentals of air pollution engineering, Courier Dover Publications, 2012.

[14] J. Lee, D. Santavicca, Experimental diagnostics for the study of combustion instabilities in lean premixed combustors, J. Propul. Power 19 (5) (2003) 735–750.

[15] A. K. Gupta, Flame characteristics and challenges with high temperature air combustion, in: Proccedings of 2000 International Joint Power Generation Conference, 2000, pp. 23–26.

[16] M. Katsuki, T. Hasegawa, The science and technology of combustion in highly preheated air, in: Symp. (Int.) Combust., Vol. 27, 1998, pp. 3135–3146.

[17] J. Wünning, J. Wünning, Flameless oxidation to reduce thermal NO-formation, Prog. Energ. Combust. 23 (1) (1997) 81–94.

[18] B. Dally, E. Riesmeier, N. Peters, Effect of fuel mixture on moderate and intense low oxygen dilution combustion, Combust. Flame 137 (4) (2004) 418–431.

[19] R. Lückerath, W. Meier, M. Aigner, FLOX® combustion at high pressure with different fuel compositions, J. Eng. Gas Turb. Power 130 (1) (2008) 011505.

[20] S. Kruse, B. Kerschgens, L. Berger, E. Varea, H. Pitsch, Experimental and numerical study of MILD combustion for gas turbine applications, Appl. Energy 148 (2015) 456–465.

[21] G. G. Szegö, B. B. Dally, G. J. Nathan, Operational characteristics of a parallel jet MILD combustion burner system, Combust. Flame 156 (2) (2009) 429–438.

[22] P. Li, B. B. Dally, J. Mi, F. Wang, Mild oxy-combustion of gaseous fuels in a laboratory-scale furnace, Combust. Flame 160 (5) (2013) 933–946.

[23] M. Derudi, R. Rota, Experimental study of the mild combustion of liquid hydrocarbons, Proc. Combust. Inst. 33 (2) (2011) 3325–3332.

[24] R. Weber, S. Orsino, N. Lallemant, A. Verlaan, Combustion of natural gas with high-temperature air and large quantities of flue gas, Proc. Combust. Inst. 28 (1) (2000) 1315–1321.

[25] Y. Huang, V. Yang, Dynamics and stability of lean-premixed swirl-stabilized combustion, Progress in Energy and Combustion Science 35 (4) (2009) 293–364.

[26] A. R. Masri, A. Kourmatzis, W. O'Loughlin, J. D. Gounder, From dilute to dense turbulent sprays: Combustion, auto-ignition and atomization, in: Experiments and numerical simulations of turbulent combustion of diluted sprays, Springer, 2014, pp. 1–29.

[27] M. Linne, Imaging in the optically dense regions of a spray: A review of developing techniques, Prog. Energ. Combust. 39 (5) (2013) 403–440.

[28] A. H. Lefebvre, Airblast atomization, Prog. Energ. Combust. 6 (3) (1980) 233–261.

[29] F. Lacas, P. Versaevel, P. Scouflaire, G. Coeur-Joly, Design and performance of an ultrasonic atomization system for experimental combustion applications, Particle & Particle Systems Characterization 11 (2) (1994) 166–171.

[30] J. B. Heywood, Internal combustion engine fundamentals, McGraw-Hill, New York, 1988.

[31] P. Marmottant, E. Villermaux, On spray formation, Journal of fluid mechanics 498 (2004) 73–111.

[32] M. Arai, M. Tabata, H. Hiroyasu, M. Shimizu, Disintegrating process and spray characterization of fuel jet injected by a diesel nozzle, SAE Tech. Pap. 840275.

[33] B. Merci, D. Roekaerts, A. Sadiki, Experiments and numerical simulations of diluted spray turbulent combustion, Springer, 2011.

[34] Y.-C. Chen, S. H. Stårner, S. H.rner, A. R. Masri, A detailed experimental investigation of well-defined, turbulent evaporating spray jets of acetone, Int. J. Multiphase Flow 32 (4) (2006) 389–412.

[35] A. Masri, J. Gounder, Turbulent spray flames of acetone and ethanol approaching extinction, Combustion Science and Technology 182 (4-6) (2010) 702–715.

[36] S. H. Stårner, J. Gounder, A. R. Masri, Effects of turbulence and carrier fluid on simple, turbulent spray jet flames, Combust. Flame 143 (4) (2005) 420–432.

[37] W. O'Loughlin, A. Masri, A new burner for studying auto-ignition in turbulent dilute sprays, Combust. Flame 158 (8) (2011) 1577–1590.

[38] W. O'Loughlin, A. R. Masri, The structure of the auto-ignition region of

turbulent dilute methanol sprays issuing in a vitiated co-flow, Flow Turbul. Combust. 89 (1) (2012) 13–35.

[39] A. Kourmatzis, P. X. Pham, A. R. Masri, Air assisted atomization and spray density characterization of ethanol and a range of biodiesels, Fuel 108 (2013) 758–770.

[40] A. Kourmatzis, W. O'Loughlin, A. Masri, Effects of turbulence, evaporation and heat release on the dispersion of droplets in dilute spray jets and flames, Flow Turbul. Combust. 91 (2) (2013) 405–427.

[41] C. Heye, V. Raman, A. R. Masri, Influence of spray/combustion interactions on auto-ignition of methanol spray flames, Proc. Combust. Inst. 35 (2) (2015) 1639–1648.

[42] R. Hadef, K. Merkle, B. Lenze, W. Leuckel, An experimental study of airblast atomizer spray flames, Journal of the Institute of Energy 73 (494) (2000) 50–55.

[43] J. Abraham, V. Magi, Entrainment characteristics of sprays for diesel and disi applications, SAE Tech. Pap. 981934.

[44] J. A. Friedman, M. Renksizbulut, Investigating a methanol spray flame interacting with an annular air jet using phase-doppler interferometry and planar laser-induced fluorescence, Combust. Flame 117 (4) (1999) 661–684.

[45] J. D. Gounder, A. Kourmatzis, A. R. Masri, Turbulent piloted dilute spray flames: Flow fields and droplet dynamics, Combust. Flame 159 (11) (2012) 3372–3397.

[46] W. Kosiwczuk, A. Cessou, B. L. M. Trinit, Simultaneous velocity field measurements in two-phase flows for turbulent mixing of sprays by means of two-phase piv, Experiments in Fluids 39 (5) (2005) 895–908.

[47] S. Sharma, R. Kumar, A. Chowdhury, Y. Yoon, S. Kumar, On the effect of spray parameters on CO and NO_x emissions in a liquid fuel fired flameless combustor, Fuel 199 (2017) 229–238.

[48] A. Kourmatzis, P. X. Pham, A. R. Masri, Characterization of atomization and combustion in moderately dense turbulent spray flames, Combust. Flame 162 (4) (2015) 978–996.

[49] R. J. Sornek, R. Dobashi, T. Hirano, Effect of turbulence on vaporization, mixing, and combustion of liquid-fuel sprays, Combust. Flame 120 (4) (2000) 479–491.

[50] B. B. Dally, A. N. Karpetis, R. S. Barlow, Structure of turbulent non-premixed jet flames in a diluted hot coflow, Proc. Combust. Inst. 29 (1) (2002) 1147–1154.

[51] P. R. Medwell, P. A. M. Kalt, B. B. Dally, Imaging of diluted turbulent ethylene flames stabilized on a jet in hot coflow (JHC) burner, Combust. Flame 152 (1) (2008) 100–113.

[52] S. M. Al-Noman, S. K. Choi, S. H. Chung, Autoignition characteristics of laminar lifted jet flames of pre-vaporized iso-octane in heated coflow air, Fuel 162 (2015) 171–178.

[53] B. Choi, K. Kim, S. Chung, Autoignited laminar lifted flames of propane in coflow jets with tribrachial edge and mild combustion, Combust. Flame 156 (2) (2009) 396–404.

[54] S. Chung, B. Lee, On the characteristics of laminar lifted flames in a non-premixed jet, Combust. Flame 86 (1-2) (1991) 62–72.

[55] B. C. Choi, S. H. Chung, Autoignited laminar lifted flames of

methane/hydrogen mixtures in heated coflow air, Combust. Flame 159 (4) (2012) 1481–1488.

[56] S. K. Choi, S. M. Al-Noman, S. H. Chung, Simulation of non-autoignited and autoignited laminar non-premixed jet flames of syngas in heated coflow air, Combust. Sci. Technol. 187 (1-2) (2015) 132–147.

[57] M. de Joannon, P. Sabia, G. Cozzolino, G. Sorrentino, A. Cavaliere, Pyrolitic and Oxidative Structures in Hot Oxidant Diluted Oxidant (HODO) MILD Combustion, Combust. Sci. Technol. 184 (7-8) (2012) 1207–1218.

[58] M. de Joannon, P. Sabia, G. Sorrentino, A. Cavaliere, Numerical study of mild combustion in hot diluted diffusion ignition (HDDI) regime, Proc. Combust. Inst. 32 (2) (2009) 3147–3154.

[59] M. de Joannon, G. Sorrentino, A. Cavaliere, MILD combustion in diffusion-controlled regimes of hot diluted fuel, Combust. Flame 159 (5) (2012) 1832–1839.

[60] M. Saha, B. B. Dally, P. R. Medwell, A. Chinnici, Burning characteristics of Victorian brown coal under MILD combustion conditions, Combust. Flame 172 (2016) 252–270.

[61] R. Weber, J. P. Smart, W. vd Kamp, On the (MILD) combustion of gaseous, liquid, and solid fuels in high temperature preheated air, Proc. Combust. Inst. 30 (2) (2005) 2623–2629.

[62] P. R. Medwell, B. B. Dally, Experimental observation of lifted flames in a heated and diluted coflow, Energy Fuels 26 (9) (2012) 5519–5527.

[63] J. Sidey, E. Mastorakos, Visualization of MILD combustion from jets in cross-flow, Proc. Combust. Inst. 35 (3) (2015) 3537–3545.

[64] R. L. Gordon, A. R. Masri, E. Mastorakos, Simultaneous Rayleigh temperature, OH- and CH_2O-LIF imaging of methane jets in a vitiated coflow, Combust. Flame 155 (1) (2008) 181–195.

[65] E. Oldenhof, M. Tummers, E. Van Veen, D. Roekaerts, Ignition kernel formation and lift-off behaviour of jet-in-hot-coflow flames, Combust. Flame 157 (6) (2010) 1167–1178.

[66] E. Oldenhof, M. Tummers, E. Van Veen, D. Roekaerts, Role of entrainment in the stabilisation of jet-in-hot-coflow flames, Combust. Flame 158 (8) (2011) 1553–1563.

[67] R. Cabra, J. Y. Chen, R. W. Dibble, A. N. Karpetis, R. S. Barlow, Lifted methane-air jet flames in a vitiated coflow, Combust. Flame 143 (4) (2005) 491–506.

[68] S. Kumar, P. Paul, H. Mukunda, Prediction of flame liftoff height of diffusion/partially premixed jet flames and modeling of mild combustion burners, Combust. Sci. Technol. 179 (10) (2007) 2219–2253.

[69] C. Duwig, B. Li, Z. Li, M. Aldn, High resolution imaging of flameless and distributed turbulent combustion, Combust. Flame 159 (1) (2012) 306–316.

[70] Y. Minamoto, N. Swaminathan, Scalar gradient behaviour in MILD combustion, Combust. Flame 161 (4) (2013) 1063–1075.

[71] Y. Minamoto, T. Dunstan, N. Swaminathan, R. Cant, DNS of EGR-type turbulent flame in MILD condition, Proc. Combust. Inst. 34 (2) (2013) 3231–3238.

[72] M. Saha, B. B. Dally, P. R. Medwell, E. M. Cleary, Moderate or intense low oxygen dilution (MILD) combustion characteristics of pulverized coal in a self-recuperative furnace, Energy Fuels 28 (9) (2014) 6046–6057.

[73] C. Esarte, M. Peg, M. P. Ruiz, A. Millera, R. Bilbao, M. U. Alzueta, Pyrolysis of ethanol: gas and soot products formed, Ind. Eng. Chem. Res. 50 (8) (2011) 4412–4419.

[74] W. M. Pitts, Assessment of theories for the behavior and blowout of lifted turbulent jet diffusion flames, in: Symposium (international) on combustion, Vol. 22, Elsevier, 1989, pp. 809–816.

[75] Y.-C. Chen, R. W. Bilger, Stabilization mechanisms of lifted laminar flames in axisymmetric jet flows, Combust. Flame 123 (1) (2000) 23–45.

[76] L. Vanquickenborne, A. Van Tiggelen, The stabilization mechanism of lifted diffusion flames, Combust. Flame 10 (1) (1966) 59–69.

[77] L. Muñiz, M. Mungal, Instantaneous flame-stabilization velocities in lifted-jet diffusion flames, Combust. Flame 111 (1) (1997) 16–31.

[78] G. Kalghatgi, Lift-off heights and visible lengths of vertical turbulent jet diffusion flames in still air, Combust. Sci. Technol. 41 (1-2).

[79] K. M. Lyons, Toward an understanding of the stabilization mechanisms of lifted turbulent jet flames: Experiments, Prog. Energ. Combust. 33 (2) (2007) 211–231.

[80] J. Buckmaster, Edge-flames, Progress in Energy and Combustion Science 28 (5) (2002) 435–475.

[81] A. Upatnieks, J. F. Driscoll, C. C. Rasmussen, S. L. Ceccio, Liftoff of turbulent jet flames-assessment of edge flame and other concepts using cinema-PIV, Combust. Flame 138 (3) (2004) 259–272.

[82] S. Chung, Stabilization, propagation and instability of tribrachial triple flames, Proc. Combust. Inst. 31 (1) (2007) 877–892.

[83] B. Lee, S. Chung, Stabilization of lifted tribrachial flames in a laminar non-premixed jet, Combust. Flame 109 (1) (1997) 163–172.

[84] R. Schefer, P. Goix, Mechanism of flame stabilization in turbulent, lifted-jet flames, Combustion and Flame 112 (4) (1998) 559–574.

[85] C. Maurey, A. Cessou, B. Lecordier, D. Stepowski, Statistical flow dynamic properties conditioned on the oscillating stabilization location of turbulent lifted flame, Proc. Combust. Inst. 28 (1) (2000) 545–551.

[86] L. K. Su, D. Han, M. Mungal, Measurements of velocity and fuel concentration in the stabilization region of lifted jet diffusion flames, Proc. Combust. Inst. 28 (1) (2000) 327–334.

[87] M. Evans, P. Medwell, Z. Tian, J. Ye, A. Frassoldati, A. Cuoci, Effects of oxidant stream composition on non-premixed laminar flames with heated and diluted coflows, Combust. Flame 178 (2016) 297–310.

[88] A. Mardani, S. Tabejamaat, M. Ghamari, Numerical study of influence of molecular diffusion in the mild combustion regime, Combustion Theory and Modelling 14 (5) (2010) 747–774.

[89] S. H. Kim, K. Y. Huh, B. Dally, Conditional moment closure modeling of turbulent nonpremixed combustion in diluted hot coflow, Proc. Combust. Inst. 30 (1) (2005) 751–757.

[90] C. Markides, E. Mastorakos, An experimental study of hydrogen autoignition in a turbulent co-flow of heated air, Proc. Combust. Inst. 30 (1) (2005) 883–891.

[91] C. Markides, G. De Paola, E. Mastorakos, Measurements and simulations of mixing and autoignition of an n-heptane plume in a turbulent flow of heated air, Experimental Thermal and Fluid Science 31 (5) (2007) 393–401.

[92] P. R. Medwell, P. A. M. Kalt, B. B. Dally, Simultaneous imaging of OH, formaldehyde, and temperature of turbulent nonpremixed jet flames in a heated and diluted coflow, Combust. Flame 148 (1) (2007) 48–61.

[93] R. Cabra, T. Myhrvold, J. Y. Chen, R. W. Dibble, A. N. Karpetis, R. S. Barlow, Simultaneous laser Raman-Rayleigh-LIF measurements and numerical modeling results of a lifted turbulent H_2/N_2 jet flame in a vitiated coflow, Proc. Combust. Inst. 29 (2) (2002) 1881–1888.

[94] H. F. Coward, G. W. Jones, Limits of flammability of gases and vapors (1952).

[95] E. Abtahizadeh, A. Sepman, F. Hernández-Pérez, J. van Oijen, A. Mokhov, P. de Goey, H. Levinsky, Numerical and experimental investigations on the influence of preheating and dilution on transition of laminar coflow diffusion flames to mild combustion regime, Combust. Flame 160 (11) (2013) 2359–2374.

[96] P. Coelho, N. Peters, Numerical simulation of a mild combustion burner, Combust. Flame 124 (3) (2001) 503–518.

[97] J. Sidey, E. Mastorakos, R. Gordon, Simulations of Autoignition and Laminar Premixed Flames in Methane/Air Mixtures Diluted with Hot Products, Combust. Sci. Technol. 186 (4-5) (2014) 453–465.

[98] P. R. Medwell, M. J. Evans, Q. N. Chan, V. R. Katta, Laminar flame calculations for analyzing trends in autoignitive jet flames in a hot and vitiated coflow, Energy Fuels 30 (10) (2016) 8680–8690.

[99] C. Duwig, L. Fuchs, Large eddy simulation of a H_2/N_2 lifted flame in a vitiated co-flow, Combust. Sci. Technol. 180 (3) (2008) 453–480.

[100] E. Abtahizadeh, J. van Oijen, P. de Goey, Numerical study of mild combustion with entrainment of burned gas into oxidizer and/or fuel streams, Combust. Flame 159 (6) (2012) 2155–2165.

[101] T. Faravelli, A. Frassoldati, E. Ranzi, Kinetic modeling of the interactions between NO and hydrocarbons in the oxidation of hydrocarbons at low temperatures, Combustion and Flame 132 (1) (2003) 188–207.

[102] B. I. Shraiman, E. D. Siggia, Scalar turbulence, Nature 405 (6787) (2000) 639–646.

[103] H. Pitsch, S. Fedotov, Investigation of scalar dissipation rate fluctuations in non-premixed turbulent combustion using a stochastic approach, Combustion Theory and Modelling 5 (1) (2001) 41–57.

[104] C. Galletti, A. Parente, L. Tognotti, Numerical and experimental investigation of a mild combustion burner, Combust. Flame 151 (4) (2007) 649–664.

[105] J. Aminian, C. Galletti, S. Shahhosseini, L. Tognotti, Numerical investigation of a MILD combustion burner: analysis of mixing field, chemical kinetics and turbulence-chemistry interaction, Flow, turbulence and combustion 88 (4) (2012) 597–623.

[106] M. Severin, H. Ax, O. Lammel, M. Stöhr, Investigation of flame stabilization in premixed high momentum jet flames at elevated pressure by laser measurement techniques, in: In: Proceedings. 8th International Seminar on Flame Structure, Berlin, Germany, 2014.

[107] V. K. Arghode, A. E. E. Khalil, A. K. Gupta, Fuel dilution and liquid fuel operational effects on ultra-high thermal intensity distributed combustor, Appl. Energy 95 (2012) 132–138.

[108] M. Saha, A. Chinnici, B. B. Dally, P. R. Medwell, Numerical study of pulverized coal MILD combustion in a self-recuperative furnace, Energy & Fuels 29 (11) (2015) 7650–7669.

[109] C. K. Westbrook, Chemical kinetics of hydrocarbon ignition in practical combustion systems, Proc. Combust. Inst. 28 (2) (2000) 1563–1577.

[110] M. Frenklach, H. Wang, M. J. Rabinowitz, Optimization and analysis of large chemical kinetic mechanisms using the solution mapping method - combustion of methane, Prog. Energ. Combust. 18 (1) (1992) 47–73.

[111] H. Curran, J. M. Simmie, P. Dagaut, D. Voisin, M. Cathonnet, The ignition and oxidation of allene and propyne: Experiments and kinetic modeling, Symp. (Int.) Combust. 26 (1) (1996) 613–620.

[112] H. Yamada, K. Suzaki, H. Sakanashi, N. Choi, A. Tezaki, Kinetic measurements in homogeneous charge compression of dimethyl ether: role of intermediate formaldehyde controlling chain branching in the low-temperature oxidation mechanism, Combust. Flame 140 (1) (2005) 24–33.

[113] H. C. Rodrigues, M. Tummers, E. van Veen, D. Roekaerts, Effects of coflow temperature and composition on ethanol spray flames in hot-diluted coflow, Int. J. Heat. Fluid Fl. 51 (2015) 309–323.

[114] P. Sabia, M. L. Lavadera, P. Giudicianni, G. Sorrentino, R. Ragucci, M. de Joannon, CO_2 and H_2O effect on propane auto-ignition delay times under mild combustion operative conditions, Combust. Flame 162 (3) (2015) 533–543.

[115] P. Sabia, M. L. Lavadera, G. Sorrentino, P. Giudicianni, R. Ragucci, M. de Joannon, H_2O and CO_2 Dilution in MILD Combustion of Simple Hydrocarbons, Flow, Turbulence and Combustion 96 (2) (2016) 433–448.

[116] M. Ihme, Y. C. See, LES flamelet modeling of a three-stream MILD combustor: Analysis of flame sensitivity to scalar inflow conditions, Proc. Combust. Inst. 33 (1) (2011) 1309–1317.

[117] A. Mardani, S. Tabejamaat, M. B. Mohammadi, Numerical study of the effect of turbulence on rate of reactions in the MILD combustion regime, Combustion Theory and Modelling 15 (6) (2011) 753–772.

[118] A. Cavigiolo, M. A. Galbiati, A. Effuggi, D. Gelosa, R. Rota, Mild combustion in a laboratory-scale apparatus, Combust. Sci. Technol. 175 (8) (2003) 1347–1367.

[119] V. K. Arghode, A. K. Gupta, Investigation of forward flow distributed combustion for gas turbine application, Appl. Energy 88 (1) (2011) 29–40.

[120] V. K. Arghode, A. K. Gupta, Investigation of reverse flow distributed combustion for gas turbine application, Appl. Energy 88 (4) (2011) 1096–1104.

[121] R. Sadanandan, R. Lückerath, W. Meier, C. Wahl, Flame characteristics and emissions in flameless combustion under gas turbine relevant conditions, J. Propul. Power 27 (5) (2011) 970–980.

[122] M. Mancini, P. Schwöppe, R. Weber, S. Orsino, On mathematical modelling of flameless combustion, Combust. Flame 150 (1) (2007) 54–59.

[123] B. B. Dally, S. H. Shim, R. A. Craig, P. J. Ashman, G. G. Szegö, On the burning of sawdust in a MILD combustion furnace, Energy Fuels 24 (6) (2010) 3462–3470.

[124] F. Biagioli, F. Güthe, Effect of pressure and fuel-air unmixedness on NO_x emissions from industrial gas turbine burners, Combust. Flame 151 (1) (2007) 274–288.

[125] C. K. Law, Combustion physics, Cambridge university press, 2010.

[126] G. Jomaas, X. Zheng, D. Zhu, C. Law, Experimental determination of counterflow ignition temperatures and laminar flame speeds of C2-C3 hydrocarbons

at atmospheric and elevated pressures, Proc. Combust. Inst. 30 (1) (2005) 193–200.

[127] S. Liao, D. Jiang, Z. Huang, K. Zeng, Q. Cheng, Determination of the laminar burning velocities for mixtures of ethanol and air at elevated temperatures, Appl. Therm. Eng. 27 (2) (2007) 374–380.

[128] R. Seiser, H. Pitsch, K. Seshadri, W. Pitz, H. Gurran, Extinction and autoignition of n-heptane in counterflow configuration, Proc. Combust. Inst. 28 (2) (2000) 2029–2037.

[129] C.-J. Sung, C. K. Law, Fundamental combustion properties of H_2/CO mixtures: ignition and flame propagation at elevated pressures, Combust. Sci. Technol. 180 (6) (2008) 1097–1116.

[130] H.-P. S. Shen, J. Steinberg, J. Vanderover, M. A. Oehlschlaeger, A shock tube study of the ignition of n-heptane, n-decane, n-dodecane, and n-tetradecane at elevated pressures, Energy Fuels 23 (5) (2009) 2482–2489.

[131] S. Saxena, I. D. Bedoya, Fundamental phenomena affecting low temperature combustion and HCCI engines, high load limits and strategies for extending these limits, Prog. Energ. Combust. 39 (5) (2013) 457–488.

[132] M. Yao, Z. Zheng, H. Liu, Progress and recent trends in homogeneous charge compression ignition (HCCI) engines, Prog. Energ. Combust. 35 (5) (2009) 398–437.

[133] A. E. E. Khalil, A. K. Gupta, K. M. Bryden, S. C. Lee, Mixture preparation effects on distributed combustion for gas turbine applications, ASME J. Energy Resour. Technol 134 (3) (2012) 032201.

[134] A. E. Khalil, A. K. Gupta, Impact of pressure on high intensity colorless distributed combustion, Fuel.

[135] A. E. Khalil, A. K. Gupta, Clean combustion in gas turbine engines using Butyl Nonanoate biofuel, Fuel 116 (2014) 522–528.

[136] D. Burtraw, K. Palmer, R. Bharvirkar, A. Paul, Cost-effective reduction of NOx emissions from electricity generation, J Air Waste Manag. Assoc. 51 (10) (2001) 1476–1489.

[137] S. R. Turns, An introduction to combustion, McGraw-Hill, New York, 1996.

[138] C. Fenimore, Formation of nitric oxide in premixed hydrocarbon flames, in: Symposium (International) on Combustion, Vol. 13, 1971, pp. 373–380.

[139] J. A. Miller, C. T. Bowman, Mechanism and modeling of nitrogen chemistry in combustion, Prog. Energ. Combust. 15 (4) (1989) 287–338.

[140] Pollution Prevention and Abatement Handbook, Vol. 382, The World Bank Group, 1998.

[141] L. Muzio, G. Quartucy, J. Cichanowiczy, Overview and status of post-combustion NOx control: SNCR, SCR and hybrid technologies, International journal of environment and pollution 17 (1-2) (2002) 4–30.

[142] W. Chen, L. Smoot, S. Hill, T. Fletcher, Global rate expression for nitric oxide reburning. part 2, Energy Fuels 10 (5) (1996) 1046–1052.

[143] J. T. Oden, An Introduction to Mathematical Modeling, Hoboken, NJ, USA: John Wiley & Sons, Inc., 2011, Ch. Introduction to Quantum Mechanics, pp. 93–113.

[144] C. Foot, Atomic Physics, Oxford University Press, UK, 2005, Ch. Early Atomic Physics, pp. xvi–xliv.

[145] P. Dagdigian, Laser spectroscopy for sensing, Woodhead Publishing Limited, 2014, Ch. Fundamentals of optical spectroscopy, pp. 3–33.

[146] T. Corcoran, Laser spectroscopy for sensing, Woodhead Publishing Limited, 2014, Ch. Laser-induced fluorescence spectroscopy (LIF), pp. 235–257.

[147] D. C. Kyritsis, V. S. Santoro, A. Gomez, The effect of temperature correction on the measured thickness of formaldehyde zones in diffusion flames for 355 nm excitation, Exp. Fluids. 37 (5) (2004) 769–772.

[148] J. M. Seitzman, A. Üngüt, P. H. Paul, R. K. Hanson, Imaging and characterization of OH structures in a turbulent nonpremixed flame, Symp. (Int.) Combust. 23 (1) (1990) 637–644.

[149] E. L. Degl'Innocenti, Atomic Spectroscopy and Radiative Processes, Springer, 2014.

[150] D. R. Crosley, Collisional effects on laser-induced fluorescence flame measurements, Opt. Eng. 20 (4) (1981) 511–521.

[151] K. Kohse-Hóinghaus, J. Jeffries, Applied combustion diagnostics, Taylor & Francis, 2002.

[152] P. R. Medwell, Laser diagnostics in MILD combustion, Ph.D. thesis (2007).

[153] J. W. Daily, Saturation of fluorescence in flames with a Gaussian laser beam, Appl. Opt. 17 (2) (1978) 225–229.

[154] G. Sutton, A. Levick, G. Edwards, D. Greenhalgh, A combustion temperature and species standard for the calibration of laser diagnostic techniques, Combust. Flame 147 (1) (2006) 39–48.

[155] P. R. Medwell, B. B. Dally, Effect of fuel composition on jet flames in a heated and diluted oxidant stream, Combust. Flame 159 (10) (2012) 3138–3145.

[156] C. Lawn, Distributions of instantaneous heat release by the cross-correlation of chemiluminescent emissions, Combust. Flame 123 (1) (2000) 227–240.

[157] B. Higgins, M. McQuay, F. Lacas, J.-C. Rolon, N. Darabiha, S. Candel, Systematic measurements of OH chemiluminescence for fuel-lean, high-pressure, premixed, laminar flames, Fuel 80 (1) (2001) 67–74.

[158] L. C. Haber, U. Vandsburger, W. R. Saunders, V. K. Khanna, An examination of the relationship between chemiluminescent light emissions and heat release rate under non-adiabatic conditions, in: ASME Turbo Expo 2000: Power for Land, Sea, and Air, American Society of Mechanical Engineers, 2000, pp. V002T02A041–V002T02A041.

[159] L. Haber, U. Vandsburger, W. Saunders, V. Khanna, An experimental examination of the relationship between chemiluminescent light emissions and heat-release rate under non-adiabatic conditions, Report, DTIC Document (2001).

[160] C. Gibson, P. Gray, J. Griffiths, S. Hasko, Spontaneous ignition of hydrocarbon and related fuels: A fundamental study of thermokinetic interactions, Symp. (Int.) Combust. 20 (1) (1985) 101–109.

[161] C. Brackmann, J. Bood, M. AldÉn, G. Pengloan, O. Andersson, Quantitative measurements of species and temperature in a DME-air counterflow diffusion flame using laser diagnostic methods, Combust. Sci. Technol. 178 (6) (2006) 1165–1184.

[162] C. Espey, J. E. Dec, T. A. Litzinger, D. A. Santavicca, Planar laser rayleigh scattering for quantitative vapor-fuel imaging in a diesel jet, Combust. Flame 109 (1) (1997) 65–86.

[163] F.-Q. Zhao, H. Hiroyasu, The applications of laser Rayleigh scattering to combustion diagnostics, Prog. Energ. Combust. 19 (6) (1993) 447–485.

[164] J. A. Sutton, J. F. Driscoll, Rayleigh scattering cross sections of combustion species at 266, 355, and 532 nm for thermometry applications, Opt. Lett. 29 (22) (2004) 2620–2622.

[165] F. Fuest, R. S. Barlow, J.-Y. Chen, A. Dreizler, Raman/Rayleigh scattering and CO-LIF measurements in laminar and turbulent jet flames of dimethyl ether, Combust. Flame 159 (8) (2012) 2533–2562.

[166] C. S. Yoo, T. Lu, J. H. Chen, C. K. Law, Direct numerical simulations of ignition of a lean n-heptane/air mixture with temperature inhomogeneities at constant volume: Parametric study, Combust. Flame 158 (9) (2011) 1727–1741.

[167] W. Gardiner, Y. Hidaka, T. Tanzawa, Refractivity of combustion gases, Combust. Flame 40 (1981) 213–219.

[168] Z. Li, X. Yu, G. Lequien, T. Lind, M. Jansons, O. Andersson, M. Richter, Comparison of the lift-off lengths obtained by simultaneous OH-LIF and OH* chemiluminescence imaging in an optical heavy-duty diesel engine, Tech. rep. (2015).

[169] M. Tamura, P. A. Berg, J. E. Harrington, J. Luque, J. B. Jeffries, G. P. Smith, D. R. Crosley, Collisional quenching of CH (A), OH (A), and NO (A) in low pressure hydrocarbon flames, Combust. Flame 114 (3) (1998) 502–514.

[170] H. Pitsch, M. Chen, N. Peters, Unsteady flamelet modeling of turbulent hydrogen-air diffusion flames, Symp. (Int.) Combust. 27 (1) (1998) 1057–1064.

[171] M. Evans, P. Medwell, H. Wu, A. Stagni, M. Ihme, Classification and lift-off height prediction of non-premixed MILD and autoignitive flames, Proc. Combust. Inst. 36 (3) (2017) 4297-4304.

[172] O. Desjardins, G. Blanquart, G. Balarac, H. Pitsch, High order conservative finite difference scheme for variable density low Mach number turbulent flows, J. Comput. Phys. 227 (15) (2008) 7125–7159.

[173] G.-S. Jiang, C.-W. Shu, Efficient implementation of weighted ENO schemes, J. Comput. Phys. 126 (1) (1996) 202–228.

[174] M. Germano, U. Piomelli, P. Moin, W. H. Cabot, A dynamic subgrid-scale eddy viscosity model, Physics of Fluids A: Fluid Dynamics 3 (7) (1991) 1760–1765.

[175] C. Meneveau, T. S. Lund, W. H. Cabot, A Lagrangian dynamic subgrid-scale model of turbulence, J. Fluid Mech. 319 (1996) 353–385.

[176] C. D. Pierce, P. Moin, A dynamic model for subgrid-scale variance and dissipation rate of a conserved scalar, Phys. Fluids 10 (12) (1998) 3041.

[177] B. Jochim, M. Korkmaz, H. Pitsch, Scalar dissipation rate based multi-zone model for early-injected and conventional diesel engine combustion, Combust. Flame 175 (2017) 138–154.

[178] N. Peters, Laminar diffusion flamelet models in non-premixed turbulent combustion, Symp. (Int.) Combust. 10 (3) (1984) 319-339.

[179] N. Peters, Laminar flamelet concepts in turbulent combustion, Symp. (Int.) Combust. 21 (1) (1988) 1231-1250.

[180] H. Pitsch, FlameMaster A C++ computer program for 0D combustion and 1D laminar flame calculations. (1998).

[181] H. C. Rodrigues, M. J. Tummers, E. H. van Veen, D. Roekaerts, Spray flame structure in conventional and hot-diluted combustion regime, Combust. Flame 162 (3) (2015) 759–773.

[182] P. R. Medwell, Q. N. Chan, P. A. M. Kalt, Z. T. Alwahabi, B. B. Dally, G. J. Nathan, Development of temperature imaging using two-line atomic fluorescence, Appl. Opt. 48 (6) (2009) 1237–1248.

Appendix A: Supplementary Data for Chapter 7

The following pages contain the supplementary data for the paper entitled: *Structural differences of ethanol and DME jet flames in a hot diluted coflow*

Fuel	T(K)	Z_{st}	X_{CO}	X_{OH}	X_{H}	X_{O}	X_{H_2}
n-heptane	1250/1222/950	0.0098	2.4E-7	2.2E-5	3.2E-9	1.9E-7	3.2E-7
n-heptane	1250/1174/950	0.0288	1.3E-7	2.8E-5	2.2E-9	3.1E-7	1.8E-7
ethanol	1250/1210/950	0.0164	2.4E-7	2.2E-5	3.2E-9	1.9E-7	3.2E-7
ethanol	1250/1144/950	0.0477	1.2E-7	2.8E-5	2.2E-9	3.1E-7	1.7E-7
ethylene	1250/1223/950/934	0.01	2.4E-7	2.2E-5	3.2E-9	1.9E-7	3.2E-7
ethylene	1250/1176/950/903	0.0296	1.2E-7	2.8E-5	2.2E-9	3.1E-7	1.7E-7

Table 1: Inputs including minor species for various cases in the closed homogeneous reactor model.

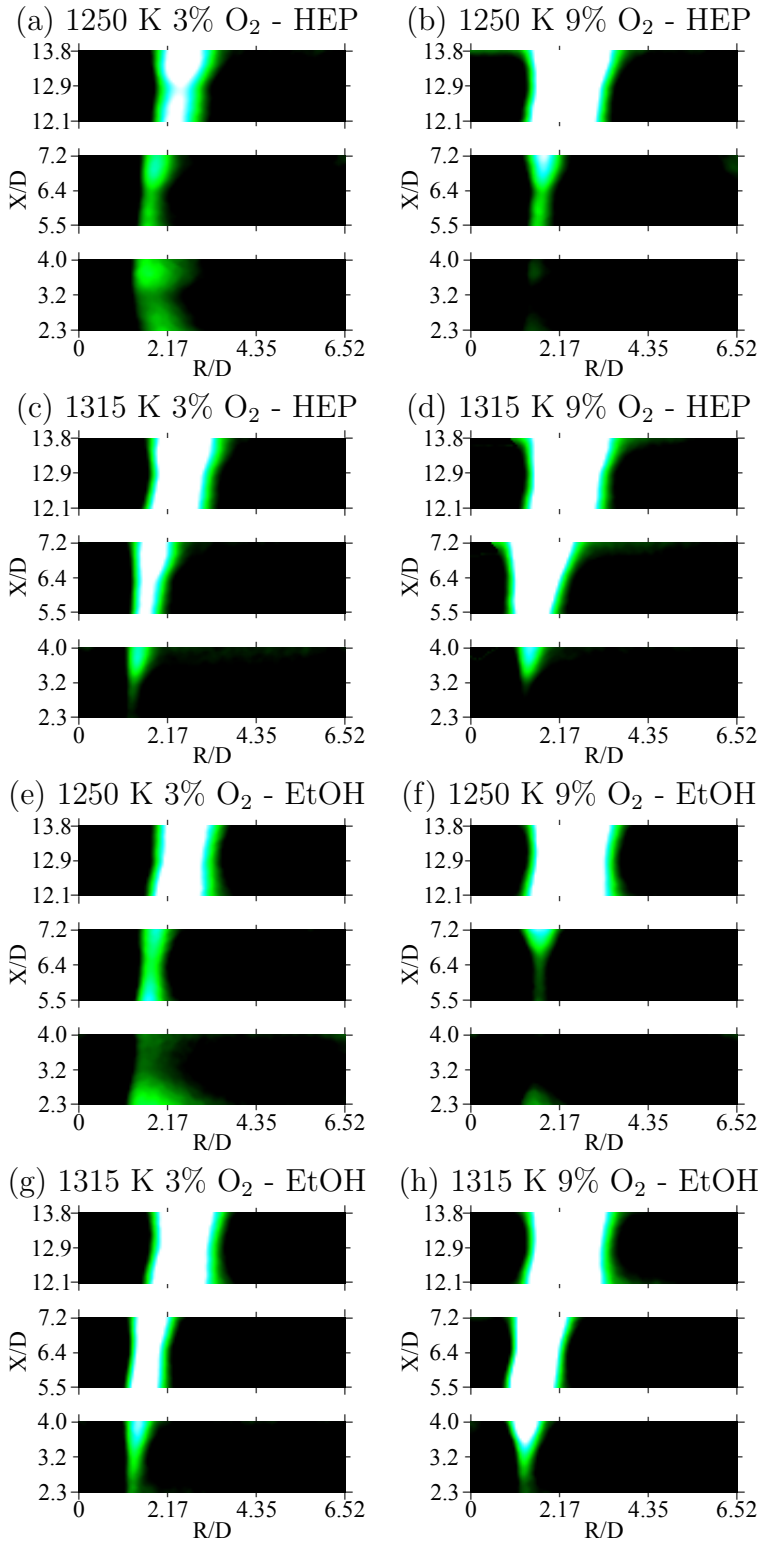

Figure 1: Averaged OH images for *n*-heptane (HEP) and ethanol (EtOH) flames in various coflows. These images are centred at X/D = 3.2 (15 mm), X/D = 6.4 (29 mm) and X/D = 12.9 (59 mm) above the jet exit plane, respectively. The left edge of each image is coincident with the jet centreline, and R is the radial distance from the jet centreline. Each image is 8 × 30 mm.

Appendix B: Papers Included in this Thesis-by-publication

Journal articles

J. Ye, P.R. Medwell, E. Varea, S. Kruse, B.B. Dally, H.G. Pitsch, An experimental study on MILD combustion of prevaporised liquid fuels, Appl. Energy 151(2015) 93-101

J. Ye, P.R. Medwell, B.B. Dally, M.J. Evans, The transition of ethanol flames from conventional to MILD combustion, Combust. Flame 171 (2016) 173-184.

J. Ye, P.R. Medwell, M.J. Evans, B.B. Dally, Characteristics of Turbulent *n*-Heptane Jet Flames in a Hot and Diluted Coflow, accepted on 23rd May 2017, Combust. Flame, DOI:10.1016/j.combustflame.2017.05.027.

J. Ye, P. R. Medwell, K. Kleinheinz, M. J. Evans, B. B. Dally, H. G. Pitsch, Structural Differences of Ethanol and DME Jet Flames in a Hot Diluted Coflow, submitted to Combust. Flame on 4th June 2017, CNF-D-17-00396

Appendix C: Publications Related to this Thesis

Journal articles

M.J. Evans, P.R. Medwell, Z.F. Tian, **J. Ye**, A. Frassoldati, A. Cuoci, Effects of Oxidant Stream Composition on Non-Premixed Laminar Flames with Heated and Diluted Coflows, Combust. Flame 178 (2017) 297310.

M.J. Evans, A. Chinnici, P.R. Medwell, **J. Ye**, Ignition Features of Methane and Ethylene Fuel-Blends in Hot and Diluted Coflows, Fuel 203 (2017) 279289.

Conference papers

J. Ye, P.R. Medwell, B.B. Dally, M.J. Evans (2015), Quantitative Rayleigh temperature imaging in turbulent flames of prevaporised n-heptane, In Proceedings of the 7th Australian Conference on Laser Diagnostics in Fluid Mechanics and Combustion, The University of Melbourne, Melbourne, Australia. 9-11 December 2015. ISBN: 978-0-646-94892-8.

J. Ye, P.R. Medwell, M.J. Evans, B.B. Dally (2015), The impact of carrier gas on ethanol flame behaviour in a Jet in Hot Coflow (JHC) burner, In Proceedings of the Australian Combustion Symposium, The University of Melbourne, Melbourne, Australia. 7-9 December 2015. ISSN: 1839-8170 (Print), 1839-8162 (Online).

M.J. Evans, P.R. Medwell **J. Ye** (2015), Laser-Induced Fluorescence of Hydroxyl in Ethylene Jet Flames in Hot and Diluted Coows, In Proceedings of the 7th Australian Conference on Laser Diagnostics in Fluid Mechanics and Combustion, The University of Melbourne, Melbourne, Australia. 9-11 December 2015. ISBN: 978-0-646-94892-8.